DEVELOPMENT OF HETEROGENEOUS NANOCATALYSTS FOR OXIDATION, REDUCTION AND PHOTO-DEGRADATION REACTIONS

A Thesis submitted in the partial fulfillment of the requirements for the award of the degree of

DOCTOR OF PHILOSOPHY

IN

CHEMICAL ENGINEERING

By

Ms. VIVIDHA KONDBA LANDGE

(ROLL NO: 718154)

Under the guidance of

PROF. SHIRISH H. SONAWANE

Professor

and

PROF. G. UDAY BHASKAR BABU

Associate Professor

DEPARTMENT OF CHEMICAL ENGINEERING

NATIONAL INSTITUTE OF TECHNOLOGY

WARANGAL-506 004 (T.S), INDIA

June 2023

Dedicated

to

- **My beloved Mother and Father, without them it was not possible to be at this platform.**
- **To my lovely husband, without whom I could not imagine the path of research. He is always a pillar of strength for me to do all my research work.**
- **All of my Teachers and Professors who educated me and pushed me to think positively.**

CERTIFICATE

This is to certify that the thesis entitled **"Development of Heterogeneous Nanocatalysts for Oxidation, Reduction and Photo-Degradation Reactions",** that is being submitted by **Ms.Vividha Kondba Landge,** in partial fulfillment for the award of Doctor of Philosophy (**Ph. D)** in the Department of Chemical Engineering, National Institute of Technology, Warangal, is a record of bonafide work carried out by him under my guidance and supervision. The results of embodied in this thesis have not been submitted to any other Universities or Institutes for the award of any degree or diploma.

Dr. Shirish Hari Sonawane
Professor
Department of Chemical Engineering
National Institute of Technology, Warangal.

Dr. G. Uday Bhaskar Babu
Associate Professor
Department of Chemical Engineering
National Institute of Technology, Warangal.

DECLARATION

This is to certify that the work presented in the thesis entitled **"Development of Heterogeneous Nanocatalysts for Oxidation, Reduction and Photo-Degradation Reactions"**, is a bonafied work done by me under the supervision of Prof. Shirish H. Sonawane, and Prof. G. Uday Bhaskar Babu, and it was not submitted elsewhere for the award of any degree.

I declare that this written submission represents my idea in my own words and where other's ideas or words have not been included. I have adequately cited and referenced the original sources. I also declare that I have adhered to all principles of academic honesty and integrity and have not misinterpreted or fabricated or falsified any idea/data/fact/source in my submission. I understand that any violation of the above will be a cause for disciplinary action by the Institute and can also evoke penal action from the sources which have thus not been properly cited or from whom proper permission has not taken when needed.

Date:

Place: Warangal

(Ms. Vividha Kondba Landge)
Research Scholar,
Roll No.718154

ACKNOWLEDGEMENT

I take the opportunity to express my heartfelt adulation and gratitude to my supervisor, **Dr. SHIRISH H. SONAWANE**, Professor, and **Dr. G. UDAY BHASKAR BABU,** Associate professor, Chemical Engineering Department, National Institute of Technology, Warangal for their unreserved guidance, constructive suggestions, thought provoking discussions and unabashed inspiration in nurturing this research work. It has been a benediction for me to spend many opportune moments under the guidance of the perfectionist at the acme of professionalism. The present work is a testimony to his alacrity, inspiration and ardent personal interest, taken by him during the course of this thesis work in its present form.

I wish to sincerely thank university authorities, **Prof. BIDYADHAR SUBUDHI**, Director, National Institute of Technology, Warangal and other top officials who gave me an opportunity to carry out research work.

I also sincerely thank **Dr. P. V. Suresh**, Professor, Head, Chemical Engineering Department, National Institute of Technology, Warangal for his continuous support towards carrying out research work, timely suggestions, support and providing the necessary departmental facilities and services during successful completion of research work.

I wish to express my sincere and whole hearted thanks and gratitude to my doctoral scrutiny committee (DSC) members, **Dr. S. Srinath,** Professor, **Dr. Vidyasagar Shilapuram**, Associate professor, Department of Chemical Engineering, and **Dr. Prakash Saudagar**, Associate Professor, Department of Biotechnology, National Institute of Technology, Warangal for their kind help, encouragement and valuable suggestions for successful completion of research work.

I would like to extend my thanks to all the faculty members in Department of Chemical Engineering for their valuable suggestions and encouragement.

I am also thankful to all the supporting and technical staff of Department of Chemical Engineering who has directly or indirectly helped me during the course of my work.

I am thankful to all my fellow research scholars and colleagues specially from sonoprocess facility, **Dr. Prashant Suryawanshi, Dr. Uday D. Bagale, Dr. Rajesh Kumar, Dr. M. Yadagiri, Dr. D. Srinivasa Rao, Dr. P. Narasimha, Dr. Swapnil Adsul, Dr. Vikas S.**

Hakke, Dr. Shital B. Podtar, Mr. P. Dilipkumar, Mr. Yogesh Patil, Mr. Surya Teja, Mr. Sivaprakash S., Mrs. Suvarna Khelkar, Mrs. Anita Zade, Mrs. Sneha Korpe, Dr. Subadarshini Das, Mr. Shashi Gupta, Dr. Gajanan Surywanshi, Dr. Harshal Patil, Dr. Abhay Lingayat and many other friends, for always standing by my side and sharing a great relationship as compassionate friends. I will always cherish the warmth shown by them.

I take this opportunity to sincerely acknowledge the **Science and Engineering Research Board (SERB) division of Government of India, Sanction No. EMR/20I6/007585**, 2018 for providing the financial assistance.

Words are inadequate to express my thanks to all my family members for their constant support, co-operation, love and affection whose blessings made my journey worth effort. My special appreciation is to my father **Sri. Kondba Tukaram Landge**, mother **Mrs. Kanta Kondba Landge**, who has been a constant source of encouragement for my higher studies. The support of my husband, **Mr. Vikas S . Hakke**, and my beautiful daughter, **Ms. Medhanshi V. Hakke**, has been invaluable to me while I have carried out this study.

I express my gratitude towards my lovely sister **Mrs. Sneha Sagar Kalambe**, and supporting brother **Mr. Chaitanya Kondba Lange**, and all family members for their love and support.

(Ms. Vividha Kondba Landge)

Abstract

The determination of product yields, including selectivity and activity, is typically contingent upon the specific reaction conditions and reactants employed. The yields of products can be altered through catalyst modification, which involves the incorporation of supports, promoters, and preparation techniques. The incorporation of a secondary metal or metal oxide as a promoter to create nanocomposites (NCs) has proven effective in enhancing both the yield and selectivity of the process. The occurrence of synergistic and bi-functional effects typically results in an enhancement of reaction rates. Furthermore, these could potentially result in the formation of novel reaction routes.

The process of modifying a catalyst can be accomplished through a variety of techniques, including hydrothermal, chemical coprecipitation, sol-gel, and solvothermal methods. The majority of these techniques necessitate a multi-step process, rigorous temperature and pressure conditions, and hazardous chemicals, resulting in a time-consuming procedure. The sonochemical technique is not only rapid, environmentally sustainable, and economical approach but also can offer shortest mechanism, different reaction pathways, nanostructures with multiple surface defects necessary for the unique morphology. Furthermore, the sonochemical method has demonstrated its utility, versatility, and potential in synthesizing novel materials possessing exceptional characteristics.

Thus, the present work reports the synthesis and characterization of bimetallic Pt-Cu/C (flower-shaped) and Cu-Ni/TiO_2 NCs; hybrid inorganic (metal)-organic Pt-Co/cellulose nanofibers (CNFs) and Ag-Co/CNFs NCs; and binary metal oxide Bi_2O_3-ZnO/bentonite clay and Cu-ZnO/TiO_2 NCs using the sonochemical approach as heterogeneous catalysts for the selected catalytic reactions, i.e., oxidation (Glycerol oxidation reaction), reduction (4-nitrophenol reduction) and degradation reaction (Congo red photodegradation).

The catalytic activity of the synthesized Pt−Cu/C and Cu-Ni/TiO_2 NCs was studied for the glycerol (GLY) oxidation reaction. The GLY conversion of 96 % was achieved within 1 h of reaction time with the selectivity (S) of 64 % towards glyceric acid when Pt-Cu/C was used as

catalyst. While when the reaction was conducted with Cu-Ni/TiO_2 catalyst conversion of 94 % was achieved within 30 min of reaction time with ultrasound assistance whereas normal batch reaction resulted in 29 % conversion after 30 min of reaction time. Yield (Y) of 91 % was obtained towards lactic acid within 20 min of reaction time while after 1.25 h of reaction time $Y_{Lactic\ acid}$ = 28 % & $Y_{Formic\ acid}$ = 59 % was obtained.

Further, the catalytic performance of Pt-Co/CNF and Ag-Co/CNF was evaluated for reduction of 4-nitrophenol (4-NP) to 4-aminophenol (4-AP). The complete conversion of 4-NP was obtained within 98 s of reaction time over Pt-Co/CNF NC catalyst with kapp = 0.028 s^{-1} whereas the reduction of 4-NP was completed within 110 s (kapp = 0.0172 s^{-1}) with Ag-Co/CNF. Moreover, the Bi_2O_3-ZnO/bentonite clay and Cu-ZnO/TiO_2 NC catalysts exhibited good catalytic activity with kapp = 0.0291 min^{-1} and kapp = 0.091 min^{-1} respectively towards degradation of CR. The superior visible light absorption capacity was obtained for Cu-ZnO/TiO_2 NC catalyst resulting in complete degradation of CR within 20 min of sun-light irradiation.

Overall, it was observed that, the synthesized NCs showed remarkable enhancement in the conversion of reactants, and selectivity of products without compromising the stability of these heterogeneous NC catalysts. The reusability studies (4-5 times) of as-prepared NC catalysts showed no significant loss in the activity of catalyst and conversion of reactants.

Keywords: Heterogeneous catalysts, nanocomposites, sonochemical approach, glycerol oxidation, reduction, photocatalytic degradation.

Table of Contents

List of Figures

List of Schemes

List of Tables

Abbreviations

IUPAC = International Union of Pure and Applied Chemistry

NP = Nanoparticle

NC = Nanocomposite

S = Selectivity

MOF = Metal-organic frameworks

GO = Graphene oxide

rGO = Reduced graphene oxide

GLY = Glycerol

CR = Congo red

4-NP = 4-nitrophenol

LPO = Liquid phase oxidation

GA = Glyceric acid

TA = Tartronic acid

OA = Oxalic acid

LA = Lactic acid

GLYA = Glycolic acid

AA = Acetic acid

FA = Formic acid

DHA = Dihydroxyacetone

HPA = Hydroxypiruvic acid

GLYAD = Glyceraldehyde

AOP = Advanced oxidation process

4-AP = 4-aminophenol

LH = Langmuir-Hinshelwood

VB = Valence band

CB = Conduction band

Y = Yield

S_{GA} = Selectivity of Glyceric acid

TOF = Turn over frequency

X = Conversion

X_{GLY} = Glycerol conversion

S_{LA} = Selectivity to lactic acid

K = rate constant

CNC = Cellulose nanocrystal

HNC = Hybrid/hetero nanocomposites

BNP = Bimetallic nanoparticle

Eg = Band gap

MOF = Metal-organic framework

MB = Methylene blue

XRD = X-ray diffraction

JCPDS = Joint Committee on Powder Diffraction Standard

HR-TEM = High resolution transmission electron microscopy

SEM = scanning electron microscopy

EDX = Energy dispersive X-ray analysis

FTIR = Fourier transform infrared spectrophotometry

ICP-OES = Inductively coupled plasma optical emission spectroscopy

BET = Brunauer–Emmett–Teller

BJH = Barrett–Joyner–Halenda

^{1}H-NMR = proton nuclear magnetic resonance

HPLC = high-performance liquid chromatography

FE-SEM = Field emission scanning electron microscopy

NHE- Normal hydrogen electrode

CNF = Cellulose nanofibers

CA = Cellulose acetate

CI = Crystallinity index

EM = electron mediator

RP = reduction photocatalyst

OP = oxidation photocatalyst

Chapter 1.

Introduction and Objectives

1.1 Introduction to catalysis

In the fields of chemistry, physics, and biology, catalysis plays a vital role. As an increasing percentage of industrial processes between 85% and 90% include at least one catalyst phase, it has grown to be one of the most crucial areas in chemistry, chemical engineering, and, more lately, environmental chemistry [1]. A catalyst is a material that can speed up or slow down a chemical reaction without being consumed, and catalysis is best understood as the quickening of a chemical reaction caused by the existence of a catalyst. A catalyst, according to the International Union of Pure and Applied Chemistry (IUPAC), is a material that improves the pace of a reaction without changing the overall standard Gibbs energy change in the reaction; the process is known as catalysis [2].

Use of a catalyst that preferentially speeds up one reaction compared to the other can affect the distribution of products when a single substance or mixture of substances experiences two or more parallel reactions that result in distinct products. By selecting the appropriate catalyst, one reaction can be made to happen to the point where it virtually excludes another. This type of discrimination is the basis for many significant uses of catalysis [1,3]. The principal role of a catalyst is to decrease the activation energy of a chemical reaction and, in the context of a reaction that produces multiple products, to enhance selectivity. The latter is a significant concern as it helps prevent the production of various undesirable by-products. [4,5].

Catalysis is frequently divided into heterogeneous, homogeneous, and bio-catalysis categories. [6]. In homogeneous catalysis, both the reactants and the catalyst are in the same phase. Most of the time, everything will be in the form of a gas or a liquid. However extracting homogeneous catalysts from solution has proven to be a significant issue, and they are costly transition metal complexes. Many homogeneous catalysts have limited temperature ranges of operation and exhibit sluggish decomposition rates in solution, limiting their usefulness. To accelerate chemical processes, bio-catalysis makes use of naturally occurring substances like enzymes or even complete cells. A substrate is the reactant in an enzyme-catalyzed reaction, which is converted by an enzyme into the desired product. Proteins are the most common type of enzyme, and they are used in many different biochemical processes.

The limited application, difficulty in maintaining homogeneity, lower conversion rates, poor selectivity and the cost for the production of homogenous catalyst were the major issues for

application of homogenous catalyst [3]. Whereas, the use of the bio-catalyst produced by microorganisms is restricted since it requires a precise, complex process. In addition to this, there are restrictions on its manufacture in large quantities. The heterogeneous catalysis refers to the catalytic system in which catalyst is present in a different phase from the reactants. In heterogeneous catalysis, the catalyst is often a solid, whereas the reactants are either liquids or gases. In this case, a cycle of molecular adsorption, reaction, and desorption occurs at the catalyst surface which determines the reaction mechanism. Heterogeneous catalysis is very important because it enables faster, large-scale production and the selective product formation [3].

1.2 Heterogeneous catalysis

Heterogeneous catalysis is widely utilized in various industrial processes due to its remarkable ability to enhance reaction rates in a cost-effective manner, while ensuring high conversion and selectivity of the final product. The capacity for heterogeneous catalysts to be recycled facilitates environmentally conscious and sustainable production practices, while mitigating the issue of secondary pollution. Currently, heterogeneous catalysts hold significant importance in the production of over 80% of global chemical products [7]. Several industries rely on heterogeneous catalysis, including: petroleum refining, energy generation, synthetic fibre and plastics manufacture, the production of a wide variety of speciality chemicals and chemical intermediates, food processing, medicine and pharmaceutical compounds production, value added chemicals and so on, more recently for the improvement of environmental concerns (pollution, selectivity in order to prevent futile by-products) [1,5,8].

It's important to take into account that heterogeneous catalysts make up the vast majority of the industrial catalyst field. The catalyst may be essential to the reaction's progression, or it may simply boost the process's efficiency. An improvement in the efficacy of an industrial process is generally favourable to the environment since it eliminates waste products, more efficiently utilises reactants, uses lower temperatures and hence less energy, and so on [6]. The efficacy of a heterogeneous catalytic reaction is determined by three fundamental elementary processes, namely adsorption, surface reactions, and desorption, which are linked to a solid surface from a scientific perspective. The progress of heterogeneous catalysis is closely linked to the understanding of surface and interface science. This involves addressing significant challenges in three key domains: catalyst synthesis and design, in situ characterization, and comprehending the intricacies of catalysis. The process of catalyst design and synthesis

involves the deliberate selection of an appropriate active component to achieve the desired chemical reactions in catalysis. The achievement of accurate regulation over catalytic constituents on a catalyst support necessitates the utilization of advanced synthesis methodologies and scientific expertise to facilitate the scaling up process and meet the demands of practical manufacturing.

An instance that exemplifies this phenomenon is the production of elevated alcohols from syngas, necessitating the presence of two discrete metal sites in close proximity on a surface to facilitate a collaborative catalytic impact. The incorporation of multiple catalysts within a unified environment is a crucial aspect of enhancing process intensification [9,10].

1.2.1 Metal nanoparticle used as catalyst

Metallic nanoparticles (NPs) are known to have significant impact in the field of catalysis. Metallic NPs that possess a greater surface area and a higher number of active sites have been observed to facilitate accelerated reactions and augment the yield of the final product [11]. The particles in question can be categorized into two primary groups, namely noble-metal-supported metal NPs (such as Au, Pt, Ag, etc.) and non-noble-metal-based NPs (such as Fe, Cu, Ni, Co, etc.).

The benefits of utilizing nanoscale particles in heterogeneous catalysis have been acknowledged for a considerable period of time. Metallic NPs, especially those that are dispersed on the surface of an oxide or other support, exhibit superior catalytic activity and selectivity in comparison to their bulk counterparts [12,13]. The specific catalytic activity of metal NPs can be significantly enhanced by the increasing dispersion, which is characterized by an increasing surface-to-volume ratio, as the particle size decreases. Moreover, the chemical characteristics of these particles can be entirely transformed by the quantum-confinement effects that occur in very small particles. Consequently, a significant amount of attention has been directed towards the production of NPs with accurate size manipulation. The synthesis of nanocatalysts with adjustable size, shape, and composition has been made possible by the significant progress in colloid chemistry in recent years [14]. These nanocatalysts have been utilized as exemplary catalytic systems to explore the correlations between synthesis, structure, and activity in nanocatalysts [15,16].

1.2.2 Metal oxides NPs used as catalyst

The catalytic performance of metal oxides such as ZnO, TiO_2, CuO, CeO_2, etc. can be improved by reducing their particle size to the nanoscale, resulting in increased catalytic activity per unit weight [17–19]. This phenomenon is observed in catalysis. The primary focus of initial investigations was centred on the examination of the size impact. However, there has been a recent expansion and shift in research to encompass the influence of the oxide particle morphology, which is linked to the catalyst preparation technique [20]. In the field of catalysis science involving metal oxides, recent studies have facilitated the creation of catalysts possessing elevated selectivity through the implementation of novel preparation and activation methodologies [21]. Currently, it is widely acknowledged that the efficacy of a solid catalyst is contingent upon various factors, including the dimensions of its solid particles, their morphology, which may confer advantages to specific facets and is critical for reactions that are sensitive to structure, degree of crystallinity, chemical composition (whether it is bulk or surface), and the methods employed for their preparation and activation [22]. Recent advancements in the production methods of metal oxide catalysts have yielded catalysts that demonstrate active singular sites, which theoretically result in 100% selectivity. Nanocrystals exhibit exceptional catalytic performance owing to their high density of surface sites, which is attributed to their small size, typically a few nanometres. In order to facilitate efficient dispersion of metal oxide particles and synergistic activation of substrates, it is essential to make use of appropriate support materials like carbons, alumina, zeolites, silica, mesoporous silicas like Mobil Composition of Matter No. 41 (MCM-41) and Santa Barbara Amorphous-15 (SBA-15), silica-alumina, and metal-organic frameworks (MOFs) [23–25]. This can lead to an increase in electron conductivity, which is a significant parameter in redox reactions, as well as thermal conductivity, which is a critical factor in exo/endothermal reactions in industrial reactors, among other benefits. Catalyst performance is based on a number of characteristics, including activity, selectivity, stability, and regeneration capability. Over the past six decades, enhanced research and improved chemical engineering techniques for reactors have contributed to the refinement of these properties in metal oxide-based catalytic processes utilized in industrial settings.

1.2.3 Significance of supports

The catalytic efficacy of metal NPs is significantly influenced by the characteristics of the substrate. The support plays a crucial role in facilitating efficient pathways towards the target product, while particle size stabilization serves to mitigate spontaneous growth of small metal NPs [9]. Important requirements for catalyst supports are a large surface area, strong interaction between the metal and the support, and the presence of active sites that take part in the process of the reaction. Insoluble solids such as active carbons, organic polymers, and inorganic metal oxides with large surface areas are commonly utilized as support materials [26]. The availability of suspensions containing graphene oxide (GO), reduced GO, and other graphene-based materials has presented novel prospects for the advancement of supported magnetic NPs as catalysts [27]. Graphene-based materials possess a multitude of advantageous properties that are absent in conventional solid supports, rendering them highly effective as supports [19].

1.3 Heterogeneous catalysis and Green Chemistry

Catalysts have the ability to significantly increase the rate of chemical reactions, often by several orders of magnitude. This allows the reactions to occur under optimal thermodynamic conditions, while also reducing the required temperature and pressure levels. Efficient catalysts, when combined with optimised reactor and total plant design, play a crucial role in minimising the investment and operation costs of chemical processes [6]. The utilisation of catalysis has been observed to contribute to the reduction of atmospheric pollution, the development of ecologically sustainable catalytic technologies, and the innovation of novel energy generation processes. As such, it is widely regarded as a fundamental aspect of green chemistry in the context of environmental preservation. The chemical industry is increasingly recognising the necessity for implementing environmentally sustainable processes. The current movement towards 'Green Chemistry' or 'Sustainable Technology' requires a fundamental change in the traditional approach to process efficiency, which has historically prioritised chemical yield. Instead, the new approach assigns economic value to the elimination of waste at the source and the avoidance of toxic and/or hazardous substances [28]. The field of green chemistry pertains to the ecological implications of chemical products and their manufacturing procedures.

The formulation of twelve principles of green chemistry has been suggested as a framework for contemplating the conception, advancement, and execution of chemical products and procedures. The aforementioned principles empower scientists and engineers to safeguard and

enhance the economy, society, and the environment through the exploration of inventive and resourceful methods to curtail waste, preserve energy, and identify substitutes for perilous substances [29]. The adherence to the standards of Green chemistry necessitates the exploration of novel chemical products and processes that are more ecologically sound. The attainment of an optimal synthesis can be facilitated through the utilisation of various technologies that align with the fundamentals of green chemistry. These technologies encompass catalysis, alternative energy sources, process intensification, and supercritical fluids [30]. Given that the separation stage is the primary contributor to waste generation in chemical processes, it would be prudent to prioritise efforts towards its optimisation. Chemical processes generate a significant quantity of waste on a daily basis. Utilising stoichiometric equivalents, specifically, results in the generation of undesired by-products such as inorganic salts [31]. In this particular context, certain areas of synthetic methodology have been identified as presenting significant challenges. The chemical processes of acid-catalyzed reactions, selective oxidations, halogenations, base-catalyzed reactions, reductions, metal-catalyzed reactions, and phase-transfer-catalyzed reactions are of interest [32].

The current study is aimed to synthesize heterogeneous catalysts using a green and energy-efficient method involving cavitation assistance. Various compositions of the catalyst were prepared and analysed. The utilization of a nanoscale bimetallic catalyst composition has been observed in the synthesis of value-added products from biomass-derived chemicals, specifically glycerol. Additionally, this catalyst composition has demonstrated effective degradation of complex pollutants such as congo-red and 4-nitrophenol.

1.4 Catalytic conversions using heterogeneous catalysts

Catalysis has the potential to promote eco-friendly chemical processes by substituting reagents or facilitating more effective processes. The exhibition of their efficacy in diminishing the environmental repercussions of processes and minimizing their expenses will expedite the adoption of sustainable practices in chemistry [6,32]. The utilization of catalytic alternatives is gaining popularity over stoichiometric chemical procedures, enabling chemists to decrease energy and resource usage. This development has been observed in recent times [33]. The concept of greener catalysis involves a shift from stoichiometric processes towards catalytic reactions that employ a variety of catalysts, including organic, organometallic, inorganic, and biological catalysts. Catalysis can serve as a viable approach to mitigate environmental degradation and reduce the emission of various noxious substances. Several significant

processes rely on heterogeneous catalysis, including cracking and hydrotreating of crude oil, alkylations, ethylene epoxidation, water-gas shift reaction, and methane steam reforming, methanation, biomass conversion, hydrogen production, CO_2 conversion, waste water treatment processes, etc. were reported to be effectively catalyzed over various heterogeneous catalysts namely microporous zeolites, mesoporous silicas, and nanostructured metals/metal oxides such as, Co–Mo, Ni–Mo, Ni–W (sulfidic form), HF, solid acids, spinel ferrite NPs, Ag, Ni, Cu, Co, Mo, Au, Pd, Pt, Rh, Ru, Fr-Cr, Cu-Zn, CeO_2, Ni/Al_2O_3, CuO, etc.) [1,34–41].

Kumar et al. [42] used a new generation nanoscale La_2CuO_4 perovskite catalyst to show that benzene can be oxidized in one step with H_2O_2 under mild conditions. The efficiency of converting benzene to phenolic substances was found to be 51 %, and the product's specificity was higher than 99 %. About 65 % of the hydrogen peroxide used in the procedure was actually utilized.

The utilisation of heterogeneous catalysts presents a potential solution to the challenge of separation, as they possess the advantage of being conveniently separated and recycled after the completion of a process. This eliminates the necessity for an aqueous quench or other separation measures that may be detrimental, and also reduces the requirement for raw materials [32]. Therefore, it is indisputable that heterogeneous catalysis has emerged as a fundamental aspect of the Green Chemistry paradigm [28].

The principal areas of heterogeneous catalysis and catalytic reactions encompass selective or total oxidation, reduction, acid and base catalysis, photocatalysis, wastewater treatment, and biomass conversion, as documented in several sources [1,5,38,43,44]. The conversion of alcohols, methanol, CO, olefins, alkenes, and other organic substrates into oxygenic compounds with added value is a significant and crucial chemical reaction, as indicated by various studies [21,38,43,45,46]. Furthermore, catalytic hydrogenation is a widely recognised and essential technique in the field of catalytic organic synthesis. The application of this substance is prevalent in the production of fine and specialty chemicals [47]. Despite being a well-established technology extensively utilised in industrial organic synthesis, catalytic hydrogenation has been found to have novel applications that occasionally emerge in unexpected domains.

1.4.1 Heterogeneous catalytic oxidation reaction

The oxidation transformations have consistently garnered significant attention due to their crucial role in industrial manufacturing and fundamental investigations in organic synthesis and modifications [43]. It can be asserted that oxidation reactions in the production of fine chemicals present a significant demand for environmentally sustainable catalytic alternatives. Oxidation processes are commonly executed using inorganic or organic oxidants, such as permanganates, chromates, organic peroxides, and manganese dioxide, which are often stoichiometric and pose potential hazards and toxicity concerns [48].

The utilisation of conventional hazardous oxidants in stoichiometric proportions results in significant quantities of waste during the separation phase. The implementation of catalytic metal-acid-bromide systems in the production of aromatic carboxylic acids causes emissions due to solvent combustion and corrosion-related issues for the reaction vessels. Furthermore, the utilisation of hazardous organic peroxides generates organic waste by-products [32]. It is evident that there exists a distinct requirement for catalytic substitutes that utilise pristine primary oxidising agents, such as oxygen or hydrogen peroxide, which are environmentally friendly. Hydrogen peroxide is considered a more secure substitute for its organic counterparts due to its by-product being solely water, although this may pose challenges in organic processing. Additionally, catalytic no-solvent air/oxygen systems hold significant appeal in terms of environmental sustainability.

Numerous investigations have been conducted regarding the utilisation of catalysts based on transition metals and metal oxides for catalytic oxidation, with a focus on both economic and environmental considerations. In the recent past, there has been a surge in research endeavours aimed at introducing innovative and environmentally sustainable catalytic systems for oxidation transformations. The trend towards substituting traditional methods with newer catalytic conversions employing diverse metallic catalysts under cleaner and more sustainable conditions has persisted. In recent times, researchers have directed significant attention towards heterogeneous catalytic systems as a means of addressing the limitations of homogeneous counterparts. This is due to the regenerability, reusability, ease of handling, and insolubility in solvents that are characteristic of heterogeneous catalytic systems [8,35,43].

1.4.1.1 Heterogeneous catalytic oxidation of glycerol

The utilization of non-fossil resources is crucial in addressing environmental concerns and promoting the development of a sustainable society, particularly in the context of chemicals

and energy resources. Cellulosic biomass is a potential source of chemicals, among other possibilities. In recent years, there has been extensive research conducted on the conversion of biomass and biomass-derived products. Amidst various oxidation processes, the liquid phase oxidation (LPO) of bio-inferred sugars and polyols is one of the foremost vital routes to upgrade inexhaustible biomass to valuable chemicals, significantly for production of carboxylic acids. Glycerol (GLY) is one such polyol and the coproduct of biodiesel production, thus is a biomass-derived feedstock [49]. In the past decades, it has become a key raw material because of its low price and large availability [9]. GLY is an excellent choice for obtaining many valuable products such as glyceric acid (GA), tartronic acid (TA), oxalic acid (OA), lactic acid (LA), glycolic acid (GLYA), acetic acid (AA), and formic acid (FA) and hence, is getting importance because of the booming biorefinery and pharmaceutical industry [11].

Various heterogeneous catalysts comprising of noble and non-noble metals (Pt, Pd, Ag, Au, Cu, Co, Ni, etc.) have been studied for the selective oxidation of glycerol. Jin et al. [50] reported excellent combined yield of 88 % for TA and OA from GLY, using cobalt-based catalyst in the presence of molecular oxygen, after 24 hours of reaction time. The oxidation of GLY into LA was investigated by Arcanjo et al. [51] utilizing activated carbon with Pd as heterogeneous catalysts. A GLY conversion of approximately 99 % was attained with a selectivity of 68 % towards LA through the utilization of 10 % Pd/C catalysts at a reaction temperature of 230 ^{o}C. Palacio et al. [52] investigated GLY oxidation to LA using Cerium oxide supported Co_3O_4 particles as catalysts at 250 °C under basic environment and obtained selective GLY conversion of 85.7 % to LA (79.8 % selectivity).

As reported earlier, the oxidation of glycerol follows two main reaction pathways as presented in Scheme 1.1. One involves the oxidation of secondary alcohol, leading to the generation of dihydroxyacetone (DHA) and hydroxypiruvic acid (HPA), while the other pathway involves the oxidation of primary alcohols, resulting in the formation of glyceraldehyde (GLYAD) and GA [53]. The process of selectively oxidizing higher alcohols through the use of heterogeneous catalysts holds significant importance in the production of fine chemicals that possess enhanced value. Despite the industrial establishment of the primary alcohol oxidation process, there exists a dearth of fundamental comprehension pertaining to the intricacy of the catalysts and their dynamics during reaction conditions, particularly in the presence of higher alcohols and liquid-phase reaction media. Furthermore, it is imperative to create novel materials that exhibit enhanced levels of activity, selectivity, and stability. In consideration with this, valorization of GLY through partial oxidation was chosen as the first system and a model oxidation reaction

in the present study.

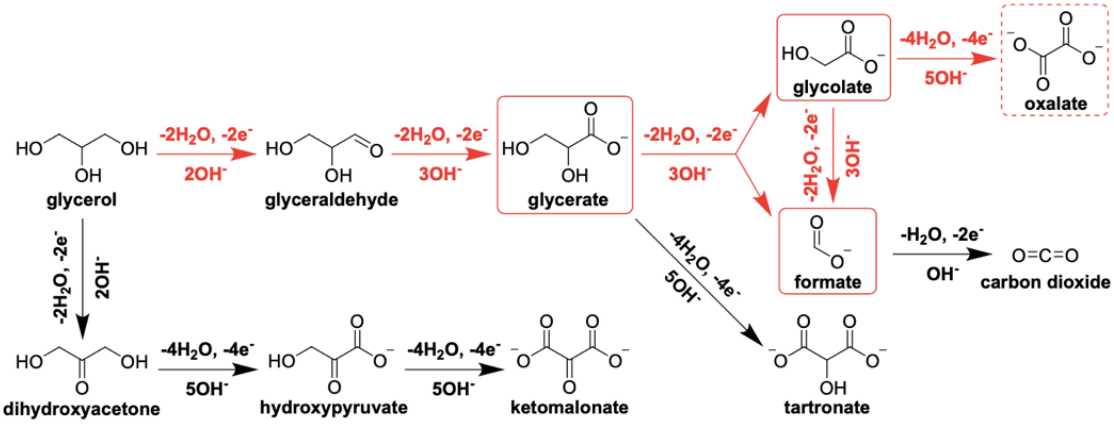

Scheme 1.1 Prospective reaction mechanisms for the alkaline GLY oxidation to diverse value-added products [Reprinted from Ref. [54] with permission, copyright Elsevier].

1.4.2 Catalytic treatment of organic pollutants (Wastewater treatment)

In recent years, the increasing rate of environmental pollution due to the rapid growth of industrialisation is posing a major threat to the humanity and ecosystem, as huge amounts of lethal pollutants in industrial wastewater are discharged into water streams without any effective treatment [10]. Different physical, chemical and biological techniques, for instance, flocculation, adsorption, ozonation, chlorination, coagulation, biodegradation, etc. are often employed for the abatement of such organic pollutants present in the wastewater released from various industries. However, employing the above methods just convert the contaminants from one form to another, rather than removing them forever. To overcome these issues, extremely efficient and ecologically benign advanced oxidation processes (AOPs) appear to be the most appropriate method towards the elimination of organic pollutants from wastewater [55]. In modern times, various techniques including UV photolysis/photocatalysis, adsorption, reduction, and (photo) degradation have been employed for the elimination of organic contaminants from sources such as groundwater, freshwater sediments, and wastewater [5]. Catalytic reduction and photocatalytic degradation are of most importance to manufacturing and treatment processes used for reducing noxious organic molecules to safer products.

1.4.2.1 Heterogeneous catalytic reduction of 4-nitrophenol

Nitrophenols are among the most common organic pollutants found in industrial wastewater. Nitrophenols such as 4-nitrophenol (4-NP) are highly toxic to living beings, even in trace amounts, as they can harm the kidney, blood, central nervous system, and liver of humans and animals owing to their extremely mutagenic and carcinogenic nature. However, because of the

significant stability and low water solubility, the degradation of 4-NP to a harmless sub- stance is quite challenging [5]. Conversely, 4-aminophenol (4-AP) is less toxic and can be easily removed and mineralised than 4-NP. Thus, the organic transformation of 4-NP to 4-AP through reduction is imperative, as 4-AP is far more beneficial than 4-NP. For the catalytic hydrogenation, 4-NP must interact with hydrogen (hydride ion) to obtain 4-AP [10]. Sodium borohydride ($NaBH_4$) has been thoroughly investigated as a preferred water-soluble reducing agent and a viable substitute for hydrogen sources in the reduction of hazardous nitro compounds to valuable amino compounds in an aqueous environment [5].

However, the reaction displays high kinetic barriers among equally resisting 4-NP and BH_4^- negative ions; hence, a catalyst is necessary to overcome the kinetic barrier to achieve hydrogenation reaction [8]. In the recent decade, nanomaterials are more attractively explored for their catalytic activity and performances. To overcome the issues of lower hydrogen production rate and kinetic barrier of reaction, the new generation of nanomaterials needs to be explored with a more stable structure, and efficient hydrogen generation. Recently, a variety of competent BNPs have been explored and utilized to accelerate the 4-NP reduction for instance AgCu [56], Ag-Co [10], Hg-Pd [57], PtNi [58], AuAg [59], Pd-Co [60], AuPt [61], AgNi [24], and etc.

According to literature the 4-NP reduction follows pseudo-first-order-reaction kinetics with Langmuir-Hinshelwood (LH) mechanism [20,62,63]. The possible reaction mechanism for 4-NP reduction using Hg-Pd alloy proposed by Harika et. al [57] is as described in Scheme 1.2.

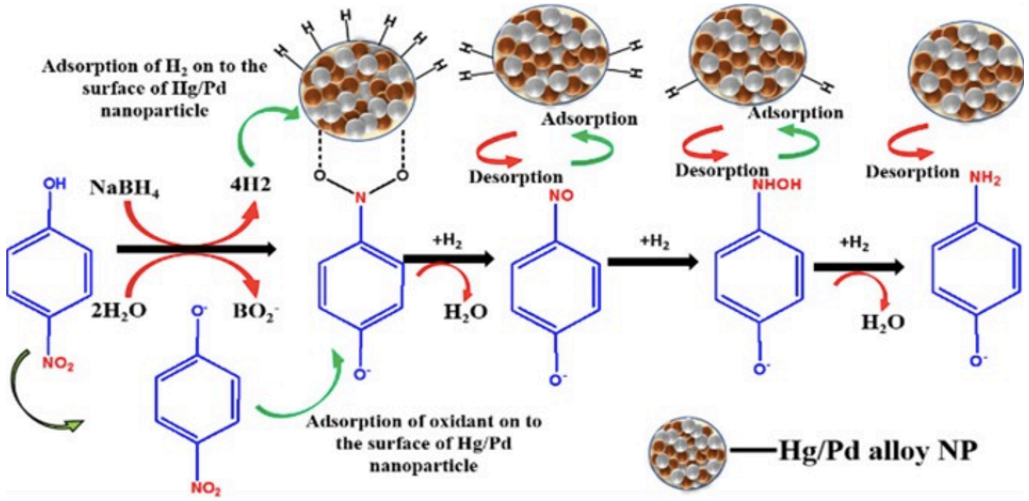

Scheme 1.2 Representative catalytic pathway for 4-NP reduction to 4-AP over Hg/Pd NPs [Reprinted from Ref. [57] with permission, copyright Elsevier].

As stated earlier, to retain the stability by preventing aggregation of the BNPs is still a challenging task and this arises the necessity for opting an appropriate support which may assist

to evade aggregation to certain extent. Hence, reduction of 4-NP using heterogeneous nanocomposite (NC) was used as the model reduction reaction for reduction of organic pollutants as second system in the present study.

1.4.2.2 Photocatalytic degradation of Congo red (Azo dye)

Rhodamine-B, direct black 38, methyl orange, congo red (CR), and other synthetic organic dyes have a minimum of one azo group (-N = N-) that produces distinctive conjugates with other groups that impart colour. The azo group is widely recognised as a human carcinogen. Azo dyes find application in a wide array of industries such as leather, textile, beauty care products, paper, food and packaging industries. The CR is not only a robust azo dye but also a potent organic pollutant. In the presence of aqueous media, its aromatic amine groups exhibit toxicity and can be a threat to humans as well as other livelihoods. Owing to its hazardous nature, especially for human beings, this dye polluted wastewater is becoming a notorious natural danger to our environment. This necessitates removal of these dyes and other organic contaminants from the environment. In this regard, the photocatalytic degradation of CR was chosen to be the third system as a model photocatalytic reaction for degradation of azo dye in present work.

The mechanism of CR dye degradation is based on the advance oxidation process (AOP) in conjugation with heterogeneous photocatalysis. In AOP, the generation of the electron (e^-) and hole (h^+) takes place which induces the formation of potent oxidizing radicals, namely superoxide ($O_2^{-\bullet}$) and hydroxyl ($^{\bullet}OH$), which play a vital role in the mineralization of organic pollutants. Moreover, upon UV-light irradiation, hydrogen atoms generated from water molecules account for the degradation of contaminants by reducing them. When the UV light illuminates the photocatalyst, the electrons present in the valence band (VB) of the photocatalyst get excited and moves towards the conduction band (CB). This results in the generation of the equivalent amount of holes in the VB, leads to a series of reactions which, generate $^{\bullet}OH$ and hydroperoxyl ($HO_2^{-\bullet}$) radicals. The probable mechanism of CR dye degradation on the surface of TiO_2/ZnO–Ag NCs as reported by Pragathiswaran et al. [64] is as illustrated in Figure 1.1. During degradation, initially, the CR dye molecules get adsorbed on the NC surface, and after subjecting to UV irradiation, e^- and h^+ pairs are generated on the ZnO and TiO_2. Followed by the generation of $^{\bullet}OH$, $O_2^{-\bullet}$, and $HO_2^{-\bullet}$ the degradation of CR dye molecules occurs.

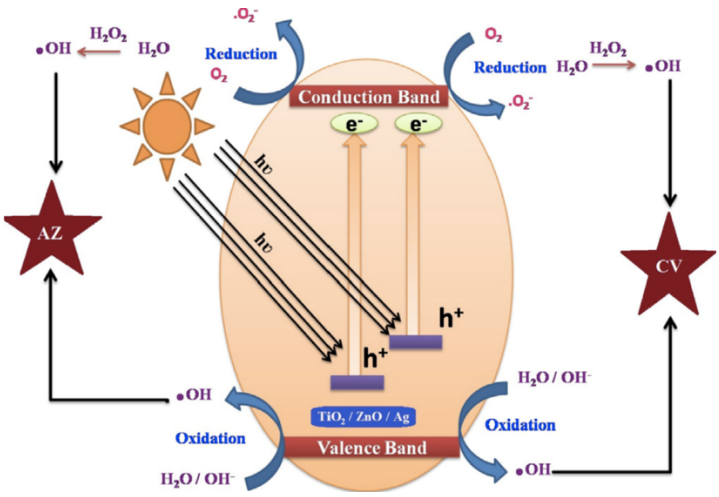

Figure 1.1 Dye degradation processes of TiO_2/ZnO–Ag nanomaterial [Reprinted from Ref. [64] with permission, copyright Elsevier].

1.5 Need for catalyst modification

In recent decades, heterogeneous catalysts consisting of noble and non-noble metals as well as metal oxides have gained prominence due to their demonstrated efficacy in facilitating a diverse range of chemical reactions, including but not limited to oxidation, hydrogenation, and redox reactions [1,3–5,11,65–68]. However, high cost, need for non-commercial ligands, and stability are some inherent issues posed by them, all of which are extremely unfavourable from industrial standpoint and severely restrict their possible application [43]. Thus, future industrial progress necessitates the cruciality of continued investigation into the advancement of novel catalysts endowed with improved attributes and traits. The incorporation of metal and metal oxide catalysis in advanced research has facilitated the creation of highly selective catalysts and novel preparation methodologies [16,37].

A solid catalyst's performance is influenced by its particle size, morphology, composition, and preparation method [15,69]. It is well known that as the size of catalysts is reduced to the nanoscale, catalytic activity can dramatically improve due to the considerable increase in catalytic sites [7]. The emergence of nanoscience has facilitated the prioritisation of bottom-up approaches over top-down methodologies. The utilisation of bottom-up methodologies in the production of heterogeneous catalysts has yielded catalysts featuring individual sites, which have contributed to notable enhancements in selectivity. Nanocrystals, possessing dimensions on the order of a few nanometres, exhibit superior catalytic performance. Though, nanocatalysts are well known for their high activity, they are prone to instability issues caused either due to sintering, leaching or agglomeration [43]. The utilization of a support material

such as silica, carbon, graphene oxide, alumina, among others, can prevent the agglomeration of nanoparticles (NPs) and enhance the stability and recyclability of metallic catalysts, while also mitigating the excessive use of metal reagents [10,70]. As a result, the most important criterion for the design and synthesis of heterogeneous catalysts is the selection of an appropriate, safe, and recyclable support [43]. The support may also play a role in activation of substrate, improvement in electron conductivity during redox reactions, augmentation of thermal conductivity for exo/endothermal reactions, and other processes [10,70]. Furthermore, selectivity, along with activity and stability, is one of the most significant aspects in determining an effective and sustainable catalyst [7]. Thus, researchers are striving to develop catalysts with high activity, improved stability, and exceptional selectivity [37].

The catalytic performance of a catalyst can be altered through catalyst modification techniques such as the addition of supports, promoters, and changes in preparation method, as illustrated in Figure 1.2. The incorporation of an additional metal as a catalyst promoter has been shown to effectively enhance the production of targeted products. Enhancing the yield is a crucial aspect in biomass processing owing to the elevated reactivity of the starting molecules, which results in the generation of undesired by-products that diminish the ultimate yield and pose challenges in the isolation of the intended product. The utilisation of bimetallic catalysts presents a compelling approach due to its multifaceted potentialities. The practical implications of introducing a second metal into a catalyst can be categorised into three primary domains, namely: (i) augmentation of catalytic activity, (ii) alteration of selectivity, and (iii) enhancement of catalyst stability. The phenomenon of promotion can be attributed to a variety of factors, ranging from the basic reduction of the first metal by hydrogen spillover facilitated by the second metal, to more intricate metal interactions.

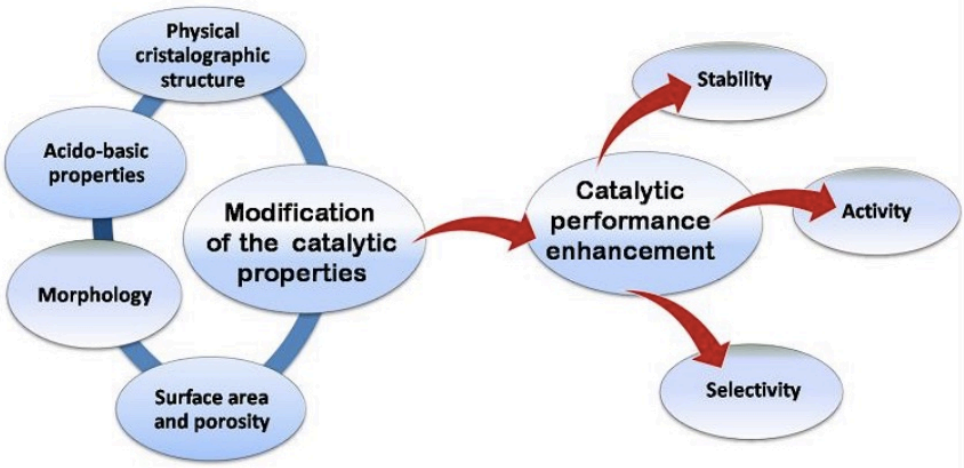

Figure 1.2 Effects of altering catalytic characteristics on catalytic activity.

The catalytic activity and selectivity are commonly influenced by geometric and electronic factors, whereas catalyst stability is enhanced by stabilising effects. The occurrence of synergistic and bi-functional effects typically results in enhanced reaction rates, while also potentially giving rise to novel reaction pathways. An ancillary consequence of promotion arises when the second metallic element assumes a non-metallic role, thereby conferring an additional functionality to the catalyst. This may manifest in the introduction of acid or redox sites, facilitated by the presence of metal oxides. In such instances, the chemical reaction may occur utilizing a bifunctional catalyst, thereby potentially altering the selectivity in contrast to a catalyst composed solely of metal. Distinguishing between a bimetallic catalyst and a bifunctional catalyst can pose a challenge and is contingent upon the extent of reduction of the metals in question. The formation of metal oxides can occur if one of the metals is not fully reduced.

The electronic effect is a significant factor in bimetallic nanocatalysts, as it governs the charge transfer phenomenon. The structural modifications of bimetallic nanocatalysts can occur through the process of alloying the constituent elements. The introduction of bimetallic nanocatalysts provides an additional degree of freedom, as compared to monometallic ones. The comparative catalytic performances of diverse bimetallic nanoparticles have been evaluated. Different methods and correlations have been developed with the help of physical

and spectroscopic measurements. The structural and miscibility characteristics of bimetallic nanocatalysts, as depicted in Figure 1.3, are contingent upon the preparation conditions.

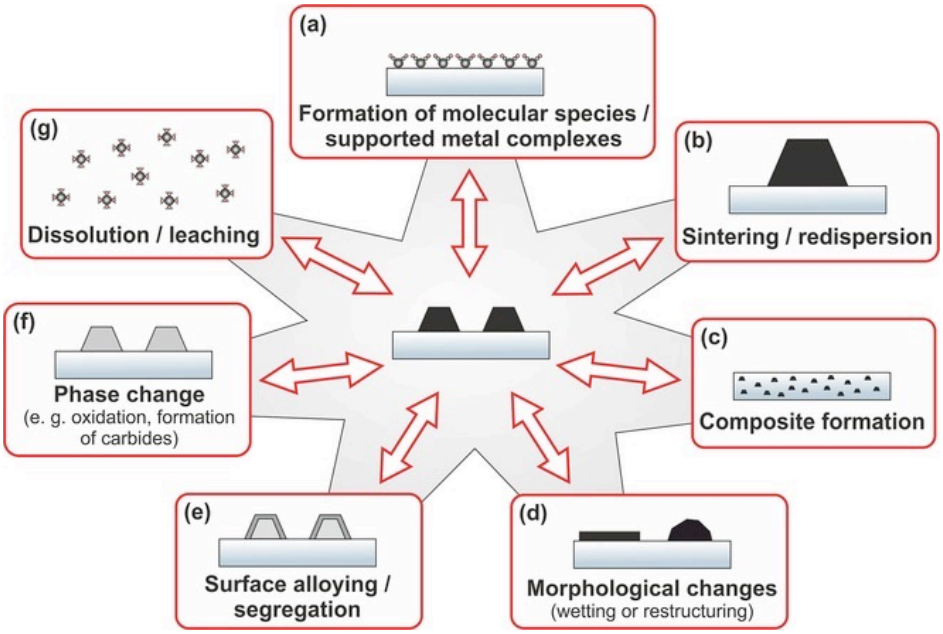

Figure 1.3 Metal catalyst structural alterations and their supports under various conditions [Reprinted from Ref. [71] with permission, copyright Wiley-VCH Verlag GmbH&Co. KGaA, Weinheim].

The traditional catalyst was investigated with the aim of obtaining a high yield while optimizing resource utilization and maximizing chemical reaction conversion. The latest catalysts of the new generation are produced in varying sizes and shapes, possessing distinct surface morphologies that hold significant value in chemical conversion processes. Various catalysts, including Ni-based NCs, C-based, and Co-based materials, have been synthesized at the nanoscale with different metal compositions. These catalysts are utilized not only to achieve favourable conversion conditions in chemical reactions, but also to enhance reaction selectivity. The methods such as acid, based and enzymatic surface treatments was commonly found in the surface modified catalyst. The catalysts that have undergone surface modification exhibit a restricted lifespan and may also be subject to reutilization following the modification process.

The synthesis of bimetallic crystalline structures through the combination of two metal NPs with a minimal amount of binder has emerged as a novel research focus. Numerous techniques have been devised to produce bimetallic catalysts, enabling precise regulation of the creation of bimetallic nanostructures. In the synthesis of BNPs, two primary procedures are commonly delineated. One approach to achieve the synthesis of BNP involves the utilization of seed-mediated reduction and generation. The second category involves the synthesis of BNPs

through a process of concomitant reduction and stabilization. The most commonly utilized techniques for synthesizing supported catalysts involve impregnating precursor salts onto the support, either simultaneously or successively, or utilizing deposition-precipitation. However, these methods have the disadvantage of limited control over the final composition of the nanoparticles and the potential for bimetallic interaction.

The utilization of natural polymer-based metallic catalysts represents a novel approach for catalyst modification. The utilization of alkali metals or alkaline earth oxides (namely CaO and MgO) for the purpose of modifying reforming/oxidation reactions has been widely adopted. This is due to their ability to counteract the acidic sites present in γ-Al_2O_3 and subsequently improve overall stability, as reported in previous studies [72].

1.6 Problem statement and motivation

Typically, the product yields, including selectivity and performance, are established based on the reaction conditions and reactants employed. The yields of products can be altered by modifying the catalyst through the addition of supports, promoters, or changes in the preparation method. The incorporation of a secondary metal or metal oxide as a promoter in the formation of NCs has been shown to effectively enhance both the yield and selectivity of the process [65]. Enhancing the yield is a crucial aspect in biomass processing owing to the elevated functionality of the primary molecules, which results in the generation of by-products that diminish the ultimate yield and complicate the isolation of the intended product. The utilization of NC catalyst presents a compelling approach due to its multifaceted potentialities. The practical implications of introducing a second metal/metal oxide can be categorized into three primary areas: (i) enhancement of catalytic activity, (ii) alteration of selectivity, and (iii) improvement of catalyst stability. Promotion can be a result of various metal interactions, ranging from the facilitation of the reduction of the first metal by hydrogen spillover through the second metal/metal oxide, to more intricate mechanisms.

The catalytic activity and selectivity are commonly influenced by geometric and electronic factors, whereas the stability of the catalyst is enhanced by stabilizing effects. The occurrence of synergistic and bi-functional effects typically results in enhanced reaction rates, and may also facilitate the emergence of novel reaction pathways. An ancillary consequence of promotion arises when the secondary metal assumes a non-metallic role, thereby conferring an additional functionality to the catalyst. This is exemplified by the introduction of acid or redox sites through the incorporation of metal oxides. In such instances, the chemical reaction could

occur utilizing a bifunctional catalyst, potentially leading to altered selectivity in comparison to a catalyst composed solely of metal.

The catalyst modification can be achieved through various methods such as hydrothermal, chemical coprecipitation, sol-gel, and solvothermal approach etc. Most of these methods require a multiple- step procedures, harsh temperature and pressure conditions, toxic chemicals and are time consuming. The sonochemical technique is a rapid, environmentally sustainable, and economical approach. The sonochemical approach has demonstrated its utility, versatility, and potential as a means of synthesising novel materials possessing atypical characteristics [73]. The sonochemical approach exploits the acoustic cavitations effects from ultrasonic exposure to initiate or promote the chemical process [74].

The products of sonochemical synthesis exhibit distinctive characteristics in comparison to materials synthesised through alternative methods, owing to the generation of particles possessing significantly reduced dimensions and elevated surface area [42]. Here, therefore, we present a simple one-pot method for manufacturing NCs utilising ultrasonic irradiation, demonstrating both the technical ease and promising results of this method using seed mediated reduction approach and simultaneous/co-reduction approach was employed. The appropriate utilization of renewable resources such as water, air and biomass is the necessity of today's world. In this regard, the need for the improvement in selectivity and yield for highly functional biomass transformation and the abatement of recalcitrant pollutants from wastewater by employing principles of green chemistry have motivated to carry out the present work in glycerol volarization and wastewater treatment using heterogenous NC catalysts.

1.7 Objectives of the work

The work aims to develop the NC catalysts through modification by employing NCs comprised of alkali metals for glycerol oxidation to enhance their selective performance, use of one-dimensional biopolymeric cellulose nanofibers having large surface area for reduction reaction and application of novel S-scheme and Z-scheme heterojunctions for photocatalytic degradation. The objectives of this dissertation are set as follows:

1. Development of Pt-Cu/C and Cu-Ni/TiO_2 NC catalysts via catalyst modification for the improvement in the yield and selectivity of heterogeneous catalytic oxidation of glycerol to value added products.
2. Application of cellulose: most abundant biopolymer as an efficient support for the Pt-Co and Ag-Co BNPs for the reduction of 4-nitrophenol.

3. Fabrication of a Z-scheme Cu-ZnO/TiO_2 heterojunction and of S-scheme Bi_2O_3-ZnO/bentonite clay heterojunction photocatalysts for the spectral sensitivity improvement evaluated for the degradation of congo-red, an azo dye.

1.8 Organization of the thesis

The work carried out in this thesis is outlined in six chapters which presents introduction and the state-of-the-art of the research, followed by three chapters showing the main findings of the doctoral project, and finally, one chapter that summarizes the general conclusions and future perspectives. An outline of these chapters is given below, with descriptions of how they are related.

Chapter 1 introduces the general background of catalysis and its importance to the chemical industry, specifically the selective glycerol oxidation: a biomass-derived substrate transformation and abatement of recalcitrant pollutants (4-NP reduction and CR degradation) which motivated the development of the present research project. The scope of the thesis, objectives addressed, and overview of chapters are also described.

Chapter 2 includes the literature review and an overview of the synthetic methods for developing heterogeneous NC catalysts. Further, the studies conducted by researchers to improve the selectivity and yield of glycerol oxidation products and the application of nanomaterials and NC-based advanced oxidation processes for removing 4-NP and azo dyes from wastewater are provided. In addition, challenges and perspectives are discussed from the viewpoint of heterogeneous NC catalyst development and their catalytic performance for selected catalytic reactions.

Chapter 3 describes the synthesis, characterization, and catalytic performance evaluation of the supported bimetallic Pt-Cu/C and Cu-Ni/TiO_2 NC catalysts for selective glycerol oxidation. The glycerol oxidation products' probable reaction mechanism, yield, and selectivity have been investigated.

Chapter 4 demonstrates the synthesis, characterization, and catalytic performance of Pt-Co/CNF and Ag-Co/CNF NC catalysts to reduce recalcitrant pollutant 4-NP from wastewater. In addition, the effect of catalyst loading and initial concentration of reactants on the reaction kinetics was also reported.

Chapter 5 describes the synthesis and characterization of the binary metal oxide Bi_2O_3-ZnO/bentonite clay S-scheme heterojunction and the metal-metal oxide Cu-ZnO/TiO_2 Z-scheme heterojunction NC photocatalysts for the photocatalytic degradation of CR: a

recalcitrant azo dye. The catalytic performance and optimization of various process parameters, such as initial dye concentration, catalyst loading, and UV/sunlight exposure time, were investigated and reported.

Finally, Chapter 6 provides a summary of the research conducted in Chapters 3 to 5 and discusses the impact of the findings within the field of nanomaterials for catalytic purposes. The subsequent section of the chapter delineates the proposed suggestions for forthcoming research endeavors, predicated on the attained outcomes.

References

[1] J. C. Vedrine, Importance, features and uses of metal oxide catalysts in heterogeneous catalysis, Chinese J. Catal. 40 (2019) 1627–1636. https://doi.org/10.1016/S1872-2067(18)63162-6.

[2] K. J. Laidler, A glossary of terms used in chemical kinetics, including reaction dynamics (IUPAC Recommendations 1996), Pure Appl. Chem. 68 (1996) 149–192. https://doi.org/10.1351/pac199668010149.

[3] M. Aazza, H. Ahlafi, H. Moussout, C. Mounir, A. Fadel, A. Addad, H. Ahla, H. Moussout, C. Mounir, A. Fadel, A. Addad, Catalytic reduction of nitro-phenolic compounds over Ag , Ni and Co nanoparticles catalysts supported on γ -Al_2O_3, J. Environ. Chem. Eng. 8 (2020). https://doi.org/10.1016/j.jece.2020.103707.

[4] X. Jin, H. Yan, C. Zeng, P.S. Thapa, B. Subramaniam, R. V Chaudhari, Phase transformed PtFe nanocomposites show enhanced catalytic performances in oxidation of glycerol to tartronic acid, Ind. Eng. Chem. Res. (2017). https://doi.org/10.1021/acs.iecr.7b01473.

[5] M. Nasrollahzadeh, M. Sajjadi, S. Iravani, R.S. Varma, Green-synthesized nanocatalysts and nanomaterials for water treatment: Current challenges and future perspectives, J. Hazard. Mater. 401 (2021) 123401. https://doi.org/10.1016/j.jhazmat.2020.123401.

[6] I. Chorkendorff, J.W. Niemantsverdriet, Concepts of modern catalysis and kinetics, Second, WILEY-VCH Verlag GmbH & Co. KGaA, Weinheim, 2005. https://doi.org/10.1002/3527602658.

[7] Z. Li, M. Li, Z. Bian, Y. Kathiraser, S. Kawi, Design of highly stable and selective core /yolk–shell nanocatalysts-A review, Applied Catal. B, Environ. 188 (2016) 324–341. https://doi.org/10.1016/j.apcatb.2016.01.067.

[8] S. Schauermann, N. Nilius, S. Shaikhutdinov, H. Freund, Nanoparticles for heterogeneous catalysis: New mechanistic insights, Acc. Chem. Res. 46 (2013) 1673–1681. https://doi.org/10.1021/ar300225s.

[9] V. K. Landge, S. H. Sonawane, R. V. Chaudhari, G. U. B. Babu, Selective oxidation of glycerol: a biomass-derived feedstock using the Pt-Cu Janus catalyst for value-added products, Ind. Eng. Chem. Res. 60 (2021) 185–195. https://doi.org/10.1021/acs.iecr.0c04626.

[10] V. K. Landge, S. H. Sonawane, S. Manickam, G. U. Bhaskar Babu, G. Boczkaj, Ultrasound-assisted wet-impregnation of Ag-Co nanoparticles on cellulose nanofibers: Enhanced catalytic hydrogenation of 4-nitrophenol, J. Environ. Chem. Eng. 9 (2021) 105719. https://doi.org/10.1016/j.jece.2021.105719.

[11] A. Villa, A. Jouve, F.J. Sanchez Trujillo, D. Motta, L. Prati, N. Dimitratos, Exploring the effect of Au/Pt ratio on glycerol oxidation in presence and absence of a base, Catalysts. 8 (2018). https://doi.org/10.3390/catal8020054.

[12] N. Hussain, P. Gogoi, P. Khare, M.R. Das, Nickel nanoparticles supported on reduced graphene oxide sheets: a phosphine free, magnetically recoverable and cost effective catalyst for Sonogashira cross-coupling reactions, RSC Adv. 5 (2015) 103105–103115. https://doi.org/10.1039/c5ra22601e.

[13] Y. Bin Choi, N. Nunotani, K. Morita, N. Imanaka, Selective glycerol oxidation to glyceric acid under mild conditions using Pt/CeO_2–ZrO_2–Fe_2O_3/SBA-16 catalysts, J. Asian Ceram. Soc. 10 (2022) 178–187. https://doi.org/10.1080/21870764.2022.202898.

[14] C.N. Florica Papa, B.I. , Akane Miyazaki, F. Papa, C. Negrila, A. Miyazaki, I. Balint, Morphology and chemical state of PVP-protected Pt, Pt-Cu, and Pt-Ag nanoparticles prepared by alkaline polyol method, J. Nanoparticle Res. 13 (2011) 5057–5064. https://doi.org/10.1007/s11051-011-0486-9.

[15] X. Jin, C. Zeng, W. Yan, M. Zhao, P. Bobba, H. Shi, P.S. Thapa, B. Subramaniam, R. V. Chaudhari, Lattice distortion induced electronic coupling results in exceptional

enhancement in the activity of bimetallic PtMn nanocatalysts, Appl. Catal. A Gen. 534 (2017) 46–57. https://doi.org/10.1016/j.apcata.2017.01.021.

[16] X. Jin, M. Zhao, W. Yan, C. Zeng, P. Bobba, P.S. Thapa, B. Subramaniam, R. V. Chaudhari, Anisotropic growth of PtFe nanoclusters induced by lattice-mismatch: Efficient catalysts for oxidation of biopolyols to carboxylic acid derivatives, J. Catal. 337 (2016) 272–283. https://doi.org/10.1016/j.jcat.2016.02.015.

[17] K. Salehi, H. Daraei, P. Teymouri, B. Shahmoradi, A. Maleki, Cu-doped ZnO nanoparticle for removal of reactive black 5 : application of artificial neural networks and multiple linear regression for modeling and optimization, Desalin. Water Treat. 57 (2016) 22074–22080. https://doi.org/10.1080/19443994.2015.1130658.

[18] T. Linda, S. Muthupoongodi, X.S. Shajan, S. Balakumar, Photocatalytic Degradation of congo red and crystal violet dyes on Cellulose/PVC/ZnO composites under UV light irradiation, Mater. Today Proc. 3 (2016) 2035–2041. https://doi.org/10.1016/j.matpr.2016.04.106.

[19] T. Quang, Q. Viet, V. Hoang, N. Thi, H. Giang, Statistical screening and optimization of photocatalytic degradation of methylene blue by ZnO–TiO_2/rGO nanocomposite, Colloids Surfaces A Physicochem. Eng. Asp. 629 (2021) 127464.

[20] Y. Y. Y. Zhang, H. Fang, Y.Y.Y. Zhang, M. Wen, D. Wu, Q. Wu, Active cobalt induced high catalytic performances of cobalt ferrite nanobrushes for the reduction of p-Nitrophenol, J. Colloid Interface Sci. 535 (2018) 499–504. https://doi.org/10.1016/j.jcis.2018.10.022.

[21] L. Han, P. Cui, H. He, H. Liu, Z. Peng, J. Yang, A seed-mediated approach to the morphology-controlled synthesis of bimetallic Copper-Platinum alloy nanoparticles with enhanced electrocatalytic performance for the methanol oxidation reaction, J. Power Sources. 286 (2015) 488–494. https://doi.org/10.1016/j.jpowsour.2015.04.003.

[22] S. Ahmad, X. Su, C. Yang, X. Wang, X. Liu, J. Wang, Space-confined growth of layered basic zinc acetate nanosheets and their orderly fragmented ZnO nanoparticles on clay platelets, J. Hazard. Mater. 371 (2019) 213–223. https://doi.org/10.1016/j.jhazmat.2019.02.111.

[23] H. Yan, S. Yao, B. Yin, W. Liang, X. Jin, X. Feng, Y. Liu, X. Chen, C. Yang, Synergistic effects of bimetallic PtRu/MCM-41 nanocatalysts for glycerol oxidation in base-free medium: Structure and electronic coupling dependent activity, Appl. Catal. B Environ. 259 (2019) 118070. https://doi.org/10.1016/j.apcatb.2019.118070.

[24] R. Dhanda, M. Kidwai, Reduced graphene oxide supported Ag_xNi_{100-x} alloy nanoparticles: A highly active and reusable catalyst for the reduction of nitroarenes, J. Mater. Chem. A. 3 (2015) 19563–19574. https://doi.org/10.1039/c5ta03779d.

[25] M. Yadav, S. Garg, A. Chandra, K. Hernadi, Immobilization of green BiOX (X= Cl, Br and I) photocatalysts on ceramic fibers for enhanced photocatalytic degradation of recalcitrant organic pollutants and efficient regeneration process, Ceram. Int. 45 (2019) 17715–17722. https://doi.org/10.1016/j.ceramint.2019.05.340.

[26] Z. Han, R. Xie, Y. Song, G. Fan, L. Yang, F. Li, Efficient and stable platinum nanocatalysts supported over Ca-doped $ZnAl_2O_4$ spinels for base-free selective oxidation of glycerol to glyceric acid, Mol. Catal. 477 (2019) 110559. https://doi.org/10.1016/j.mcat.2019.110559.

[27] M.B. Shekardasht, M.H. Givianrad, P. Gharbani, Z. Mirjafary, A. Mehrizad, Preparation of a novel Z-scheme g-C_3N_4/RGO/$Bi_2Fe_4O_9$ nanophotocatalyst for degradation of Congo Red dye under visible light, Diam. Relat. Mater. 109 (2020) 108008. https://doi.org/10.1016/j.diamond.2020.108008.

[28] I. V Machado, J.R.N. Santos, M.A.P. Januario, A.G. Corr, Greener organic synthetic methods : Sonochemistry and heterogeneous catalysis promoted multicomponent reactions, Ultrason. Sonochem. 78 (2021) 105704. https://doi.org/10.1016/j.ultsonch.2021.105704.

[29] A.M. Frey, Design of heterogeneous catalysts, Technical University of Denmark, 2009. https://doi.org/10.1002/9783527625321.

[30] P.T. Anastas, M.M. Kirchhoff, Origins, current status, and future challenges of green chemistry, Acc. Chem. Res. 35 (2002) 686–694. https://doi.org/10.1021/ar010065m.

[31] R.A. Sheldon, The: E factor 25 years on: The rise of green chemistry and sustainability, Green Chem. 19 (2017) 18–43. https://doi.org/10.1039/c6gc02157c.

[32] J. H. Clark, Catalysis for green chemistry, Pure Appl. Chem. 73 (2001) 103–111. https://doi.org/10.1351/pac200173010103.

[33] P. Anastas, N. Eghbali, Green Chemistry: Principles and Practice, Chem. Soc. Rev. 39 (2010) 301–312. https://doi.org/10.1039/b918763b.

[34] C. M. Magdalane, G.M.A. Priyadharsini, K. Kaviyarasu, A.I. Jothi, G.G. Simiyon, Synthesis and characterization of TiO_2 doped cobalt ferrite nanoparticles via microwave method: Investigation of photocatalytic performance of congo red degradation dye, Surfaces and Interfaces. 25 (2021) 101296. https://doi.org/10.1016/j.surfin.2021.101296

[35] L. Liu, A. Corma, Metal catalysts for heterogeneous catalysis : From single atoms to nanoclusters and nanoparticles, Chem. Rev. 118 (2018) 4981–5079. https://doi.org /10.1021/acs.chemrev.7b00776.

[36] R. Lanza, P. Canu, S.G. Jaras, Partial oxidation of methane over Pt-Ru bimetallic catalyst for syngas production, Appl. Catal. A Gen. 348 (2008) 221–228. https://doi.org /10.1016/j.apcata.2008.06.044.

[37] R. Herrera, P. Priecel, M. Lin, J.A. Lopez-sanchez, Z. Zhong, A versatile sonication-assisted deposition–reduction method for preparing supported metal catalysts for catalytic applications, Ultrason. - Sonochemistry. 35 (2017) 631–639. https://doi.org/10. 1016 /j.ultsonch.2016.01.018.

[38] B. Michele, G. Pierre, P. Catherine, Conversion of biomass into chemicals over metal catalysts, Chem. Rev. 114 (2013) 1827–1870.

[39] Y. Liang, W. Li, X. Wang, R. Zhou, H. Ding, TiO_2–ZnO/Au ternary heterojunction nanocomposite: Excellent antibacterial property and visible-light photocatalytic hydrogen production efficiency, Ceram. Int. 48 (2021) 2826–2832. https://doi.org/10. 1016/j.ceramint.2021.10.072.

[40] E. Gong, S. Ali, C.B. Hiragond, H.S. Kim, N.S. Powar, D. Kim, H. Kim, Solar fuels : research and development strategies to accelerate photocatalytic CO_2 conversion into hydrocarbon fuels, Energy Environ. Sci. (2021). https://doi.org/10.1039/d1ee02714j.

[41] D. N. Yadav, K.A. Kishore, B. Bethi, ZnO nanophotocatalysts coupled with ceramic membrane method for treatment of Rhodamine-B dye waste water, Environ. Dev. Sustain. (2017). https://doi.org/10.1007/s10668-017-9977-x.

[42] P. Rajesh Kumar, Prashant L. Suryawanshi, Sarang P. Gumfekar, Bharat A. Bhanvase, S. H. Sonawane. Sonochemical synthesis of Pt-Co/C electrocatalyst for PEM fuel cell applications, Surfaces and Interfaces. (2018). https://doi.org/10.1016/j.surfin.2018.04. 002.

[43] M. Nasrollahzadeh, M. Sajjadi, M. Shokouhimehr, R.S. Varma, Recent developments in palladium (nano) catalysts supported on polymers for selective and sustainable oxidation processes, Coord. Chem. Rev. 397 (2019) 54–75. https://doi.org/10.1016/j. ccr.2019.06.010.

[44] F. Lin, R. Doong, Bifunctional Au-Fe_3O_4 heterostructures for magnetically recyclable catalysis of nitrophenol reduction, J. Phys. Chem. C. 115 (2011) 6591–6598.

[45] C. Wang, H. Yin, S. Dai, S. Sun, A general approach to noble metal-metal oxide

dumbbell nanoparticles and their catalytic application for CO oxidation, Chem. Mater. 22 (2010) 3277–3282. https://doi.org/10.1021/cm100603r.

[46] S. M. Islam, A. S. Roy, P. Mondal, S. Mondal, M. Mubarak, D. Hossain, S. Sarkar, Selective oxidation of olefins and aromatic alcohols with tert-butylhydroperoxide catalyzed by polymer-anchored transition-metal complexes, J. Appl. Polym. Sci. 120 (2011) 2743–2753. https://doi.org/10.1002/app.33104.

[47] H.-U. Blaser, C. Malan, B. Pugin, F. Spindler, H. Steiner, M. Studer, Selective hydrogenation for fine chemicals: Recent trends and new developments, Adv. Synth. Catal. 345 (2003) 103–151. https://doi.org/https://doi.org/10.1002/adsc.200390000.

[48] I. Arends, R. Sheldon, U. Hanefeld, 1 Introduction: Green chemistry and catalysis, in: I. Arends, R. Sheldon, U. Hanefeld (Eds.), Green Chem. Catal., WILEY-VCH Verlag GmbH & Co. KGaA, Weinheim, 2007: pp. 1–48. https://doi.org/10.1002/978352761100

[49] D. Li, H. Gong, L. Lin, W. Ma, Q. Zhou, K. Kong, R. Huang, Z. Hou, Selective aerobic oxidation of glycerol over zirconium phosphate-supported vanadium catalyst, Mol. Catal. 474 (2019) 110404. https://doi.org/10.1016/j.mcat.2019.110404.

[50] X. Jin, M. Zhao, C. Zeng, W. Yan, Z. Song, Oxidation of glycerol to dicarboxylic acids using cobalt catalysts, ACS Catal. Oxid. (2016). https://doi.org/10.1021/acscatal.6b00961.

[51] M. Rosiene, A. Arcanjo, I.J. Silva, E. Rodriguez-castellon, A. Infantes-molina, R.S. Vieira, Conversion of glycerol into lactic acid using Pd or Pt supported on carbon as catalyst, Catal. Today. 279 (2017) 317–326. https://doi.org/10.1016/j.cattod.2016.02.01.

[52] R. Palacio, S. Torres, D. Lopez, D. Hernandez, Selective glycerol conversion to lactic acid on Co_3O_4/CeO_2 catalysts, Catal. Today. 302 (2018) 196–202. https://doi.org/ 10.1016 /j.cattod.2017.05.053.

[53] C. Zhang, T. Wang, X. Liu, Y. Ding, Selective oxidation of glycerol to lactic acid over activated carbon supported Pt catalyst in alkaline solution, Cuihua Xuebao/Chinese J. Catal. 37 (2016) 502–509. https://doi.org/10.1016/S1872-2067(15)61055-5.

[54] X. Han, H. Sheng, C. Yu, T.W. Walker, G.W. Huber, J. Qiu, S. Jin, Electrocatalytic oxidation of glycerol to formic acid by $CuCo_2O_4$ spinel oxide nanostructure catalysts, ACS Catal. 10 (2020) 6741–6752. https://doi.org/10.1021/acscatal.0c01498.

[55] V. K. Landge, S. H. Sonawane, M. Sivakumar, S.S. Sonawane, G. Uday Bhaskar Babu, G. Boczkaj, S-scheme heterojunction Bi_2O_3-ZnO/Bentonite clay composite with enhanced photocatalytic performance, Sustain. Energy Technol. Assessments. 45 (2021)

101194. https://doi.org/10.1016/j.seta.2021.101194.

[56] V. K. Landge, V. S. Hakke, M. Kakunuri, G.U.B. Babu, G. Boczkaj, S.H. Sonawane, Synthesis of bimetallic Co–Pt/cellulose nanocomposites for catalytic reduction of p - nitrophenol , React. Chem. Eng. (2022). https://doi.org/10.1039/d1re00422k.

[57] V. K. Harika, H. K. Sadhanala, I. Perelshtein, A. Gedanken, Sonication-assisted synthesis of bimetallic Hg/Pd alloy nanoparticles for catalytic reduction of nitrophenol and its derivatives, Ultrason. Sonochem. (2019). https://doi.org/10.1016 /j. ultsonch.2019.104804.

[58] S. K. Ghosh, M. Mandal, S. Kundu, S. Nath, T. Pal, Bimetallic Pt-Ni nanoparticles can catalyze reduction of aromatic nitro compounds by sodium borohydride in aqueous solution, Appl. Catal. A Gen. 268 (2004) 61–66. https://doi.org/10.1016/j.apcata.2004. 03.017.

[59] H. Chen, X. Fan, J. Ma, G. Zhang, F. Zhang, Y. Li, Green route for microwave-assisted preparation of AuAg-alloy-decorated graphene hybrids with superior 4-NP reduction catalytic activity, Ind. Eng. Chem. Res. 53 (2014) 17976–17980. https://doi.org/10.1021/ie503251h.

[60] T. A. Revathy, T. Sivaranjani, A. A. Boopathi, S. Sampath, V. Narayanan, A. Stephen, Pd–Co alloy as an efficient recyclable catalyst for the reduction of hazardous 4-nitrophenol, Res. Chem. Intermed. 45 (2019) 815–832. https://doi.org/10.1007/s11164-018-3645-0.

[61] J. Zhang, G. Chen, D. Guay, M. Chaker, D. Ma, Highly active PtAu alloy nanoparticle catalysts for the reduction of 4-nitrophenol, Nanoscale. 6 (2014) 2125–2130. https://doi.org/10.1039/c3nr04715f.

[62] X. T. Tran, M. Hussain, H.T. Kim, Facile and fast synthesis of a reduced graphene oxide/carbon nanotube/iron/silver hybrid and its enhanced performance in catalytic reduction of 4–nitrophenol, Solid State Sci. 100 (2020) 106107. https://doi.org/10.1016 /j.solidstatesciences.2019.106107.

[63] S. Kapoor, A. Sheoran, M. Riyaz, J. Agarwal, N. Goel, S. Singhal, Enhanced catalytic performance of Cu/Cu_2O nanoparticles via introduction of graphene as support for reduction of nitrophenols and ring opening of epoxides with amines established by experimental and theoretical investigations, J. Catal. 381 (2020) 329–346. https://doi.org /10.1016/j.jcat.2019.11.012.

[64] C. Pragathiswaran, C. Smitha, B.M. Abbubakkar, P. Govindhan, N.A. Krishnan,

Synthesis and characterization of TiO_2/ZnO-Ag nanocomposite for photocatalytic degradation of dyes and anti-microbial activity, Mater. Today Proc. 45 (2021) 3357–3364. https://doi.org/10.1016/j.matpr.2020.12.664.

[65] C. Xu, Y. Du, C. Li, J. Yang, G. Yang, Insight into effect of acid / base nature of supports on selectivity of glycerol oxidation over supported Au-Pt bimetallic catalysts, Applied Catal. B, Environ. 164 (2015) 334–343. https://doi.org/10.1016/j.apcatb.2014.09.048.

[66] S. Pandey, S.B. Mishra, Catalytic reduction of p-nitrophenol by using platinum nanoparticles stabilised by guar gum, Carbohydr. Polym. 113 (2014) 525–531. https://doi.org/10.1016/j.carbpol.2014.07.047.

[67] P. Sharma, M.R. Das, Removal of a cationic dye from aqueous solution using graphene oxide nanosheets : Investigation of adsorption parameters, J. Chem. Eng. Data. (2012). https://doi.org/10.1021/je301020n.

[68] P. Pascariu, C. Cojocaru, N. Olaru, P. Samoila, A. Airinei, M. Ignat, L. Sacarescu, D. Timpu, Novel rare earth (RE-La , Er , Sm) metal doped ZnO photocatalysts for degradation of Congo-Red dye: Synthesis, characterization and kinetic studies, J. Environ. Manage. 239 (2019) 225–234. https://doi.org/10.1016/j.jenvman.2019.03.060.

[69] Y.X. Wang, H.J. Zhou, P.C. Sun, T.H. Chen, Exceptional methanol electro-oxidation activity by bimetallic concave and dendritic Pt-Cu nanocrystals catalysts, J. Power Sources. 245 (2014) 663–670. https://doi.org/10.1016/j.jpowsour.2013.07.015.

[70] D. Dutta, R. Hazarika, P.D. Dutta, T. Goswami, P. Sengupta, D.K. Dutta, Synthesis of Ag-Ag_2S Janus nanoparticles supported on environmentally benign cellulose template and their catalytic applications, RSC Adv. (2016). https://doi.org/10.1039/C6RA16941.

[71] K. F. Kalz, R. Kraehnert, M. Dvoyashkin, R. Dittmeyer, R. Glaser, U. Krewer, K. Reuter, J.-D. Grunwaldt, Future challenges in heterogeneous catalysis: Understanding catalysts under dynamic reaction conditions, ChemCatChem. 9 (2017) 17–29. https://doi.org/10.1002/cctc.201600996.

[72] K. F. M. Elias, A.F. Lucredio, E. M. Assaf, Effect of CaO addition on acid properties of Ni–Ca/Al_2O_3 catalysts applied to ethanol steam reforming, Int. J. Hydrogen Energy. 38 (2013) 4407–4417. https://doi.org/10.1016/j.ijhydene.2013.01.162.

[73] U. O. Bhagwat, J. J. Wu, A.M. Asiri, S. Anandan, Photocatalytic degradation of congo red using $PbTiO_3$ nanorods synthesized via a sonochemical approach, Chemistry Select. 3 (2018) 11851–11858. https://doi.org/10.1002/slct.201802303.

[74] F. J. Prince N. Amaniampong, Quang Thang Trinh, Jithin John Varghese, Ronan

Behling, Sabine Valange, Samir H. Mushrif, Unraveling the mechanism of the oxidation of glycerol to dicarboxylic acids over a sonochemically synthesized copper oxide catalyst, Green Chem. (2018). https://doi.org/10.1039/C8GC00961A.

Chapter 2.

Literature Survey

2.1 Heterogeneous nanostructures for catalysis

Heterogeneous catalysis serves as the foundation for numerous contemporary chemical technologies. Heterogeneous catalysis finds application in a diverse range of fields including chemical production, energy generation, conversion and retention, as well as environmentally friendly technologies [1]. In recent years, a significant avenue of exploration in the field of nanocatalyst synthesis pertains to the progression from single-component nanoparticles (NPs) to multi-component hetero/hybrid nanostructures. These hetero-nanostructures consist of distinct domains of diverse materials that are systematically arranged. The scientific community has shown significant interest in multicomponent hetero-nanostructures, which comprise multiple nanometre-scale components. This is due to the synergistic effects that arise from the interactions between these distinct nanometre-scale entities. The hetero-nanostructures, also referred to as hetero nanocomposites (HNCs), are frequently utilised to describe multi-component nanostructures. Such HNCs offer advantages in three distinct aspects. One key aspect is to acknowledge the concept of multifunctionality, whereby diverse functionalities can be amalgamated by independently optimising the material parameters and dimensions of individual components. The second benefit lies in the provision of innovative functionalities that are not present in individual component materials or structures. The third benefit lies in the attainment of improved characteristics and surpassing the inherent limitations of monophasic substances [2]. The critical length scales of numerous physical and chemical properties are in the nanometre range. As a result, the close proximity of nanocomponents in HNCs facilitates robust interactions between these components. This may enable a logical modulation of the physical and chemical properties of each individual component. As an illustration, gold nanoparticles (Au NPs) typically exhibit chemical inactivity. However, when deposited on a metal-oxide substrate, these Au NPs have demonstrated notable catalytic efficacy in the oxidation of carbon monoxide [3].

Numerous catalysts that hold significant commercial value consist of catalytically active NPs that are dispersed on oxide supports with high surface areas. The catalysts in question are commonly intricate multi-component heterogeneous noble metals that are fine-tuned to operate for numerous turnovers, at elevated reaction rates, and with notable selectivity. Frequently, additives are incorporated to enhance their efficacy, specificity, and durability [4]. The intricate

composition and structure of said catalysts afford the ability to adjust their chemical and adsorption properties, thereby enhancing their efficacy in a targeted reaction [1].

HNCs have been fabricated in both thin-film and powder configurations, relying on the immiscibility of the constituent phases to achieve the random incorporation of nanoscale grains within a matrix [5]. Hybrid structures can be formed by linking various NPs together using covalent bonding with the aid of linker molecules [6]. The fabrication of highly ordered 3D binary superlattices can be achieved through the co-assembly of various types of NPs with specific size ratios, utilising the Van der Waals interactions between the particles [7,8]. The solution-phase synthetic methodologies employed for the growth of single-component NPs have been expanded to encompass the growth of multicomponent NPs. In this approach, the individual inorganic components are grown atop one another without the use of linker molecules. The aforementioned composite entities are comprised of core/shell NPs exhibiting symmetry [9–12], asymmetric heterodimers [13–16], and additional heterostructures with multiple components [17–20]. The production of HNCs typically involves the stepwise deposition of a second and third component onto pre-existing seed particles. The aforementioned technique can be classified as seed-mediated growth [21–24].

The primary methods for synthesising inorganic HNCs include heterogeneous nucleation [4,25,26], asymmetric modification at interfaces [27], and non-epitaxial deposition on the full surface of the first NP followed by thermal dewetting of the shell into a single domain [28]. The achievement of successful synthesis of HNCs is highly dependent on the promotion of heterogeneous nucleation and the suppression of homogeneous nucleation, which refers to the formation of distinct NPs of the second component [2,26]. It is a well-established fact that in the case of a heterojunction formed between a metal and metal oxide, the material characteristics in the vicinity of the interface on both sides are altered from their bulk properties. There are several potential causes for this phenomenon, such as surface reconstruction in the vicinity of the junction, crystal strain induced by lattice mismatch, and electron interaction or transfer across the interface [29,30].

The creation of HNCs necessitates the inhibition of homogeneous nucleation of the second or third component, which could potentially compete with heterogeneous nucleation on pre-existing or in situ generated seeds, as previously noted. In accordance with the classical theory of heterogeneous nucleation, it is possible to attain this objective by reducing the concentration of the precursor to a level below supersaturation, at which point homogeneous nucleation would be deemed favourable [31]. Moreover, it is imperative that the Gibbs free energy term

for the adhesive energy at the interface between the seeds and the overgrown particles is negative, as prescribed for epitaxial growth in literature [32,33].

The phenomenon of lattice mismatch not only governs the natural tendency towards hetero-nanostructures, but also regulates the resultant morphology of the product by modulating the degree of lattice mismatch. For moderate variations in lattice constants, there are no barriers to nucleation and epitaxial growth. In cases where there exist significant disparities, the expansion is restricted to specific crystal planes through the reduction of lattice mismatch. This process subsequently results in the development of anisotropic structures [28,34]. Simultaneously, it is feasible to differentiate between phase separated hetero-nanostructures and ternary phases, provided that there is adequate molecular monitoring during the synthesis process and the ternary phases conform to the phase diagrams, despite the presence of lattice match [13,14,16]. However, the epitaxial relationship between the two distinct kinds of materials is crucial for modifying material characteristics through heterogeneous conjugation. The significance of such HNCs is reinforced by the ongoing extensive investigation into their utilisation in various domains [35]. The present discourse provides a succinct overview of diverse techniques for the production of multicomponent HNCs, as per the current state of the art as follows.

2.1.1 Seeded growth approach for synthesis of heterogeneous nanostructures

The most widely exploited class of strategies to synthesize HNCs relies on the so-called ‘‘seeded growth’’ approach. According to this scheme, the environment for generating HNC contains preformed NCs of a target material, referred to as the ‘‘seeds’’, which serve as primary substrate centres for accommodating secondary inorganic portions of different materials upon reaction of the respective molecular precursors. This approach is founded on a key principle of the “Classical Nucleation Theory” following heterogeneous deposition on a highly faceted NC seed, a secondary material can either attain continuous shell (hence, leading to a HNC with an onion- like geometry) or develop into a discrete section (hence, giving rise to a heterodimer HNC), if complete ‘‘wetting’’ is either realized for any of the facets exposed, or selectively for just a few of them, respectively (Figure 2.1a). On the other hand, under conditions favouring only partial ‘‘wetting’’ regime, one or more sufficiently extended facets of the original seeds can accommodate multiple domains of the foreign material (Figure 2.1b). As an intermediate evolutionary case, a transformation from a metastable onion-like architecture (e.g., due to formation of an amorphous shell) to a phase-segregated heterodimer heterostructure could be expected as a convenient pathway toward lowering of interfacial strain as crystallization

proceeds (Figure 2.1c). However, the interplay of kinetic processes associated, for example, with solution supersaturation, reactant diffusion, and/or the inherent chemical reactivity of the seeds and/or the particular molecular precursor selected, as well as operation of unusual mechanisms by which misfit strain may be relieved can greatly complicate mechanistic interpretation [36].

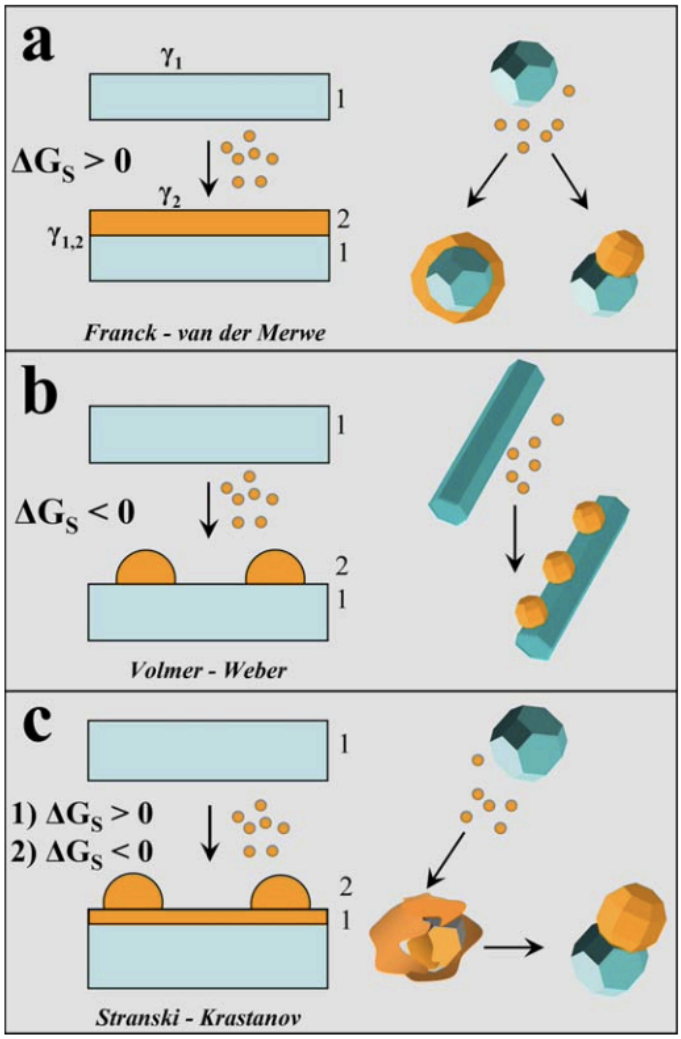

Figure 2.1 Comparative sketches illustrating possible heterogeneous deposition modes for a secondary material (referred to as "2") that is deposited from the respective molecular pre- cursors onto a preformed seed substrate of a different material (referred to as "1"): [Reprinted from Ref. [37] with permission, copyright Wiley-VCH Verlag GmbH & Co. KGaA].

In their study, Ma et al. [9] utilised a successive reduction and deposition method to synthesise core-shell Ag@Pt NPs with a diameter of 30-50 nm and spherical/elliptical shape. These NPs were supported on sepiolite nanofibers and were employed for the catalytic reduction of

nitrophenols in water. In the course of a standard synthesis, the silver precursor, $AgNO_3$ (0.527 mL, 10 mg/mL), underwent initial reduction via ascorbic acid (10 mL, 5.4 mg/mL) for a duration of 30 minutes under magnetic stirring at a temperature of 80 °C. The platinum precursor, $H_2PtCl_6 \cdot 6H_2O$, was subjected to reduction using ascorbic acid for a duration of 1 hour under magnetic stirring at a temperature of 80 °C. The concentration of $H_2PtCl_6 \cdot 6H_2O$ was 10 mg/mL and the volume used was 3.2 mL, while the concentration of ascorbic acid was 21.6 mg/mL and the volume used was 10 mL. The observed transformation of the red silver colloid to a darker hue suggests that the silver cores underwent a process of being enveloped by platinum shells. Subsequently, a suspension of sepiolite nanofibers (consisting of 0.9393 g sepiolite) was introduced into the colloid and agitated for a duration of 4 hours. The reduction process of Pt and Ag precursors involved the presence of protective and dispersant components, namely 0.45 g of sodium citrate and 0.17 g of PVP. Subsequently, the heterogeneous mixture underwent centrifugation to achieve separation, followed by a thorough rinse with deionized water. The resulting product was then subjected to a drying process at a temperature of 50 °C for a duration of 12 hours under vacuum conditions. The end product obtained was the Ag@Pt/sepiolite catalyst, with a composition ratio of Ag to Pt being 1:1.

The formation of Au@Fe_3O_4 heterodimer NPs, ranging from dumbbell to flowerlike shapes, was demonstrated by Wei et al. through the manipulation of the ratio of multiply twinned Au seeds to $Fe(CO)_5$, along with the incorporation of 2 to 6 Fe_3O_4 domains [38]. Furthermore, the elongation of the reaction time results in a progressive enlargement of the Fe_3O_4 domains. The prevalence of heterogeneous nucleation at the interface of $2d_{111}$-(Au) and d_{111}-(Fe_3O_4) is attributed to the small lattice mismatch. This phenomenon can be observed through optical spectroscopy [39].

As evidenced by the creation of heterostructures consisting of Au and MnO, the synthetic method can be readily extended to other material compositions [40]. Heterodimers of Au@MnO were synthesised by utilising pre-existing Au NPs as seeds. This method was preferred due to its superior control over particle size, which was achieved through the synthesis of hydrophobic gold NPs utilising tert-butylamine borane complex as a reducing agent. The particles that are capped with oleylamine exhibit a range of sizes between 2 and 8 nm, which can be achieved by altering the reaction temperature or through a subsequent growth reaction that involves the addition of $HAuCl_4$ and oleylamine to pre-existing Au particles [41].

2.1.2 Anisotropic growth induced lattice distortion and electronic coupling approach for synthesis of heterogeneous nanostructures

Classic bottom up synthetic methodologies are primarily focused on ligand-mediated surface index for morphologically influenced catalysis (facet dependent catalysis), which can be attributed to activity enhancements of HNCs [42]. But recent research in nanomaterials has discovered that electron transfer and metal-metal interfacial strain can intrinsically enhance structural coherence and surface properties of bimetallic crystals [43-45], where extensive studies have shown that rather than forcing two metal species to form BNPs using polymer stabilizers, lattice strain induced by difference in lattice parameters among the metal species can be used as a driving force to generate unique NPs. Interfacial strain often induce unusual lattice stretch or contraction in bimetallic crystals. Such lattice distortion undoubtedly leads to tunable surface electronic properties and thus affecting catalytic activities of bimetals. This is because that the strong cohesive interaction at metal–metal interface ("ligand" effect) involves charge transfer or rehybridization of electron orbitals of two metals. The perturbation of a metal's orbitals intrinsically shift d band towards/away from Fermi level [43]. Therefore, in the area of catalysis, this finding offers a new methodology and provides immense potential for innovative catalyst design [42,46]. Engineering optimal electronic coupling by altering metal-metal interfacial lattice strain and understanding its impact on catalytic activity of bimetallic materials have been attracting attracting extensive attention in recent years [43,44,47].
Jin et al. [30] have developed PtMn HNC supported on CeO_2 by lattice distortion induced electronic coupling with a polymer free one pot self-assembly method using solvothermal technique conducted at 200 °C under N_2 atmosphere (~2.2 MPa) for about 12 h. The anisotropic growth was induced by large lattice constant mismatch between the two metals (Pt: FCC, 0.39 nm; Mn: BCC, 0.89 nm). They have obtained, well-controlled bud- and cauliflower-shaped PtMn clusters immobilized on CeO_2 with the particle size of about 14.3 to 49 nm.

2.1.3 Biphasic ultrasound assisted deposition reduction method for synthesis of heterogeneous nanostructures

A technique based on performing seeded growth at a liquid/liquid interface under mild conditions was devised to synthesize heterodimers coupling a magnetic section and a noble metal domain [48,49]. In the reported technique, an aqueous metal salt solution was brought in contact with an immiscible organic solvent (such as dichlorobenzene, dichloromethane, hexane, etc.) in which surfactant-capped γ-Fe_2O_3/Fe_3O_4 or FePt seeds were dissolved. Upon

ultrasonic irradiation under inert atmosphere, an emulsion was formed that supposedly consisted of continuous aqueous phase containing ‘‘colloidosomes’’, namely organic microdroplets stabilized by the hydrophobic seeds self-assembled at the organic/water interfaces [48]. The seeding NCs provided catalytic sites onto which the Ag^+ or $AuCl_4^-$ ions were reduced to the respective Ag or Au upon sonication, respectively. As the seeds were only partially exposed to the aqueous phase, metal deposition was spatially restricted to a small surface region and proceeded self-catalytically, thus resulting in a single metal domain on each seed. The ‘‘colloidosome’’-based approach was extended to the synthesis of solid Ag-hollow γ-Fe_2O_3 heterodimers starting from hollow γ-Fe_2O_3 seeds prepared by manipulating the Kirkendall effect [49].

Masjedi-arani and Salavati-niasari [50] did a systematic work on sonochemical synthesis of supported catalysts. This selected nucleation and growth initiated by ultrosonication has also been extended to the synthesis of Ag-FePt and Ag-Au hetero-NPs [51].

2.1.4 Co-reduction approach for synthesis of heterogeneous nanostructures

Co-reduction is arguably the most straightforward method for generating alloyed and intermetallic nanocatalysts. This method involves the simultaneous reduction of two metals containing precursors to zerovalent atoms, which then nucleate and grow together to generate HNCs. In some cases, a subsequent annealing step (typically, in an inert atmosphere) is required to obtain a homogeneous alloy (e.g., Au−Ag or Pd−Pt) or, for some bimetallic combinations, structural ordering for the formation of intermetallic compounds. Co-reduction can lead to a large number of bimetallic Ag-Ni/RGO [52], Pt-Ni [53], Pd-Co [54], Pt-Cu [55], etc. nanocatalysts where the final structure can be tailored by varying experimental parameters such as the reduction potentials of the metal ions involved, the strength of the reducing agent, the nature of coordination ligand, the capping agent, and the reaction temperature. An environmentally friendly one-pot co-reduction method by the ultrasound assistance for the decoration of ultrasmall Pd-Ag NPs on graphene as high active anode catalyst towards ethanol oxidation was reported by Douk et al. [56]

The nucleation and growth of nanocrystals depends critically on the reduction rate of the metal precursor or, equally, the rate at which metal atoms are generated in the solution. On a more fundamental level, this process is governed by the rate at which electrons are transferred from the reductant to the metal precursor.

2.1.5. Impregnation method for synthesis of heterogeneous nanostructures

Impregnation is a widely used preparation method for the synthesis of HNC catalysts. The impregnation methodology is where the support is contacted with an aqueous metallic solution (single or multiple) and then oven dried and calcined under suitable thermal conditions. Two types of impregnation methods can be used, (i) based on the volume of metallic solution with respect to the pore volume of support, namely incipient wetness and (ii) wet impregnation using excess solvent. In the case of incipient wetness, the active component solution volume is equal to the pore volume of the support and in the case of the wet impregnation methodology the volume of solution is much higher than the total pore volume of the support.

To date various HNCs were reported employing impregnation method namely, Cu-Ni/CeO_2, Fe-biochar, Fe-activated carbon, CNF-$Al(OH)_3$, Ag/γAl_2O_3, Ni/γAl_2O_3, Co/γAl_2O_3, Ni-Ca/Al_2O_3, etc. [57–63]. Temperature of stirring, time of heating, calcination temperature, and the nature of supporting material are some of the crucial conditions that control the characteristics of the final catalyst. Chemical reaction between the precursor solutions and the metal support may occur during the calcination phase of the period, under particular conditions causing various active phase-support interactions. The advantage of this method is that highly dispersed metal particles on the surface of supports can be obtained.

Summary of some reported hetero-nanostructured catalysts, their synthesis methods along with application is given in Table 2.1 given below.

Table 2.1 Synthesis and applications of different hetero-nanostructured catalysts

Catalyst	Catalyst synthesis	Application	Findings	Ref.
Pt/Ca-doped $ZnAl_2O_4$ spinels	Chemical reduction of Zn $(NO_3)_2 \cdot 6H_2O$, $Ca(NO_3)_2 \cdot 4H_2O$, & $Al(NO_3)_3 \cdot 9H_2O$ with urea (180 °C for 10 h) in pot followed by reduction of H_2PtCl_6 with $NaBH_4$ at room temperature in the presence of Ca-doped $ZnAl_2O_4$ spinels with aging of 4 h.	GLY oxidation	Uniform distribution of spherical Pt NPs (3.11 nm) over Ca-doped $ZnAl_2O_4$.	[64]
ZrP supported on Vanadium	ZrP was prepared via precipitation method by dropwise addition of aqueous solution of $NH_4H_2PO_4$ in $ZrOCl_2 \cdot 8H_2O$ aqueous solution while ZrP@V was prepared by mixing ZrP and $VOSO_4$ in agate mortar, and then continuously grinded for 30 min followed by calcination at 550 °C for 3 h in a muffle furnace.	GLY oxidation	Amorphous ZrP consists of stacked thin nanosheets (50–100 nm), amorphous oligomeric V (< 4 nm)	[65]
AuCu-Nb_2O_5	Niobia was first modified with copper by wet impregnation, and then gold was loaded on the surface of as-prepared material by deposition- reduction method.	GLY oxidation	Au size on support 5.4 nm	[66]
Mesoporous CuNiAlO supported Au	Polymetallic mixed oxides of Cu, Ni and Al were prepared by calcinating the polymetallic hydrotalcites with co-precipitation method followed by hydrothermal treatment at 100 °C for 24 h in an autoclave. Then, calcined at 450 °C for 8 h under N_2 atmosphere. Au loading was done by wet chemical reduction.	GLY oxidation	Au size on support was 2~6 nm.	[67]
Pt/CeO_2–ZrO_2–Fe_2O_3/SBA-16	CeZrFeO/SBA-16 was synthesized using a co-precipitation technique at room temperature for 12 h. Pt loading onto CeZrFe/SBA-16 was carried out by the impregnation method at 90 °C for 2 h, and calcined at 500 °C for 4 h in atmospheric air.	GLY oxidation	Pt 10-40 nm on the aggregates of Pt/CeO_2–ZrO_2–Fe_2O_3/SBA-16 with size 0.1 to 5 μm.	[68]
CuCoO Spinel Oxide	$CuCo_2O_4$ spinels on carbon fiber paper were prepared via hydrothermal method in an autoclave at 120 °C for 6 h followed by calcination at 300 °C for 3 h under air atmosphere.	GLY oxidation	Vertically grown nanoplates with high density and uniform distribution over CFP indicates Spinel structures	[69]

Hg/Pd	Hg/Pd alloy was synthesized via sonication induced biphasic approach through colloidosomes. The immiscible mixture of liquid Hg and $Pd(NO_3)_2$ maintained at 65 ºC was exposed to ultrasonic irradiation for an hour followed by washing and drying.	4-NP reduction	Spherical Hg/Pd alloy NPs with 2-3 nm particle size	[70]
Ag@NC	AgNPs@nanocellulose based membrane was fabricated by in-situ reduction of silver salt over the surface of nanometer thick polydopamine coated synthesized nanocellulose (NC) for 12 h at room temperature.	4-NP reduction	Crystallite size = 2.54 nm, cellulose fibers avg diameter = 35 nm, Ag NPs avg particle size = 12.10 nm	[71]
HZnO Nds	Hexagonal ZnO nanodisks (HZnO Nds) were synthesized by chemical precipitation method at 80 ºC and 3 h stirring followed by washing, drying and annealing 450 ºC for 4.	4-NP reduction	Nanoporous HZnO Nds (pore size 50 nm and length 300 nm).	[72]
Ag-Pd	$AgNO_3$ and $PdCl_2$ aqueous solutions were added one after other in gum solution and stirred for 30 min resulting into a colloidal solution, which was then autoclaved at 121 °C and 15 psi for 15 min.	4-NP reduction	Uniformly dispersed, spherical Ag-Pd (Avg. particle size = 21 nm)	[73]
CoCu/SBA-16	Mesoporous SBA-16 was dispersed in the mixed solution of $Co(NO_3)_2.6H_2O$ and $Cu(NO_3)_2.3H_2O$ using sonication for an hour. To this solution then mixed solution of reducing agents $NaBH_4$ and NH_3BH_3 was added dropwise to obtain CoCu/SBA-16 by chemical reduction method.	4-NP reduction	Avg particle size of CoCu NPs = 2.5 – 6.1	[74]
Cu_2O/ZnO	One pot solvothermal method was used to prepare Cu_2O/ZnO using absolute ethanol as a solvent and reducing agent in an autoclave at 170 °C for 8 h.	CR degradation	Avg. crystallite size = 29.24 nm. Uniform distribution of spherical Cu_2O NPs with 7 nm mean size on flake-like ZnO having 20–40 nm length was detected.	[75]
$PbTiO_3$ nanorods	$PbTiO_3$ was prepared via sonication induced biphasic approach. The titanium tetraisopropoxide dispersed in isopropyl alcohol and aqueous lead nitrate were	CR degradation	Crystallite size of $PbTiO_3$	[76]

	mixed and sonicated with pH maintained at 12 for two hours followed by washing, vacuum drying (100 °C for 4 h) and annealing at 700 °C for 2 h.		nanorods is 35 nm. Aggregates of $PbTiO_3$ nanorods having irregular shape with diameter of 100 nm was reported.	
Cts decorated Fe_3O_4 Nsps	Chitosan (Cts) decorated Fe_3O_4 nanospheres (Nsps) were prepared by one-pot hydrothermal method in an autoclave operated at at 180 °C for 12 h.	CR degradation	Fe_3O_4 had a sphere-like shape over Cts matrix and avg particle size of 310 nm.	[77]
TiO_2 doped cobalt ferrite	TiO_2 doped $CoFe_2O_4$ nanostructures were prepared by microwave method irradiated at 2:54 GHz frequency (850 W power) using microwave oven for 15 min followed by addition of tetrahydrofuran and ascorbic acid. Afterwards annealing at 500 °C for 3 h was performed.	CR degradation	crystallite size of TiO_2 doped $CoFe_2O_4$ is 25 nm.	[78]
ZnO-CuO/ES	ZnO-CuO/Egg shell (ES) was prepared through electro-chemical method operated under normal atmosphere at 273 K and 120 mA cm^{-2} of constant current density followed by washing and drying and then calcining at 823 K for 3 hrs.	CR degradation	Avg size = 45 nm.	[79]
g-C_3N_4/RGO/BFO	$Bi_2Fe_4O_9$ (BFO) was synthesized through hydrothermal method in an autoclave operated at 200 °C for 24 h followed by washing and drying. Later BFO, RGO and g-C_3N_4 were mixed together and stirred prior to introduce in autoclave operated at 130 °C for 2 h.	CR degradation	g-C_3N_4/BFO well-deposited on RGO showing spherical morphology and size less than 300 nm.	[80]
Ternary metal selenide-chitosan microspheres (ZBiSe-CM)	At first, zinc–bismuth-selenide NPs (ZBiSe-NPs) were successfully synthesized via the solvothermal process (pH-11, 85 °C for 5 h) and then supported with chitosan to prevent leaching of the catalyst.	CR degradation	crystallite size of ZBiSe-NPs was 27.04 nm. average size of the ZBiSe-CM microspheres was 812 μm with spherical shape.	[81]

2.2 Significance of ultrasound assisted synthesis of HNC

Ultrasound sonication plays a crucial and multifaceted role in the synthesis of heterogeneous metal nanocatalysts, which are catalytic materials consisting of metal NPs dispersed on a support material. The significance of ultrasound sonication in this context stems from its ability to influence various aspects of the synthesis process, ultimately leading to the production of well-dispersed, highly active, and stable nanocatalysts. Here's a closer look at the important roles of ultrasound sonication in this synthesis:

Homogeneous Dispersion: Ultrasound waves create intense cavitation and mechanical agitation in the reaction mixture. This action helps to break down aggregates and agglomerates of metal precursors, ensuring that they are uniformly dispersed in the solvent or on the support material [82]. This uniform dispersion of precursors is essential to achieve even distribution of metal NPs on the catalyst support.

Nucleation and Particle Growth: Ultrasound-induced cavitation promotes rapid and controlled nucleation of metal particles from precursor solutions. The localized high pressures and temperatures created during cavitation facilitate the formation of nuclei, leading to the growth of NPs with controlled sizes and shapes [83]. This control over particle size is vital in tailoring the catalytic activity and selectivity of the nanocatalyst.

Enhanced Mass Transfer: The agitation caused by ultrasound enhances the mass transfer of reactants to the surface of the catalyst support and the metal NPs. This is particularly important for reactions involving gaseous reactants or reactants with low solubility in the solvent. Efficient mass transfer ensures that the catalytic sites are accessible and that reactions proceed at a higher rate [84].

Stabilizer Dispersion: Many nanocatalyst syntheses involve the use of stabilizing agents or surfactants to prevent NP aggregation. Ultrasound can assist in dispersing and evenly distributing these stabilizers, ensuring their effective coverage on the metal nanoparticle surface. This prevents unwanted particle growth and maintains the stability of the nanocatalyst [85].

Promotion of Redox Reactions: Ultrasound can facilitate redox reactions by generating reactive species through sonochemical processes. These reactive species can help in reducing metal precursors to form NPs or promoting the deposition of metal NPs onto the support material [86].

Support Interaction: Ultrasound can promote the interaction between metal precursors and the catalyst support material. This interaction can lead to stronger anchoring of metal NPs on the support, enhancing the stability and durability of the nanocatalyst [86].

Shorter Reaction Times: Ultrasound-assisted synthesis often accelerates reaction rates due to increased collision frequencies and energy input. This can lead to shorter reaction times compared to conventional synthesis methods [83].

Reduced Agglomeration: The mechanical forces generated by ultrasound minimize the agglomeration and growth of NPs during the synthesis process. This results in better-controlled particle sizes and improved overall catalytic performance.

In summary, ultrasound sonication is a valuable tool in the synthesis of heterogeneous metal nanocatalysts due to its ability to promote uniform dispersion of precursors, control particle size, enhance mass transfer, stabilize nanoparticles, and influence interactions with support materials. These effects collectively contribute to the production of nanocatalysts with enhanced catalytic activity, selectivity, and stability, making ultrasound-assisted synthesis an indispensable technique in the field of heterogeneous catalysis [86].

2.3 Glycerol, a Biomass derived platform chemical for numerous value-added products

The development of green technology, sustainable utilization of renewable resources, and treatment of wastewater are the prime challenges faced by chemical industries due to the increasing global energy demand and environmental concern since the last decade [87]. In this context, the catalytic transformation of biomass and its subsidiaries to valuable chemicals has been the topic of interest among the researchers [88]. Biodiesel as an alternative fuel can be produced from biomass resources by transesterification (Scheme 2.1) [89]. With the mass production of biodiesel, GLY as the main by-product in bio- diesel production is in a large surplus.

Scheme 2.1 Transesterification of biomass for bio-diesel and glycerol production.

GLY was listed as one of the 12 biomass platform chemicals by the US department of energy in 2004 [90], which is a highly functional molecule containing three hydroxyl groups and can be converted into a variety of important and value-added chemicals and intermediates through different transformation paths (Scheme 2.2)[89–92]. The main ways of GLY conversion are as follows: (i) selective oxidation to DHA and GA; (ii) hydrogenolysis to propylene glycol and ethylene glycol; (iii) dehydration by acid catalysis to acrolein and 1-hydroxyacetone; (iv) chlorination to epoxy chloropropane, an important intermediate for the synthesis of epoxy resins; (v) pyrolysis gasification for the production of gaseous fuels like H_2 or H_2+CO; and (vi) esterification to monoglycerides and diacyl esters [92].

Among the transformation processes of GLY, heterogeneous catalytic oxidation of GLY using O_2 as oxidant is appealing, which can oxidize GLY to various important derivatives (such as aldehydes, ketones, and carboxylic acids), widely used in the field of cosmetics, food, medicine and other industries [65, 93]. However, GLY has terminal and secondary hydroxyl groups to be oxidized, and some oxidation products can be further oxidized, resulting in multiple paths and various corresponding oxidation products (Scheme 2.3).

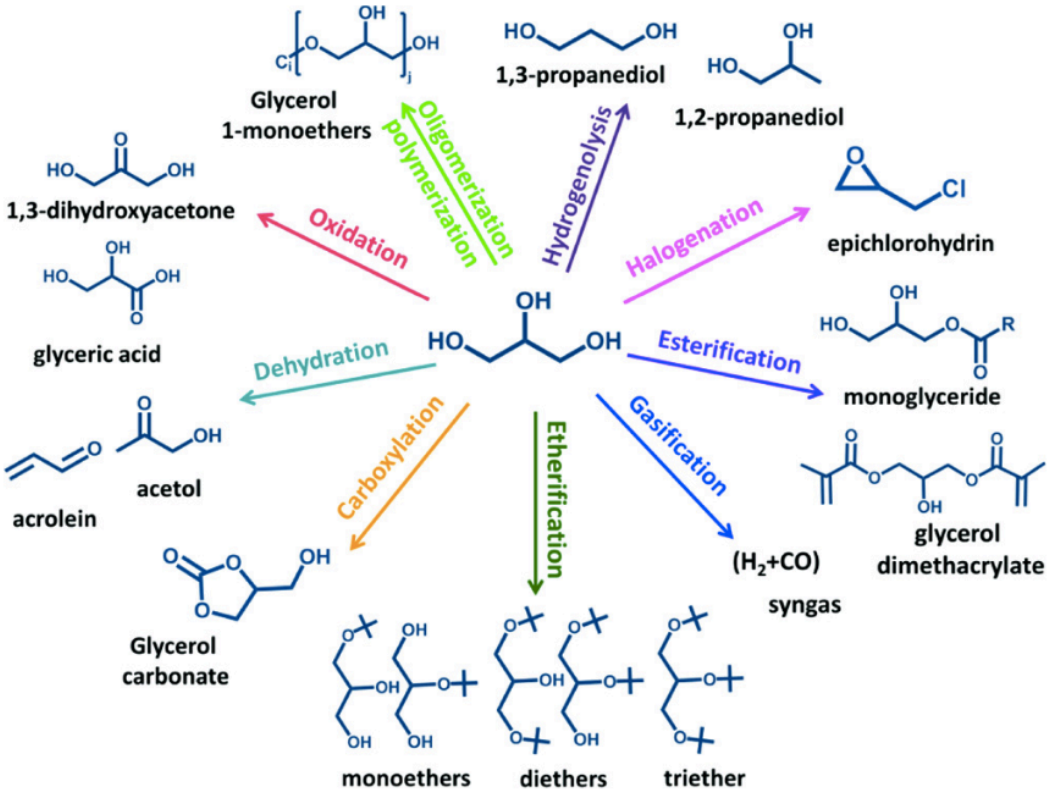

Scheme 2.2 Possible transformation reactions of Glycerol [Reprinted from Ref. [90] with permission, copyright Elsevier].

As mentioned earlier, volarization of GLY through partial oxidation is an excellent choice for obtaining many valuable products such as GA, TA, OA, LA, GLYA, AA, and FA [94, 95]. TA, GA, OA, LA, and GLYA are getting importance because of the booming biorefinery and pharmaceutical industry [96]. These oxidation products of GLY are often distributed wildly because of the diverse reaction pathways. GA is the dominant product, with LA, TA, and GLYA being major coproducts. TA, a C3 dicarboxylic acid, has wide application in the pharmaceutical and polymer industries as a versatile intermediate [97]. LA assumes a significant role in the synthesis of biodegradable polymers, that is, polylactic acid [96]. GLYA is a key constituent for cosmetic, food, and textile industries.

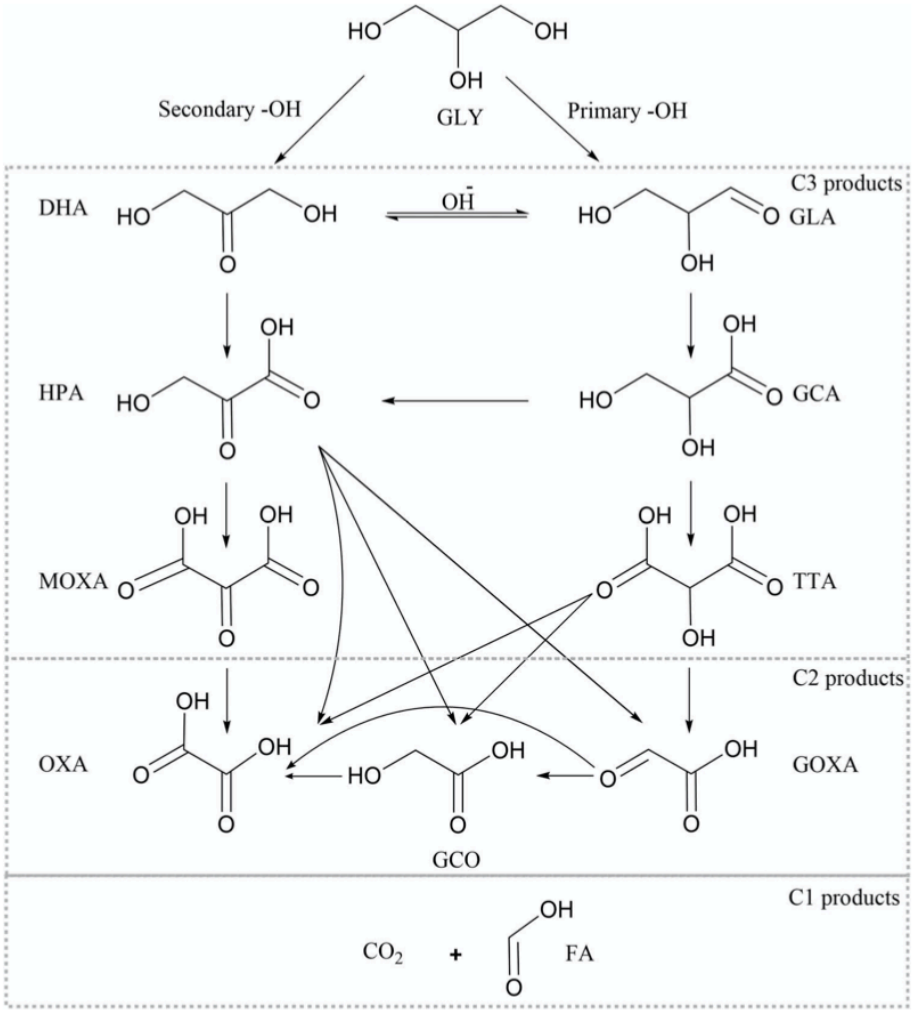

Scheme 2.3 Glycerol oxidation possible pathways. Under basic conditions, GLA and DHA inter- conversion is possible. Nomenclature: GLY = glycerol; DHA = dihydroxyacetone; GLA = glyceraldehyde; GCA = glyceric acid; HPA = hydroxypyruvic acid; TTA = tartronic acid; MOXA = mesoxalic acid; GOXA = glycoxylic acid; OXA = oxalic acid; GCO = glycolic acid [Reprinted from Ref. [98] with permission, copyright Taylor & Francis].

Owing to the structural sensitivity of the reaction, the activity and products selectivity (S) not only depend on the active metal sites, but also is affected by many other factors, such as the pH of the reaction system, the structure, and characters of metal and support. Along these lines, for obtaining the chemo-selective orientation of GLY oxidation, there is a dire need to plan highly efficient, novel heterogeneous catalysts.

2.3.1 Overview of reaction kinetics and mechanism of selective oxidation of glycerol using various heterogeneous nanocatalysts

As discussed earlier, controlling the reaction S is fundamental to obtain the desired product in case of GLY oxidation. Metal-catalyzed aerobic GLY oxidation may undergo different mechanisms, but generally, GLY oxidation mechanism usually involves GLY adsorption, O_2 adsorption on the catalyst surface, hydroxyl, and carbonyl group dehydrogenation, H_2O formation and products desorption [99]. Depending on the GLY purity degree and its impurities nature, the catalyst used, the reaction conditions (temperature, pressure, pH, substrate concentration, oxidants, and solvents) and the type of reactor, different GLY conversions and product S's may be achieved. Major factors are the reactional media pH, a strong base (-OH) presence/absence, and the catalyst nature and properties which may suppress some reactional routes in favour of others, originating different proposed reaction mechanisms [64,94,100-104]. Glycerol oxidation was denominated "structure sensitive", thus the catalyst's characteristics such as surface nature or metal particle size may shift the reaction route, thus tailoring oxidation S [105,106].

The selective oxidation of GLY using noble metals such as Pt/Pd as catalysts is an attractive method as its operating conditions are generally moderate. To date, the catalysts investigated for the GLY oxidation are mostly composed of NPs of supported noble metals, namely, Pt [107], Au [66], Ag [108], and Pd [105], in neutral as well as basic media supported over carbons (i.e. carbon nanotubes [105], and activated carbon [107]) or oxides (i.e. Al_2O_3 [108], SiO_2 [109], Co_2O_4 [69], CeO_2 [110], Nb_2O_5 [66], and TiO_2 [102]) (T: 30-80 °C, 0.1-0.8 MPa O_2, 2-4 pH), with GA often obtained as the prime product. However, limited improvement in the activity and S has been achieved by changing the properties of supports [103]. Based on the research of monometallic catalysts, great attention was paid to the promoter (such as Bi, Sb, Au and Ag etc.) modified noble metal catalysts, which can prominently improve the catalytic performance and tune the selectivity of oxidation products. After Shen et al. [111] first reported the Au-Pt catalyst for GLY oxidation, more efficient Pt and Pd based bimetallic catalysts such

as Au-Pt [102,112-113], Au-Pd [114], Pt-Ru [103], Pd-Ag [109] have been developed. Reaction kinetics strongly affect oxidation product selectivity and stability. For example, the DHA oxidation rate into HPA with nitrogen-doped carbon nanotubes supported Pt catalyst doped with Bi was higher compared with the catalyst doped with Sb, and as both showed similar activity, the latter catalyst was more selective to DHA [115].

Shen et al. [111] have explored aerobic oxidation of GLY to LA in the presence of NaOH (GLY:NaOH molar ratio =1:4) at atmospheric pressure of O_2 and 363 K on Au–Pt/TiO_2 catalyst. They have proposed the selective LA formation through oxidative dehydrogenation of GLY to GLYAD and DHA intermediates on Au-Pt NP surfaces, followed by base-catalyzed dehydration and benzylic acid rearrangement of these intermediates to LA, or their further oxidation to GA by Au–Pt/TiO_2. They have also studied the GLY oxidation over Au/TiO_2 and Pt/TiO_2 catalysts under similar reaction conditions. The results suggests that the activity of Au-Pt/TiO_2 catalyst (517.1 h^{-1}) was much improved than Au/TiO_2 (374.4 h^{-1}) and Pt/TiO_2 (405.2 h^{-1}). They have concluded that, the improved performance of the bimetallic Au-Pt catalysts, compared to the monometallic Au and Pt catalysts, is not due to the coexistence of Au and Pt, but due to the interaction and synergism between the two metals. Such interaction and synergism also led to excellent reusability of the Au-Pt catalysts up-to 5 recycle runs in comparison with monometallic Au and Pt. This suggests the excellent applicability of bimetallic nanomaterials in the field of catalysis specifically for oxidation of GLY.

Purushothaman et al. [112] have demonstrated one pot conversion of GLY to LA using monometallic Au and Pt as well as bimetallic (Au–Pt) catalysts supported on nanocrystalline CeO_2 (n-CeO_2) in aqueous solution in the presence of NaOH and oxygen. The monometallic Au and Pt catalysts on nCeO_2 resulted in about 76% and 80% glycerol conversion (X_{GLY}), corresponding with a catalyst a turn over frequency (TOF) of about 1040 and 1120 mol/(mol h^{-1}) respectively and the S for LA (S_{LA}) was 60% for Au and 68% for Pt. Whereas, the bimetallic system shows good activity (TOF = 1170 h^{-1} for a batch time of 20 min) with a high S_{LA} of 80% at excellent X_{GLY} of 99% (373 K, NaOH to glycerol ratio of 4 mol/mol, and 5 bar oxygen). The Au–Pt/nCeO_2 catalyst was recycled 5 times in a batch set-up without a significant drop in activity and S_{LA}, indicative for good catalyst stability. The reaction mechanism that follows the oxidation of GLY to LA over Au-Pt/nCeO_2 catalyst follows the dehydrogenation-dehydration-rearrangement-rehydration steps under basic conditions (Scheme 2.4). Initially oxidative dehydrogenation of GLY to GLYAD takes place which is in equilibrium with DHA

which upon dehydration forms pyruvaldehyde as an intermediate. This pyruvaldehyde then undergo rearrangement and rehydration to produce LA.

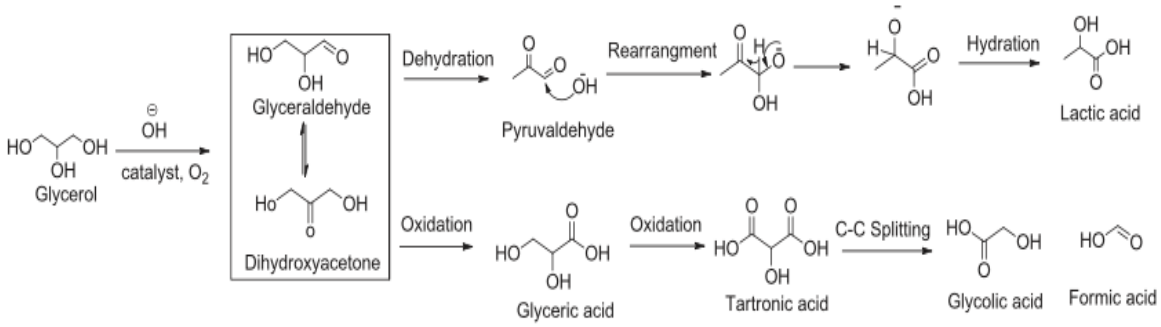

Scheme 2.4 The GLY oxidation pathway proposed by Purushothaman et al. [112] for the conversion of GLY to LA and byproducts [Reprinted from Ref. [112] with permission, copyright Elsevier].

Further, Rodriguez et al. [114] have attempted LPO of GLY at T = 333 K, P(O_2) = 11 bar gauge, 80 ml of 0.10 M GLY, 1.0 M NaOH solution, 0.03 g of Au-Pd/C catalyst and a stirring speed of 1200 rpm. Authors have evaluated bimetallic catalysts with different Pd:Au ratios and found enhanced activity compared to pure Au or Pd catalysts and this increase in activity was reported as the result of isolated Pd sites in contact with Au. The kinetic evaluation showed an increase in specific activity for Au–Pd/C catalysts with a TOF of ~20 times higher than for Pd and ~4 times higher than for Au. At X_{GLY} of 50% and 30 minutes of reaction time, the S_{GA} over Au-Pd/C catalyst was found to be 80-82% which is almost comparable to Pd (78%) whereas with pure Au it was reported to be 48%.

It is assumed that under highly basic conditions glycerol undergoes facile deprotonation of one of the two terminal -CH_2OH groups to form a $HOCH_2CHOHCH_2O$- species that adsorbs on the catalytic surface. They have considered the oxidation of GLY over Au-Pd/C to occur through a reasonable mechanistic step that uses both Au and Pd in which the Pd site interacts with the hydrogen atom of the C-H group while Au stabilizes the oxygen atom of the alkoxy group to facilitate C-H bond rupture and formation of GLYAD (Scheme 2.5). GLYAD is easily converted to the GA (glycerate under basic reaction conditions).

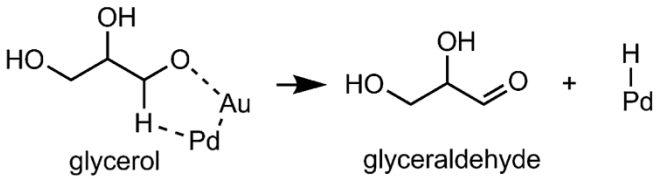

Scheme 2.5 The mechanistic step proposed by Rodriguez et al. [114] of bimetallic interaction of glycerate on Au–Pd site pair during GLY oxidation [Reprinted from Ref. [114] with permission, copyright Elsevier].

Yan et al. [103] have reported the oxidation of GLY to GA using molecular O_2 as an oxidant in base free medium at 80 °C, 1 MPa O_2 for 12 h using bimetallic PtRu/MCM-41 as catalyst. The bimetallic Pt-Ru showed superior S of GA (S_{GA}) over pure Pt catalyst. They have reported that the Ru/MCM-41 catalyst is almost inactive for the GLY oxidation as indicated in Figure 2.2. In contrast, the introduction of Ru greatly enhances the TOF from 328.1 to 823.9 h^{-1}. This clearly shows the promotional effect of Ru. Meanwhile, the catalytic performance of the $Pt_{0.8}Ru_{1.6}$/MCM-41 catalyst was even worse than that of the Pt/MCM-41 catalyst. The $Pt_{0.8}Ru_{0.8}$/MCM-41 catalyst exhibited excellent activity (TOF: 823.9 h^{-1}) and selectivity of GA (74.1%) in base-free medium, indicating that the structure formed between Pt and Ru promotes GLY oxidation. The reported PtRu/MCM-41 catalyst showed excellent catalytic activity (TOF: 823.9 h^{-1}), S_{GA} (80.1%) and good stability up to 5 recycle runs.

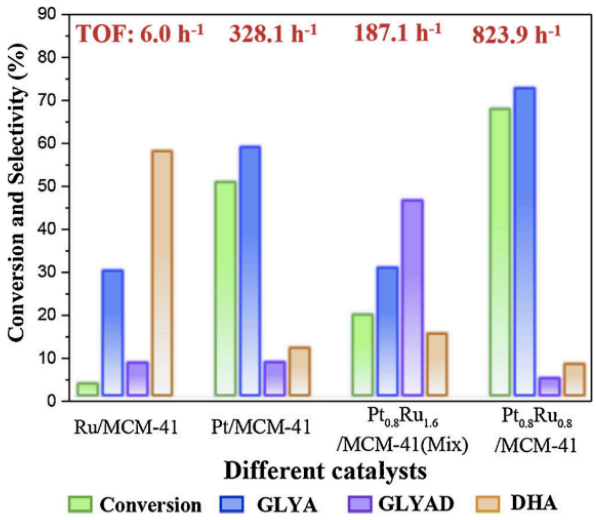

Figure 2.2 Catalytic performances of the Ru/MCM-41, Pt/MCM-41, $Pt_{0.8}Ru_{1.6}$/ MCM-41 (Mix) and $Pt_{0.8}Ru_{0.8}$/MCM-41 catalysts in glycerol oxidation (experimental conditions: 25 mL aqueous solution of glycerol (0.22 M), 0.2 g solid catalysts, 8 h) [Reprinted from Ref. [103] with permission, copyright Elsevier].

Because of the scarcity of precious noble metals, considerable attention is focused on the designing of efficient inexpensive catalysts, consisting of noble metals and secondary non-noble metals having controlled morphologies. Recently, Amaniampong et al. [116] reported oxidation of GLY over CuO nanoleaves prepared under ultrasonic irradiation (CuO-NLs) with H_2O_2 under aqueous, base free, and mild operating conditions (GLY amount = 0.100 g, temperature = 80 °C, reaction time = 4 h, CuO catalyst = 0.05 g, volume of solvent (H_2O) = 2mL, glycerol/H_2O_2 molar ratio = 0.5) to dicarboxylic acids. Authors have also synthesized the CuO catalyst via conventional method (CuO-CM). It was found that the combined yield of 63% for dicarboxylic acids (TA = 26% and OA = 37%) with CuO-CM catalyst under similar reaction conditions after 6 h of reaction was lower than the combined yield of 78% (TA = 22% and OA 56%) obtained with CuO-NLs. Further, to demonstrate the superior performances of highly crystalline CuO NLs, authors have conducted recycling experiments of CuO NLs and CuO (CM) at 80 °C, with a glycerol/H_2O_2 molar ratio of 0.5. As shown in Figure 2.3, a rapid decrease in OA and TA yields was observed over CuO (CM) cycle after cycle. The total yield of dicarboxylic acids dropped from 63% to only 7% after 6 catalytic cycles. Conversely, CuO NLs were more robust than CuO (CM) and the total yield in dicarboxylic acids remained higher than 70% up to the 5th catalytic cycle (vs 78% for the first cycle). This suggests the potential of ultrasonic irradiation for the catalyst synthesis and the dependence of GLY oxidation on the employed catalyst preparation method.

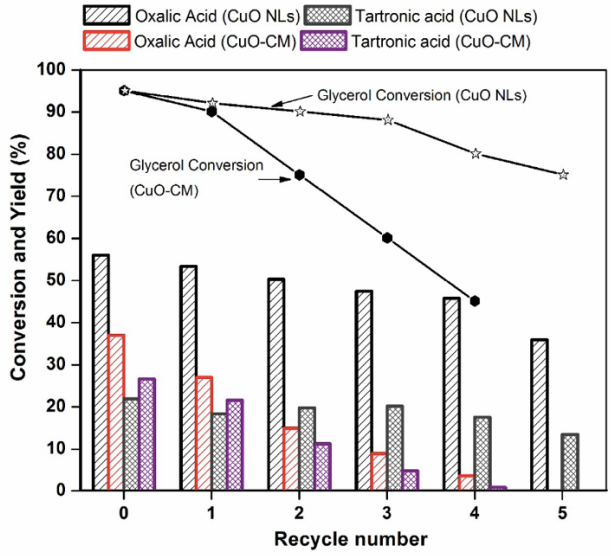

Figure 2.3 Recycle experiments over CuO NLs and CuO-CM catalysts. Reaction conditions: 0.05 g of CuO, 0.1 g of GLY, 80 °C reaction temperature, 2 mL of H_2O, 4 h reaction time and GLY/H_2O_2 molar ratio of 0.5 [Reprinted from Ref. [116] with permission, copyright Royal Society of Chemistry].

Jin et al. [97] reported excellent combined yield of 88 % for TA and OA from GLY, using cobalt-based catalyst in the presence of molecular oxygen at 70 °C, after 24 hours of reaction time. Jin et al [30] further studied the effect catalyst morphology and composition on the GLY oxidation using $PtMn/CeO_2$ catalyst. The results indicated a strong influence of catalyst morphology and composition on the GLY oxidation (Figure 2.4) as they have observed a peak activity value of 17,836.9 h^{-1} on $PtMn_1$ (Pt/Mn: 1/1 molar ratio) clusters, dropping significantly for $PtMn_{1.5}$ (9911 h^{-1}) and $PtMn_2$ (3231 h^{-1}) catalysts.

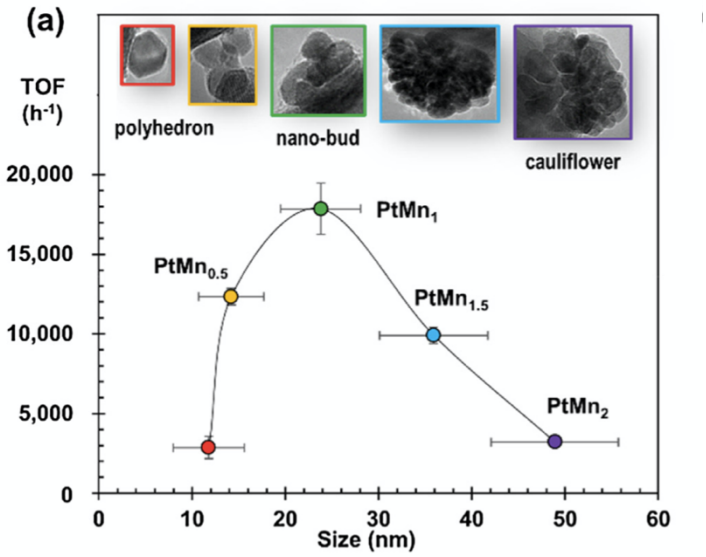

Figure 2.4 Composition-dependent catalytic performances of PtMn catalysts for GLY oxidation [Reprinted from Ref. [30] with permission, copyright Elsevier].

Arcanjo et al. [117] studied the oxidation of GLY into LA using activated carbon supported Pd as heterogeneous catalysts. They achieved a GLY conversion of about 99% with selectivity of 68% for LA using 10% Pd/C catalysts at 230 °C of reaction temperature. Palacio et al. [113] investigated GLY oxidation to LA using CeO_2 supported Co_3O_4 NPs as catalysts at 250 °C under basic environment. They have obtained selective GLY conversion of 85.7% to LA (79.8 % selectivity) using Co_3O_4/CeO_2 catalysts and demonstrated the selective catalytic activity of the Co_3O_4/CeO_2.

Very recently Choi et al. [68] have designed an excellent catalyst that facilitated the GLY oxidation under mild conditions of an atmospheric open-air system at room temperature of 30°C without any additives or gas flow in base free conditions. The catalyst $Pt/CeO_2–ZrO_2–Fe_2O_3$/SBA-16 was designed to supply an active oxygen species from inside the crystal lattice where $CeO_2–ZrO_2 –Fe_2O_3$ acts as a promoter and Pt as an activator were dispersed onto a high

surface area mesoporous silica Santa Barbara Amorphous No. 16 (SBA-16), resulting in Pt/CeO2–ZrO2 –Fe2O3/SBA-16 catalysts (Figure 2.5). The CeO_2–ZrO_2–Fe_2O_3 solid solution showed high oxygen release and storage abilities, where Fe_2O_3 was introduced into the CeO_2–ZrO_2 lattice to enhance the redox properties, owing to the redox cycle between $Ce^{3+/4+}$ and $Fe^{2+/3+}$, and to facilitate the oxide ion migration through the replacement of the Ce^{4+} and Zr^{4+} sites for the lower-valent $Fe^{2+/3+}$ ions.

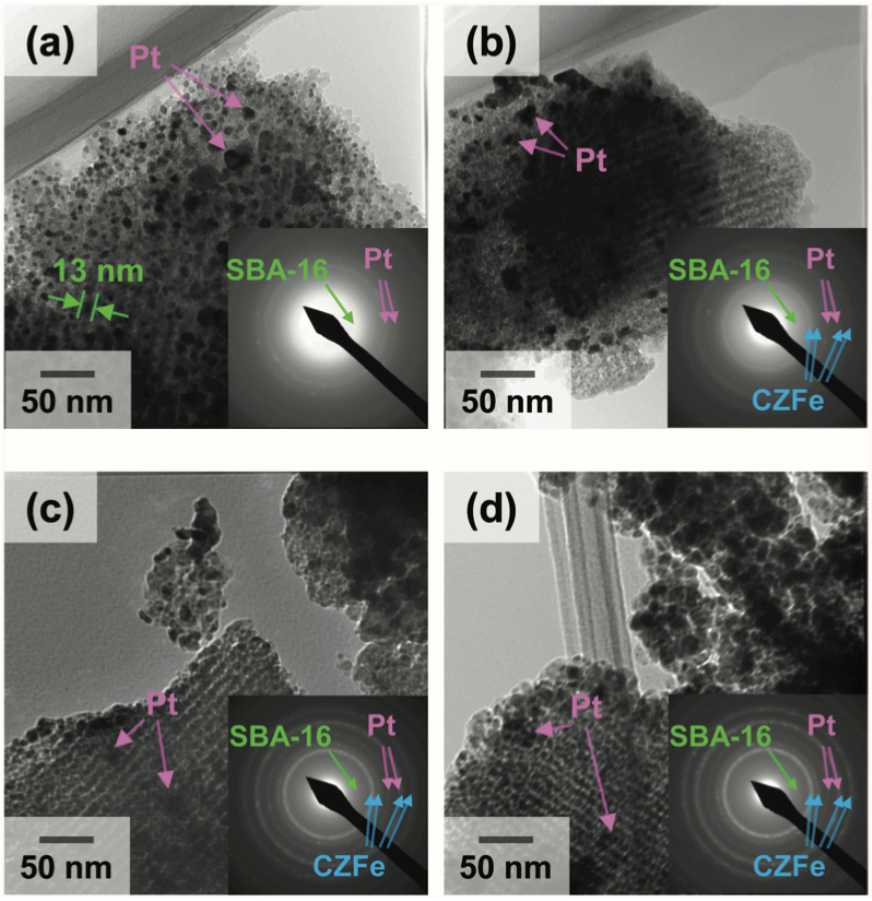

Figure 2.5 TEM images for the Pt/*x* wt% CZFe/SBA catalysts with (a) *x* = 0, (b) *x* = 16, (c) *x* = 40, and (d) *x* = 60. Electron diffraction images are shown in the insets [Reprinted from Ref. [68] with permission, copyright Taylor & Francis].

Authors have noticed that, at a low loading amount of CeO_2–ZrO_2–Fe_2O_3 (16 wt%$Ce_{0.64}Zr_{0.16}Fe_{0.20}O_{2-\delta}$/SBA-16), the oxygen release, storage abilities and high acidity of the catalyst afforded a high GLYAD yield, owing to the enhancement of the oxidation ability of the Pt activator and the acceleration of the desorption of GLYAD. The increase in CeO_2–ZrO_2–Fe_2O_3 loading amount further improved the oxygen release and storage abilities and lowered the catalyst acidity induced by crystallite growth and particle aggregation. The high oxygen release and storage abilities, as well as the low acidity, contributed to the high GA yield; the

highest activity for GA production was obtained for the 7 wt% Pt/40 wt%$Ce_{0.64}Zr_{0.16}Fe_{0.20}O_{2-\delta}$/SBA-16 catalyst. The GA yield increased up to 68.2% after 10 h of reaction in atmospheric air at 30°C. The various catalyst and their performance reported for selective oxidation of GLY towards GA is given in Table 2.2 given below.

Table 2.2 Literature reports on GLY oxidation using mono and multi-metallic catalysts.

Catalyst	NaOH/GLY ratio	T (^oC)	time (h)	PO_2 (MPa)	Catalyst loading	X (%)	S_{GA} (%)	Ref.
Au-Pt/TiO_2	4	80	0.5	0.3	-	90	58	[97]
Au/HY	4	60	2	0.3	0.3 g	80	-	[88]
Pt/AC	4	90	6	0.1	0.25 g	58.5	18.4	[102]
Pt-Fe/CeO_2	4	70	2	0.1	2.2 kg/m^3	57.1	71.1	[105]
Au-Pt/CeO_2	4	100	0.5	0.5	-	99	10.5	[107]
Pt-Mn/CeO_2	4	70	24	0.1	0.05 g	100	24.9	[30]
$Co_{0.15}/Mg_3Al_{-s}$	6	70	6	-	0.2 g	47	49.1	[92]
Pt-Au/HLT	-	60	-	0.1	-	57	72	[108]
Pt-Fe/CeO_2	4	70	6-10	0.1	0.10 g	100	15.1	[29]
Cu-Pt/AC	1.5	90	4	0.1	0.25 g	80	16.7	[114]

2.4 Abatement of recalcitrant water contaminants (4-nitrophenol and congo red: an azo dye) using hetero-nanostructures

An immense array of organic compounds are currently widely used, and many of these are potent contaminants when they are released into freshwater ecosystems. In a great majority of industrial processes water is used as a solvent, reaction or transport medium, therefore it is not surprising that many efforts in the last two decades have been made for the abatement of pollutants from industrial aqueous waste streams. Industrial plants generate increasing amounts of wastewater, contaminated with toxic and hazardous organic compounds, which cause severe problems for the environment [20,115]. The principal cause of this event is the high amounts of toxic and recalcitrant pollutants, mainly nitrophenols and azo dyes, which are widely used in the pharmaceutical and textile industries [18,78] for the production of herbicides, insecticides, synthetic dyes, and paints, and as a corrosion inhibitor and pH indicator, among other applications [116,117]. Nitrophenols such as 4-NP and azo dyes are highly toxic to living beings, even in trace amounts, as they can harm the kidney, blood, central nervous system, and liver of humans and animals owing to their extremely mutagenic and carcinogenic nature [118].

Owing to their hazardous nature, especially for human beings, this dye polluted wastewater is becoming a notorious natural danger to our environment. This necessitates removal of phenols, azo dyes and other organic contaminants from the environment. In recent era, several pathways such as UV photolysis/photocatalysis, adsorption, reduction and (photo) degradation, have been exploited for the abatement of organic pollutants from groundwater, freshwater sediments, wastewater, etc. [119]. Thus, developing novel technologies for the effectual treatment of wastewater comprising organic pollutants is of extraordinary importance across the globe.

2.4.1 Summary on catalytic reduction of 4-nitrophenol using HNCs and the reaction kinetics

Manufacturing and wastewater treatment processes in the chemical industry have greatly benefited from revolutionary advances in the field of catalysis. Catalytic reduction is one of the important manufacturing and treatment processes used for reducing noxious organic molecules to safer products. The reduction of 4-NP is a noteworthy organic transformation reaction to its reduction product, 4-AP, as nitrophenols are the most frequently found recalcitrant pollutants in wastewater and conversely, 4-AP is less toxic and can be easily removed and mineralised than 4-NP [120]. 4-AP also finds its application in developing analgesic and antipyretic drugs, photographic developers and in many other applications such as anti-corrosion agents and lubricants.

However, the reduction of 4-NP to 4-AP is challenging as it is highly stable and less soluble in water making its conversion into an ecologically safer product complex [121]. For the reduction of 4-NP to 4-AP, it must interact with hydrogen (hydride ion). A strong reducing agent like sodium borohydride ($NaBH_4$) is commonly used to reduce dyes into non-toxic constituents as it is a good source of hydride ions . However, the catalytic activity of $NaBH_4$ for the reduction of 4-NP is inadequate because the release of hydrogen ions through self-hydrolysis is insufficient and the stability of 4-NP is also very high [57]. Moreover, mutual repulsion caused by negatively charged 4-NP and BH_4^- ions creates high kinetic barriers [120,122]. Although the reaction was a thermodynamically feasible process involving E_0 for 4-NP/4-AP = – 0.76 V and H_3BO_3/ BH_4^- = – 1.33 V versus normal hydrogen electrode, it was kinetically restricted in the absence of a catalyst (no change in the absorption even after 2 days) [123]. Due to these issues related to 4-NP reduction, the presence of a catalyst to overcome all barriers is essential.

Pradhan et al. [124] primarily introduced 4-NP reduction as a model reaction using Ag NPs. The catalytic reduction reaction was real-time monitored via UV-visible spectroscopy by observing the decrease in the absorption band at 400 nm belonging to the 4-nitrophenolate ion (intermediate product) and increase in the band at 300 nm related to 4-AP. The absorption peak of 4-NP changes from 317 to 400 nm immediately when treated with an aqueous solution of $NaBH_4$ (Figure 2.6 a), which corresponds to a color change of light yellow to yellow-green due to the formation of 4-nitrophenolate ion [123]. After addition of a small amount (1.0 mg) of the catalyst, the reduction commences and the time-dependent absorption spectra show a decrease in intensity of the absorption peak at 400 nm and a concomitant increase of a new peak at 295 nm corresponding to 4-AP (Figure 2.6 b). After the completion of reduction reaction, the peak due to the nitro compound was no longer observed, which indicated that the catalytic reduction of 4-NP had proceeded successfully.

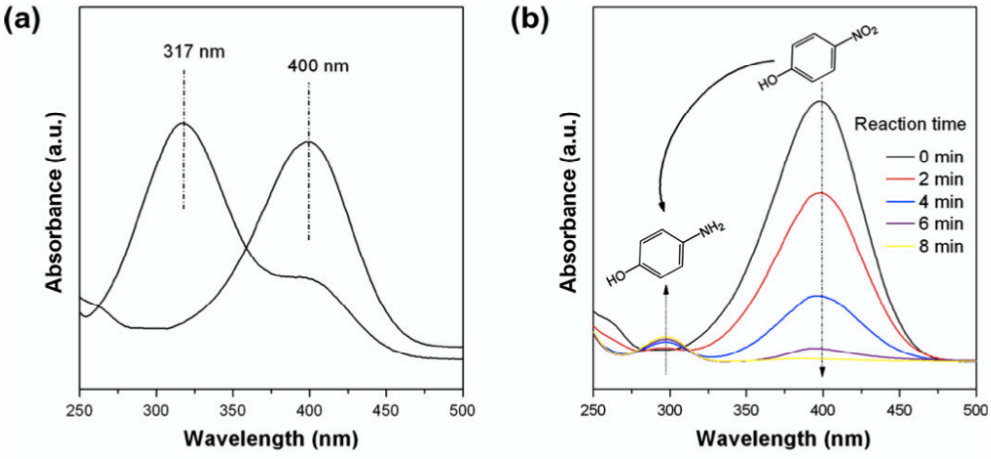

Figure 2.6 UV–vis spectra of (a) 4-NP before and after adding $NaBH_4$ solution and (b) the reduction of 4-NP in aqueous solution recorded every 2 min using heterogeneous catalyst [Reprinted from Ref. [123] with permission, copyright Elsevier].

Thereof, the 4-NP reduction with $NaBH_4$ as a reducing agent in conjunction with metal catalysts, such as Au [125-128], Pd [129–132], Pt [133], Ag [60,128,134-136], Co [60,115,137], Cu [138,139], etc. and their assemblies on dendrimers, polymeric matrices, microgels, metal-immobilized silica-coated supports, and graphene oxide, has gained more attention due to its eco-friendly and straightforward reduction process. But, the application of noble metal catalysts is not practically feasible because of the scarcity and expensive material cost. The use of alloys comprising of noble metals with easily available, economic non-noble metals can be an affordable alternative to the noble metal catalyst without compromising the efficiency of catalyst. As it can reduce the required quantity of noble metals and offers

unprecedented synergistic effects that enhances the electronics and catalytic properties of the alloys [52,70,73,123,140].

In recent years, the proficiency of bimetallic nanostructures in accelerating the reduction of 4-NP has been explored through BNPs such as Ag-Cu [141], Hg-Pd [70], Cu-Ni [57], Au-Ag [142], Pd-Co [54], Au-Pt [143], Pt-Ni [53], etc. The results obtained from these studies marked the remarkable enhancement in the catalytic performance of noble metal NPs upon alloying with other metals for the reduction of 4-NP.

Based on this, Ghosh et al. [53] have synthesized bimetallic Pt-Ni alloyed NPs via co-reduction of respective metal salts for the catalytic application in 4-NP reduction. Authors have also studied the effect of Pt-Ni alloy composition on catalytic activity towards 4-NP reduction As can be seen in Figure 2.7, the catalytic activity of bimetallic particles was ca. 15 times higher than that of monometallic Pt particles. They have concluded that the catalytic effects were due to the active sites on Pt and Ni acting as catalytically enhancing agents i. e. promoter. Upon alloying with Ni, the local electronic structure of Pt was profoundly affected in the Pt–Ni matrix and the electron density on the alloyed cluster Pt-Ni depends on the metal composition.

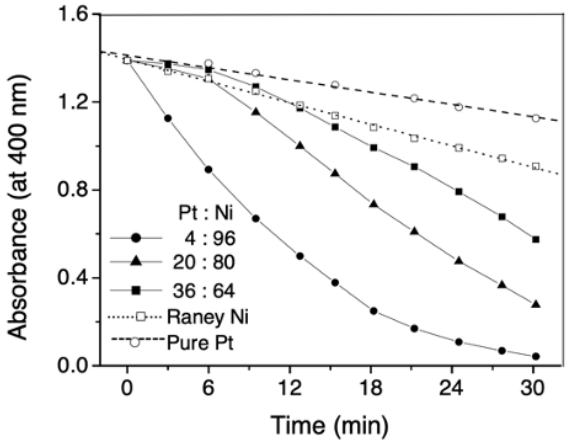

Figure 2.7 Absorbance as a function of time for the reduction of 4-NP using pure Pt, Raney Ni and different compositions of the Pt-Ni alloy catalysts. [Reprinted from Ref. [53] with permission, copyright Elsevier].

They have also suggested the electron transfer mechanism during 4-NP reduction as, the electron transfer took place between 4-nitrophenolate (oxidant) ion and BH_4^- (reductant) through the metal particles. The rate of electron transfer at the particle surface was influenced by a two-step mechanism: (a) adsorption of 4-nitrophenolate ion onto the catalyst surface and (b) interfacial electron transfer and desorption of 4-aminophenolate away from the surface. The adsorption of substrates is driven by chemical interaction (chemisorption) between the particle

surface and the substrates. The adsorption of 4-nitrophenolate ions onto the particle surface thus helped to overcome the kinetic barrier of the reaction.

Later, Chi et al. [123] reported the 4-NP reduction over the core-shell structured Fe_3O_4@SiO_2–Ag magnetic NCs using $NaBH_4$. The rate of reduction reaction catalyzed by Fe_3O_4@SiO_2–Ag was also estimated by the authors by assuming the rate of 4-NP reduction to be independent of the concentration of $NaBH_4$ because this reagent was used in large excess compared to 4-NP. Therefore, the kinetic data were fitted by a first-order rate law. Linear relationship between $\ln(C/C_0)$ and reaction time was obtained in the reduction catalyzed by Fe_3O_4@SiO_2–Ag NC, and the rate constant k was calculated to be 7.67 X 10^{-3} s^{-1}. According to the authors, the good catalytic activity of Fe_3O_4@SiO_2–Ag NC was derived from its highly dispersed and small-sized Ag NPs. Highly dispersed Ag NPs can make 4-nitrophenolate ion easily accessible to the Ag NPs that serve as an electron relay in the system for an oxidant and a reductant. The small size of Ag NPs makes a large potential difference, thus leading to a high rate of reduction. In addition, a smaller particle size can result in a larger surface-to-volume ratio and more exposed atoms on the surface, which act as the potential catalytic sites.

Further, Wu et al.[131] have promoted the use of renewable natural resources to prepare a variety of hybrid inorganic–organic materials for the purpose of catalysis by evaluating the catalytic performance of cellulose nanocrystal (CNC)-supported Pd NPs for the 4-NP reduction. They have proposed a one step and environment-friendly synthesis of CNC supported Pd NPs without employing any other reductants, capping or dispersing agents. CNs played a dual role as a supporting matrix and a reductant and they were used to obtain stable dispersions of Pd NPs. They have obtained the conversion of 97.7 % after 10 min with the pseudo-first-order k of is 5.7 X 10^{-3} s^{-1} at room temperature. The authors have also studied the stability of Pd NPs and Pd NPs stabilized on CNCs and the results showed that the Pd NPs stabilized on CNCs were stable for several months or even longer, while the unsupported Pd NPs resulted in self-aggregation and adsorption onto the wall of the container in order to decrease their surface energy.

Sogukomerogullari, et al. [130] have explored the immobilization of Pd NPs onto the amine functionalized graphene nanosheets (Pd/GNS-NH_2) for the catalytic reduction of 4-NP. The 4-NP reduction reaction conditions were 4-NP = 20 μmol in the aqueous sodium borohydride (0.2 mmol) solution and Pd/GNS-NH_2 (0.48 μmol Pd) at room temperature under air. Pd/GNS-NH_2 nanocatalyst was synthesized by the deposition-reduction method and the excellent activity of nanocatalyst have been detected with 65.9 min^{-1} initial TOF value.

Further, Nariya et al. [144] have applied magnetic silver cyclodextrin NC (Ag NC) as catalyst for reduction of nitro aromatics and organic dyes (Reaction conditions: 10 mg Ag NC, 3 mL 4-NP (0.359 mmol), 35 °C, 3 mL $NaBH_4$ (5.385 mmol)). After performing control experiments authors have noticed that, Fe_2O_3 alone cannot function as a catalyst, while in the presence of Ag NC the reaction takes place in 11 min with k = 0.6787 min^{-1} indicating good catalytic activity of Ag NC towards reduction of 4-NP. The recycling studies performed by the authors indicates that the catalyst can efficiently reduce 4-NP up to 5 catalytic cycles without significant loss in its activity whereas catalyst poisoning causes a decrease in the catalytic activity after the 5th cycle.

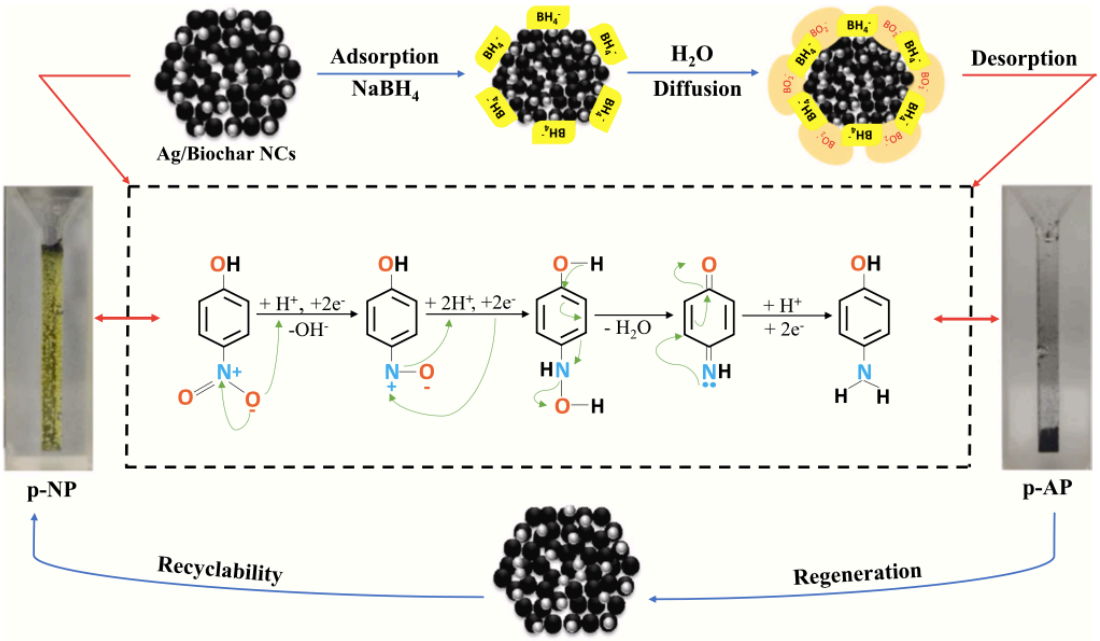

Figure 2.8 Detailed mechanism proposed by Behera et al. in catalytic conversion of 4-NP by AB NCs [Reprinted from Ref. [18] with permission, copyright Elsevier].

In addition Deka et al. [74] have reported the reduction of 4-NP using mesoporous silica supported mono and bimetallic Co, Cu and CoCu NPs as catalyst. They have observed excellent catalytic performance of mesoporous silica supported CoCu NPs ($Co_{40}Cu_{60}$@S16LC-20) for the reduction of 4-NP to 4-AP in comparison to the monometallic counterparts i. e. Cu@S16LC-20 and Co@S16LC-20 with k = 3.85×10^{-2} s^{-1} for $Co_{40}Cu_{60}$@S16LC-20 after 80s. Behera et al. [18] have innovatively explored the utilization of biochar as support for Ag NPs and its catalytic activity was assessed on 4-NP reduction. Catalytic activity of Ag/biochar NCs (AB-NCs) was found to be remarkably higher than that of Ag NPs and biochar.

Authors were able to achieve 98.6% conversion of 4-NP ($k = 0.496\ min^{-1}$) in 8 min of reaction time with AB-NCs catalyst loading of 600 mg/L, 4-NP concentration 100 mg/L and 300 µL of $NaBH_4$ (15 mM). The authors have also proposed a plausible reaction mechanism comprising of four steps: adsorption, diffusion, reduction and desorption (Figure 2.8). In the first place, a steady adsorption of $NaBH_4$ and 4-NP molecules may have occurred on the extrinsic surface of AB-NCs followed by diffusion of active sites of NCs with BH_4^- ions and 4-NP molecules. Here, active site commits to the active functional pores or/and domains in AB- NCs that linger in near proximity with 4-NP and $NaBH_4$ molecules in a reaction, thereby triggering the catalytic efficiency. Further, after diffusion step is complete, these effective sites alleviate the electron transfer facility from $NaBH_4$ to 4-NP, and converting it to 4-AP. This step progresses in diminishing the activation energy barrier. Eventually, all the 4-AP molecules get desorb from AB-NCs surface and assimilate in water.

Table 2.3. Overview on the available literature for catalytic reduction of 4-NP.

Catalyst	4-NP (mM)	$NaBH_4$ (M)	Catalyst loading (g/L)	Reaction time (min)	k_{app} (s^{-1})	Ref.
Calcium alginate/Ag	0.1	0.1	1.200	8	-	[146]
Fe_3O_4@SiO_2-Ag	0.12	0.012	1.699	8	0.00767	[123]
Pd@CNC	0.12	0.038	0.085	10	0.005.7	[131]
Pt–Au/rGO	0.7	0.5	0.002	10	0.0038	[147]
Ag-Ag_2S	0.1	0.2	1.818	10	0.0105	[135]
Ag/CNF	0.0018	0.053×10^{-3}	5	5.42	0.0008	[136]
Ag/zeolite	2.5	0.25	0.200	2.67	-	[148]
Ag@KF-HTO-PDA	0.036	0.020	1.52	20	0.0031	[149]
cellulose-based Ag NPs	2	0.5	0.625	20	-	[134]
Cu_2O-chitosan	0.1	3	0.285	5	0.0038	[150]
C@Co	20 ppm	0.1	0.222	2	0.033	[151]
Nitrogen and phosphorus co-doped carbon	0.5	0.05	1	20	0.00065	[118]
rGO/CNT/Fe/Ag	0.12	0.5	0.0704	6	0.01466	[152]
Fe_3O_4/Ag@Ca−AlLDH@ starch bioNC	0.1	0.1	0.333	8	0.0076	[153]
Co_3O_4/CoP	0.1	0.1	0.03	3	0.026	[154]
AgNPs@NC	1	0.2	0.030	11	0.00325	[71]
$BaWO_4$/NRGO-g-C_3N_4	0.1	0.1	0.17	1	0.1883	[155]
Pd@Fe_3O_4/chitosan-agar microcapsules	0.125	0.05	-	3	0.0051	[129]

Co_3O_4	3.59	0.408	1	2.67	-	[154]
Cu/GO/MnO_2	2.5	0.25	0.1	5	-	[156]
PtCo/N-rGO	0.7	0.5	1	9	0.0124	[157]
NRGO-$FeWO_4$-Fe_2O_3	0.1	0.1	0.33	0.75	0.0434	[158]
rGO supported $NiCo_2O_4$	0.7	0.1	0.083	6	0.012	[159]
F-Ni/Cu-P-RT	0.5	0.2	1.67	0.33	0.235	[160]

Very recently, H. Helmiyati et al. [145] have synthesized the combined sodium alginate (SA) and carboxymethyl cellulose (CMC) biopolymers functionalized with Fe_3O_4 NPs to immobilize Cu NPs to form Fe_3O_4@SA–CMC–CuNP NCs catalyst for 4-NP reduction. The authors have reported higher catalytic activity of Fe_3O_4@SA–CMC–CuNP NC than individual components Fe_3O_4 and Fe_3O_4@SA–CMC. The 95% reduction of 4-NP, k = 0.359 min^{-1} was reported in 1.5 min with 30 mg of Fe_3O_4@SA–CMC–CuNP NCs catalyst, 3 mL 4-NP (0.001 M) and 0.3 mL $NaBH_4$ (0.1 M). The Table 2.3 gives a brief overview on the reported literature for catalytic reduction of 4-NP over heterogeneous catalysts.

2.4.2 State of the art literature on photocatalytic degradation of Congo red di-azo dye

The advancement in the current state of technology is the major cause of environmental ecological changes. The pollutant such as dyes are the major source of dangerous contaminants discharged from different companies, such as the paper, textile, paints, cosmetic, printing, food, pulp, and pharmaceutical industries [161,162]. Keeping in view the tendency of toxic chemicals and dyes to cause skin problems, coughing, dyspnea, eye irritation, liver and kidney damage, lung disease, ulcers, respiratory problems, and cancer, there is utmost need to improve water quality by removing these hazardous materials [163]. Dye effluents are high in colour, pH, suspended solids (SS), chemical oxygen demand (COD), biochemical oxygen demand (BOD) [164], metals [165] , temperature[166] and salts[167]. Synthetic textile dyes are often recalcitrant and carcinogenic by nature due to the presence of –N=N– bond. Those dyes mainly consist of complex aromatic structures that are hardly biodegradable. CR is one of the most prominent sulfonated substituted benzidine di-azo dye. CR has linear symmetry with two phenyl rings in the center joined to two terminal naphthalene by diazo bonds (Figure 2.9)[161]. The UV–visible spectra of CR showed three distinct bands at 498 nm, 347 nm, and 235 nm attributed to the chromophore group, naphthalene, and benzoic ring respectively (Figure 2.10)

[168]. It is a highly toxic anionic dye that is widely used in paper, rubber, and textile factories and its degradation is needed to avoid its hazards where azo bonds are degraded [169].

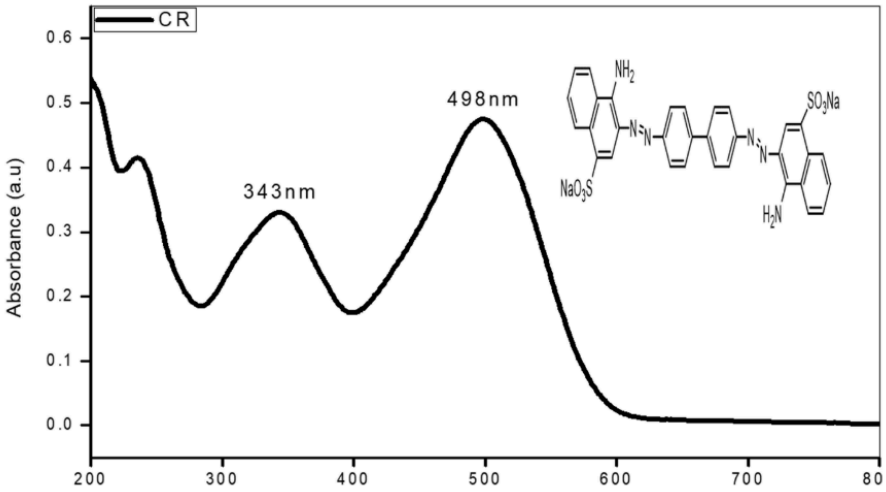

Figure 2.9 UV-visible spectrum of CR dye [Reprinted from Ref. [168] with permission, copyright Springer].

Methods for the treatment of dye-contaminated waters include reverse osmosis, coagulation, flocculation, ion exchange, activated carbon adsorption, advanced oxidation, ozonation, photocatalysis, Fenton process, photo-Fenton, electrochemical oxidation and filtration [76]. All of these approaches have short comings like incomplete mineralization, chemical consumption, disposal of dense solution, laboratory scale, pH dependence, high consumption of energy, high material costs, sludge treatment, etc. [161]. Alternatively, semiconductors such as titanium dioxide and zinc oxide have shown excellent photocatalytic activity due to a positive band position that develops more electrons and holes under UV light [170]. The process of dye degradation/decolorization via the use of photon-active nanomaterials as adsorbents is called photocatalysis. The whole process initiates a redox reaction which spontaneously generates radicals (e.g hydroxides, peroxides, and superoxides) while forming electron-hole pairs. The radicals combine with the organic pollutants (e.g. dyes in wastewater) and mineralize them into compounds such as CO_2 and H_2 [171]. Recently, the photocatalytic capacity has been improved by modifying material surfaces using metal doped, non-metal doped and coupled systems [79,80,172,173]. Nano adsorbent materials are broadly referred to as either organic or inorganic with distinguishing features of photosensitivity, high surface area, high thermal chemical and mechanical stability, appreciable electrostatic features, compressibility, tunability of pore volume and band gap (Eg), high magnetic and adsorptive capacity and enhanced solubility properties due to short intra-particle diffusion [174]. These distinguishing features

account for their application in the photocatalysis of recalcitrant dye molecules in industrial effluents.

The use of the photocatalytic technique in nanotechnology is described as a photon-induced molecular transformation that occurs at the surface of exciting photoactive nanomaterial adsorbing organic pollutants (e.g dye molecules) from the wastewater. The mechanism of the degradation process starts with the capturing of photon energy from light by the photocatalyst leading to the excitation of the electrons from the VB to the CB, forming oxidizing and reducing sites (Figure 2.10). For electronic excitation to occur, the energy of the photon captured by the material must be equal to or greater than the energy of its Eg. This excitation leads to the generation of hydroxyl radicals (•OH), superoxide radical anions ($•O_2$), and hydroperoxyl radicals (•OOH), which are oxidizing species. Dyes adsorbed already by the nano adsorbents from the wastewater combine with the electrons in the CB resulting in the formation of dye radical anions and consequently degradation of the dye molecules [169,175]. For instance, in the photodegradation process of azo dyes present in textile wastewater, the energy of photons captured via UV or sunlight generates electron-hole pairs (e^- and h^+) which migrate to the surface and site of the adsorbed azo dyes. This migration set-up a redox reaction (Figure 2.10), which produces oxidizing radicals that attacks the adsorbed azo dye molecules and degrade them into non-toxic substances such as H_2O and CO_2 [176]. Photocatalyst nano-adsorbents used for this process can be bio-based, metal-organic frameworks (MOFs), carbon-based, polymeric-based or inorganic. However, commonly used nano adsorbents in photocatalysis are the inorganic metal oxides [169]. This is due to their promising potentials such as photon detection and capturing, electronic structure, carrier transportation and Eg [174].

To enhance the reactivity of catalysts, HNPd catalysts were developed by coating small amounts of a transition or noble metal onto a freshly prepared metal surface. There has been a lot of interest in the synthesis and utilization of HNPd catalysts for the removal of contaminants, especially from wastewater. Catalysis on HNPd alloys advanced over the past few decades. The HNPd catalysts were studied due to their enhanced activity, selectivity, and stability resulting from the ensemble, electronic, and bifunctional effects between the two different metal components. The incorporation of a second metal into the catalyst may lead to modifications or changes in the geometric as well as the electronic characteristics of the catalyst. This results in the modification of the adsorption characteristics of the bimetallic/ hetero nanostructured catalyst's surface and in some cases alters its reduction and deactivation

behaviour. Ali et al. revealed that bimetallic catalysts exhibit different physicochemical properties than those of monometallic catalysts [177]. Heterogeneous catalysis occurs on the catalyst surface. Therefore, the surface structure and chemistry of bimetallic catalysts in terms of the geometric and electronic structures of metal atoms on the surface are the most significant parameters.

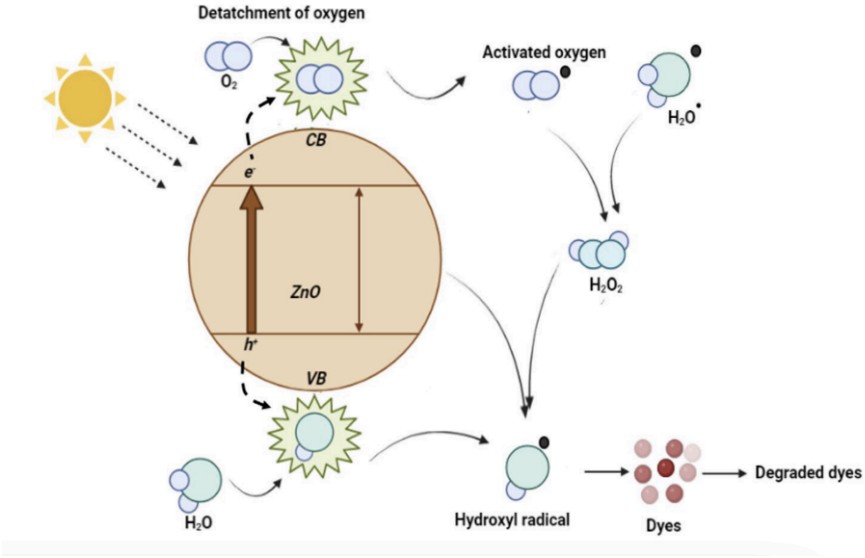

Figure 2.10 Mechanism of Azo dye degradation in photocatalysis [Reprinted from Ref. [174] with permission, copyright Elsevier].

Bhagwat et al. [76] synthesized lead titania ($PbTiO_3$) nanorods through sonochemical approach for the CR dye degradation. About 92 % dye was degraded at pH 6 in the existence of $PbTiO_3$ nanorods under visible light after 150 min (Initial CR concentration = 7 mg/L, catalyst loading = 0.75 g). Authors have further studied the impact of various experimental parameters such as photocatalyst dosage, pH, and initial dye concentration on CR degradation. According to authors, the dye degradation is completed in two stages, one is absorption and next one is degradation of dye. The result obtained after visible light irradiation on CR absorbed in $PbTiO_3$ shows the typical absorption peak at 497 nm for CR slowly decreased with increase in irradiation time and at last, the absorption peak disappears and the color of the CR solution turns red to colorless (Figure 2.11a). The pseudo-first-order reaction can be explained by the kinetics model by plotting -ln (C/C_0) against time t (Figure 2.11b), C_0 is the initial concentration of dye and C is the concentration of CR dye at different time intervals.

Different bimetallic catalysts supported on alumina-mesoporous silica were studied in the photodegradation of methylene blue (MB), CR and mixed dyes (MB + CR). The photodegradation order for all the dyes treated is Co-Fe/Al_2O_3-MCM-41 > Fe-Mn/Al_2O_3-MCM-41 > Mn-Co/Al_2O_3-MCM-41 > Fe/Al_2O_3-MCM- 41 > Co/Al_2O_3-MCM-41 > Mn/Al_2O_3-

MCM-41. The results indicate that adding a second metal improves the catalytic activity and performance of the monometallic catalyst [178].

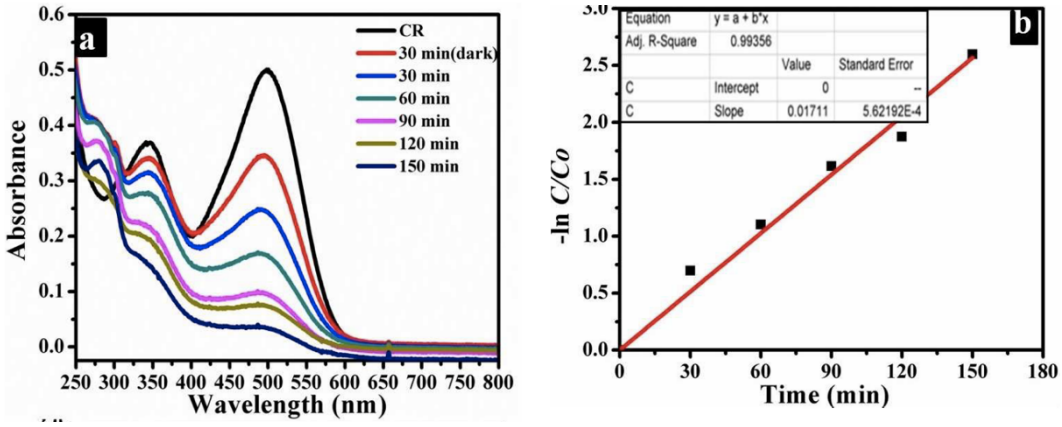

Figure 2.11 (a) UV-Vis absorption spectrum of $PbTiO_3$ nanorods in the existence of CR dye depends on time under irradiation (b) first order plot for degradation of CR [Reprinted from Ref. [76] with permission, copyright Wiley].

CR was also treated using H_2O_2 and Co-Fe supported on polyacrylamide hydrogel (PAM) as the oxidant and catalyst (with a loading of 0.05 g L^{-1}), respectively, at neutral pH, reaching about 96.45 % efficiency within 60 min. In addition, Fe/PAM and Co/PAM were used to determine the effect of second metal incorporation in the CR removal leading to 85.19 % and 84.76 % degradation within 75 min, respectively [179].

Recently, Cu-Ni supported on ginger powder (GP) has been used to treat three kinds of dye [180]. The 3.0 g L^{-1} Cu-Ni (combined with sodium borohydride electrolyte) showed good catalytic activity for the removal of various dyes, i.e., Rhodamine B (RhB), Methyl Orange (MO), and CR, with 95.98 % removal. Moreover, the Cu-Ni catalyst was compared with the Cu-Ag catalyst, showing similar degradation efficiencies for all the dyes studied at a very short reaction time. The reusability of Cu-Ni/GP and Cu-Ag/GP catalysts was found to be five cycles. However, Cu-Ag can degrade the dye in a shorter time approximately half the time relative to Cu-Ni. The recyclability results indicated that Cu-Ag/GP has excellent reusability and stability compared with those of Cu-Ni/GP.

Pradhan et al. [178] have explored the application of Fe-Mn catalyst to treat MB and CR dyes. Specifically, Fe-Mn/Al_2O_3-MCM-41 exhibited 97 % and 90 % MB and CR dye degradation, respectively. Mu et al. [181] reported a high adsorption capacity of 248.76 mg g^{-1} for graphene/polyaniline/Fe_3O_4 NCs towards CR dye removal. Furthermore, Sathiyavimal et al. [182] were able to obtain 90 % oxidative photodegradation of CR and MB within 150 min over

chitosan-coated $CuSO_4$ NC, synthesised from Psidium guajava aqueous leaf extract. Here, electrons are generated from the valance bond due to the presence of sunlight.

Further, TiO_2 doped $CoFe_2O_4$ nanostructures were designed by Magdalane et al. [78] using microwave method. The TiO_2 doped $CoFe_2O_4$ spinel ferrite nanostructures showed a Eg of 2.88 eV. The overall percentage of decomposition of CR dye was found to be 85 and 97 % with the addition of only catalyst and catalyst/H_2O_2 at pH value 3.0. The decolourisation of dye solution was observed nearly at 120 min of time in the acid medium. But in the case of only catalyst, the dye was decomposed after 250 min. The reason must be the negatively charged CR dye was more attracted towards the positive charge on the catalyst in acidic medium due to robust electrostatic attraction of negatively charged dye and positively charged catalyst in case of acid medium. This leads to strong adsorption of dye molecules on the surface of the reaction catalyst. Hence, the degradation found to be faster in acid medium than the basic medium. Whereas, in the basic condition the percentage of degradation was found to be less, due to strong repulsive force in between anionic dye and catalyst with more negative charge of the base [183]. From the result, it can be inferred that the degradation is more beneficial in acidic condition.

Khan, et al. [81] studied the CR degradation over ternary metal selenide-chitosan microspheres (ZBiSe-CM) synthesized via solvothermal process. The ZBiSe-NPs showed high photocatalytic degradation efficiency (up to 99.63 %) for 40 ppm concentration of CR at catalyst dosage 0.225 g, pH 8.0, and temperature 36-38 °C for 2 h of solar light illumination. Photodegradation of CR dye in the presence of ZBiSe-CM follows pseudo-first-order kinetics ($k = 0.10\ min^{-1}$) and the ZBiSe-CM degraded CR dye in five consecutive cycles with high decontamination efficiency.

Further, the efficiency of a novel Z-scheme g-C_3N_4/RGO/BFO NC prepared using hydrothermal method was evaluated in degradation of aqueous solution of CR dye under visible light by Shekardasht, et al. [80]. The results showed that the percentage of CR removal under visible light, without photo catalyst, was negligible and removal of CR by BFO, g-C_3N_4, g-C_3N_4/BFO and g-C_3N_4/ RGO/BFO were 34.76, 52.54, 69.76, and 87.7 %, respectively and the efficiency of g-C_3N_4/RGO/BFO NC in removal of CR is higher than others. This increment in photocatalytic activity of g-C_3N_4/RGO/BFO NC could be explained by migration of photoinduced charges via RGO between g-C_3N_4 and BFO. The stability of NC was also confirmed through five recycling experiments.

Very recently, photocatalytic degradation of CR was explored by Maruthupandy et al. [77] over Cts decorated Fe_3O_4 nanospheres prepared using one-pot hydrothermal process. The Cts/ Fe_3O_4 nanospheres demonstrated 98 % efficient photocatalytic activity against CR dye molecules (k = 0.096 min^{-1}) upon 60 min exposure to visible light compared to Fe_3O_4 nanospheres (77 % for 60 min, k = 0.114 min^{-1}). The Table 2.4 presents a brief comparative study on the degradation of CR over various photocatalysts reported earlier.

Table 2.4 Comparative study for the degradation of CR using different photocatalysts.

Catalyst	Initial CR concentration	Catalyst Dosage (g/L)	Reaction time (min)	CR degradation (%)	Ref.
Zn-doped $CdTiO_3/TiO_2$	50 cc	0.6	15	90	[184]
ZnO	20 ppm	0.24	60	90	[185]
$PbTiO_3$	1 x 10^{-5} M	0.75	150	92	[76]
Fe	50 mg/L	1	120	90	[186]
TiO_2	25 µmol/L	0.5	30	87	[187]
Cts-g-poly(acrylamide)/ZnS	2 x 10-5 M	0.2 (g)	120	75	[188]
Mn doped ZnO/rGO	20 mg/L	0.8	160	100	[189]
Sulfated TiO_2/WO_3	20 ppm	0.5	120	95	[190]
BiOCl/PANI/Fe^0	50 mg/L	1	120	80	[191]
Cellulose/ PVC/ZnO	3 ppm	0.6	120	90	[192]
Cts-capped FeNiSe- CHM	60 ppm	0.2 (g)	140	99	[176]
g-C_3N_4/RGO/$Bi_2Fe_4O_9$	10 mg/L	0.5	60	87	[80]
ZnO-CuO/ES	10 mg/L	1	240	83	[193]
Layered basic zinc acetate (LBZA)/Bentonite Clay	100 mg/L	0.50	210	67.4	[194]
Pd-ZnO	16 mg/L	0.05 (g)	60	100	[195]

2.5 Gaps identification based on the state of art literature

Last decade has witnessed tremendous development in the field of nanocatalyst is especially development of HNCs for catalytic applications owing to the synergistic properties induced by interactions between the different nanometer-scale materials. The state-of-the-art literature suggests that, the catalytic properties of hetero nanostructured catalysts highly depend on their

shape, size, structure, composition, and surface properties, which are greatly influenced by the synthesis method. Although a lot of achievements have been made on the synthesis of hetero nanocatalysts, these catalysts suffer from one or more drawbacks such as the requirement of intricate surface modification, the utilization of toxic reagents, harsh temperature and pressure conditions, complex multiple-step and time-consuming preparation processes, and most importantly poor stability/reusability. Present synthesis techniques for HNCs are often complex and costly. Thus, future research should attempt to decrease the preparation cost by searching for and testing new low-cost raw materials and developing green, simple and more practical methods. These challenges promote us to explore and design a high-performance supported hetero nanosctructured catalyst with facile synthesis procedure, unique architecture and fine metal/metal oxide dispersion. Literature study shows that the synthesis of NCs via ultrasound assistance have a great potential in terms of green approach of nanomaterial synthesis with fine tuning of the catalytic properties and offering enhanced stability of the NCs. Though it's a very powerful approach, very few reports are available on the synthesis of NC catalyst using ultrasound assistance for catalytic applications.

Upon the critical review of the previous works in the literature on HNCs for catalysis applications it was noted that, tremendous research efforts are being devoted into utilizing the biomass waste as a major source of green energy to maintain the economic, environmental, and social sustainability and wastewater treatment. Specifically, there is an emerging consensus on the significance of glycerol (an underutilised waste from biodiesel industry) as a cheap, non-toxic, and renewable source for valuable chemicals synthesis. Being a highly functional entity, GLY is an excellent choice for obtaining many valuable products such as GA, TA, OA, LA, GLYA, AA, and FA through its oxidation. Though a lot of research is dedicated on to the oxidation of GLY, the harsh reaction conditions, control over the selectivity and yield of a particular product, especially secondary oxidation products from the array of products is still a major challenge faced by the research community. In addition the selective oxidation of GLY was attempted in the presence of base and mostly over noble metal catalysts, but then the to obtain secondary oxidation products in their pure form demands further downstream processing, very limited literature is available on the base free oxidation of GLY. Thus, there is a need to develop economic catalysts that accelerates the reaction under base free and mild process conditions.

Another major application of HNCs in catalysis is wastewater treatment. As the water contamination has generated significant concern due to its adverse effects, mainly on human

health and ecosystem. Literature suggests photocatalytic degradation of recalcitrant pollutants from the wastewater as a potential approach for the removal of toxic contaminants from aqueous solutions. Extensive work is focused on the development of photocatalytic nanomaterials for the wastewater application. Semiconductor materials (metal oxides, chalcogenides, and chalcohalides) are one of the most used materials for the photocatalytic process because they can conduct electricity in the presence of light at room temperature. However, the challenges corresponding to their uses as photocatalyst includes photo-corrosion, frequent electron-hole recombination, large band gap, low photon detection and capturing propensity and agglomeration of powdered NPs. One of the significant challenges for the scientific community, involved in photocatalytic research, is to investigate the photo-catalytic performance of the novel nanomaterials in outdoor conditions, i.e. using sunlight to degrade pollutants in real wastewater. Solar energy can be used as an alternative source of energy that not only is renewable but also inexhaustible and clean. Photocatalysis is a widely studied application of solar energy. It is a new version of green technology, which aims in accelerating reactions and can be used in the degradation of contaminants. Doping, hybridization, and coupling with other semiconductor photocatalysts boost the photocatalytic performance of the semiconductors.

In view of this, for the effective utilization of renewable resources like biomass and water through biomass transformation using oxidation and abatement of organic pollutants from wastewater, design and development of suitable NC catalysts using catalyst modification by ultrasound assistance, doping and synthesis of heterojunction photocatalyst was focused in this work to cater to the requirements for emerging catalysts with improved selectivity, catalytic activity, recyclability, and efficacy.

References

[1] S. Schauermann, N. Nilius, S. Shaikhutdinov, H. Freund, Nanoparticles for heterogeneous catalysis: New mechanistic insights, Acc. Chem. Res. 46 (2013) 1673–1681. https://doi.org/10.1021/ar300225s.

[2] H. Zeng, S. Sun, Syntheses, properties, and potential applications of multicomponent magnetic nanoparticles, Adv. Funct. Mater. 18 (2008) 391–400. https://doi.org/10.1002/adfm.200701211.

[3] A.S.K. Hashmi, G.J. Hutchings, Gold Catalysis, Angew. Chemie - Int. Ed. 45 (2006) 7896–7936. https://doi.org/10.1002/anie.200602454.

[4] Z. Wu, L. Li, T. Liao, X. Chen, W. Jiang, W. Luo, J. Yang, Z. Sun, Janus nanoarchitectures: From structural design to catalytic applications, (2018). https://doi.org/10.1016/j.nantod.2018.08.009.

[5] H. Zheng, J. Wang, S.E. Lofland, Z. Ma, L. Mohaddes-Ardabili, T. Zhao, L. Salamanca-Riba, S.R. Shinde, S.B. Ogale, F. Bai, D. Viehland, Y. Jia, D.G. Schlom, M. Wuttig, A. Roytburd, R. Ramesh, Multiferroic $BaTiO_3$-$CoFe_2O_4$ Nanostructures., Science. 303 (2004) 661–663. https://doi.org/10.1126/science.1094207.

[6] S.B. Potdar, B.V.S. Praveen, S.H. Sonawane, Sonochemical approach for synthesis of zinc oxide-poly methyl methacrylate hybrid nanoparticles and its application in corrosion inhibition, Ultrason. Sonochem. 68 (2020) 105200. https://doi.org/10.1016/j.ultsonch.2020.105200.

[7] F.X. Redl, K.-S. Cho, C.B. Murray, S. O Brien, Three-dimensional binary superlattices of magnetic nanocrystals and semiconductor quantum dots, Nature. 423 (2003) 968–971. https://doi.org/10.1038/nature01702.

[8] E. V Shevchenko, D. V Talapin, N.A. Kotov, S. O Brien, C.B. Murray, Structural diversity in binary nanoparticle superlattices, Nature. 439 (2006) 55–59. https://doi.org/10.1038/nature04414.

[9] Y. Ma, X. Wu, G. Zhang, Core-shell Ag@Pt nanoparticles supported on sepiolite nanofibers for the catalytic reduction of nitrophenols in water: Enhanced catalytic performance and DFT study, Appl. Catal. B Environ. 205 (2017) 262–270. https://doi.org/10.1016/j.apcatb.2016.12.025.

[10] N. Hikmah, N.F. Idrus, J. Jai, A. Hadi, Synthesis and characterization of silver-copper core-shell nanoparticles using polyol method for antimicrobial agent, IOP Conf. Ser. Earth Environ. Sci. 36 (2016). https://doi.org/10.1088/1755-1315/36/1/012050.

[11] A. Strab, R. Maier, R. Guttel, Continuous synthesis of nanostructured Co_3O_4@SiO_2 core-shell particles in a laminar-flow reactor, Chemie-Ingenieur-Technik. 89 (2017) 963–967. https://doi.org/10.1002/cite.201600162.

[12] H. Zheng, M.S. Matseke, T.S. Munonde, The unique Pd @ Pt /C core-shell nanoparticles as methanol-tolerant catalysts using sonochemical synthesis, Ultrason. Sonochem. 57 (2019) 166–171. https://doi.org/10.1016/j.ultsonch.2019.05.023.

[13] B. Nakhjavan, M.N. Tahir, F. Natalio, M. Panthöfer, H. Gao, M. Dietzsch, R. Andre, T.

Gasi, V. Ksenofontov, R. Branscheid, U. Kolb, W. Tremel, Ni@Fe_2O_3 heterodimers: Controlled synthesis and magnetically recyclable catalytic application for dehalogenation reactions, Nanoscale. 4 (2012) 4571–4577. https://doi.org/10.1039/c2nr12121b.

[14] B. Nakhjavan, M.N. Tahir, F. Natalio, H. Gao, K. Schneider, T. Schladt, I. Ament, R. Branscheid, S. Weber, U. Kolb, C. Sönnichsen, L.M. Schreiber, W. Tremel, Phase separated Cu@Fe_3O_4 heterodimer nanoparticles from organometallic reactants, J. Mater. Chem. 21 (2011) 8605. https://doi.org/10.1039/c1jm10922g.

[15] Y. Jang, J. Chung, S. Kim, S.W. Jun, B.H. Kim, D.W. Lee, B.M. Kim, T. Hyeon, Simple synthesis of Pd–Fe_3O_4 heterodimer nanocrystals and their application as a magnetically recyclable catalyst for Suzuki cross-coupling reactions, Phys. Chem. Chem. Phys. 13 (2011) 2512. https://doi.org/10.1039/c0cp01680b.

[16] B. Nakhjavan, M.N. Tahir, M. Panthofer, H. Gao, T. Gasi, V. Ksenofontov, R. Branscheid, S. Weber, U. Kolb, L.M. Schreiber, W. Tremel, Controlling phase formation in solids: rational synthesis of phase separated Co@Fe_2O_3 heteroparticles and $CoFe_2O_4$ nanoparticles, Chem. Commun. 47 (2011) 8898. https://doi.org/10.1039/c1cc13204k.

[17] S.R. Yousefi, O. Amiri, M. Salavati-Niasari, Control sonochemical parameter to prepare pure $Zn_{0.35}Fe_{2.65}O_4$ nanostructures and study their photocatalytic activity, Ultrason. Sonochem. 58 (2019) 104619. https://doi.org/10.1016/j.ultsonch.2019.104619.

[18] M. Behera, N. Tiwari, S. Banerjee, A.R. Sheik, M. Kumar, M. Pal, P. Pal, R.P. Chatterjee, S. Chakrabortty, S.K. Tripathy, Ag/biochar nanocomposites demonstrate remarkable catalytic activity towards reduction of p-nitrophenol via restricted agglomeration and leaching characteristics, Colloids Surfaces A Physicochem. Eng. Asp. 642 (2022) 128616. https://doi.org/10.1016/j.colsurfa.2022.128616.

[19] X. Fang, J. Zhao, D. Fang, Hydrodechlorination of 4-chlorophenol on Pd – Cu / activated carbon bimetallic catalysts, 101 (2018) 21751. https://doi.org/10.5004/dwt.2018.21751.

[20] L. Cui, Z. Bai, Z. Li, Z. Liu, H. Ma, X. Chen, K. Lin, J. Hao, Y. Cui, F. Tian, A recyclable photocatalyst Cu_2O/Fe_3O_4@C/Cu nanocomposite for efficient photocatalytic reduction of 4-nitrophenol, Appl. Surf. Sci. 602 (2022) 154403. https://doi.org/10.1016/j.apsusc.2022.154403.

[21] L. Han, P. Cui, H. He, H. Liu, Z. Peng, J. Yang, A seed-mediated approach to the morphology-controlled synthesis of bimetallic copper - Platinum alloy nanoparticles

with enhanced electrocatalytic performance for the methanol oxidation reaction, J. Power Sources. 286 (2015) 488–494. https://doi.org/10.1016/j.jpowsour.2015.04.003.

[22] T. Teranishi, M. Saruyama, M. Kanehara, Seed-mediated synthesis of metal sulfide patchy nanoparticles, Nanoscale. 1 (2009) 225–228. https://doi.org/10.1039/b9nr00110.

[23] V.K. Landge, S.H. Sonawane, R. V. Chaudhari, G.U.B. Babu, selective oxidation of glycerol: A biomass-derived feedstock using the pt-cu janus catalyst for value-added products, Ind. Eng. Chem. Res. 60 (2021) 185–195. https://doi.org/10.1021/acs.iecr.0c04626.

[24] T.D. Schladt, T. Graf, O. Kohler, H. Bauer, M. Dietzsch, J. Mertins, R. Branscheid, U. Kolb, W. Tremel, Synthesis and magnetic properties of FePt@MnO nano-heteroparticles, Chem. Mater. 24 (2012) 525–535. https://doi.org/10.1021/cm2030685.

[25] H. Yu, Y. Jiao, N. Li, J. Pang, W. Li, X. Zhang, X. Li, Au-CeO_2 Janus-like nanoparticles fabricated by block copolymer templates and their catalytic activity in the degradation of methyl orange, Appl. Surf. Sci. 427 (2018) 771–778. https://doi.org/10.1016/j.apsusc.2017.08.112.

[26] I. Schick, S. Lorenz, D. Gehrig, S. Tenzer, W. Storck, K. Fischer, D. Strand, F. Laquai, W. Tremel, Inorganic Janus particles for biomedical applications, Beilstein J. Nanotechnol. 5 (2014) 2346–2362. https://doi.org/10.3762/bjnano.5.244.

[27] B. Wu, S. Tang, M. Chen, N. Zheng, Amphiphilic modification and asymmetric silica encapsulation of hydrophobic Au-Fe_3O_4 dumbbell nanoparticles, Chem. Commun. 50 (2014) 174–176. https://doi.org/10.1039/c3cc47634k.

[28] H. Gu, R. Zheng, X. Zhang, B. Xu, Facile one-pot synthesis of bifunctional heterodimers of nanoparticles: A conjugate of quantum dot and magnetic nanoparticles, J. Am. Chem. Soc. 126 (2004) 5664–5665. https://doi.org/10.1021/ja0496423.

[29] X. Jin, H. Yan, C. Zeng, P.S. Thapa, B. Subramaniam, R. V Chaudhari, Phase transformed PtFe nanocomposites show enhanced catalytic performances in oxidation of glycerol to tartronic acid, Ind. Eng. Chem. Res. (2017). https://doi.org/10.1021/acs.iecr.7b01473.

[30] X. Jin, C. Zeng, W. Yan, M. Zhao, P. Bobba, H. Shi, P.S. Thapa, B. Subramaniam, R. V. Chaudhari, Lattice distortion induced electronic coupling results in exceptional enhancement in the activity of bimetallic PtMn nanocatalysts, Appl. Catal. A Gen. 534 (2017) 46–57. https://doi.org/10.1016/j.apcata.2017.01.021.

[31] V.K. Lamer, R.H. Dinegar, Theory, Production and mechanism of formation of

monodispersed hydrosols, J. Am. Chem. Soc. 72 (1950) 4847–4854.

[32] C. Wang, C. Xu, H. Zeng, S. Sun, Recent progress in syntheses and applications of dumbbell-like nanoparticles, Adv. Mater. 21 (2009) 3045–3052. https://doi.org/10.1002/adma.200900320.

[33] H. Yu, M. Chen, P.M. Rice, S.X. Wang, R.L. White, S. Sun, Dumbbell-like bifunctional Au−Fe_3O_4 nanoparticles, Nano Lett. 5 (2005) 379–382. https://doi.org/10.1021/nl047955q.

[34] C. Wang, Y. Wei, H. Jiang, S. Sun, Tug-of-war in nanoparticles: Competitive growth of Au on Au−Fe_3O_4 nanoparticles, Nano Lett. 9 (2009) 4544–4547. https://doi.org/10.1021/nl903077t.

[35] C. Wang, H. Yin, S. Dai, S. Sun, A general approach to noble metal-metal oxide dumbbell nanoparticles and their catalytic application for CO oxidation, Chem. Mater. 22 (2010) 3277–3282. https://doi.org/10.1021/cm100603r.

[36] L. Carbone, P.D. Cozzoli, Colloidal heterostructured nanocrystals: Synthesis and growth mechanisms, Nano Today. 5 (2010) 449–493. https://doi.org/10.1016/j.nantod.2010.08.006.

[37] M. Casavola, R. Buonsanti, G. Caputo, P.D. Cozzoli, Colloidal strategies for preparing oxide-based hybrid nanocrystals, Eur. J. Inorg. Chem. (2008) 837–854. https://doi.org/10.1002/ejic.200701047.

[38] Y. Wei, R. Klajn, A.O. Pinchuk, B.A. Grzybowski, Synthesis, shape control, and optical properties of hybrid Au/Fe_3O_4 “nanoflowers,” Small. 4 (2008) 1635–1639. https://doi.org/10.1002/smll.200800511.

[39] W. Shi, H. Zeng, Y. Sahoo, T.Y. Ohulchanskyy, Y. Ding, Z.L. Wang, M. Swihart, P.N. Prasad, A general approach to binary and ternary hybrid nanocrystals, Nano Lett. 6 (2006) 875–881. https://doi.org/10.1021/nl0600833.

[40] S.-H. Choi, H. Bin Na, Y. Il Park, K. An, S.G. Kwon, Y. Jang, M. Park, J. Moon, J.S. Son, I.C. Song, W.K. Moon, T. Hyeon, Simple and generalized synthesis of oxide−metal heterostructured nanoparticles and their applications in multimodal biomedical probes, J. Am. Chem. Soc. 130 (2008) 15573–15580. https://doi.org/10. 1021/ja805311x.

[41] S. Peng, Y. Lee, C. Wang, H. Yin, S. Dai, S. Sun, A facile synthesis of monodisperse Au nanoparticles and their catalysis of CO oxidation, Nano Res. 1 (2008) 229–234. https://doi.org/10.1007/s12274-008-8026-3.

[42] A. Holewinski, H. Xin, E. Nikolla, S. Linic, Identifying optimal active sites for

heterogeneous catalysis by metal alloys based on molecular descriptors and electronic structure engineering, Curr. Opin. Chem. Eng. 2 (2013) 312–319. https://doi.org/10.1016/j.coche.2013.04.006.

[43] E. Gross, G.A. Somorjai, the impact of electronic charge on catalytic reactivity and selectivity of metal-oxide supported metallic nanoparticles, Top. Catal. 56 (2013) 1049–1058. https://doi.org/10.1007/s11244-013-0069-3.

[44] J. Wu, P. Li, Y.-T. (Frank) Pan, S. Warren, X. Yin, H. Yang, Surface lattice-engineered bimetallic nanoparticles and their catalytic properties, Chem. Soc. Rev. 41 (2012) 8066–8074. https://doi.org/10.1039/C2CS35189G.

[45] A. Kirkeminde, S. Ren, Interdiffusion Induced Exchange Coupling of L10-FePd/α-Fe Magnetic Nanocomposites, Nano Lett. 14 (2014) 4493–4498. https://doi.org/10.1021/nl502167m.

[46] H. Liao, A. Fisher, Z.J. Xu, Surface segregation in bimetallic nanoparticles: A critical issue in electrocatalyst engineering, Small. 11 (2015) 3221–3246. https://doi.org/10.1002/smll.201403380.

[47] Z. Quan, Y. Wang, J. Fang, High-index faceted noble metal nanocrystals, Acc. Chem. Res. 46 (2013) 191–202. https://doi.org/10.1021/ar200293n.

[48] H. Gu, Z. Yang, J. Gao, C.K. Chang, B. Xu, Heterodimers of nanoparticles: Formation at a liquid-liquid interface and particle-specific surface modification by functional molecules, J. Am. Chem. Soc. 127 (2005) 34–35. https://doi.org/10.1021/ja045220h.

[49] Y. Pan, J. Gao, B. Zhang, X. Zhang, B. Xu, Colloidosome-based synthesis of a multifunctional nanostructure of silver and hollow iron oxide nanoparticles, Langmuir. 26 (2010) 4184–4187. https://doi.org/10.1021/la904067q.

[50] M. Masjedi-arani, M. Salavati-niasari, Cd_2SiO_4/Graphene nanocomposite : Ultrasonic assisted synthesis, characterization and electrochemical hydrogen storage application, Ultrason. Sonochem. 43 (2018) 136–145. https://doi.org/10.1016/j.ultsonch.2018.01.009.

[51] H. Gu, Z. Yang, J. Gao, C.K. Chang, B. Xu, Heterodimers of nanoparticles: Formation at a liquid−liquid interface and particle-specific surface modification by functional molecules, J. Am. Chem. Soc. 127 (2005) 34–35. https://doi.org/10.1021/ja045220h.

[52] R. Dhanda, M. Kidwai, Reduced graphene oxide supported Ag_xNi_{100-x} alloy nanoparticles: A highly active and reusable catalyst for the reduction of nitroarenes, J. Mater. Chem. A. 3 (2015) 19563–19574. https://doi.org/10.1039/c5ta03779d.

[53] S.K. Ghosh, M. Mandal, S. Kundu, S. Nath, T. Pal, Bimetallic Pt-Ni nanoparticles can catalyze reduction of aromatic nitro compounds by sodium borohydride in aqueous solution, Appl. Catal. A Gen. 268 (2004) 61–66. https://doi.org/10.1016/j.apcata.2004.03.017.

[54] T.A. Revathy, T. Sivaranjani, A.A. Boopathi, S. Sampath, V. Narayanan, A. Stephen, Pd–Co alloy as an efficient recyclable catalyst for the reduction of hazardous 4-nitrophenol, Res. Chem. Intermed. 45 (2019) 815–832. https://doi.org/10.1007/s11164-018-3645-0.

[55] Y.X. Wang, H.J. Zhou, P.C. Sun, T.H. Chen, Exceptional methanol electro-oxidation activity by bimetallic concave and dendritic Pt-Cu nanocrystals catalysts, J. Power Sources. 245 (2014) 663–670. https://doi.org/10.1016/j.jpowsour.2013.07.015.

[56] A.S. Douk, H. Saravani, M. Farsadrooh, M. Noroozifar, An environmentally friendly one-pot synthesis method by the ultrasound assistance for the decoration of ultrasmall Pd-Ag NPs on graphene as high active anode catalyst towards ethanol oxidation, Ultrason. Sonochem. (2019) 104616. https://doi.org/10.1016/j.ultsonch.2019.104616.

[57] M. Kohantorabi, M.R. Gholami, Kinetic Analysis of the Reduction of 4-Nitrophenol Catalyzed by CeO_2 Nanorods-Supported CuNi Nanoparticles, Ind. Eng. Chem. Res. 56 (2017) 1159–1167. https://doi.org/10.1021/acs.iecr.6b04208.

[58] J.H. Park, J.J. Wang, D.C. Seo, Comparison of catalytic activity for treating recalcitrant organic pollutant in heterogeneous Fenton oxidation with iron-impregnated biochar and activated carbon, J. Water Process Eng. 42 (2021) 102141. https://doi.org/10.1016/j.jwpe.2021.102141.

[59] N. Mahfoudhi, S. Boufi, Porous material from cellulose nanofibrils coated with aluminum hydroxyde as an effective adsorbent for fluoride, J. Environ. Chem. Eng. 8 (2020) 103779. https://doi.org/10.1016/j.jece.2020.103779.

[60] M. Aazza, H. Ahlafi, H. Moussout, C. Mounir, A. Fadel, A. Addad, Catalytic reduction of nitro-phenolic compounds over Ag, Ni and Co nanoparticles catalysts supported on γ-Al_2O_3, J. Environ. Chem. Eng. 8 (2020). https://doi.org/10.1016/j.jece.2020.103707.

[61] S. Sharma, S. Basu, Visible-light-driven efficient photocatalytic abatement of recalcitrant pollutants by centimeter-length MoO_3/SiO_2 monoliths with long service life, Appl. Mater. Today. 23 (2021) 101033. https://doi.org/10.1016/j.apmt.2021.101033.

[62] K.F.M. Elias, A.F. Lucrédio, E.M. Assaf, Effect of CaO addition on acid properties of Ni–Ca/Al_2O_3 catalysts applied to ethanol steam reforming, Int. J. Hydrogen Energy. 38

(2013) 4407–4417. https://doi.org/https://doi.org/10.1016/j.ijhydene.2013.01.162.

[63] S.G. Babu, P. Karthik, M.C. John, S.K. Lakhera, M. Ashokkumar, J. Khim, B. Neppolian, Synergistic effect of sono-photocatalytic process for the degradation of organic pollutants using CuO-TiO_2/rGO, Ultrason. Sonochem. 50 (2019) 218–223. https://doi.org/10.1016/j.ultsonch.2018.09.021.

[64] Z. Han, R. Xie, Y. Song, G. Fan, L. Yang, F. Li, Efficient and stable platinum nanocatalysts supported over Ca-doped $ZnAl_2O_4$ spinels for base-free selective oxidation of glycerol to glyceric acid, Mol. Catal. 477 (2019) 110559. https://doi.org/10.1016/j.mcat.2019.110559.

[65] D. Li, H. Gong, L. Lin, W. Ma, Q. Zhou, K. Kong, R. Huang, Z. Hou, Selective aerobic oxidation of glycerol over zirconium phosphate-supported vanadium catalyst, Mol. Catal. 474 (2019) 110404. https://doi.org/10.1016/j.mcat.2019.110404.

[66] L. Wolski, Factors affecting the activity and selectivity of niobia-based gold catalysts in liquid phase glycerol oxidation, Catal. Today. 354 (2020) 36–43. https://doi.org/10.1016/j.cattod.2019.07.015.

[67] X. Wang, G. Wu, T. Jin, J. Xu, S. Song, Selective Oxidation of Glycerol Using 3 % H_2O_2 Catalyzed by Supported Nano-Au Catalysts, Catalysts. 8 (2018) 505. https://doi.org/10.3390/catal8110505.

[68] Y. Bin Choi, N. Nunotani, K. Morita, N. Imanaka, Selective glycerol oxidation to glyceric acid under mild conditions using Pt/CeO_2–ZrO_2–Fe_2O_3/SBA-16 catalysts, J. Asian Ceram. Soc. 10 (2022) 178–187. https://doi.org/10.1080/21870764.2022.2028980.

[69] X. Han, H. Sheng, C. Yu, T.W. Walker, G.W. Huber, J. Qiu, S. Jin, Electrocatalytic oxidation of glycerol to formic acid by $CuCo_2O_4$ spinel oxide nanostructure catalysts, ACS Catal. 10 (2020) 6741–6752. https://doi.org/10.1021/acscatal.0c01498.

[70] V.K. Harika, H.K. Sadhanala, I. Perelshtein, A. Gedanken, Sonication-assisted synthesis of bimetallic Hg/Pd Alloy nanoparticles for catalytic reduction of nitrophenol and its derivatives, Ultrason. Sonochem. (2019). https://doi.org/10.1016/j.ultsonch.2019.104804.

[71] T.K. Das, S. Remanan, S. Ghosh, N.C. Das, An environment friendly free-standing cellulose membrane derived for catalytic reduction of 4-nitrophenol: A sustainable approach, J. Environ. Chem. Eng. 9 (2021) 104596. https://doi.org/10.1016/j.jece.2020.104596.

[72] M. Maruthupandy, T. Muneeswaran, G. Chackaravarthi, T. Vennila, M. Anand, W.S. Cho, F. Quero, Development of hexagonal ZnO nanodisks for potential catalytic reduction of p-nitrophenol, Mater. Chem. Phys. 285 (2022) 126145. https://doi.org/10.1016/j.matchemphys.2022.126145.

[73] S. Velpula, S.R. Beedu, K. Rupula, Bimetallic nanocomposite (Ag-Au, Ag-Pd, Au-Pd) synthesis using gum kondagogu a natural biopolymer and their catalytic potentials in the degradation of 4-nitrophenol, Int. J. Biol. Macromol. 190 (2021) 159–169. https://doi.org/10. 1016/j.ijbiomac.2021.08.211.

[74] J.R. Deka, D. Saikia, N.F. Lu, K.T. Chen, H.M. Kao, Y.C. Yang, Space confined synthesis of highly dispersed bimetallic CoCu nanoparticles as effective catalysts for ammonia borane dehydrogenation and 4-nitrophenol reduction, Appl. Surf. Sci. 538 (2021) 148091. https://doi.org/10.1016/j.apsusc.2020.148091.

[75] A.M. Mohammed, S.S. Mohtar, F. Aziz, M. Aziz, A. Ul-Hamid, W.N. Wan Salleh, N. Yusof, J. Jaafar, A.F. Ismail, Ultrafast degradation of Congo Red dye using a facile one-pot solvothermal synthesis of cuprous oxide/titanium dioxide and cuprous oxide/zinc oxide p-n heterojunction photocatalyst, Mater. Sci. Semicond. Process. 122 (2021) 105481. https://doi.org/10.1016/j.mssp.2020.105481.

[76] U.O. Bhagwat, J.J. Wu, A.M. Asiri, S. Anandan, Photocatalytic degradation of congo red using $PbTiO_3$ nanorods synthesized via a sonochemical approach, ChemistrySelect. 3 (2018) 11851–11858. https://doi.org/10.1002/slct.201802303.

[77] M. Maruthupandy, T. Muneeswaran, T. Vennila, M. Anand, W.-S. Cho, F. Quero, Development of chitosan decorated Fe_3O_4 nanospheres for potential enhancement of photocatalytic degradation of Congo red dye molecules, Spectrochim. Acta Part A Mol. Biomol. Spectrosc. 267 (2022) 120511. https://doi.org/10.1016/j.saa.2021.120511.

[78] C.M. Magdalane, G.M.A. Priyadharsini, K. Kaviyarasu, A.I. Jothi, G.G. Simiyon, Synthesis and characterization of TiO_2 doped cobalt ferrite nanoparticles via microwave method: Investigation of photocatalytic performance of congo red degradation dye, Surfaces and Interfaces. 25 (2021) 101296. https://doi.org/10.1016/j.surfin.2021. 101296.

[79] N.F. Khairol, N. Sapawe, M. Danish, Photocatalytic study of ZnO-CuO/ES on degradation of congo red, Mater. Today Proc. 19 (2019) 1333–1339. https://doi.org/10.1016/j.matpr.2019.11.146.

[80] M.B. Shekardasht, M.H. Givianrad, P. Gharbani, Z. Mirjafary, A. Mehrizad, Preparation

of a novel Z-scheme g-C_3N_4/RGO/$Bi_2Fe_4O_9$ nanophotocatalyst for degradation of Congo Red dye under visible light, Diam. Relat. Mater. 109 (2020) 108008. https://doi.org/10.1016/j.diamond.2020.108008.

[81] S. Khan, A. Khan, N. Ali, S. Ahmad, W. Ahmad, S. Malik, N. Ali, H. Khan, S. Shah, M. Bilal, Degradation of Congo red dye using ternary metal selenide-chitosan microspheres as robust and reusable catalysts, Environ. Technol. Innov. 22 (2021) 101402. https://doi.org/10.1016/j.eti.2021.101402.

[82] D. Liu, J.-C. Liu, W. Cai, J. Ma, H. Bin Yang, H. Xiao, J. Li, Y. Xiong, Y. Huang, B. Liu, Selective photoelectrochemical oxidation of glycerol to high value-added dihydroxyacetone, Nat. Commun. 10 (2019) 1779. https://doi.org/10.1038/s41467-019-09788-5.

[83] B. Michèle, G. Pierre, P. Catherine, Conversion of biomass into chemicals over metal catalysts, Chem. Rev. 114 (2013) 1827–1870.

[84] M.S. Ahmad, M.H. Ab Rahim, T.M. Alqahtani, T. Witoon, J. Lim, C.K. Cheng, A review on advances in green treatment of glycerol waste with a focus on electro-oxidation pathway, Chemosphere. 276 (2021) 130128. https://doi.org/10.1016/j.chemosphere.2021.130128.

[85] Z. He, X. Ning, G. Yang, H. Wang, Y. Cao, F. Peng, H. Yu, Selective oxidation of glycerol over supported noble metal catalysts, Catal. Today. (2020) 0–1. https://doi.org/10.1016/j.cattod.2020.04.019.

[86] J.C. Beltrán-Prieto, K. Kolomazník, J. Pecha, A review of catalytic systems for glycerol oxidation: Alternatives for waste valorization, Aust. J. Chem. 66 (2013) 511–521. https://doi.org/10.1071/CH12514.

[87] G. Bagnato, A. Iulianelli, A. Sanna, A. Basile, Glycerol production and transformation: A critical review with particular emphasis on glycerol reforming reaction for producing hydrogen in conventional and membrane reactors, Membranes (Basel). 7 (2017) 17. https://doi.org/10.3390/membranes7020017.

[88] J. Cai, H. Ma, J. Zhang, Z. Du, Y. Huang, J. Gao, J. Xu, Catalytic oxidation of glycerol to tartronic acid over Au/HY catalyst under mild conditions, Chinese J. Catal. 35 (2014) 1653–1660. https://doi.org/10.1016/S1872-2067(14)60132-7.

[89] A. El Roz, P. Fongarland, F. Dumeignil, M. Capron, Glycerol to glyceraldehyde oxidation reaction over Pt-based catalysts under base-free conditions, Front. Chem. 7 (2019) 1–9. https://doi.org/10.3389/fchem.2019.00156.

[90] M. Pagliaro, R. Ciriminna, H. Kimura, M. Rossi, C. Della Pina, From glycerol to value-added products, Angew. Chemie - Int. Ed. 46 (2007) 4434–4440. https://doi.org/10.1002/anie.200604694.

[91] M. Morales, P.Y. Dapsens, I. Giovinazzo, J. Witte, C. Mondelli, S. Papadokonstantakis, K. Hungerbuhler, J. Perez-Ramirez, Environmental and economic assessment of lactic acid production from glycerol using cascade bio- and chemocatalysis, Energy Environ. Sci. 8 (2015) 558–567. https://doi.org/10.1039/C4EE03352C.

[92] X. Jin, M. Zhao, C. Zeng, W. Yan, Z. Song, Oxidation of glycerol to dicarboxylic acids using cobalt catalysts, ACS Catal. Oxid. (2016). https://doi.org/10.1021/acscatal.6b00961.

[93] P.M. Walgode, R.P.V. Faria, A.E. Rodrigues, A review of aerobic glycerol oxidation processes using heterogeneous catalysts: a sustainable pathway for the production of dihydroxyacetone, Catal. Rev. - Sci. Eng. 63 (2021) 422–511. https://doi.org/10.1080/01614940.2020.1747253.

[94] Y. Xiao, J. Greeley, A. Varma, Z. Zhao, G. Xiao, An experimental and theoretical study of glycerol oxidation to 1,3-dihydroxyacetone over bimetallic Pt-Bi catalysts, AIChE J. 63 (2017) 705–715. https://doi.org/10.1002/aic.15418.

[95] B. Katryniok, H. Kimura, E. Skrzyńska, J.-S. Girardon, P. Fongarland, M. Capron, R. Ducoulombier, N. Mimura, S. Paul, F. Dumeignil, Selective catalytic oxidation of glycerol: perspectives for high value chemicals, Green Chem. 13 (2011) 1960. https://doi.org/10.1039/c1gc15320j.

[96] W. Hu, D. Knight, B. Lowry, A. Varma, Selective oxidation of glycerol to dihydroxyacetone over Pt−Bi/C catalyst: Optimization of catalyst and reaction conditions, Ind. Eng. Chem. Res. 49 (2010) 10876–10882. https://doi.org/10.1021/ie1005096.

[97] A. Villa, A. Jouve, F.J. Sanchez Trujillo, D. Motta, L. Prati, N. Dimitratos, Exploring the effect of Au/Pt ratio on glycerol oxidation in presence and absence of a base, Catalysts. 8 (2018). https://doi.org/10.3390/catal8020054.

[98] H. Yan, S. Yao, B. Yin, W. Liang, X. Jin, X. Feng, Y. Liu, X. Chen, C. Yang, Synergistic effects of bimetallic PtRu/MCM-41 nanocatalysts for glycerol oxidation in base-free medium: Structure and electronic coupling dependent activity, Appl. Catal. B Environ. 259 (2019) 118070. https://doi.org/10.1016/j.apcatb.2019.118070.

[99] E. Skrzynska, A. Wondołowska-Grabowska, M. Capron, F. Dumeignil, Crude glycerol

as a raw material for the liquid phase oxidation reaction, Appl. Catal. A Gen. 482 (2014) 245–257. https://doi.org/10.1016/j.apcata.2014.06.005.

[100] L.S. Ribeiro, E.G. Rodrigues, J.J. Delgado, X. Chen, M.F.R. Pereira, J.J.M. Orfao, Pd, Pt, and Pt-Cu catalysts supported on carbon nanotube (CNT) for the selective oxidation of glycerol in alkaline and base-free conditions, Ind. Eng. Chem. Res. 55 (2016) 8548–8556. https://doi.org/10.1021/acs.iecr.6b01732.

[101] C.L. Bianchi, P. Canton, N. Dimitratos, F. Porta, L. Prati, Selective oxidation of glycerol with oxygen using mono and bimetallic catalysts based on Au, Pd and Pt metals, Catal. Today. 102–103 (2005) 203–212. https://doi.org/10.1016/j.cattod.2005.02.003.

[102] C. Zhang, T. Wang, X. Liu, Y. Ding, Selective oxidation of glycerol to lactic acid over activated carbon supported Pt catalyst in alkaline solution, Cuihua Xuebao/Chinese J. Catal. 37 (2016) 502–509. https://doi.org/10.1016/S1872-2067(15)61055-5.

[103] S. Zaid, A. Addad, M. Capron, F. Dumeignil, Performance of Ag/Al_2O_3 catalysts in the liquid phase oxidation of glycerol – effect of preparation method and reaction conditions, Catal. Sci. Technol. (2015). https://doi.org/10.1039/C5CY01581B.

[104] S. Hirasawa, H. Watanabe, T. Kizuka, Y. Nakagawa, K. Tomishige, Performance, structure and mechanism of Pd-Ag alloy catalyst for selective oxidation of glycerol to dihydroxyacetone, J. Catal. 300 (2013) 205–216. https://doi.org/10.1016/j.jcat.2013.01.014.

[105] X. Jin, M. Zhao, W. Yan, C. Zeng, P. Bobba, P.S. Thapa, B. Subramaniam, R. V. Chaudhari, Anisotropic growth of PtFe nanoclusters induced by lattice-mismatch: Efficient catalysts for oxidation of biopolyols to carboxylic acid derivatives, J. Catal. 337 (2016) 272–283. https://doi.org/10.1016/j.jcat.2016.02.015.

[106] Y. Shen, S. Zhang, H. Li, Y. Ren, H. Liu, Efficient synthesis of lactic acid by aerobic oxidation of glycerol on $Au-Pt/TiO_2$ catalysts, Chem. - A Eur. J. 16 (2010) 7368–7371. https://doi.org/10.1002/chem.201000740.

[107] R.K.P. Purushothaman, J. van Haveren, D.S. van Es, I. Melian-Cabrera, J.D. Meeldijk, H.J. Heeres, An efficient one pot conversion of glycerol to lactic acid using bimetallic gold-platinum catalysts on a nanocrystalline CeO_2 support, Appl. Catal. B Environ. 147 (2014) 92–100. https://doi.org/10.1016/j.apcatb.2013.07.068.

[108] C. Xu, Y. Du, C. Li, J. Yang, G. Yang, Insight into effect of acid / base nature of supports on selectivity of glycerol oxidation over supported Au-Pt bimetallic catalysts, Applied Catal. B, Environ. 164 (2015) 334–343. https://doi.org/10.1016/j.apcatb.2014.09.048.

[109] A.A. Rodriguez, C.T. Williams, J.R. Monnier, Selective liquid-phase oxidation of glycerol over Au – Pd / C bimetallic catalysts prepared by electroless deposition, Appl. Catal. A, Gen. 475 (2014) 161–168. https://doi.org/10.1016/j.apcata.2014.01.011.

[110] R. Nie, D. Liang, L. Shen, J. Gao, P. Chen, Z. Hou, Selective oxidation of glycerol with oxygen in base-free solution over MWCNTs supported PtSb alloy nanoparticles, Appl. Catal. B Environ. 127 (2012) 212–220. https://doi.org/10.1016/j.apcatb.2012.08.026.

[111] F.J. Prince N. Amaniampong, Quang Thang Trinh, Jithin John Varghese, Ronan Behling, Sabine Valange, Samir H. Mushrif, Unraveling the mechanism of the oxidation of glycerol to dicarboxylic acids over a sonochemically synthesized copper oxide catalyst, Green Chem. (2018). https://doi.org/10.1039/C8GC00961A.

[112] M. Rosiene, A. Arcanjo, I.J. Silva, E. Rodriguez-castellon, A. Infantes-molina, R.S. Vieira, Conversion of glycerol into lactic acid using Pd or Pt supported on carbon as catalyst, Catal. Today. 279 (2017) 317–326. https://doi.org/10.1016/j.cattod.2016.02.015.

[113] R. Palacio, S. Torres, D. Lopez, D. Hernandez, Selective glycerol conversion to lactic acid on Co_3O_4/CeO_2 catalysts, Catal. Today. 302 (2018) 196–202. https://doi.org/10.1016/j.cattod.2017.05.053.

[114] C. Zhang, T. Wang, X. Liu, Y. Ding, Cu-promoted Pt/activated carbon catalyst for glycerol oxidation to lactic acid, J. Mol. Catal. A Chem. 424 (2016) 91–97. https://doi.org/10.1016/j.molcata.2016.08.018.

[115] V. V. Butova, V.A. Polyakov, E.A. Erofeeva, Y. V. Rusalev, M.A. Gritsai, I. V. Ozhogin, G.S. Borodkin, D.Y. Kirsanova, Z.M. Gadzhimagomedova, A.A. Guda, A. V. Soldatov, Cobalt nanoparticles embedded in porous N-doped carbon support as a superior catalyst for the p-nitrophenol reduction, Appl. Surf. Sci. 592 (2022) 153292. https://doi.org/10.1016/j.apsusc.2022.153292.

[116] P. Pascariu, C. Cojocaru, N. Olaru, P. Samoila, A. Airinei, M. Ignat, L. Sacarescu, D. Timpu, Novel rare earth (RE-La, Er, Sm) metal doped ZnO photocatalysts for degradation of Congo-Red dye: Synthesis, characterization and kinetic studies, J. Environ. Manage. 239 (2019) 225–234. https://doi.org/10.1016/j.jenvman.2019.03.060.

[117] V.K. Landge, V.S. Hakke, M. Kakunuri, G.U.B. Babu, G. Boczkaj, S.H. Sonawane, Synthesis of bimetallic Co–Pt/cellulose nanocomposites for catalytic reduction of p - nitrophenol , React. Chem. Eng. (2022). https://doi.org/10.1039/d1re00422k.

[118] X. Xie, J. Shi, Y. Pu, Z. Wang, L. Zhang, D. Wang, Cellulose derived nitrogen and

phosphorus co-dopedcarbon-based catalysts for catalytic reduction of p-nitrophenol, J. Colloid Interface Sci. (2020). https://doi.org/10.1016/j.jcis.2020.03.035.

[119] M. Nasrollahzadeh, M. Sajjadi, S. Iravani, R.S. Varma, Green-synthesized nanocatalysts and nanomaterials for water treatment: Current challenges and future perspectives, J. Hazard. Mater. 401 (2021) 123401. https://doi.org/10.1016/j.jhazmat.2020.123401.

[120] A.F. Baye, R. Appiah-ntiamoah, H. Kim, Synergism of transition metal (Co, Ni, Fe, Mn) nanoparticles and "active support" Fe_3O_4@C for catalytic reduction of 4-nitrophenol, Sci. Total Environ. (2019) 135492. https://doi.org/10.1016/j.scitotenv.2019.135492.

[121] S. Kapoor, A. Sheoran, M. Riyaz, J. Agarwal, N. Goel, S. Singhal, Enhanced catalytic performance of Cu/Cu_2O nanoparticles via introduction of graphene as support for reduction of nitrophenols and ring opening of epoxides with amines established by experimental and theoretical investigations, J. Catal. 381 (2020) 329–346. https://doi.org/10.1016/j.jcat.2019.11.012.

[122] V.K. Landge, S.H. Sonawane, S. Manickam, G.U. Bhaskar Babu, G. Boczkaj, Ultrasound-assisted wet-impregnation of Ag-Co nanoparticles on cellulose nanofibers: Enhanced catalytic hydrogenation of 4-nitrophenol, J. Environ. Chem. Eng. 9 (2021) 105719. https://doi.org/10.1016/j.jece.2021.105719.

[123] Y. Chi, Q. Yuan, Y. Li, J. Tu, L. Zhao, N. Li, X. Li, Synthesis of Fe_3O_4@SiO_2-Ag magnetic nanocomposite based on small-sized and highly dispersed silver nanoparticles for catalytic reduction of 4-nitrophenol, J. Colloid Interface Sci. 383 (2012) 96–102. https://doi.org/10.1016/j.jcis.2012.06.027.

[124] N. Pradhan, A. Pal, T. Pal, Silver nanoparticle catalyzed reduction of aromatic nitro compounds, Colloids Surfaces A Physicochem. Eng. Asp. 196 (2002) 247–257. https://doi.org/10.1016/S0927-7757(01)01040-8.

[125] F. Yan, Z. Hu, Q. Tian, B. Wang, Facile synthesis of porous hollow Au nanoshells with enhanced catalytic properties towards reduction of p-nitrophenol, Inorg. Chem. Commun. 116 (2020) 107896. https://doi.org/10.1016/j.inoche.2020.107896.

[126] Z. Cao, H. Chen, S. Zhu, Z. Chen, C. Xu, D. Qi, U. Ziener, Inverse miniemulsion-based preparation of raspberry-like Au/SiO_2 nanocomposite particles with high catalytic activity towards reduction of p -nitrophenol, Colloids Surfaces A Physicochem. Eng. Asp. 489 (2016) 223–233. https://doi.org/10.1016/j.colsurfa.2015.11.001.

[127] X. Xu, Y. Liu, Y. Gao, H. Li, Preparation of Au @ silica Janus nanosheets and their catalytic application, Colloids Surfaces A Physicochem. Eng. Asp. (2017).

https://doi.org/10.1016/j.colsurfa.2017.06.048.

[128] N. Cyril, J. Baben, P. V Nair, L. Joseph, C.T. Sunila, Catalytic activity of Derris trifoliata stabilized gold and silver nanoparticles in the reduction of isomers of nitrophenol and azo violet, Nano-Structures & Nano-Objects. 22 (2020) 100430. https://doi.org/10.1016/j.nanoso.2020.100430.

[129] T. Baran, M. Nasrollahzadeh, Facile synthesis of palladium nanoparticles immobilized on magnetic biodegradable microcapsules used as effective and recyclable catalyst in Suzuki-Miyaura reaction and p-nitrophenol reduction, Carbohydr. Polym. 222 (2019) 115029. https://doi.org/10.1016/j.carbpol.2019.115029.

[130] H. Gamze, Y. Karataş, M. Celebi, M. Gülcan, Palladium nanoparticles decorated on amine functionalized graphene nanosheets as excellent nanocatalyst for the hydrogenation of nitrophenols to aminophenol counterparts, J. Hazard. Mater. 369 (2019) 96–107. https://doi.org/10.1016/j.jhazmat.2019.02.027.

[131] X. Wu, C. Lu, W. Zhang, G. Yuan, R. Xiong, X. Zhang, A novel reagentless approach for synthesizing cellulose nanocrystal-supported palladium nanoparticles with enhanced catalytic performance, J. Mater. Chem. A. 1 (2013) 8645–8652. https://doi.org/10.1039/c3ta11236e.

[132] Z. Li, C. Han, Palladium nanoflowers supported on amino-fullerene as novel catalyst for reduction of 4-nitrophenol, Chinese Chem. Lett. 2 (2019) 10–12. https://doi.org/10.1016/j.cclet.2019.06.047.

[133] S. Pandey, S.B. Mishra, Catalytic reduction of p-nitrophenol by using platinum nanoparticles stabilised by guar gum, Carbohydr. Polym. 113 (2014) 525–531. https://doi.org/10.1016/j.carbpol.2014.07.047.

[134] P. Xu, C. Cen, N. Chen, H. Lin, Q. Wang, N. Xu, J. Tang, Z. Teng, Facile fabrication of silver nanoparticles deposited cellulose microfiber nanocomposites for catalytic application, J. Colloid Interface Sci. 526 (2018) 194–200. https://doi.org/10.1016/j.jcis.2018.04.045.

[135] D. Dutta, R. Hazarika, P.D. Dutta, T. Goswami, P. Sengupta, D.K. Dutta, Synthesis of Ag-Ag_2S Janus nanoparticles supported on environmentally benign cellulose template and their catalytic applications, RSC Adv. (2016). https://doi.org/10.1039/C6RA16941D.

[136] F. Torkamani, S. Azizian, Green and simple synthesis of Ag nanoparticles loaded onto cellulosic fiber as efficient and low-cost catalyst for reduction of 4-nitrophenol, J. Mol.

Liq. 214 (2016) 270–275. https://doi.org/10.1016/j.molliq.2015.12.071.

[137] A. Mondal, A. Mondal, B. Adhikary, Cobalt nanoparticles as reusable catalysts for reduction of 4-nitrophenol under mild conditions, 40 (2017) 321–328. https://doi.org/10.1007/s12034-017-1367-3.

[138] K. Zhao, J. Wang, W. Kong, P. Zhu, facile green synthesis and characterization of copper nanoparticles by aconitic acid for catalytic reduction of nitrophenols, J. of Environmental Chem. Eng. (2019) 103517. https://doi.org/10.1016/j.jece.2019.103 517.

[139] G. Wu, X. Liang, L. Zhang, Z. Tang, M. Al-Mamun, H. Zhao, X. Su, Fabrication of highly stable metal oxide hollow nanospheres and their catalytic activity toward 4-nitrophenol reduction, ACS Appl. Mater. Interfaces. 9 (2017) 18207–18214. https://doi.org/10.1021/acsami.7b03120.

[140] J. Krajczewski, K. Kolataj, A. Kudelski, K. Koł, A. Kudelski, Enhanced catalytic activity of solid and hollow platinum-cobalt nanoparticles towards reduction of 4-nitrophenol, Appl. Surf. Sci. 388 (2016) 624–630. https://doi.org/10.1016/j.apsusc.2016.04.089.

[141] A.D. Verma, S. Pal, P. Verma, V. Srivastava, R.K. Mandal, I. Sinha, Ag-Cu bimetallic nanocatalysts for p-nitrophenol reduction using a green hydrogen source, J. Environ. Chem. Eng. 5 (2017) 6148–6155. https://doi.org/10.1016/j.jece.2017.11.057.

[142] H. Chen, X. Fan, J. Ma, G. Zhang, F. Zhang, Y. Li, Green route for microwave-assisted preparation of AuAg-alloy-decorated graphene hybrids with superior 4-NP reduction catalytic activity, Ind. Eng. Chem. Res. 53 (2014) 17976–17980. https://doi.org/10.1021/ie503251h.

[143] J. Zhang, G. Chen, D. Guay, M. Chaker, D. Ma, Highly active PtAu alloy nanoparticle catalysts for the reduction of 4-nitrophenol, Nanoscale. 6 (2014) 2125–2130. https://doi.org/10.1039/c3nr04715f.

[144] P. Nariya, M. Das, F. Shukla, S. Thakore, Synthesis of magnetic silver cyclodextrin nanocomposite as catalyst for reduction of nitro aromatics and organic dyes, J. Mol. Liq. 300 (2020) 112279. https://doi.org/10.1016/j.molliq.2019.112279.

[145] H. Helmiyati, R.T. Yunarti, F.W. Dini, Magnetic alginate–carboxymethyl cellulose to immobilize copper nanoparticles as a green and sustainable catalyst for 4-nitrophenol reduction, Heliyon. 9 (2023) e14111. https://doi.org/10.1016/j.heliyon.2023.e14111.

[146] S. Saha, A. Pal, S. Kundu, S. Basu, T. Pal, Photochemical green synthesis of calcium-alginate-stabilized Ag and Au nanoparticles and their catalytic application to 4-

nitrophenol reduction, Langmuir. 26 (2010) 2885–2893. https://doi.org/10.1021/la 902950x.

[147] J. Lv, A. Wang, X. Ma, R. Xiang, J. Chen, J. Feng, One-pot synthesis of porous Pt – Au nanodendrites supported on reduced graphene oxide nanosheets toward catalytic reduction of 4-nitrophenol, J. Mater. Chem. A Mater. Energy Sustain. 3 (2014) 290–296. https://doi.org/10.1039/C4TA05034G.

[148] A. Hatamifard, M. Nasrollahzadeh, S.M. Sajadi, Biosynthesis, characterization and catalytic activity of an Ag/zeolite nanocomposite for base- and ligand-free oxidative hydroxylation of phenylboronic acid and reduction of a variety of dyes at room temperature, New J. Chem. 40 (2016) 2501–2513. https://doi.org/10.1039/c5nj02909k.

[149] E. Cao, W. Duan, F. Wang, A. Wang, Y. Zheng, Natural cellulose fiber derived hollow-tubular-oriented polydopamine: In-situ formation of Ag nanoparticles for reduction of 4-nitrophenol, Carbohydr. Polym. 158 (2017) 44–50. https://doi.org/10.1016/j.carbpol. 2016.12.004.

[150] Y. Guo, M. Dai, Z. Zhu, Y. Chen, H. He, T. Qin, Chitosan modified Cu_2O nanoparticles with high catalytic activity for p-nitrophenol reduction, Appl. Surf. Sci. 480 (2019) 601–610. https://doi.org/10.1016/j.apsusc.2019.02.246.

[151] M.A. Ahsan, O. Fernandez-Delgado, E. Deemer, H. Wang, A.A. El-Gendy, M.L. Curry, J.C. Noveron, Carbonization of Co-BDC MOF results in magnetic C@Co nanoparticles that catalyze the reduction of methyl orange and 4-nitrophenol in water, J. Mol. Liq. 290 (2019) 111059. https://doi.org/10.1016/j.molliq.2019.111059.

[152] X.T. Tran, M. Hussain, H.T. Kim, Facile and fast synthesis of a reduced graphene oxide/carbon nanotube/iron/silver hybrid and its enhanced performance in catalytic reduction of 4–nitrophenol, Solid State Sci. 100 (2020) 106107. https://doi.org/10.1016 /j.solidstatesciences.2019.106107.

[153] M. Dinari, F. Dadkhah, Swift reduction of 4-nitrophenol by easy recoverable magnetite-Ag/layered double hydroxide/starch bionanocomposite, Carbohydr. Polym. 228 (2020). https://doi.org/10.1016/j.carbpol.2019.115392.

[154] H.Y. Chiu, T. Wi-Afedzi, Y.T. Liu, F. Ghanbari, K.Y.A. Lin, Cobalt oxides with various 3D nanostructured morphologies for catalytic Reduction of 4-Nitrophenol: A comparative study, J. Water Process Eng. 37 (2020) 101379. https://doi.org/10.1016 /j.jwpe.2020.101379.

[155] M.M.J. Sadiq, U.S. Shenoy, D.K. Bhat, Synthesis of $BaWO_4$/NRGO–g-C_3N_4

nanocomposites with excellent multifunctional catalytic performance via microwave approach, Front. Mater. Sci. 12 (2018) 247–263. https://doi.org/10.1007/s11706-018-0433-0.

[156] S. Naghdi, M. Sajjadi, M. Nasrollahzadeh, K.Y. Rhee, S.M. Sajadi, B. Jaleh, Cuscuta reflexa leaf extract mediated green synthesis of the Cu nanoparticles on graphene oxide/manganese dioxide nanocomposite and its catalytic activity toward reduction of nitroarenes and organic dyes, J. Taiwan Inst. Chem. Eng. 86 (2018) 158–173. https://doi.org/10.1016/j.jtice.2017.12.017.

[157] X.F. Zhang, X.Y. Zhu, J.J. Feng, A.J. Wang, Solvothermal synthesis of N-doped graphene supported PtCo nanodendrites with highly catalytic activity for 4-nitrophenol reduction, Appl. Surf. Sci. 428 (2018) 798–808. https://doi.org/10.1016/j.apsusc.2017.09.200.

[158] M.M.J. Sadiq, U.S. Shenoy, D.K. Bhat, Enhanced photocatalytic performance of N-doped RGO-$FeWO_4$/Fe_3O_4 ternary nanocomposite in environmental applications, Mater. Today Chem. 4 (2017) 133–141. https://doi.org/10.1016/j.mtchem.2017.04.003.

[159] B. Jacob, M. Mohan, D. K.C., H. Thomas, $NiCo_2O_4$ nanoparticles anchored on reduced graphene oxide with enhanced catalytic activity towards the reduction of p-Nitrophenol in water, Colloids Surfaces A Physicochem. Eng. Asp. 643 (2022) 128717. https://doi.org /10.1016/j.colsurfa.2022.128717.

[160] F. Yang, J. Wang, S. Gao, S. Zhou, Y. Kong, Record-high catalytic hydrogenated activity in nitroarenes reduction derived from in-situ nascent active metals enabled by constructing bimetallic phosphate, Mol. Catal. 486 (2020) 110873. https://doi.org/10.1016/j.mcat.2020.110873.

[161] M. Naz, A. Rafiq, M. Ikram, A. Haider, S. Ossama, A. Ahmad, J. Haider, S. Naz, Elimination of dyes by catalytic reduction in the absence of light : A review, J. Mater. Sci. 56 (2021) 15572–15608. https://doi.org/10.1007/s10853-021-06279-1.

[162] M. Ikram, E. Umar, A. Raza, A. Haider, S. Naz, A. Ul-Hamid, J. Haider, I. Shahzadi, J. Hassan, S. Ali, Dye degradation performance, bactericidal behavior and molecular docking analysis of Cu-doped TiO2 nanoparticles, RSC Adv. 10 (2020) 24215–24233. https://doi.org/10.1039/D0RA04851H.

[163] M. Ikram, M.I. Khan, A. Raza, M. Imran, A. Ul-Hamid, S. Ali, Outstanding performance of silver-decorated MoS_2 nanopetals used as nanocatalyst for synthetic dye degradation, Phys. E Low-Dimensional Syst. Nanostructures. 124 (2020) 114246. https://doi.org/

10.1016/j.physe.2020.114246.

[164] D.A. Yaseen, M. Scholz, Shallow pond systems planted with Lemna minor treating azo dyes, Ecol. Eng. 94 (2016) 295–305. https://doi.org/10.1016/j.ecoleng.2016.05.081.

[165] C.B. Sekomo, D.P.L. Rousseau, S.A. Saleh, P.N.L. Lens, Heavy metal removal in duckweed and algae ponds as a polishing step for textile wastewater treatment, Ecol. Eng. 44 (2012) 102–110. https://doi.org/10.1016/j.ecoleng.2012.03.003.

[166] T.N. Ravishankar, K. Manjunatha, T. Ramakrishnappa, G. Nagaraju, D. Kumar, S. Sarakar, B.S. Anandakumar, G.T. Chandrappa, V. Reddy, J. Dupont, Comparison of the photocatalytic degradation of trypan blue by undoped and silver-doped zinc oxide nanoparticles, Mater. Sci. Semicond. Process. 26 (2014) 7–17. https://doi.org/10.1016/j.mssp.2014.03.027.

[167] D.A. Yaseen, M. Scholz, Textile dye wastewater characteristics and constituents of synthetic effluents: a critical review, Springer Berlin Heidelberg, 2019. https://doi.org/10.1007/s13762- 018-2130-z.

[168] R. Rashad, M. Khan, H. Qamar, A. Hameed, Biological and photocatalytic degradation of congo red, a diazo sulfonated substituted dye: a Review, Water, Air, Soil Pollut. (2022). https://doi.org/10.1007/s11270-022-05935-9.

[169] V.K. Landge, S.H. Sonawane, M. Sivakumar, S.S. Sonawane, G. Uday Bhaskar Babu, G. Boczkaj, S-scheme heterojunction Bi_2O_3-ZnO/Bentonite clay composite with enhanced photocatalytic performance, Sustain. Energy Technol. Assessments. 45 (2021) 101194. https://doi.org/10.1016/j.seta.2021.101194.

[170] C. Xu, P. Ravi Anusuyadevi, C. Aymonier, R. Luque, S. Marre, Nanostructured materials for photocatalysis, Chem. Soc. Rev. 48 (2019) 3868–3902. https://doi.org/10.1039/C9CS00102F.

[171] V.K. Landge, C.M. Huang, V.S. Hakke, S.H. Sonawane, S. Manickam, M.C. Hsieh, Solar energy driven Cu-ZnO/TiO_2 nanocomposite photocatalyst for the rapid degradation of congo red azo dye, Catalysts. 12 (2022). https://doi.org/10.3390/catal12060605.

[172] M. Elavarasan, K. Uma, T.C.K. Yang, Nanocubes phase adaptation of In_2O_3/TiO_2 heterojunction photocatalysts for the dye degradation and tracing of adsorbed species during photo-oxidation of ethanol, J. Taiwan Inst. Chem. Eng. 120 (2021) 169–177. https://doi.org/10.1016/j.jtice.2021.03.008.

[173] M.R.D. Khaki, B. Sajjadi, A.A.A. Raman, W.M.A.W. Daud, S. Shmshirband,

Sensitivity analysis of the photoactivity of Cu-TiO_2/ZnO during advanced oxidation reaction by Adaptive Neuro-Fuzzy Selection Technique, Meas. J. Int. Meas. Confed. 77 (2016) 155–174. https://doi.org/10.1016/j.measurement.2015.07.004.

[174] J.A. Oyetade, R.L. Machunda, A. Hilonga, Photocatalytic degradation of azo dyes in textile wastewater by Polyaniline composite catalyst-a review, Sci. African. 17 (2022) e01305. https://doi.org/10.1016/j.sciaf.2022.e01305.

[175] N.F. Khairol, N. Sapawe, M. Danish, Excellent performance integrated both adsorption and photocatalytic reaction toward degradation of congo red by CuO/Eggshell, Mater. Today Proc. 19 (2019) 1340–1345.

[176] Y. Yang, N.N.N.N. Ali, A. Khan, S.S.S.S. Khan, S.S.S.S. Khan, H. Khan, S. Xiaoqi, W. Ahmad, S. Uddin, N.N.N.N. Ali, M. Bilal, Chitosan-capped ternary metal selenide nanocatalysts for efficient degradation of Congo red dye in sunlight irradiation, Int. J. Biol. Macromol. 167 (2021) 169–181. https://doi.org/10.1016/j.ijbiomac.2020.11.167.

[177] K. Glainmer, N. Quiton, M. Lu, Y. Huang, Synthesis and catalytic utilization of bimetallic systems for wastewater remediation : A review, Chemosphere. 262 (2021) 128371. https://doi.org/10.1016/j.chemosphere.2020.128371.

[178] A.C. Pradhan, M.K. Sahoo, S. Bellamkonda, K.M. Parida, G.R. Rao, Enhanced photodegradation of dyes and mixed dyes by heterogeneous mesoporous Co–Fe/Al_2O_3–MCM-41 nanocomposites: nanoparticles formation, semiconductor behavior and mesoporosity, RSC Adv. 6 (2016) 94263–94277. https://doi.org/10.1039/C6RA19923 B.

[179] T.B. Aftab, A. Hussain, D. Li, Application of a novel bimetallic hydrogel based on iron and cobalt for the synergistic catalytic degradation of Congo Red dye, J. Chinese Chem. Soc. 66 (2019) 919–927. https://doi.org/10.1002/jccs.201800388.

[180] M. Ismail, M.I. Khan, S.B. Khan, M.A. Khan, K. Akhtar, A.M. Asiri, Green synthesis of plant supported CuAg and CuNi bimetallic nanoparticles in the reduction of nitrophenols and organic dyes for water treatment, J. Mol. Liq. 260 (2018) 78–91. https://doi.org/10.1016/j.molliq.2018.03.058.

[181] B. Mu, J. Tang, L. Zhang, A. Wang, Facile fabrication of superparamagnetic graphene/polyaniline/Fe_3O_4 nanocomposites for fast magnetic separation and efficient removal of dye, Sci. Rep. 7 (2017) 5347. https://doi.org/10.1038/s41598-017-05755-6.

[182] S. Sathiyavimal, S. Vasantharaj, T. Kaliannan, A. Pugazhendhi, Eco-biocompatibility of chitosan coated biosynthesized copper oxide nanocomposite for enhanced industrial

(Azo) dye removal from aqueous solution and antibacterial properties, Carbohydr. Polym. 241 (2020) 116243. https://doi.org/10.1016/j.carbpol.2020.116243.

[183] C. Thirupathy, S. Cathrin Lims, S. John Sundaram, A.H. Mahmoud, K. Kaviyarasu, Equilibrium synthesis and magnetic properties of $BaFe_{12}O_{19}/NiFe_2O_4$ nanocomposite prepared by co precipitation method, J. King Saud Univ. - Sci. 32 (2020) 1612–1618. https://doi.org/10.1016/j.jksus.2019.12.019.

[184] A. Moradzadeh, A. Mahjoub, M.S. Sadjadi, M.H. Sadr, N. Farhadyar, M. Seyed, M. Hossaini, N. Farhadyar, Investigation on synthesis, characterization and photo catalytic degradation of congo red by Zn-doped $CdTiO_3/TiO_2$, Polyhedron. 170 (2019) 404–411. https://doi.org/10.1016/j.poly.2019.05.060.

[185] C. Vidya, C. Manjunatha, M.N. Chandraprabha, M. Rajshekar, A.R.M.A. L, Hazard free green synthesis of ZnO nano-photo-catalyst using Artocarpus Heterophyllus leaf extract for the degradation of Congo red dye in water treatment applications, Biochem. Pharmacol. (2017). https://doi.org/10.1016/j.jece.2017.05.058.

[186] G.B. Jegadeesan, S. Amirthavarshini, J. Divya, G.I. Gunarani, Catalytic peroxygen activation by biosynthesized iron nanoparticles for enhanced degradation of Congo red dye, Adv. Powder Technol. (2019). https://doi.org/10.1016/j.apt.2019.08.034.

[187] D. Ljubas, G. Smoljani, H. Jureti, Degradation of Methyl Orange and Congo Red dyes by using TiO_2 nanoparticles activated by the solar and the solar-like radiation, J. Environ. Manage. 161 (2015) 83–91. https://doi.org/10.1016/j.jenvman.2015.06.042.

[188] D. Pathania, D. Gupta, A.H. Al-Muhtaseb, G. Sharma, A. Kumar, M. Naushad, T. Ahamad, S.M. Alshehri, Photocatalytic degradation of highly toxic dyes using chitosan-g-poly(acrylamide)/ZnS in presence of solar irradiation, J. Photochem. Photobiol. A Chem. 329 (2016) 61–68. https://doi.org/10.1016/j.jphotochem.2016.06.019.

[189] P.K. Labhane, L.B. Patle, G.H. Sonawane, S.H. Sonawane, Fabrication of ternary Mn doped ZnO nanoparticles grafted on reduced graphene oxide (RGO) sheet as an e ffi cient solar light driven photocatalyst, Chem. Phys. Lett. 710 (2018) 70–77. https://doi.org/10.1016/j.cplett.2018.08.066.

[190] S.M. Patil, S.P. Deshmukh, K. V More, V.B. Shevale, S.B. Mullani, A.G. Dhodamani, S.D. Delekar, Sulfated TiO_2/WO_3 nanocomposite: An efficient photocatalyst for degradation of Congo red and methyl red dyes under visible light irradiation, Mater. Chem. Phys. (2018). https://doi.org/10.1016/j.matchemphys.2018.12.041.

[191] R. Tanwar, S. Kumar, U. Kumar, Photocatalytic activity of PANI/Fe^0doped BiOCl

under visible light-degradation of Congo red dye, Journal Photochem. Photobiol. A Chem. 333 (2017) 105–116. https://doi.org/10.1016/j.jphotochem.2016.10.022.

[192] T. Linda, S. Muthupoongodi, X.S. Shajan, S. Balakumar, Photocatalytic degradation of congo red and crystal violet dyes on Cellulose/PVC/ZnO composites under UV light irradiation, Mater. Today Proc. 3 (2016) 2035–2041. https://doi.org/10.1016/j.matpr.2016.04.106.

[193] N.F. Khairol, N. Sapawe, M. Danish, N. Fahmi Khairol, N. Sapawe, M. Danish, N.F., Photocatalytic study of ZnO-CuO/ES on degradation of congo red, Mater. Today Proc. 19 (2019) 1333–1339. https://doi.org/10.1016/j.matpr.2019.11.146.

[194] S. Ahmad, X. Su, C. Yang, X. Wang, X. Liu, J. Wang, Space-confined growth of layered basic zinc acetate nanosheets and their orderly fragmented ZnO nanoparticles on clay platelets, J. Hazard. Mater. 371 (2019) 213–223. https://doi.org/10.1016/j.jhazmat.2019.02.111.

[195] N. Guy, S. Cakar, M. Ozacar, Comparison of palladium/zinc oxide photocatalysts prepared by different palladium doping methods for congo red degradation, J. Colloid Interface Sci. 466 (2016) 128–137. https://doi.org/10.1016/j.jcis.2015.12.009.

Chapter 3.

Selective oxidation of Glycerol over heterogeneous catalyst

3.1 Introduction

The development of green technology, and sustainable utilization of renewable resources, are the prime challenges faced by chemical industries since last decade. In this context, the catalytic transformation of biomass and its subsidiaries to valuable chemicals has been the topic of interest amongst the researchers [1]. The comprehensive utilization of biomass, i.e. the biorefinery, could not only provide power and fuels, but also generate key intermediates and platform chemicals through various reactions such as oxidation, reforming, hydrogenolysis, ammoniation and dehydration, etc. [2–5]. Among these reactions, the liquid phase oxidation of bio-inferred sugars and polyols is one amongst the foremost vital routes to upgrade inexhaustible biomass to valuable chemicals, significantly for production of carboxylic acids [6].

Glycerol (GLY) is the coproduct of biodiesel production and thus is a biomass-derived feedstock. In the past decades, it has become a key raw material because of its low price and large availability [7]. Among the transformation processes of GLY, liquid phase oxidation (LPO) of GLY over heterogeneous catalyst using O_2 as oxidant is appealing, which can oxidize GLY to various important derivatives (such as aldehydes, ketones, and carboxylic acids), widely used in the field of cosmetics, food, medicine and other industries [8]. However, GLY has terminal and secondary hydroxyl groups to be oxidized, and some oxidation products can be further oxidized, suggesting that the GLY has multiple oxidation paths and various corresponding oxidation products such as dihydroxyacetone (DHA), glyceraldehyde (GLYAD), hydroxypiruvic acid (HPA), glyceric acid (GA), tartronic acid (TA), oxalic acid (OA), lactic acid (LA), glycolic acid (GLYA), acetic acid (AA), and formic acid (FA) [9,10]. TA, GA, OA, LA, and GLYA are getting importance due to the booming bio-refinery and pharmaceutical industry [11]. These oxidation products of GLY are often distributed wildly due to the diverse reaction pathways. TA, a C_3 dicarboxylic acid has wide applications in the pharmaceutical and polymer industries as a versatile intermediate [6]. LA assumes a significant role in the synthesis of biodegradable polymer i.e. polylactic acid (PLA) [11]. GLYA is a key constituent for cosmetic, food and textile industries [12].

Since the reaction product is generally a mixture of above-mentioned oxidation products, it's a big challenge to effectively oxidize the GLY and control the reaction path to the desired

products. Moreover, the selective oxidation of GLY is a structurally sensitive reaction [13]. Hence, the catalytic activity, stability, and products selectivity strongly depend on the catalyst structure and reaction conditions [8]. In other words, the catalytic performance of GLY oxidation can be greatly optimized by adjusting the reaction conditions, active composition, nature of support, geometric and electronic structures of active metal nanoparticles (NPs). Typically, the improvement of LPO catalytic activity and the selectivity of carboxylic acid products greatly depends on the alkali added in the reaction solvent [3]. Consequently, it is essential to develop efficient, green, and selective LPO technologies for GLY oxidation for the implementation of novel conversion processes in future biorefinery.

To date, the catalysts investigated for the GLY oxidation are mostly composed of NPs of supported noble metals, viz., Pt [14], Au [15], Ag [16], and Pd [17] in neutral as well as basic media. However, Pd and Pt are characterized by having the lowest hydrogenolysis activity of Group VIII metals and maintaining good hydrogenation and dehydrogenation activity and are prone to metal leaching and deactivation caused by over-oxidation and self-poisoning by strongly adsorbed by-products [18]. During the last decade, enhancing the metal-support interaction and/or optimizing the electronic structure of the main active metals by the modification of support or the incorporation of the second metal as a promoter have gained a lot of attention as it resulted into the improvement of catalytic performance [4,19–21]. In addition, the alkaline environment is conducive to the formation of a metal surface bound hydroxide., which could then facilitate the deprotonation of the alcohol as the alkali facilitate the activation of O-H bond with noble metals (e.g. Pt), which is considered essential for the oxidation of the primary alcohol, thus enhancing the catalytic activity [22,23]. Thus, the noble metal catalysts modified with promoters of basic nature (such as Ru, Ca, Co, Cu, etc.) can prominently improve the catalytic performance and tune the selectivity of oxidation products [3,8,20]. Dehydrogenation is stimulated by Pt and the supplying of oxygen at lower potentials for further oxidation is promoted by the addition of the secondary metal. Steric interactions enable the promoters to function as site blockers, controlling the orientation of the reaction [18]. Up to now, only a limited number of base metal promoted Pt catalysts have been developed for LPO of GLY.

Zhang et al. [24] reported the similar improvement of catalytic performance of GLY oxidation over PtCo/RGO. The GA selectivity increased from 72.1 % at 57.2 % GLY conversion over Pt/RGO to 85.9 % at 70.2 % GLY conversion over PtCo/RGO. They pointed out that the electrical interaction between Co and Pt facilitated the GLY oxidation. Moreover, bimetallic

PtCo inhibited the further oxidation of intermediates. Hence, both the GLY conversion and GA selectivity were enhanced over PtCo/RGO.

Further, Yan et al. investigated PtCo/MCM-41 and PtRu/MCM-41 catalysts for GLY conversion [4,24]. They found that both structure-sensitivity and electronic coupling effect enhanced the catalytic performance of GLY oxidation to GA. Although the catalytic performance of these catalysts for LPO conversion has been improved to some extent, there is still a big gap between their catalytic activity and that under alkaline conditions. For instance, the turnover frequency (TOF) in alkaline oxidation of GLY is usually higher than 1000 h^{-1}, while it is usually lower than 1000 h^{-1} in base-free oxidation of GLY.

Jin et al. [6] reported excellent combined yield of 88 % for TA and OA from GLY, using cobalt-based catalyst in the presence of molecular oxygen, after 24 hours of reaction time. Arcanjo et al. [25] have also studied the oxidation of GLY into LA using activated carbon with Pd as heterogeneous catalysts. They achieved a GLY conversion of about 99 % with selectivity of 68 % for lactic acid using 10 % Pd/C catalysts at 230 ^{o}C of reaction temperature. In addition, Palacio et al. [26] investigated GLY oxidation to LA using Cerium oxide supported Co_3O_4 particles as catalysts at 250 °C under basic environment. They have obtained selective GLY conversion of 85.7 % to LA (79.8 % selectivity) using Co_3O_4/CeO_2 catalysts and demonstrated the selective catalytic activity of the Co_3O_4/CeO_2.

Amongst various promoters used for GLY oxidation, copper attracts much attention as it is advantageous for dehydrogenation and offers lower activity toward C−C cleavage [27]. Also, it has shown good catalytic activity toward the oxidation of polyols [28] and alcohols [29]. In several cases, selectivity and performance of the bimetallic catalysts were proved to be better over the monometallic counterparts. [30–32]**.** Thus, the investigation of the bimetallic catalyst for GLY oxidation resulted in superior activity in comparison with monometallic noble metals [27,33]**.**

Carbon materials are widely employed as supports for noble metal catalysts because of their outstanding physicochemical properties and surface characteristics, such as high surface area, good electrical conductivity, and relative stability in acidic and basic media [13,34]. There are lots of researches focusing on Pt supported on different carbons to analyze the influence of catalyst structure on the performance and establish the relationship between them [20,25,35]. Carbon materials are widely employed as supports not only because of their excellent physicochemical properties, but also because of their easy surface modification [36,37]. Numerous studies have shown that carbon materials affects the size, dispersion, stability and

electronic structure of the supported noble metal NPs, further influences the catalytic activity and the product selectivity [21,38–40].

Similar to the carbon materials, the surface properties of oxide support (such as basic sites) and its crystal structure would also affect the dispersion, size, morphology, and electronic structure of supported noble metal NPs, thereby affecting the activity and product selectivity of GLY oxidation [8]. Sobczak, et al. [41] tested V_2O_5,Nb_2O_5, Ta_2O_5, TiO_2, Al_2O_3, and AC supported Au 1 wt % sol immobilization prepared catalysts, except the commercial Au/TiO_2 prepared by deposition-precipitation method (Mintek, World Gold Council). Au/TiO_2 showed the highest GLY conversion of 91 % after 5 h, with a GA selectivity of 38 %. GLY conversion with prepared Au catalysts decreased in the following order (X_{GLY},S_{GA}): AC (76 %, 36 %) > Nb_2O_5 (67 %, 47 %) ≫ Al_2O_3 (28 %, 28 %) > V_2O_5 (20 %, 29 %) > Ta_2O_5 (13 %, 6 %). Several reports are also available on the effectiveness of TiO_2 as support for monometallic catalysts employed for base free GLY oxidation [9,15,33,42]. This suggests carbon and TiO_2 as the suitable supports for the selective GLY oxidation.

Despite the achievements on the selective oxidation of GLY, some aspects such as catalyst development to improve its stability and selectivity with greener, economic fabrication and modification techniques (use of basic promoters to modify and tune selectivity), designing of catalyst that allows the GLY selective oxidation under mild operating conditions (atmospheric pressure, application of O_2/H_2O_2 as oxidizing agent, moderate temperature: 50-90 ^oC) and enhanced reaction kinetics (rate of reaction and reaction time) still need continuous efforts and breakthroughs. In this respect, we have attempted to synthesize a bimetallic nanocomposite (NC) catalyst using two distinct methods. The potential of ultrasonic irradiation for nanomaterial synthesis and catalyst modification to obtain uniform shape, size, dispersion, catalytic activity and stability is already established. Thus, the bimetallic Pt-Cu/C NC heterogeneous catalyst was fabricated using the sonication assisted seed-mediated approach. On the other hand, the Ni-Cu bimetallic catalyst supported on TiO_2 was synthesized using the sonochemical co-reduction method. These NC catalysts were utilized to oxidize GLY in order to produce products with additional value.

3.2 Selective oxidation of glycerol over bimetallic Pt-Cu/C NC catalyst

3.2.1 Experimental procedure

3.2.1.1 Materials

Potassium (IV) hexachloroplatinate (K_2PtCl_6, 40%) (Sainergy Fuel Cell Pvt. Ltd., India) and copper sulphate pentahydrate ($CuSO_45H_2O$, 98.5%) (Hi-Media Laboratories Pvt. Ltd., India) were used as metal precursors, sodium borohydride ($NaBH_4$, 97%) (Molychem, India) was used as a reducing agent. Polyvinylpyrrolidone (PVP) (MW 40000, Hi-Media Laboratories Pvt. Ltd., India) was employed as a stabilizer. Carbon powder (products of Cabot Corporation, USA) was exploited as a support. The DI water was used as the solvent for both precursor and reducing agent solutions.

3.2.1.2 Synthesis of Pt-Cu bimetallic nanoparticles, Pt and Cu nanoparticles supported on carbon

The ultrasound probe of 19 mm tip diameter with an ultrasound generator of 22 kHz frequency and 450 W power was used for the synthesis of Pt-Cu NC structure. Primarily, the Cu-NPs were prepared by ultrasound-assisted chemical reduction of copper sulphate pentahydrate. These Cu-NPs were then used as seeds for the growth of Pt-NPs through seed mediated heterogeneous nucleation (Figure 3.1).

In a typical experiment, the stock solutions of 50 mL (0.12 M) $NaBH_4$ and 50 mL (0.02 M) $CuSO_4.5H_2O$ were prepared separately in distilled water. 0.05 g of PVP was added to both the reagents. The $CuSO_4.5H_2O$ solution was then transferred into a 250 mL flask using a graduated cylinder. The flask was placed on a magnetic stirrer with sonication for 45 minutes and continuously stirred along with the dropwise addition of $NaBH_4$ solution, at a rate of 1 mL/s, using burette. This reaction mixture of $CuSO_4.5H_2O$ and $NaBH_4$ was continuously stirred for 30 minutes to ensure the complete reduction. Then K_2PtCl_6 was added to the mixture having Pt/Cu molar ratio of 4:1, subsequently Pt ions were reduced using dropwise addition of $NaBH_4$ solution under sonication for 45 minutes. After the completion of reaction, carbon black was ultrasonically mixed with the above mixture for 30 minutes along with constant stirring. The whole mixture was then stirred for 4 h followed by centrifugation and drying at 60 ^oC for 6 h to obtain the flower shaped Pt-Cu/C bimetallic NC catalyst. For the comparison, Pt/C and Cu/C

NCs were also synthesized via ultrasound assisted chemical reduction of K_2PtCl_6 and $CuSO_4.5H_2O$ using $NaBH_4$ as mentioned earlier.

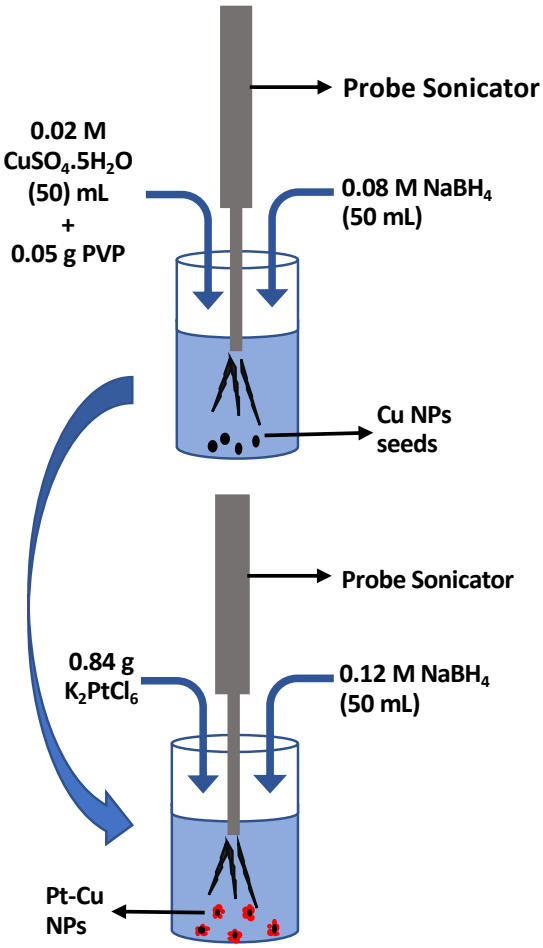

Figure 3.1 Schematic representation of ultrasound assisted synthesis of Pt-Cu/C NCs via heterogeneous nucleation.

3.2.1.3 Characterization of catalyst

The X-ray diffraction (XRD) measurements for Pt-Cu/C bimetallic NC catalyst, Pt/C and Cu/C NPs were performed on a Bruker Advance D8 powder diffractometer. Continuous X-ray scans were carried out from 10° to 100° of 2θ. The crystallite phase was estimated with the data of the Joint Committee on Powder Diffraction Standard (JCPDS).

Morphology of the NPs was studied by high resolution transmission electron microscopy (HR-TEM) by an electron microscope of JEOL JEM-2100 F model working at 200 kV. The samples for HR-TEM were prepared by dispersing the NPs in ethanol using ultrasonic dispersion, and was spread on the copper grid (3-mm) coated with amorphous carbon, followed by drying under IR lamp for 15 minutes at room temperature. TESCAN-Vega 3 LMU scanning electron

microscope (SEM) with an attached energy dispersive X-ray (EDX) analyzer was used to quantitatively measure the sample stoichiometry. Prior to the analysis, the samples were placed onto the aluminum sample holder followed by sputter coating with gold and then the analysis was performed.

The functional groups present on the surface of synthesized NPs were analyzed by a Fourier transform infrared spectrophotometer (Shimadzu FTIR 8400) in the mid-IR region (4000–400 cm^{-1}). The pellets of powdered samples having a thickness of around 1.3 mm were produced by mixing the NPs with KBr and used for the FTIR measurements. The analysis was conducted at atmospheric pressure and temperature conditions with a resolution of 4 cm^{-1}. The presence of metal particles was ensured using a UV–Vis spectrophotometer (Agilent). For this, small quantity of NPs was dispersed in ethanol using ultrasonic dispersion to obtain a dispersion of NPs. This dispersion was then added to a quartz cuvette for UV analysis. For the estimation of metal loadings inductively coupled plasma optical emission spectroscopy (ICP-OES) on a Perkin Elmer Optima 5300 DV ICP-OES instrument (Waltham, MA, USA) was carried out. The catalyst samples were dissolved in aqueous acidic solution (1 part 70 % HNO_3 to 4 parts 37 % HCl, by volume) and then digested at 150 °C for 30 min before the analysis.

The Brunauer–Emmett–Teller (BET) surface area and pore volume of the Pt-Cu/C bimetallic NC catalyst was estimated by using nitrogen (N_2) adsorption-desorption isotherm measured at −196 °C with a Micromeritics ASAP 2020 analyzer. Before the test, sample was degassed at 523 K for 5 h. The BET technique was applied to determine the specific surface area and the average pore diameter was calculated according to the formula: 4V/A. To measure the external and micro surface area t-plot method was employed. The amount of nitrogen adsorbed at a relative pressure (p/p_0) of 0.99 was used to compute the pore volume of the sample. The Barrett–Joyner–Halenda method (BJH) was utilized to estimate the pore size distribution and pore volume from analysis of the desorption curve of the N_2 isotherm.

3.2.1.4 Catalytic test for selective GLY oxidation and product analysis

The selective GLY oxidation was conducted at a constant temperature of 90 °C under atmospheric pressure, in a 50 mL three-neck flask on a magnetic stirrer operating at 700 rpm with oxygen bubbling for 4 h. GLY (0.1 M, 40 mL), NaOH (0.48 g) and 0.1 g of catalyst were uniformly mixed in such a way that the molar ratio of NaOH/GLY should be 3. Periodically, samples were taken from the reactor and filtered prior to the product analysis. The analysis of reaction mixture was carried out by proton nuclear magnetic resonance (^{1}H-NMR) spectrum recorded using Bruker AV300 MHz nuclear magnetic resonance spectrometer, and Agilent

1100 high-performance liquid chromatography (HPLC) with a refractive index detector (RID) and a Shaodex SH1821 column at 50 °C. The 0.005 M H_2SO_4 was used as a mobile phase, flowing at a rate of 0.6 mL/min. For simplicity, salt products were marked as their corresponding acids. The product samples were diluted with D_2O for recording ^{1}H-NMR spectra.

The conversion of GLY was evaluated according to Eq. 3.1:

$$X_{GLY}\ (\%) = (X_{GLY,in} - X_{GLY,out}/X_{GLY,in}) \times 100 \qquad \text{(Eq. 3.1)}$$

Where $X_{GLY,in}$ and $X_{GLY,out}$ represent the glycerol initial amount (moles) and the glycerol amount (moles) after a certain time of reaction, respectively. The product selectivity was evaluated according to Eq. 3.2

$$S(\%) = moles\ of\ desired\ product\ formed \times 100/moles\ of\ GLY_{in} \qquad \text{(Eq. 3.2)}$$

3.2.2 Results and discussion

The investigation employed a seed mediation approach to cultivate bimetallic nanocomposite catalysts with a desired flower-like morphology. This involved the growth of one set of nanoparticles on an existing base material or another set of NPs. The objective is to attain optimal exposure of the active site of the catalyst during the reaction. The bimetallic NC of Pt-Cu/C that was synthesized underwent additional analysis for the purpose of GLY oxidation. The catalyst's flower-like structure is expected to offer a large surface area for the intended reaction. The stability of the catalyst enables it to maintain consistent conversion rates and yields across up to five reaction cycles. The stability of the catalyst was evaluated through a series of experiments. The catalyst morphology, combination of metal nanoparticles, available surface area, and functional groups associated with the catalyst were confirmed through various analytical methods.

3.2.2.1 Pt-Cu/C catalyst characterization

A. XRD analysis for Pt-Cu/C, Pt/C and Cu/C catalysts

The Figure 3.2 illustrates XRD patterns of Pt, Cu, and Pt-Cu/C NPs. As shown in Figure 3.2, the Bragg's peaks at 39.8°, 46.3°, 67.6°, 81.4° and 85.8° indicates the planes [1 1 1], [2 0 0], [2 2 0], [3 1 1] and [2 2 2] of FCC structure for platinum [43] and peaks at 42.7°, 73.2°, 93.2° and 82.5° indicates [1 1 1], [2 2 0], [2 2 2] and [3 1 1] planes for FCC structure of copper [44]. This indicates that the prepared BNP are highly crystalline in nature. The shift in Cu peak of Pt-Cu/C was observed and it may have shifted due to the growth of Pt NPs over Cu NP seeds. Such a shift in peaks occurs due to the alloying of Cu and Pt NPs. The similar kind of behavior

was also noticed by Wang et al. [45]. The Debye-Scherrer equation ($D = K\lambda/(B \cos \Theta)$) was used to estimate the grain size of the Pt-Cu/C, with K taken as 1.0 while B is the whole width of the diffraction pattern at half of the utmost peak. According to the Debye-Scherrer equation, the crystallite size is found to be 3.90 nm, at 2Θ equal to 39.8°. The average particle size for the Pt-Cu/C obtained through HRTEM analysis is similar to the grain size obtained through XRD analysis. As the peaks of individual metal are seen clearly from the XRD pattern, the successful synthesis of hetero–structured, anisotropic Pt-Cu/C can be confirmed.

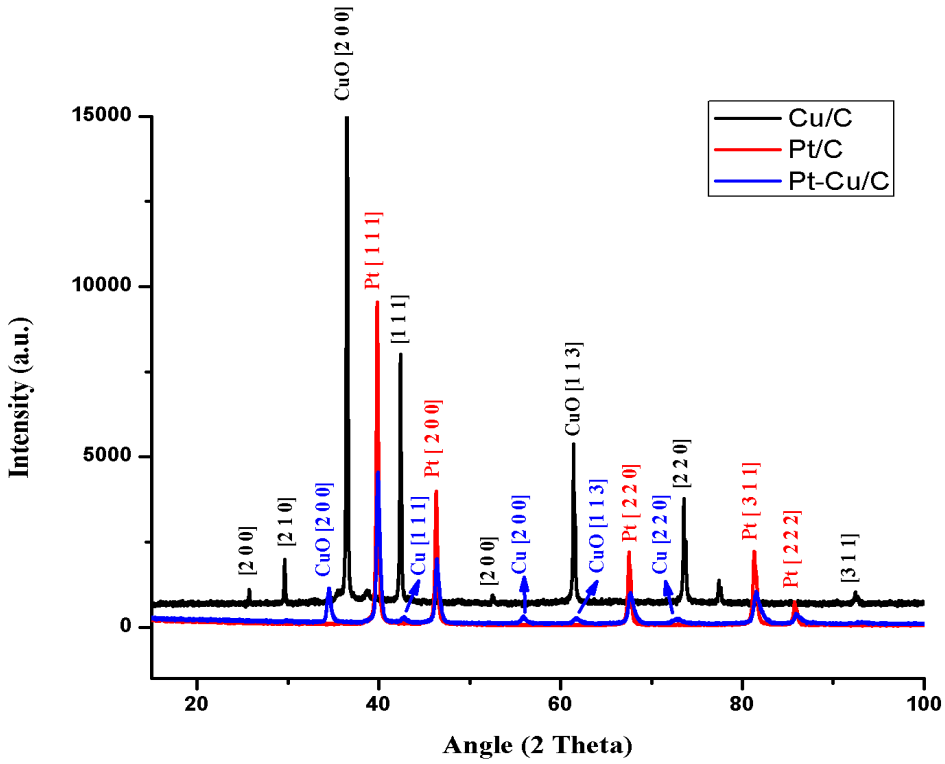

Figure 3.2 XRD pattern of Cu NP, Pt NP and Pt-Cu/C BNP.

B. Morphological analysis of Pt-Cu/C NCs, Pt NPs, and Cu NPs

For the morphological studies of as-prepared catalysts, HRTEM pictures were acquired to examine the nanostructures of the bimetallic Pt-Cu/C, Pt/C and Cu/C NP respectively. The Figure 3.3 represents HRTEM micrographs of the as-synthesized Pt/C, Cu/C and Pt-Cu/C NP. As displayed in Figure 3.3a, the synthesized Pt NP are spherical in shape and nearly monodispersed. Whereas the Cu NP shows oval shaped morphology (Figure 3.3b). However, the Pt-Cu/C reveals the distinguished flower shaped morphology on the Vulcan carbon support as seen in Figure 3.3c. The clear lattice fringes showing interplanar distance indicates a good crystalline structure of synthesized Pt-Cu BNP. The HRTEM images also confirms that both the presence of crystalline Cu and Pt NPs in the bimetallic Pt-Cu BNP. The flowerlike structure was obtained due to the growth of multiple leaves of Pt NP on the Cu seeds. Literature reports

that the crystallinity of Cu seeds controls the growth of multiple Pt leaves per Cu seed particle. Growth of multiple Pt leaves was observed due to the presence of multiple monocrystalline domains on Cu seed particle [46].

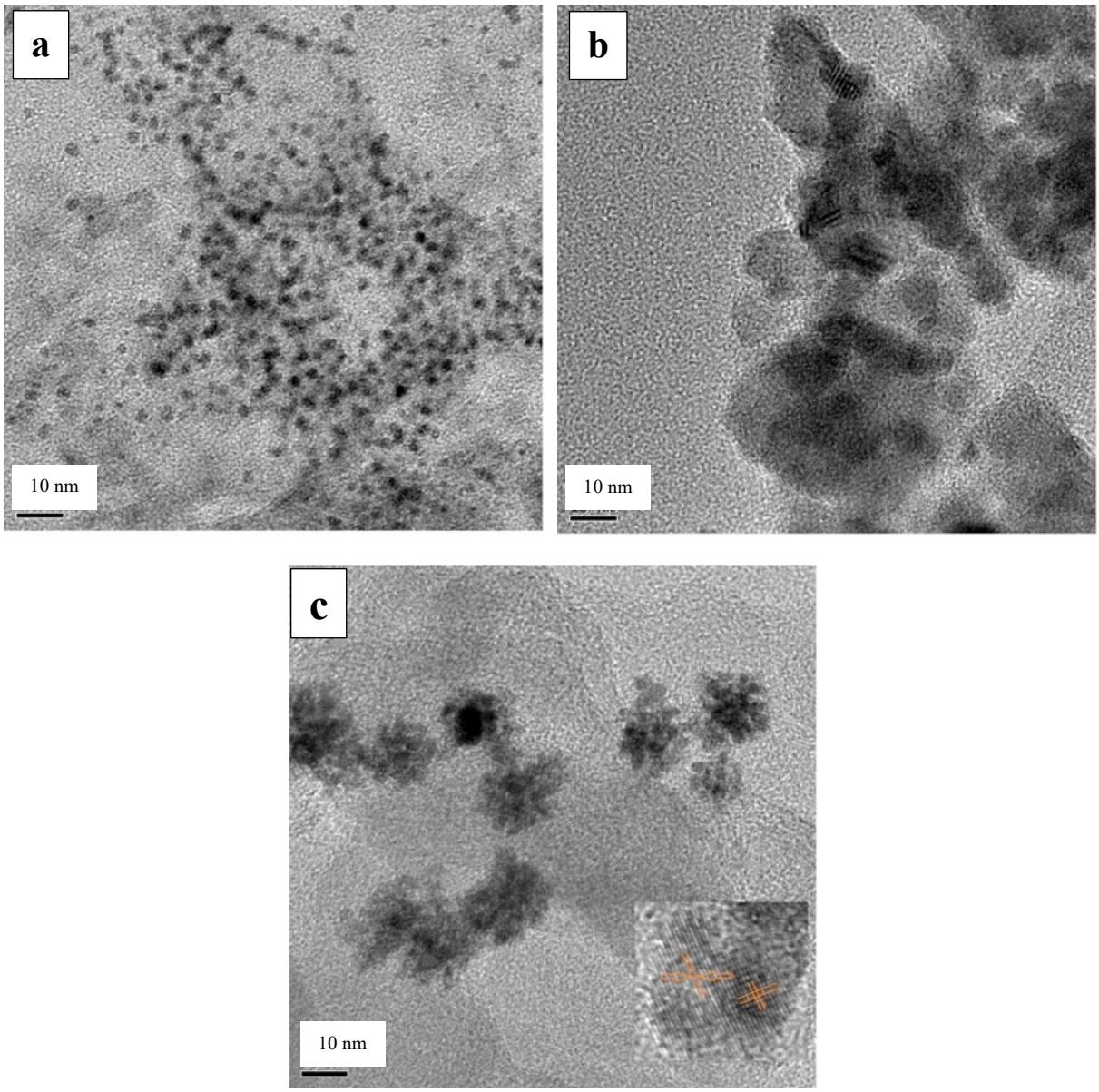

Figure 3.3 HRTEM images of Pt NP (a), Cu NP (b), and Pt-Cu/C BNP (c) at image scale 10 nm.

Jin et. al [47] has also reported synthesis of flower shaped PtMn bimetallic catalyst supported on CeO_2 synthesized via solvothermal method operated at 200 °C and N_2 pressure of 2.2 MPa upto 12 h. The lattice strain aroused as a result of the disparity in the lattice parameters of Pt and Mn was responsible for the anisotropic development of PtMn catalyst leading to the cauliflower morphology. However, in this study, the Pt-Cu supported on C were obtained at

atmospheric pressure and temperature conditions within 1.5 h with the aid of potent sonochemical approach. The seed mediated growth of Pt induced by heterogeneous nucleation over Cu ensued the flower shaped, anisotropic Pt-Cu. Thus, the sonochemical approach can be used as a powerful methodology for the synthesis and tunning of morphology for bimetallic, anisotropic NP. Further, SEM-EDX analysis was performed to investigate the density and distribution of Pt and Cu in the catalysts. Figure 3.4 demonstrates SEM-EDX analysis spectrum of the Pt-Cu catalysts. As shown in Figure 3.4, distinct peaks for Pt and Cu appeared, indicating that the preparation method was adequate and allowed an effective growth of Pt on Cu seeds. It was found that the Pt-Cu NP contains O - 4.80%, Cu - 14.17%, and Pt - 81.03% by weight, from the elemental composition analyzed using SEM-EDX. This confirms the presence of Pt and Cu in synthesized BNP.

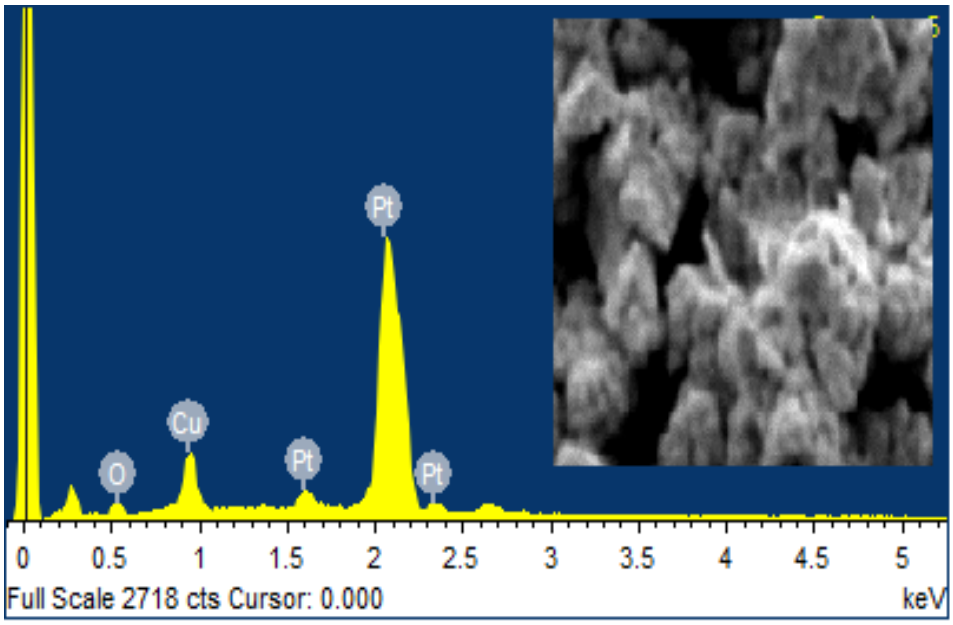

Figure 3.4 SEM-EDX analysis spectrum of Pt-Cu BNP

C. FTIR analysis of Cu NPs, Pt NPs and Pt-Cu BNPs

FTIR is a kind of vibrational spectroscopic analysis, performed to recognize the molecular functional groups appended to the exterior of Cu, Pt and Pt-Cu NPs using the characteristic stretching and bending frequencies of the functional groups. The FTIR spectra presented in Figure 3.5 depicts the characteristic band of Cu at 622.86 cm^{-1}. Further the peaks present at 1114.96 cm^{-1}, 1633.35 cm^{-1}, 2115.84 cm^{-1} and 3408.79 cm^{-1} are the indicative of –CO, -OH, Cu-H and –OH groups as per the literature [48]. The peak at 3408.79 cm^{-1} is for the O-H stretching and the peak at 1652 cm^{-1} is for the O-H bending.

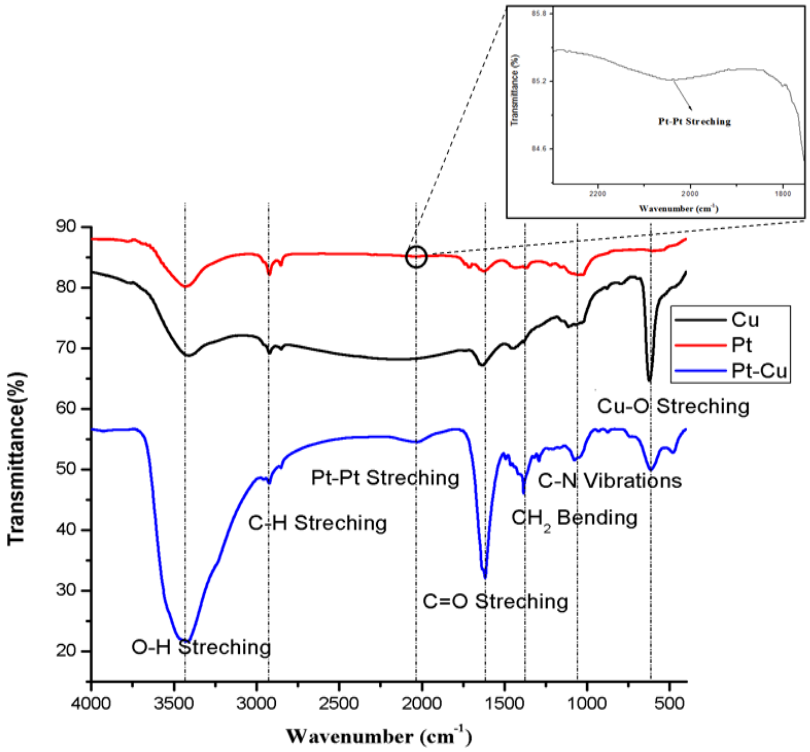

Figure 3.5 FTIR spectra of Cu NP, Pt NP and Pt-Cu BNP

D. UV-visible analysis of Cu and Pt-Cu NPs

The Figure 3.6 exhibits UV–Visible spectra of Pt-Cu/C bimetallic catalyst and shows the absorbance peaks in the UV–Vis spectrum at 250 nm and 277 nm which corresponds to Cu and Pt respectively [41]. The platinum ions show an absorbance peak of around 250 to 280 nm [42]. In this study, an absorbance peak in the UV-Vis spectra for Pt is obtained at 277 nm. This implies successful synthesis of bimetallic Pt-Cu/C BNP via sonochemical reduction approach.

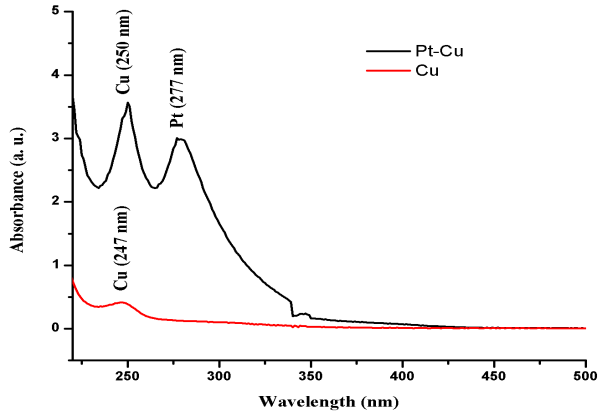

Figure 3.6 UV-Visible absorbance spectrum for Cu NP and Pt-Cu BNP

E. BET and ICP-OES analysis for Pt-Cu/C NC catalyst

The BET surface area of the as-prepared Pt-Cu/C catalyst was evaluated from N_2 adsorption-desorption isotherm at −196 °C. Before the test, sample was degassed at 523 K for 5 h in order to remove all the impurities like adsorbed gases and moisture from the sample. The N_2 adsorption-desorption isotherm and the pore size distribution of the Pt-Cu/C are represented in Figure 3.7. The obtained isotherm of the sample can be classified as Type IV isotherm (according to the IUPAC classification), with Type H3 hysteresis loop which is the characteristic loop for mesoporous material with small pore size. Moreover, significant adsorption at low relative pressures indicates the presence of micropores on the catalyst. The BET surface area, pore volume, and an average pore diameter of Pt-Cu/C BNP according to BJH method were found to be 78.5 m^2/g, 0.082 cm^3/g, and 4.91 nm respectively. Whereas, the external surface area calculated according to t-Plot method is estimated as 86.2 m^2/g. Further, the metal content analysis for Pt-Cu/C BNP carried out by ICP-OES estimated the 38.69 wt% loading of Pt on the catalyst and that of Cu as 9.31 wt% (Table 3.1).

Table 3.1. Elemental composition of Pt-Cu/C BNP catalyst on weight basis.

Elemental composition	Cu (wt%)	Pt (wt%)	O (wt%)	C (wt%)
Theoretical	10	30	-	60
SEM-EDX	9.17	32.03	4.80	53.69
ICP-OES	9.31	38.60	-	52.09

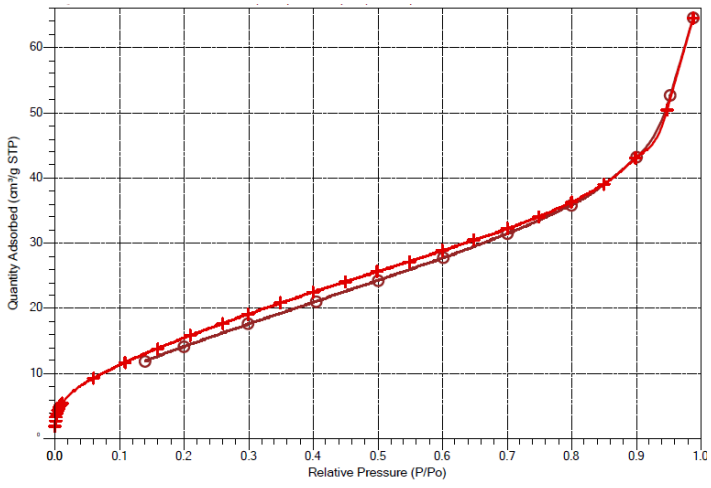

(a)

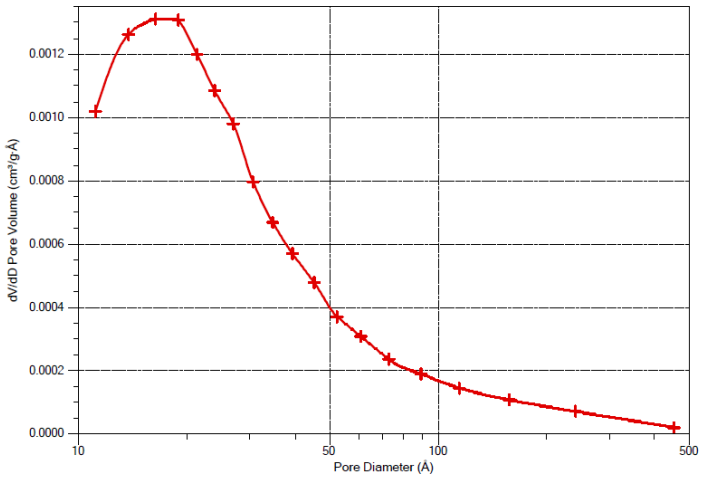

(b)

Figure 3.7 (a) N_2 adsorption-desorption isotherm for Pt-Cu/C, (b) Pore size distribution for Pt-Cu/C BNP.

3.2.2.2 Catalytic activity of Pt-Cu/C bimetallic NC catalyst

As mentioned earlier, the catalytic performance of the as prepared catalyst was examined for the selective GLY oxidation. Initially, the oxidation of GLY was studied in the presence of Pt and Cu alone. It was observed that, under 1 atm O_2 pressure and at 90 ^oC, 46.5% conversion of GLY was obtained with Pt after 4 h of reaction time whereas with Cu alone under similar reaction conditions the conversion achieved was only 28%. On the contrary, when the catalytic performance of Pt-Cu/C bimetallic catalyst was investigated, the conversion of GLY drastically increased from 46.5% to 98.8%. This remarkable enhancement in the GLY conversion was attributable to the synergism amongst the Pt and Cu in the prepared Pt-Cu BNP. In this composition of catalyst, Cu acts as a promoter and is advantageous for dehydrogenation. It also offers lower activity towards C-C cleavage which enhances the synergistic effect between Pt and Cu anisotropic bimetallic Janus structure. Zhang et al. [27] have also investigated the GLY selective oxidation using Cu-Pt alloy supported over carbon as a catalyst. They reported that the conversion of GLY obtained under the same reaction conditions using the catalyst Pt/Cu in the molar ratio of 4 to be 53%. It is believed that the enhancement in conversion obtained is because of the synergy amongst the Pt and Cu in the anisotropic Janus structure of catalyst used in this study over the Pt-Cu alloy structures reported earlier. The synthesized Pt-Cu/C BNP exhibits excellent catalytic performance over the recently reported nanocatalysts for the GLY oxidation was compared in the Table 3.2.

Table 3.2 Comparison of Pt-Cu/C catalyst performance for GLY oxidation with reported literature.

Catalyst	NaOH/ GLY ratio	T (^{0}C)	Time (h)	P_{O2} (MPa)	Catalyst loading	X (%)	S_{GA} (%)	Ref.
Au-Pt/TiO_2	4	80	0.5	0.3	-	90	58	[33]
Au/HY	4	60	2	0.3	0.3 g	80	-	[49]
Pt/AC	1.5	90	6	0.1	0.25 g	100	8	[50]
Pt/AC	4	90	6	0.1	0.25 g	58.5	18.4	[50]
Pt-Fe/CeO_2	4	70	2	0.1	2.2 kg/m^3	57.1	71.1	[14]
Au-Pt/CeO_2	4	100	0.5	0.5	-	99	10.5	[51]
Pt-Mn/CeO_2	4	70	24	0.1	0.05 g	100	24.9	[47]
$Co_{0.15}$/Mg_3 Al-s	6	70	6	-	0.2 g	47	49.1	[6]
Pt-Au/HLT	-	60	-	0.1	-	57	72	[52]
Pt-Fe/CeO_2	4	70	6-10	0.1	0.10 g	100	15.1	[53]
Cu-Pt/AC	1.5	90	4	0.1	0.25 g	80	16.7	[27]
Pt/C	3	90	4	0.1	0.1 g	46.5	23	Present Work
Cu/C	3	90	4	0.1	0.1 g	28	11.4	Present Work
Pt-Cu/C	3	90	1	0.1	0.1 g	96	65	Present Work

Under the conditions used herein, after 4 h, around 98.8% of GLY was converted. The ^{1}H-NMR of the product as presented in Figure 3.8, showed the presence of LA, TA, GA, GLYA, AA, FA and unreacted GLY [23]. Whereas, LA, TA, GA, OA and GLYA were detected in HPLC. The further oxidation products such as AA and FA are present as very minor constituents and hence were not detected by HPLC as displayed in Figure 3.9.

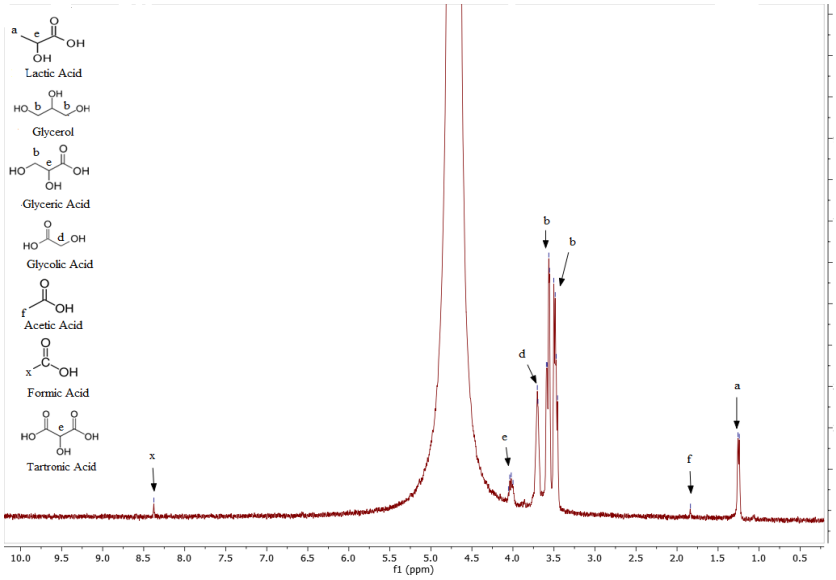

Figure 3.8 ^{1}H-NMR Spectrum of GLY oxidation reaction products (Reaction conditions: 0.1 mol/L GLY, NaOH to GLY molar ratio = 3, catalyst loading = 0.1 g, 90 °C, 4 h).

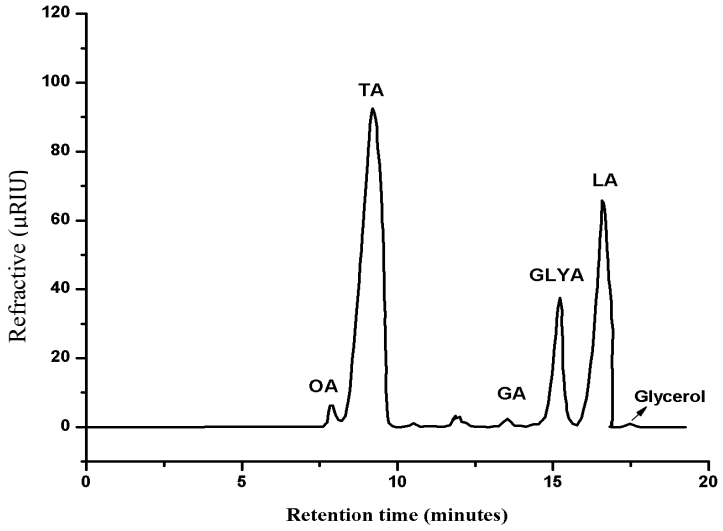

Figure 3.9 An example HPLC chromatogram of GLY oxidation reaction products (Reaction conditions: 0.1 mol/L GLY, NaOH to GLY molar ratio = 3, catalyst loading = 0.1 g, 90 °C, 4 h).

Further, the examination of the reaction products with time indicates that GA was the primary product of the reaction with Pt-Cu/C catalyst. It was observed that, as the reaction proceeds, with due course of time the yield of GA goes through a maxima (62.1%) attained at 1 hour. As the reaction time increases, the overall yield of GA diminished and, associatively, TA and GLYA were delivered with a greatest selectivity of 58% and 16%, individually after 4 h, that is, the total yield of dicarboxylic acids reached 74%. This suggests that, with the prolonged reaction time, GA was over-oxidized into C2 and C1 products, such as TA, GLYA, OA and FA. However, the catalytic performance of Pt and Cu alone for the GLY oxidation showed comparatively poor yield of TA and OA. The complete concentration profiles for the GLY oxidation products with Pt-Cu/C catalyst are as displayed in Figure 3.10. The GLY oxidation in presence of base can produce the primary alcohol- GLYAD and/or secondary alcohol –DHA with a parallel reaction mechanism. However, in the present study, the C3 oxygenated products of GLYAD overwhelmed the C3 oxygenated products of DHA. This signifies that the as-prepared Pt-Cu/C catalyst is highly selective towards the oxidation of GLYAD. As noted earlier, the GA selectivity reduces after 1 h, while for TA and GLYA it increases as reaction time increases. This explains that TA and GLYA could be the over-oxidation or decomposition products of the delivered GA. At the same time, presence of DHA was not noticed in the reaction mixture, demonstrating that the present reaction conditions are more favourable towards selective oxidation of GLY to GLYAD.

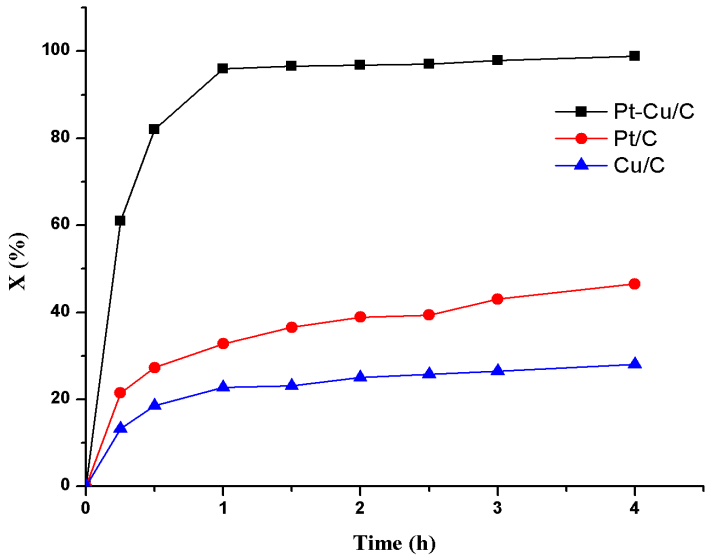
Pt-Cu/C
Pt/C
Cu/C
X (%)
Time (h)
0
20
40
60
80
100
0
1
2
3
4

(a)

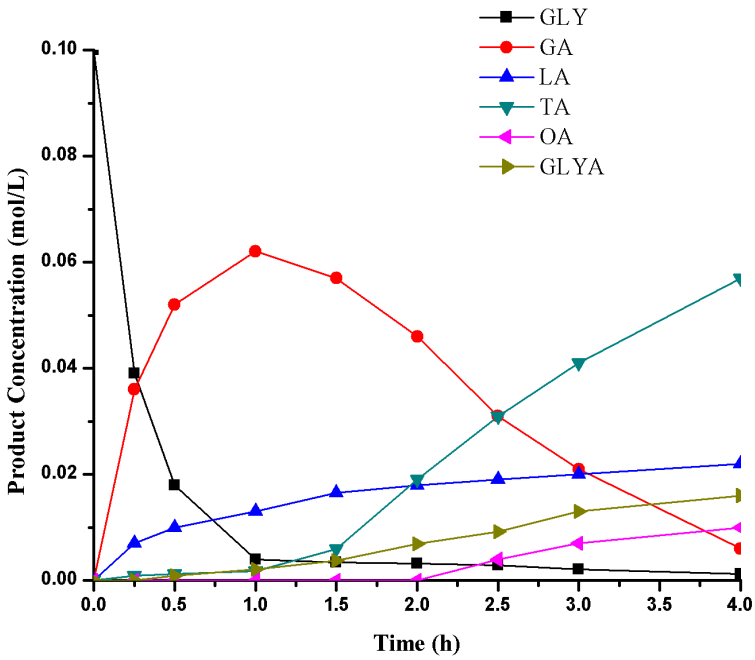
GLY
GA
LA
TA
OA
GLYA
Product Concentration (mol/L)
Time (h)
0.00
0.02
0.04
0.06
0.08
0.10
0.0
0.5
1.0
1.5
2.0
2.5
3.0
3.5
4.0

(b)

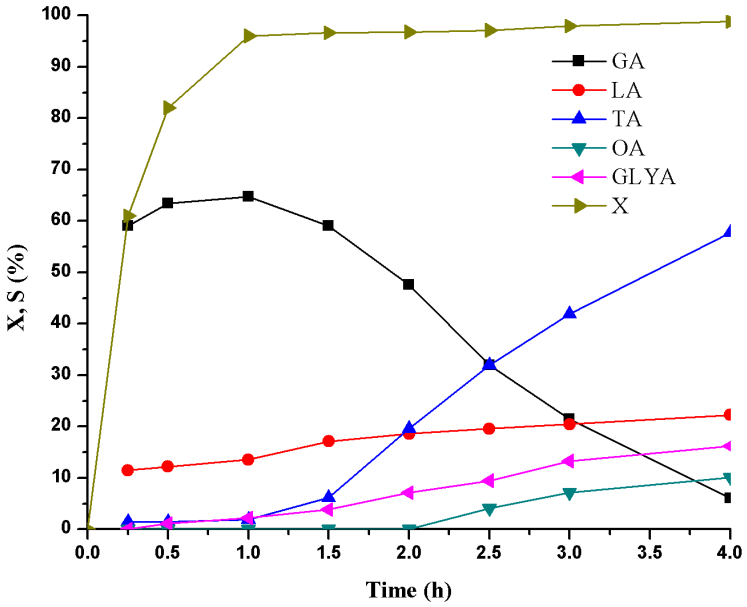

(c)

Figure 3.10 (a) GLY oxidation Reaction profile with Pt/C, Cu/C and Pt-Cu/C catalyst (b) Concentration profile for GLY oxidation, (c) Conversion and selectivity with respect to time for GLY oxidation (Reaction conditions: 0.1 mol/L GLY, NaOH to GLY molar ratio = 3, catalyst loading = 0.1 g, 90 °C)(X = conversion, S = selectivity).

A. Plausible reaction mechanism for selective oxidation of GLY over Pt-Cu/C NC catalyst

It was inferred from kinetic data presented in Figure 3.10 that the oxidation of GLY with the current catalytic system may proceed the subsequent reaction route. At first, the substrate GLY is converted to glycerolate which is then subjected to oxidative dehydrogenation to generate GLYAD. The glycerolate may also produce DHA as reported by Zang et al. [27], however with the catalytic system presented here, DHA was not noticed. In the presence of a metal catalyst, the GLAD undergoes rearrangement and oxidation to produce GA, whereas under basic conditions, dehydration and intramolecular Cannizzaro rearrangement of DHA can lead to LA. Further the reaction progresses with the overoxidation and/or decarboxylation of dominant GA generating TA, GLYA, OA and LA. According to Amaniampong et al. [54] GLYA and OA would be generated by means of (1) after the formation of GLAD, the CC bond is broken to obtain the C1 and C2 precursors to produce FA and OA, respectively; (2) The CC bond of GA is cleaved to release GLYA (further oxidizes to OA) (3) TA undergoes decarboxylation to offer

GLYA, and then oxidizes to OA. Along these lines, Figure 3.11 illustrates the possible reaction mechanism for the GLY oxidation reaction.

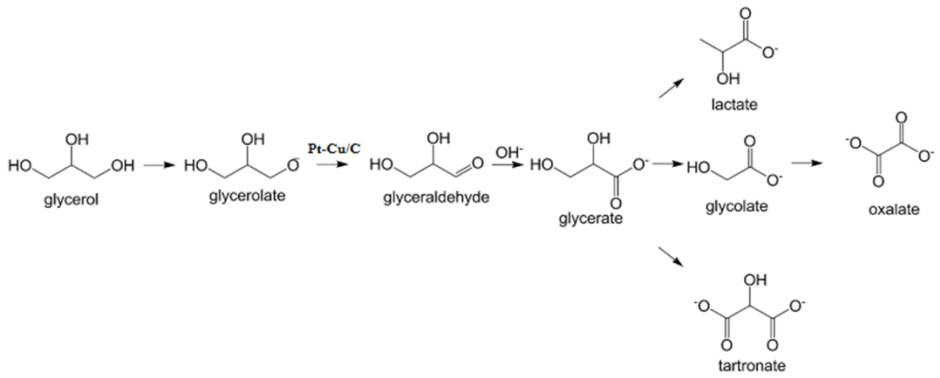

Figure 3.11 Reaction pathway for selective oxidation of GLY under basic environment.

B. Stability analysis of bimetallic Pt-Cu/C catalyst

The stability of bimetallic Pt-Cu/C catalyst was estimated through multiple recycle tests in batch production. For this, the centrifuge was used to separate the catalyst from the reaction mixture after each run. The separated catalyst was washed with DI water and dried at room temperature. This recovered catalyst was then utilized in the following run. As demonstrated in Figure 3.12, the stable GLY conversion was obtained even after the four recycle runs with GLY conversion at 96.4, 96, 96 and 95.2%, respectively.

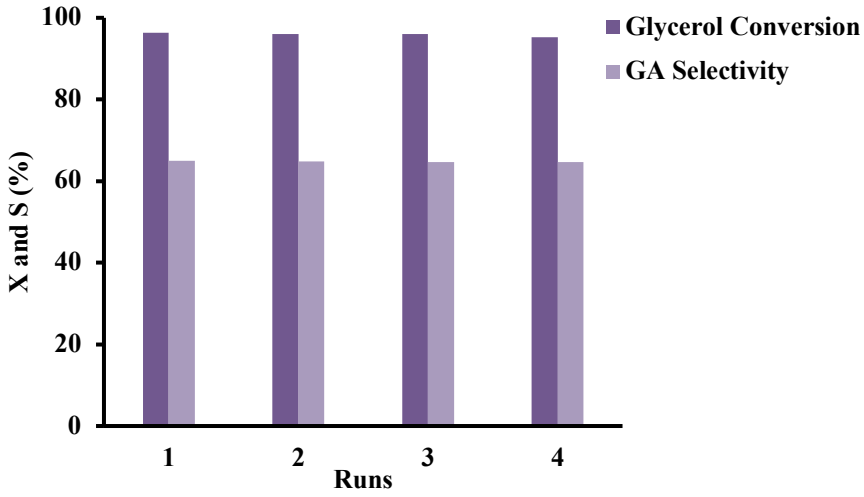

Figure 3.12 Recycle experiments for Pt-Cu/C catalyst (Reaction conditions: 0.1 mol/L GLY, NaOH to GLY molar ratio = 3, catalyst loading = 0.1 g, 90 °C, 1 h)(X = conversion, S = selectivity).

Their respective S_{GA} of about 65, 64.82, 64.7 and 64.7%. In light of the information, it very well may be reasoned that the Pt-Cu/C catalyst retains its activity, with no compromise in GA selectivity. The catalytic activity of Pt-Cu/C catalyst was found to be equally active for all four runs with no loss in GA selectivity. It indicates that reusability of the synthesized Pt-Cu/C catalyst was efficient for up to four consecutive batch experiment studies. Further, optimization studies can be carried out to enhance the selectivity of desired products. This shows that the Pt-Cu/C NC catalyst can improve the reactant conversions in catalytic reactions to a great extent. Thus, there is a need for their exploration in catalytic applications.

3.3 Selective oxidation of glycerol over bimetallic Ni-Cu/TiO_2 NC catalyst

3.3.1 Experimental procedure

3.3.1.1 Materials

$NiCl_2$•$6H_2O$ (98%) and $CuSO_4$•$5H_2O$ (98.5%) (Hi-Media Laboratories Pvt. Ltd., India) were used as metal precursors, $NaBH_4$ (97%) (Molychem, India) was used as a reducing agent. PVP (MW 40000, Hi-Media Laboratories Pvt. Ltd., India) was used as a stabilizer. TiO_2 NPs were used as a support. The DI water was used as the solvent. GLY (98%), H_2O_2 (30%), LA, AA, GA, FA, GA, and TA were used without any further treatment.

3.3.1.2 Synthesis of Ni-Cu BNPs, Ni and Cu NPs supported on TiO_2

The synthesis of Ni-Cu/TiO_2 NC catalyst was carried out utilizing the sonochemical approach. The study employed the sonication assisted conventional co-reduction method to synthesize a NC of Ni and Cu on a TiO_2 substrate. A Ni-Cu/TiO_2 hetero nanostructure was synthesized using an ultrasound probe with a tip diameter of 19 mm, an ultrasound generator operating at a frequency of 22 kHz, and a power output of 450 W. The experimental set up for the co-reduction with ultrasound cavitation assistance was shown in the Figure 3.13. Bimetallic Ni-Cu catalyst was prepared based on TiO_2 support by sonochemical co-reduction method. In a typical experiment, the stock solutions of 50 mL (0.2 M) $NaBH_4$ and 25 mL (0.1 M) $CuSO_4$•$5H_2O$ and 25 mL (0.1 M) $NiCl_2$•$6H_2O$ were prepared separately in distilled water. PVP was added to the $CuSO_4.5H_2O$ and $NiCl_2$•$6H_2O$ solution and then both the precursor solutions were transferred and mixed in a 250 mL flask followed by addition of TiO_2 NPs. The flask was placed on a magnetic stirrer with sonication for 45 minutes and continuously stirred along with the dropwise addition of $NaBH_4$ solution, at a rate of 1 mL/s, using burette. This reaction mixture of metal precursors and $NaBH_4$ was continuously stirred for 30 minutes to ensure the

complete reduction. After the completion of reaction, the bimetallic Ni-Cu/TiO_2 NCs were separated using centrifugation and dried at 90 °C for 5 h to obtain the Ni-Cu/TiO_2 NC catalyst.

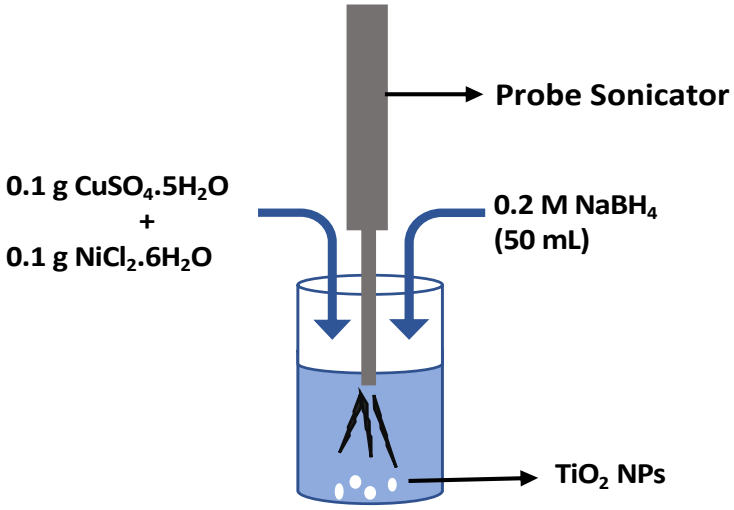

Figure 3.13 Schematic representation of ultrasound assisted synthesis of Ni-Cu/TiO_2 NCs

3.3.1.3 Characterization of Ni-Cu/TiO_2 catalyst

The crystalline structure and phase detection were carried out by XRD analysis executed on PAN analytical powder X-ray diffractometer, using Cu Kα radiation (1.5406 Å) and was scanned between 10° and 90°. The crystallite phase was estimated with the data of the JCPDS. Morphology of the NC was studied by FE-SEM on FESEM - Carl Zeiss, EVO MA 15, Oxford Instruments, equipped with EDX analyzer. The samples for FESEM were prepared by dispersing the NPs in ethanol using ultrasonic dispersion, and was spread on the copper grid (3-mm) coated with amorphous carbon, followed by drying under IR lamp for 15 minutes at room temperature. The BET surface area and pore volume of the Ni-Cu/TiO_2 bimetallic NC catalyst was estimated by using N_2 adsorption-desorption isotherm measured at −196 °C with a Micromeritics ASAP 2020 analyzer. Before the test, sample was degassed at 523 K for 5 h. The BET technique was applied to determine the specific surface area and the average pore diameter was calculated according to the formula: 4V/A.

3.3.1.4 Assessment of Ni-Cu/TiO_2 NC catalyst for selective GLY oxidation and product analysis

The selective glycerol oxidation was conducted at a constant temperature of 60 °C under atmospheric pressure. Glycerol (0.1 M, 50 mL), H_2O_2 (30% v/v, 10 mL) and catalyst (0.1 g) were mixed together in a 100 mL glass beaker with the help of magnetic stirrer operating at 500 rpm. Next the reaction was initiated with ultrasonic irradiation and conducted for 1 h.

Periodically, samples were taken from the reactor and filtered prior to the product analysis. The analysis of reaction mixture was carried out by Agilent 1100 high-performance liquid chromatography (HPLC) with a refractive index detector (RID) and a Shaodex SH1821 column at 50 °C. The 0.005 M H_2SO_4 was used as a mobile phase, flowing at a rate of 0.6 mL/min. The X_{GLY} and S of the products was computed using Eq. 3.1 and 3.2 respectively.

3.3.2 Results and discussion

3.3.2.1 Ni-Cu/TiO_2 NC catalyst characterization

A. XRD analysis of the Ni-Cu/TiO_2 NC catalyst

The XRD of synthesized Ni-Cu/TiO_2 was carried out at 40 kV and 15 mA with Cu Kα radiation and is shown in Figure 3.14. Furthermore, the crystallite size of NCs was determined using Debye-Scherer formula, $D = k\lambda/(\beta \cos\theta)$, where K is the constant (0.9), λ is the wavelength of X-ray (1.54×10^{-10}), β is the full-width half maximum (FWHM) of the peak and θ is the diffracted angle.

The crystalline structure and average crystallite size were obtained through an XRD pattern. The XRD peaks appears at 2θ = 25.169°, 35.33°, 43.15°, 47.91°, 56.14°, 62.63°, 74.84° and 82.56°. The recorded XRD pattern of Ni-Cu/TiO_2 NC catalyst is obtained in the scanning range (2θ) from 0° to 90° as illustrated in Figure 3.14. Typically, the peaks of crystalline TiO_2 anatase phase were observed at 2θ = 25.169 [101], 35.33 [004], 47.91 [200], 53.2 [105], 56.14 [211], 62.63 [204], 74.84 [215], and 82.56 [303] agreeing with the index card JCPDS 021-1272 that corresponds to anatase TiO_2 [55,56]. The distinct peak present at 43.15° corresponds to [111] phase plane of Cu with FCC structure [57], in addition as per JCPDS card no. 04-0836 the peaks present at 74.84° [220], and 82.56 ° [311] can also be indexed to Cu with FCC crystal structure [58]. Moreover, as per JCPDS card no. 01-071-4655 the characteristics peaks of Ni NP are located at 43.15° [111], 53.2° [200] and 74.84° [220]. This may indicate high metallic dispersion [59]. The dominating TiO_2 phase in the catalyst, is confirmed by the presence of the most prominent peak around 2θ = 25.169°, which corresponds to the (101) reflection of anatase. Compared to the XRD data for pure anatase however, the slightly shifted peaks of NPC indicate that the Cu and Ni metal ions probably occupy the lattice sites [60]. The XRD results also established that overall homogeneity of the composites was maintained and no new phase was formed indicating that pure Ni-Cu NPs on TiO_2 support were successfully synthesized with sonochemical co-reduction approach. According to the Debye-Scherrer equation, the crystallite size is found to be 22 nm at 2θ equal to 25.169 °.

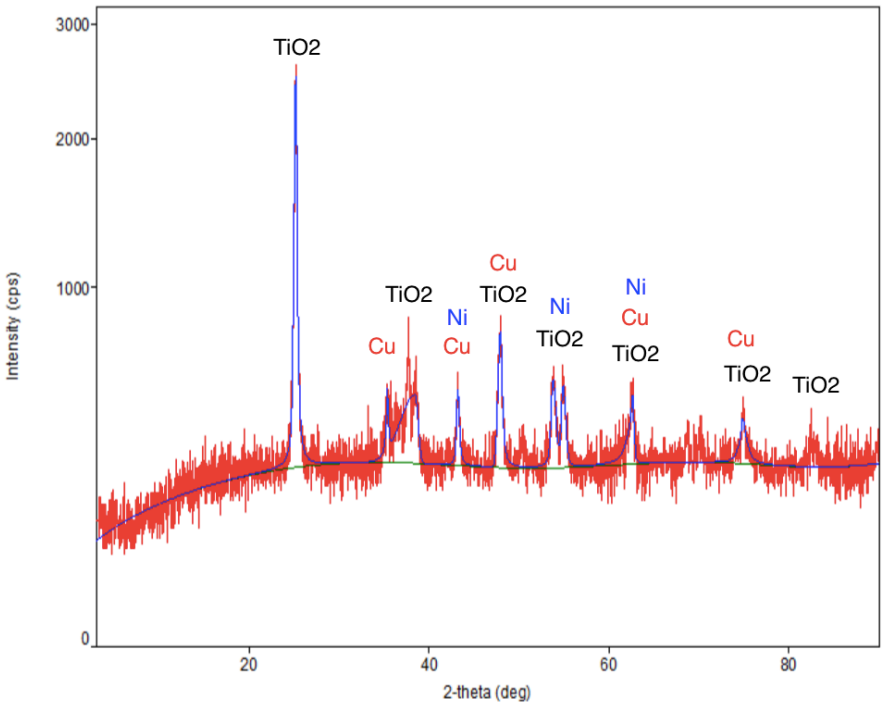

Figure 3.14 XRD pattern of Ni-Cu/C BNP

B. Ni-Cu/TiO_2 NC catalyst morphology

Morphology of the catalyst often plays an important role in its catalytic properties. The morphological characteristics of Ni-Cu/TiO_2 NC catalyst was analyzed using FESEM (Figure 3.15). It can be observed that several agglomerated Cu and Ni NPs with nearly uniform size and spherical morphology are present on the surface of TiO_2. Similar results of agglomeration was also reported by Riaz et al. [59] for Cu-Ni/TiO_2 nanostructures.

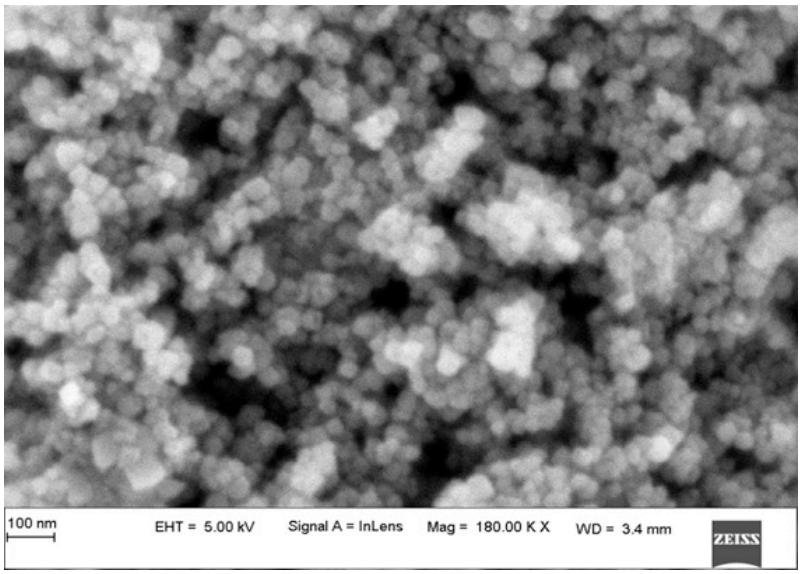

Figure 3.15 FESEM image of Ni-Cu/TiO_2 bimetallic NC catalyst

The presence of Cu and Ni on TiO_2 was further confirmed with FESEM-EDX analysis as presented in Figure 3.16 and Table 3.3. The FESEM-EDX micrograph (Figure 3.16) of Ni-Cu/TiO_2 NC reveals the sharp peaks of Cu, Ni, O, and Ti elements only, assuring the existence of Cu, Ni, and TiO_2 in the NC catalyst. In contrast, the peak corresponding to the C element arises due to the carbon tape used during EDX analysis.

Table 3.3 Elemental composition of Ni-Cu/TiO_2 NC catalyst on weight basis.

Elemental composition	Cu (wt%)	Ni (wt%)	Ti (wt%)	O (wt%)	C (wt%)
Theoretical	10	30	40	20	-
FESEM-EDX	9.48	28.03	39.13	19.27	4.09

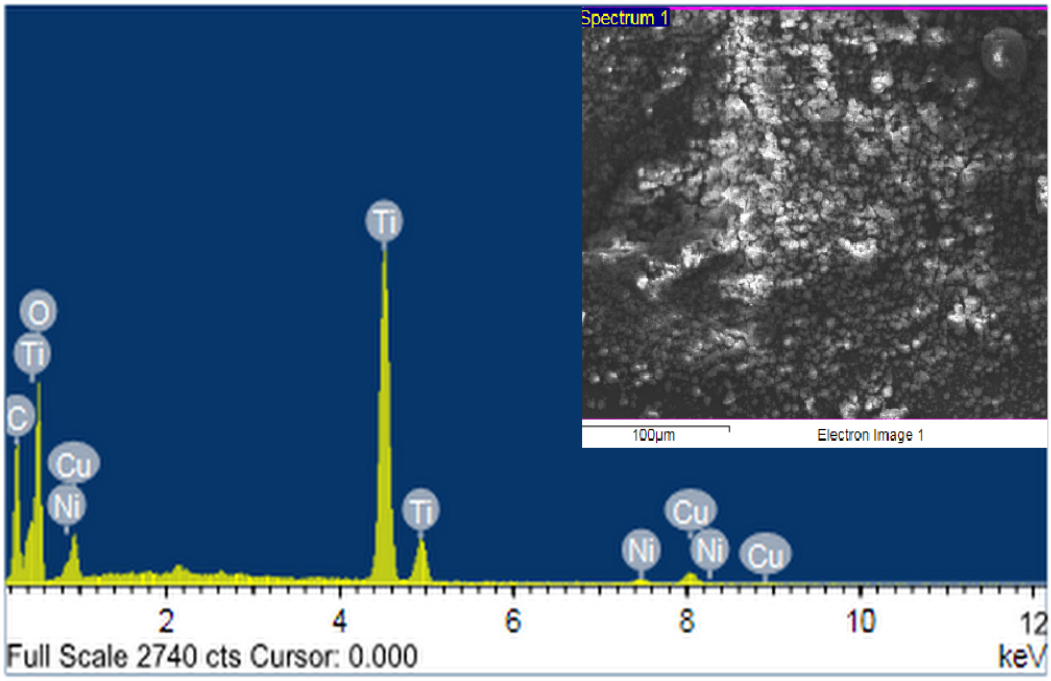

Figure 3.16 FESEM-EDX of bimetallic Ni-Cu/TiO_2 NC catalyst

The FESEM-EDX elemental dot mapping images (Figure 3.17) illustrate the elemental distribution of Ni and Cu over TiO_2 surface in the Ni-Cu/TiO_2 NC catalyst. Overall, the uniform anchoring of Cu, Ni, Ti, and O was detected from the dot mapping of the constituent elements of the as-prepared NC catalyst, implying the achievement of even dispersion of Ni and Cu over the TiO_2 surface. This proves that the uniformity in shape, size, and distribution of dopant materials over the support surface is demonstrated through the co-reduction of Cu and Ni metal precursors over TiO_2 NPs assisted by ultrasound.. Also, as evident from the FESEM image, the particle size is approximately 20-30 nm, which supports the size calculations obtained through XRD analysis which is 22 nm. This confirms the presence of both Ni and Cu NPs on the surface

of TiO_2 support and implies the successful synthesis of Ni-Cu/TiO_2 NC through the sonochemical approach.

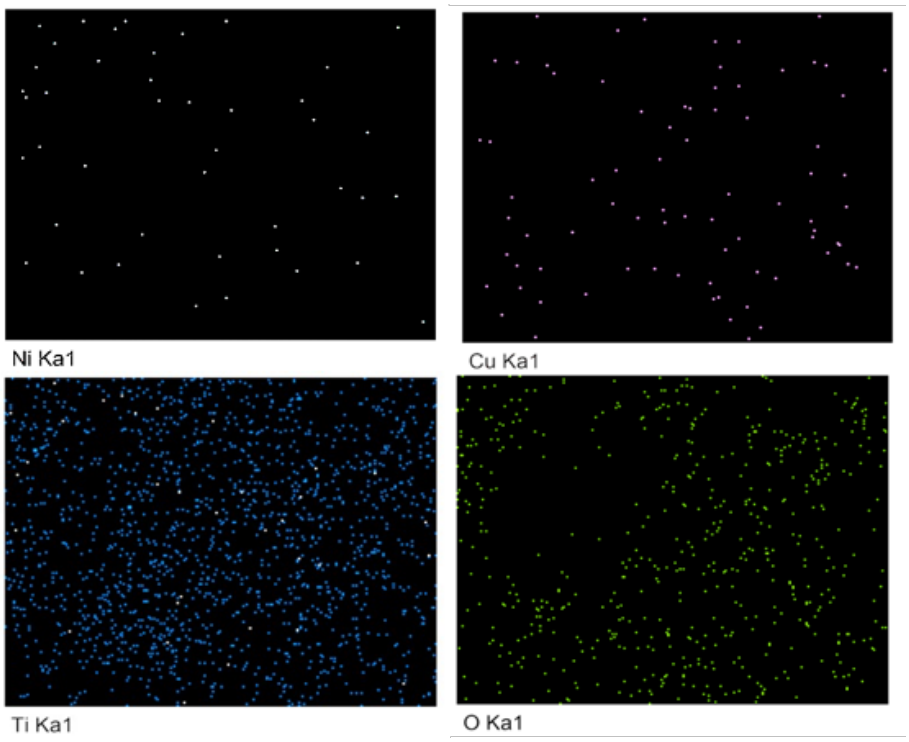

Figure 3.17 Elemental dot mapping of bimetallic Ni-Cu/TiO_2 NC catalyst.

C. BET measurements

The textural property of as-prepared Ni-Cu/TiO_2 NC is analyzed by adsorption of N_2 at -196.421 °C. The BET surface area plot is displayed in Figure 3.18. The specific surface area of Ni-Cu/TiO_2 catalyst calculated by BET method is found to be 42.2368 m^2/g. Single point adsorption total pore volume of pores less than 40.419 Å diameter at P/Po = 0.50 is 0.024 cm^3/g, and adsorption pore diameter calculated by (4V/A) BET has come out to be 22.605 Å.

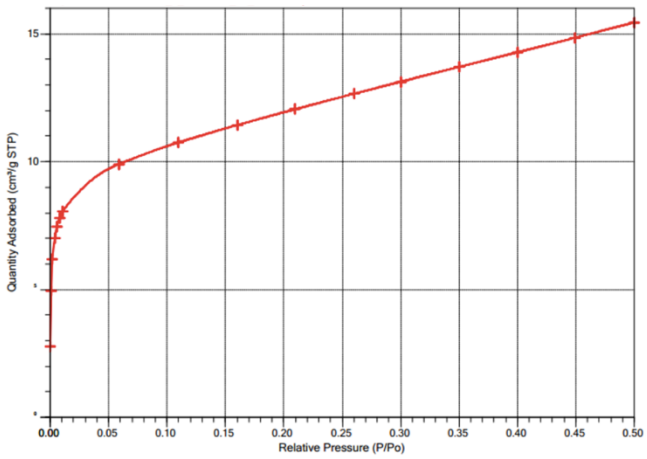

Figure 3.18 BET surface area plot of Ni-Cu/TiO_2 NC catalyst

3.3.2.2 Catalytic activity of Ni-Cu/TiO_2 bimetallic NC catalyst for GLY oxidation

As mentioned earlier, the catalytic performance of the as prepared catalyst was examined for the ultrasound induced selective GLY oxidation. Initially simple batch reaction kinetic for the oxidation of GLY was studied in the presence of Ni-Cu/TiO_2 NC catalyst. It was observed that at 60 ºC, with 5 mL of H_2O_2, 23% X of GLY was obtained after 0.5 h of reaction time. On the contrary, when the catalytic performance of Ni-Cu/TiO_2 NC was investigated for ultrasound assisted GLY oxidation with the same reaction conditions, the dramatic increase in reaction rate up to 4 folds was observed and the 91% X of GLY was obtained within 0.5 h. Under the conditions used herein with ultrasound assistance approximately complete conversion of GLY was achieved within 1 h of reaction time. The X of GLY with and without ultrasound assistance is presented in Figure 3.19.

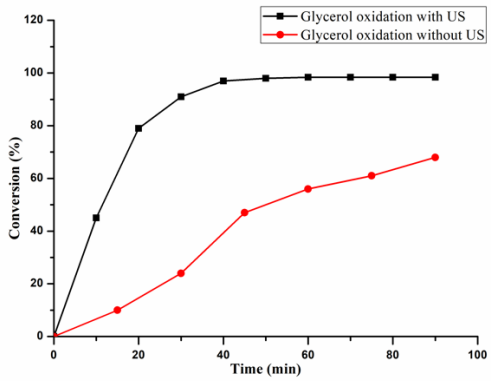

Figure 3.19 GLY conversion with and without ultrasound assistance over Ni-Cu/TiO_2 NC catalyst.

This remarkable enhancement in the GLY conversion was attributable to the acoustic cavitation. In this study, Cu acts as a promoter and is advantageous for dehydrogenation and enhances the synergistic effect between Ni and Cu. The synthesized Ni-Cu/TiO_2 bimetallic NC catalyst exhibits excellent catalytic performance over the recently reported nanocatalysts for the GLY oxidation as can be seen in Table 3.4.

Table 3.4 Comparison of Ni-Cu/TiO_2 NC catalyst performance for GLY oxidation with reported literature

Catalyst	T (°C)	Time (h)	Catalyst loading	X (%)	S_{GA} (%)	Ref
Au-Pt/TiO_2	80	0.5	GLY/metal mole fraction = 1000	90	58	[33]
Pt-Fe/CeO_2	70	2	2.2 kg/m^3	57.1	71.1	[14]
Pt-Mn/CeO_2	70	24	0.05 g	100	24.9	[47]
$Co_{0.15}$/Mg_3Al-s	70	6	0.2 g	47	49.1	[6]
Pt−Au/HT	60	6	GLY/metal mole fraction = 1000	57	72	[52]
Cu-Pt/AC	90	4	0.25 g	80	16.7	[27]
Ni-Cu/TiO_2	60	1	0.1 g	100	62 (S_{FA})	Present Work

Further, the examination of the ultrasound assisted GLY oxidation reaction products with time indicates that LA was the primary product of the reaction with Ni-Cu/TiO_2 catalyst (Figure 3.20). It was observed that, as the reaction proceeds, with due course of time the selectivity of LA goes through a maximum (84%) attained at 40 min. As the reaction time increases, the overall yield of LA diminished and, associatively, FA and OA were delivered with a greatest S_{FA} of 62%, S_{LA} of 24% and S_{OA} of 10%, individually after 70 min. Very recently, similar to the present study, increased quantities of FA with time were also observed by Underhill et al. [61]. This suggests that, with the prolonged reaction time, LA was over-oxidized into C2 and C1 products, such as GLYA, OA and FA. This is in line with earlier reports by Wu et al. [62]. Authors have reported the GLY conversion of 85.5% with 59.3% of the selectivity to DHA when the reaction ran for 6 h at 60°C with Cr(SO_3-salen)-CuMgAl-LDH (0.2 g) catalyst and 3 % H_2O_2 (30 mL). With the prolonging of the reaction time, the objective product (DHA) was over-oxidized into C1 and C2 products, such as OA and FA. Crotti et al. [63] have also obtained DHA and FA as the main products over iron complexes for the oxidation of GLY by H_2O_2 [16]. This implies that, the GLY oxidation with H_2O_2 under base free conditions favors DHA as the main product followed by FA being the scission product.

However, in present study LA is obtained as the main product followed by FA and OA. This may occur due to the local hot spots generated in the reaction mass as a result of acoustic cavitation during the course of reaction. Since the hot spots generated due to cavitation are characterized to possess extremely high temperature and pressure conditions and disappear within a fraction of second. This extremely high temperature and pressure conditions may lead to the formation of LA instead of GA or DHA as the literature suggests that higher reaction

temperature is required for the selective formation of LA [64]. Another probable reason to obtain LA is the presence of Ni-Cu/TiO_2 catalyst consisting of base metals and metal oxide. Numerous literature reports that the dehydration and intramolecular Cannizzaro rearrangement of DHA/GLYAD intermediates to LA is catalyzed by the presence of a base [25,27,51,65].

In addition to the synergistic properties resulted due to the Ni-Cu/TiO_2 NC catalyst, the unparalleled reaction rate obtained in the present study is also attributed to the presence of acoustic cavitation. As the potential of acoustic cavitation is well established to the extreme enhancement in the mass and heat transfer rates which in turn improves the reaction rates. This shows that the ultrasound assistance can improve the reactant conversions and selectivity in catalytic reactions to a great extent. Thus, there is a need for their exploration in catalytic applications. Further, the optimization studies can be carried out to enhance the selectivity of desired products.

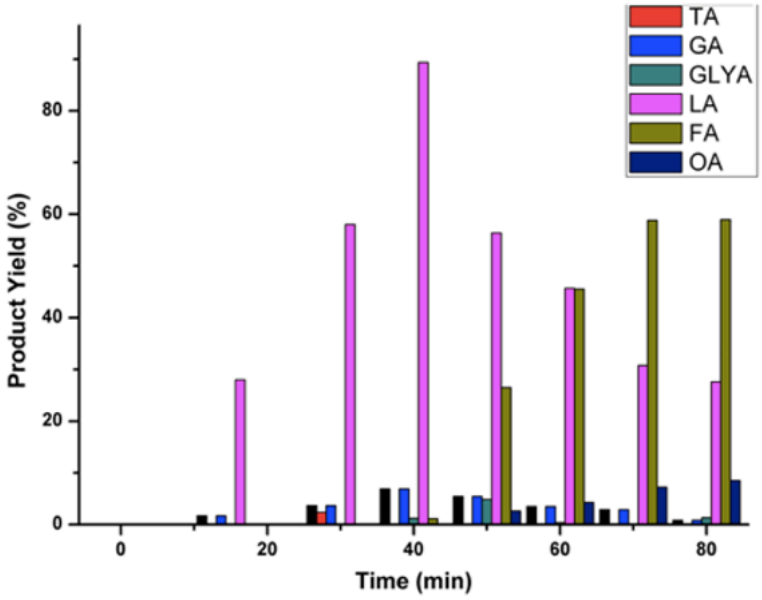

Figure 3.20 Product yield with respect to reaction time for the selective GLY oxidation over Ni-Cu/TiO_2 NC catalyst (Reaction conditions: 0.1 mol/L GLY (50 mL), 10 mL H_2O_2, catalyst loading = 0.1 g, 60 °C, Ultrasound frequency = 18 KHz).

A. Plausible reaction mechanism for selective oxidation of GLY over Ni-Cu/TiO_2 NC catalyst

Generally, the possibility of GLY oxidation over transition metal catalysts is rarely reported, so it was significant to design a highly effective transition metal heterogeneous catalyst for the selective oxidation of GLY. Based on the above results and discussion, a possible reaction pathway for LA production is proposed, as illustrated in Figure 3.21. The GLY oxidation proceeds by kinetically relevant oxidative dehydrogenation of GLY to GLYAD/DHA

intermediates on Ni-Cu/TiO_2 catalyst surface, followed by dehydration and rearrangement of these intermediates to LA induced by cavitation along with presence of Ni-Cu/TiO_2 NC catalyst consisting of base metals and metal oxide. Further over-oxidation of LA takes place over Ni-Cu/TiO_2.

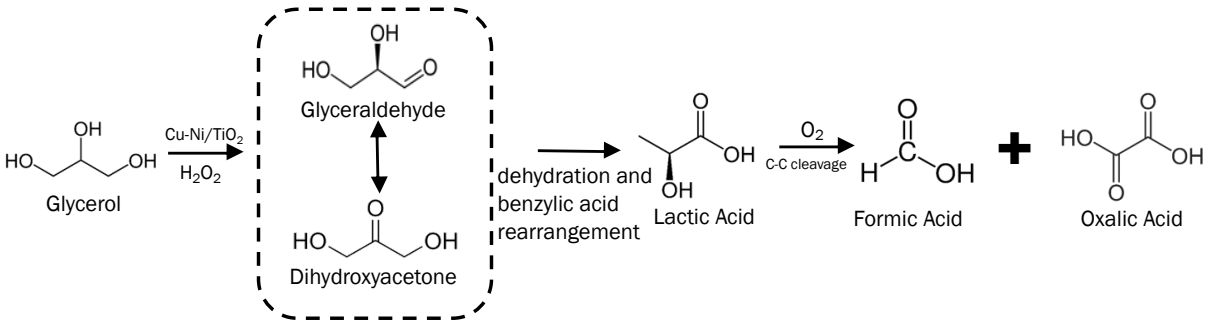

Figure 3.21 Reaction pathway for ultrasound induced oxidation of GLY with H_2O_2 over Ni-Cu/TiO_2 NC catalyst.

B. Ni-Cu/TiO_2 bimetallic NC catalyst stability

The stability of bimetallic Ni-Cu/TiO_2 NC catalyst was estimated through multiple recycle tests in ultrasound assisted batch production. For this, the centrifuge was used to separate the catalyst from the reaction mixture after each run. The separated catalyst was washed with DI water and dried at room temperature. This recovered catalyst was then utilized in the following run. As demonstrated in Figure 3.22, the stable GLY conversion was obtained even after the five recycle runs with X_{GLY} at 98.4, 98, 98, 97.5 and 97.3%, respectively. Their respective S_{LA} are about 84, 83.82, 83.7, 83 and 83%. In light of the information, it very well may be reasoned that the Ni-Cu/TiO_2 catalyst retains its activity, with no compromise in LA selectivity. The catalytic activity of Ni-Cu/TiO_2 catalyst was found to be equally active for all five runs with no significant loss in GLY conversion and LA selectivity. It indicates that reusability of the synthesized Ni-Cu/TiO_2 catalyst was efficient for upto five consecutive batch experiment studies. Further, optimization studies can be carried out to enhance the selectivity of desired products. This shows that the NC catalyst can improve the reactant conversions in catalytic reactions to a great extent. Thus, there is a need for their exploration in catalytic applications.

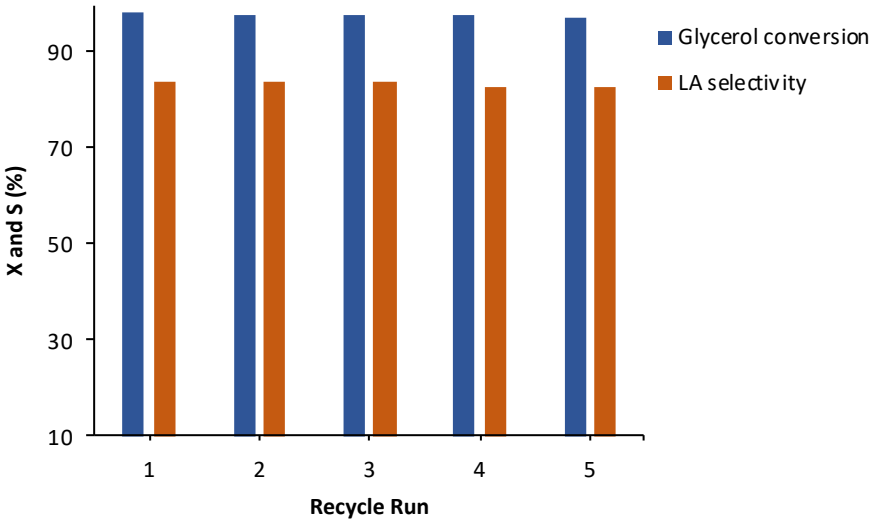

Figure 3.22 Recycle experiments for Ni-Cu/TiO_2 catalyst (Reaction conditions: 0.1 mol/L GLY (50 mL), 10 mL H_2O_2, catalyst loading = 0.1 g, 60 °C, 40 min, Ultrasound frequency = 18 KHz) (X = conversion, S = selectivity).

3.4 Comparable performance of synthesis and application of Pt-Cu/C and Ni-Cu/TiO_2 NC catalysts

Herein, ultrasound assisted heterogeneous nucleation (seed mediated growth) and co-reduction approaches were employed for the fabrication of bimetallic NCs for catalytic application in selective oxidation of GLY to value added chemicals. Heterogeneous nucleation was used for the fabrication of Pt-Cu/C NC whereas Ni-Cu/TiO_2 NC was prepared using co-reduction approach. The application of acoustic cavitation during fabrication of both the NCs resulted in the reduction of synthesis time under atmospheric conditions to a great extent. The proposed methods require a very short time of about 30 min for Ni-Cu/TiO_2 synthesis using co-reduction and 60 min for Pt-Cu/C NC synthesis using heterogeneous nucleation under atmospheric conditions, which is much less than that of the often-employed catalyst synthesis methods. For instance, conventional solvothermal method [47,66,67], hydrothermal [68–70], co-precipitation [71] demands either very high temperature and pressure conditions or longer reaction times or both (150 - 300 °C, pressure of 2 - 4 MPa up to 8 -24 h).

Different analytical techniques were used to investigate the produced NC catalysts, which supports the effective synthesis of the bimetallic nanostructure with uniform dispersion, shape and size and improved catalytic performance and stability via both approaches. However, they differ in morphological properties as the co-reduction of metal precursor with the aid of

ultrasound led to the spherical morphology (particle size = 22 nm) of the synthesized bimetallic structure, as opposed to the flower-like form (particle size = 4 nm) in the seed-mediated process. In both instances, the total surface area of the produced bimetallic NCs differed substantially, as for Pt-Cu/C it is 78.5 m^2/g and for Ni-Cu/TiO_2 it is 42.24 m^2/g. This suggests that, although seed mediated approach need more energy than the co-reduction method to generate a bimetallic structure, the seed mediate approach has benefits such as organized shape, larger surface area, and fine particle size. This approach involves the nucleation and subsequent growth of Pt NP on the Cu seeds. For the controlled morphology of BNPs, this approach is a better alternative over the conventional co-reduction method at the expense of reaction time and energy required.

Further, both the catalyst upon performance evaluation for GLY oxidation showed improved GLY conversion with faster reaction rates. However, the two secondary reaction steps occurring during the catalytic GLY oxidation are competitive, and accordingly, determine the final selectivity to GA/LA. Such reaction pathways offer directions to optimize the reaction conditions and thus the catalytic activity and selectivity. Our preliminary results on GLY oxidation confirmed, that the production of GA is favored over Pt-Cu/C NC catalyst whereas Ni-Cu/TiO_2 NC catalyst offered production of LA. In addition, though the LA production is most favorable at higher reaction temperatures as in case of hydrothermal cracking of GLY [25], the present study reports high S of LA (84%) under mild reaction conditions (60 °C) under base free conditions as a result of the synergy amongst the constituent base elements of Ni-Cu/TiO_2 NC catalyst and ultrasound assistance. It can be observed that the choice of appropriate catalyst is very essential in order to tune the selectivity and reaction mechanism.

3.5 Conclusion

In brief, the sonochemical approach was employed for the synthesis of bimetallic Pt-Cu/C and Cu-Ni/TiO_2 NCs as heterogeneous catalysts for the selective oxidation of GLY. The synthesis of bimetallic NCs was confirmed with XRD, HR-TEM, FESEM, FESEM-EDX with elemental dot mapping, FTIR, BET surface area measurements. The HRTEM analysis reflected flower shaped morphology with particle size of around 4 nm for Pt-Cu/C NCs as a result of sonication assisted seed mediated growth of Pt NPs over Cu seeds. Whereas Ni-Cu/TiO_2 NCs showed uniform dispersion of Ni and Cu on TiO_2 surface with spherical morphology and particle size of 22 nm as a result of Ni-Cu alloy formation due to the sonication assisted co-reduction of Ni and Cu metal precursors and deposition on TiO_2 NPs.

Under mild operating conditions, the GLY oxidation over Pt-Cu/C showed 96% GLY conversion within 1hour of reaction time with a S of 65% towards GA. Further, after 4 hours of reaction time GLY conversion of 98.8% was achieved with an excellent combined selectivity of 74% towards value added dicarboxylic acids (58% towards TA and 16% towards GLYA) (reaction conditions: 90 °C, 0.1 mol/L GLY, NaOH to GLY molar ratio = 3, catalyst loading = 0.1 g). On contrary to this, ultrasound induced GLY oxidation over Ni-Cu/TiO_2 showed maximum selectivity for LA as 84% with 98.4% GLY conversion (Reaction conditions: 0.1 mol/L GLY (50 mL), 10 mL H_2O_2, catalyst loading = 0.1 g, 60 °C, 40 min with ultrasonic irradiation). The synergistic effect resulted from hybrid nanostructure of respective constituent metals is the main force for the enhancement of catalytic performance. However, more research has to be conducted in order to optimize its catalytic capability and selectivity.

References

[1] B. Michele, G. Pierre, P. Catherine, Conversion of biomass into chemicals over metal catalysts, Chem. Rev. 114 (2013) 1827–1870.

[2] Y. Wang, S. Furukawa, N. Yan, Identification of an active Ni-Cu catalyst for nitrile synthesis from alcohol, ACS Catal. 9 (2019) 6681–6691. https://doi.org/10.1021/acscatal.9b00043.

[3] H. Yan, S. Yao, S. Zhao, M. Liu, W. Zhang, X. Zhou, G. Zhang, X. Jin, Y. Liu, X. Feng, X. Chen, D. Chen, C. Yang, Insight into the basic strength-dependent catalytic performance in aqueous phase oxidation of glycerol to glyceric acid, Chem. Eng. Sci. 230 (2021) 116191. https://doi.org/10.1016/j.ces.2020.116191.

[4] H. Yan, H. Qin, W. Liang, X. Jin, Y. Zhang, X. Feng, Y. Liu, X. Chen, C. Yang, Enhanced performance of bimetallic PtCo/MCM-41 catalysts for glycerol oxidation in base-free medium, Catal. Sci. Technol. 9 (2019) 4909–4919. https://doi.org/10.1039/C9CY01154D.

[5] H. Yan, S. Yao, B. Yin, W. Liang, X. Jin, X. Feng, Y. Liu, X. Chen, C. Yang, Synergistic

effects of bimetallic PtRu/MCM-41 nanocatalysts for glycerol oxidation in base-free medium: Structure and electronic coupling dependent activity, Appl. Catal. B Environ. 259 (2019) 118070. https://doi.org/10.1016/j.apcatb.2019.118070.

[6] X. Jin, M. Zhao, C. Zeng, W. Yan, Z. Song, Oxidation of glycerol to dicarboxylic acids using cobalt catalysts, ACS Catal. Oxid. (2016). https://doi.org/10.1021/acscatal.6b00961.

[7] R.M.L.M. Sandrini, J.R. Sempionatto, G. Tremiliosi-Filho, E. Herrero, J.M. Feliu, J. Souza-Garcia, C.A. Angelucci, Electrocatalytic oxidation of glycerol on platinum single crystals in alkaline media, ChemElectroChem. 6 (2019) 4238–4245. https://doi.org/10.1002/celc.201900311.

[8] Z. He, X. Ning, G. Yang, H. Wang, Y. Cao, F. Peng, H. Yu, Selective oxidation of glycerol over supported noble metal catalysts, Catal. Today. (2020) 0–1. https://doi.org/10.1016/j.cattod.2020.04.019.

[9] A. El Roz, P. Fongarland, F. Dumeignil, M. Capron, Glycerol to glyceraldehyde oxidation reaction over Pt-Based catalysts under base-free conditions, Front. Chem. 7 (2019) 1–9. https://doi.org/10.3389/fchem.2019.00156.

[10] M. Pagliaro, R. Ciriminna, H. Kimura, M. Rossi, C. Della Pina, From glycerol to value-added products, Angew. Chemie - Int. Ed. 46 (2007) 4434–4440. https://doi.org/10.1002/anie.200604694.

[11] M. Morales, P.Y. Dapsens, I. Giovinazzo, J. Witte, C. Mondelli, S. Papadokonstantakis, K. Hungerbühler, J. Perez-Ramirez, Environmental and economic assessment of lactic acid production from glycerol using cascade bio- and chemocatalysis, Energy Environ. Sci. 8 (2015) 558–567. https://doi.org/10.1039/C4EE03352C.

[12] V.K. Landge, S.H. Sonawane, R. V. Chaudhari, G.U.B. Babu, Selective oxidation of glycerol: a biomass-derived feedstock using the pt-cu janus catalyst for value-added products, Ind. Eng. Chem. Res. 60 (2021) 185–195. https://doi.org/10.1021/acs.iecr.0c04626.

[13] P.M. Walgode, R.P.V. Faria, A.E. Rodrigues, A review of aerobic glycerol oxidation processes using heterogeneous catalysts: a sustainable pathway for the production of dihydroxyacetone, Catal. Rev. - Sci. Eng. 63 (2021) 422–511. https://doi.org/10.1080/01614940.2020.1747253.

[14] X. Jin, M. Zhao, W. Yan, C. Zeng, P. Bobba, P.S. Thapa, B. Subramaniam, R. V Chaudhari, Anisotropic growth of PtFe nanoclusters induced by lattice-mismatch :

Efficient catalysts for oxidation of biopolyols to carboxylic acid derivatives, J. Catal. 337 (2016) 272–283. https://doi.org/10.1016/j.jcat.2016.02.015.

[15] G. Dodekatos and H. Tüysüz, Plasmonic Au/TiO_2 nanostructures for glycerol oxidation, Catal. Sci. Technol. (2016). https://doi.org/10.1039/C6CY01192F.

[16] S. Zaid, A. Addad, M. Capron, F. Dumeignil, Performance of Ag/Al_2O_3 catalysts in the liquid phase oxidation of glycerol– effect of preparation method and reaction conditions, Catal. Sci. Technol. (2015). https://doi.org/10.1039/C5CY01581B.

[17] X. Li, A.K. Tjiptoputro, J. Ding, J.M. Xue, Y. Zhu, Pd-Ce nanoparticles supported on functional Fe-MIL-101-NH2: An efficient catalyst for selective glycerol oxidation, Catal. Today. (2016). https://doi.org/10.1016/j.cattod.2016.03.044.

[18] J.C. Beltrán-Prieto, K. Kolomazník, J. Pecha, A review of catalytic systems for glycerol oxidation: Alternatives for waste valorization, Aust. J. Chem. 66 (2013) 511–521. https://doi.org/10.1071/CH12514.

[19] X. Jin, H. Yan, C. Zeng, P.S. Thapa, B. Subramaniam, R. V. Chaudhari, Phase transformed PtFe nanocomposites show enhanced catalytic performances in oxidation of glycerol to tartronic acid, Ind. Eng. Chem. Res. 56 (2017) 13157–13164. https://doi.org/10.1021/acs.iecr.7b01473.

[20] L.S. Ribeiro, E.G. Rodrigues, J.J. Delgado, X. Chen, M.F.R. Pereira, J.J.M. Orfao, Pd, Pt, and Pt-Cu catalysts supported on carbon nanotube (cnt) for the selective oxidation of glycerol in alkaline and base-free conditions, Ind. Eng. Chem. Res. 55 (2016) 8548–8556. https://doi.org/10.1021/acs.iecr.6b01732.

[21] R. Nie, D. Liang, L. Shen, J. Gao, P. Chen, Z. Hou, Selective oxidation of glycerol with oxygen in base-free solution over MWCNTs supported PtSb alloy nanoparticles, Appl. Catal. B Environ. 127 (2012) 212–220. https://doi.org/10.1016/j.apcatb.2012.08.026.

[22] B.N. Zope, D.D. Hibbitts, M. Neurock, R.J. Davis, Reactivity of the Gold/Water interface during selective oxidation catalysis, Science (80-.). 330 (2010) 74–78. https://doi.org/10.1126/science.1195055.

[23] C. Dai, L. Sun, H. Liao, B. Khezri, R.D. Webster, A.C. Fisher, Z.J. Xu, Electrochemical production of lactic acid from glycerol oxidation catalyzed by AuPt nanoparticles, J. Catal. 356 (2017) 14–21. https://doi.org/10.1016/j.jcat.2017.10.010.

[24] M. Zhang, J. Shi, W. Ning, Z. Hou, Reduced graphene oxide decorated with PtCo bimetallic nanoparticles: Facile fabrication and application for base-free oxidation of glycerol, Catal. Today. 298 (2017) 234–240. https://doi.org/10.1016/j.cattod.2017.04.0

13.

[25] M. Rosiene, A. Arcanjo, I.J. Silva, E. Rodriguez-castellon, A. Infantes-molina, R.S. Vieira, Conversion of glycerol into lactic acid using Pd or Pt supported on carbon as catalyst, Catal. Today. 279 (2017) 317–326. https://doi.org/10.1016/j.cattod.2016.02.015.

[26] R. Palacio, S. Torres, D. Lopez, D. Hernandez, Selective glycerol conversion to lactic acid on Co_3O_4/CeO_2 catalysts, Catal. Today. 302 (2018) 196–202. https://doi.org/10.1016/j.cattod.2017.05.053.

[27] C. Zhang, T. Wang, X. Liu, Y. Ding, Cu-promoted Pt/activated carbon catalyst for glycerol oxidation to lactic acid, J. Mol. Catal. A Chem. 424 (2016) 91–97. https://doi.org/10.1016/j.molcata.2016.08.018.

[28] S. Liu, K. Sun, B. Xu, Specific selectivity of Au-catalyzed oxidation of glycerol and other C3 - polyols in water without the presence of a base, ACS Catal. 4 (2014) 2226–2230. https://doi.org/10.1021/cs5005568.

[29] C. Ragupathi, J.J. Vijaya, R.T. Kumar, L.J. Kennedy, Selective liquid phase oxidation of benzyl alcohol catalyzed by copper aluminate nanostructures, J. Mol. Struct. 1079 (2015) 182–188. https://doi.org/10.1016/j.molstruc.2014.09.045.

[30] C. Wang, H. Daimon, S. Sun, Dumbbell-like Pt-Fe_3O_4 nanoparticles and their enhanced catalysis for oxygen reduction reaction, Nano Lett. 9 (2009) 1493–6. https://doi.org/10.1021/nl8034724.

[31] F. Papa, C. Negrila, G. Dobrescu, A. Miyazaki, I. Balint, Preparation, characterization and catalytic behavior of Pt-Cu nanoparticles in methane combustion, J. Nat. Gas Chem. 20 (2011) 537–542. https://doi.org/10.1016/S1003-9953(10)60221-6.

[32] C. Wang, H. Yin, S. Dai, S. Sun, A general approach to noble metal-metal oxide dumbbell nanoparticles and their catalytic application for CO oxidation, Chem. Mater. 22 (2010) 3277–3282. https://doi.org/10.1021/cm100603r.

[33] A. Villa, A. Jouve, F.J. Sanchez Trujillo, D. Motta, L. Prati, N. Dimitratos, Exploring the effect of Au/Pt ratio on glycerol oxidation in presence and absence of a base, Catalysts. 8 (2018). https://doi.org/10.3390/catal8020054.

[34] D.A. Bulushev, M. Zacharska, A.S. Lisitsyn, O.Y. Podyacheva, F.S. Hage, Q.M. Ramasse, U. Bangert, L.G. Bulusheva, Single atoms of Pt-group metals stabilized by n-doped carbon nanofibers for efficient hydrogen production from formic acid, ACS Catal. 6 (2016) 3442–3451. https://doi.org/10.1021/acscatal.6b00476.

[35] J. Lu, X. Liu, Q. Chen, J. Zhou, Coupling effect of nitrogen-doped carbon black and carbon nanotube in assembly gas diffusion electrode for H_2O_2 electro-generation and recalcitrant pollutant degradation, Sep. Purif. Technol. 265 (2021) 118493. https://doi.org/10.1016/j.seppur.2021.118493.

[36] J. Zhu, A. Holmen, D. Chen, Carbon nanomaterials in catalysis: Proton affinity, chemical and electronic properties, and their catalytic consequences, ChemCatChem. 5 (2013) 378–401. https://doi.org/https://doi.org/10.1002/cctc.201200471.

[37] U.N. Maiti, W.J. Lee, J.M. Lee, Y. Oh, J.Y. Kim, J.E. Kim, J. Shim, T.H. Han, S.O. Kim, 25th anniversary article: Chemically modified/doped carbon nanotubes & graphene for optimized nanostructures & nanodevices., Adv. Mater. 26 (2014) 40–66. https://doi.org/10.1002/adma.201303265.

[38] X. Ning, H. Yu, F. Peng, H. Wang, Pt nanoparticles interacting with graphitic nitrogen of N-doped carbon nanotubes: Effect of electronic properties on activity for aerobic oxidation of glycerol and electro-oxidation of CO, J. Catal. 325 (2015) 136–144. https://doi.org/https://doi.org/10.1016/j.jcat.2015.02.010.

[39] Y. Xiao, J. Greeley, A. Varma, Z. Zhao, G. Xiao, An experimental and theoretical study of glycerol oxidation to 1,3-dihydroxyacetone over bimetallic Pt-Bi catalysts, AIChE J. 63 (2017) 705–715. https://doi.org/10.1002/aic.15418.

[40] S. Hirasawa, H. Watanabe, T. Kizuka, Y. Nakagawa, K. Tomishige, Performance, structure and mechanism of Pd-Ag alloy catalyst for selective oxidation of glycerol to dihydroxyacetone, J. Catal. 300 (2013) 205–216. https://doi.org/10.1016/j.jcat.2013.01.014.

[41] I. Sobczak, K. Jagodzinska, M. Ziolek, Glycerol oxidation on gold catalysts supported on group five metal oxides—A comparative study with other metal oxides and carbon based catalysts, Catal. Today. 158 (2010) 121–129. https://doi.org/10.1016/j.cattod.2010.04.022.

[42] S.-S. Liu, K.-Q. Sun, B.-Q. Xu, Specific selectivity of Au-catalyzed oxidation of glycerol and other C3-polyols in water without the presence of a base, ACS Catal. 4 (2014) 2226–2230. https://doi.org/10.1021/cs5005568.

[43] C.N. Florica Papa, B.I., Akane Miyazaki, Morphology and chemical state of PVP-protected Pt, Pt – Cu, and Pt – Ag nanoparticles prepared by alkaline polyol method, J Nanopart Res . 13 (2011) 5057–5064. https://doi.org/10.1007/s11051-011-0486-9.

[44] J. Singh, P.D. Lodhi, K.K. Choudhary, N. Kaurav, Study of synthesis and optical

properties of Cu nanoparticles, J. Phys. Conf. Ser. 836 (2017) 7–9. https://doi.org/10.1088/1742-6596/836/1/012032.

[45] Y.X. Wang, H.J. Zhou, P.C. Sun, T.H. Chen, Exceptional methanol electro-oxidation activity by bimetallic concave and dendritic Pt-Cu nanocrystals catalysts, J. Power Sources. 245 (2014) 663–670. https://doi.org/10.1016/j.jpowsour.2013.07.015.

[46] Y. Wei, R. Klajn, A.O. Pinchuk, B.A. Grzybowski, Synthesis, shape control, and optical properties of hybrid Au/Fe_3O_4 nanoflowers, Hybrid Nanoparticles. 4 (2008) 1635–1639. https://doi.org/10.1002/smll.200800511.

[47] X. Jin, C. Zeng, W. Yan, M. Zhao, P. Bobba, H. Shi, P.S. Thapa, B. Subramaniam, R. V. Chaudhari, Lattice distortion induced electronic coupling results in exceptional enhancement in the activity of bimetallic PtMn nanocatalysts, Appl. Catal. A Gen. 534 (2017) 46–57. https://doi.org/10.1016/j.apcata.2017.01.021.

[48] Moniri, S.; Ghoranneviss, M.; Hantehzadeh, M. R.; Asadabad, M. A. Synthesis and optical characterization of copper nanoparticles prepared by laser ablation. Bull. Mater. Sci. 2017, 40, 37. https://doi.org/10.1007/s12034-016-1348-y.

[49] J. Cai, H. Ma, J. Zhang, Z. Du, Y. Huang, J. Gao, J. Xu, Catalytic oxidation of glycerol to tartronic acid over Au / HY catalyst under mild conditions, Chinese J. Catal. 35 (2014) 1653–1658. https://doi.org/10.1016/S1872-2067(14)60132-7.

[50] C. Zhang, T. Wang, X. Liu, Y. Ding, Selective oxidation of glycerol to lactic acid over activated carbon supported Pt catalyst in alkaline solution, Cuihua Xuebao/Chinese J. Catal. 37 (2016) 502–509. https://doi.org/10.1016/S1872-2067(15)61055-5.

[51] R.K.P. Purushothaman, J. van Haveren, D.S. van Es, I. Melian-Cabrera, J.D. Meeldijk, H.J. Heeres, An efficient one pot conversion of glycerol to lactic acid using bimetallic gold-platinum catalysts on a nanocrystalline CeO_2 support, Appl. Catal. B Environ. 147 (2014) 92–100. https://doi.org/10.1016/j.apcatb.2013.07.068.

[52] C. Xu, Y. Du, C. Li, J. Yang, G. Yang, Insight into effect of acid / base nature of supports on selectivity of glycerol oxidation over supported Au-Pt bimetallic catalysts, Applied Catal. B, Environ. 164 (2015) 334–343. https://doi.org/10.1016/j.apcatb.2014.09.048.

[53] X. Jin, H. Yan, C. Zeng, P.S. Thapa, B. Subramaniam, R. V Chaudhari, Phase transformed PtFe nanocomposites show enhanced catalytic performances in oxidation of glycerol to tartronic acid, Ind. Eng. Chem. Res. (2017). https://doi.org/10.1021/acs.iecr.7b01473.

[54] F.J. Prince N. Amaniampong, Quang Thang Trinh, Jithin John Varghese, Ronan Behling,

Sabine Valange, Samir H. Mushrif, Unraveling the mechanism of the oxidation of glycerol to dicarboxylic acids over a sonochemically synthesized copper oxide catalyst, Green Chem. (2018). https://doi.org/10.1039/C8GC00961A.

[55] C.A. Huerta-Aguilar, V. Palos-Barba, P. Thangarasu, R.T. Koodali, Visible light driven photo-degradation of Congo red by TiO_2–ZnO/Ag: DFT approach on synergetic effect on band gap energy, Chemosphere. 213 (2018) 481–497. https://doi.org/10.1016/j.chemosphere.2018.09.053.

[56] L. Munguti, F. Dejene, Effects of Zn:Ti molar ratios on the morphological, optical and photocatalytic properties of ZnO-TiO_2 nanocomposites for application in dye removal, Mater. Sci. Semicond. Process. 128 (2021) 105786. https://doi.org/10.1016/j.mssp.2021.105786.

[57] Y. Dong, K. Wang, Y. Tan, Q. Wang, J. Li, H. Mark, S. Zhang, Synthesis and characterization of pure copper nanostructures using wood inherent architecture as a natural template, Nanoscale Res. Lett. 13 (2018) 1–8. https://doi.org/10.1186/s11671-018-2543-0.

[58] A. Khan, A. Rashid, R. Younas, R. Chong, A chemical reduction approach to the synthesis of copper nanoparticles, Int. Nano Lett. 6 (2016) 21–26. https://doi.org/10.1007/s40089-015-0163-6.

[59] N. Riaz, F.K. Chong, B.K. Dutta, Z.B. Man, M.S. Khan, E. Nurlaela, Photodegradation of Orange II under visible light using Cu-Ni/TiO_2: Effect of calcination temperature, Chem. Eng. J. 185–186 (2012) 108–119. https://doi.org/10.1016/j.cej.2012.01.052.

[60] V.S. Kirankumar, B. Hardik, S. Sumathi, C. Wang, Q.F. Fei, B.H. Yang, Efficient and rapid degradation of Congo red dye with TiO_2 based nano-photocatalysts, (2017). https://doi.org/10.1088/1742-6596/755/1/011001.

[61] R. Underhill, M. Douthwaite, R.J. Lewis, P.J. Miedziak, R.D. Armstrong, D.J. Morgan, S.J. Freakley, T. Davies, A. Folli, D.M. Murphy, Q. He, O. Akdim, J.K. Edwards, G.J. Hutchings, Ambient base-free glycerol oxidation over bimetallic PdFe/SiO_2 by in situ generated active oxygen species, Res. Chem. Intermed. 47 (2021) 303–324. https://doi.org/10.1007/s11164-020-04333-2.

[62] G. Wu, X. Wang, T. Jiang, Q. Lin, Selective oxidation of glycerol with 3 % H_2O_2 catalyzed by LDH-hosted Cr(III) complex, Catalysts. 5 (2015) 2039–2051. https://doi.org/10.3390/catal5042039.

[63] C. Crotti, E. Farnetti, Selective oxidation of glycerol catalyzed by iron complexes, J.

Mol. Catal. A Chem. 396 (2015) 353–359. https://doi.org/10.1016/j.molcata.2014.10.021.

[64] J. Xu, H. Zhang, Y. Zhao, B. Yu, S. Chen, Y. Li, L. Hao, Z. Liu, Selective oxidation of glycerol to lactic acid under acidic conditions using AuPd/TiO_2 catalyst, Green Chem. 15 (2013) 1520–1525. https://doi.org/10.1039/c3gc40314a.

[65] Y. Shen, S. Zhang, H. Li, Y. Ren, H. Liu, Efficient synthesis of lactic acid by aerobic oxidation of glycerol on Au-Pt/TiO_2 catalysts, Chem. - A Eur. J. 16 (2010) 7368–7371. https://doi.org/10.1002/chem.201000740.

[66] A.M. Mohammed, S.S. Mohtar, F. Aziz, M. Aziz, A. Ul-Hamid, W.N. Wan Salleh, N. Yusof, J. Jaafar, A.F. Ismail, Ultrafast degradation of Congo Red dye using a facile one-pot solvothermal synthesis of cuprous oxide/titanium dioxide and cuprous oxide/zinc oxide p-n heterojunction photocatalyst, Mater. Sci. Semicond. Process. 122 (2021) 105481. https://doi.org/10.1016/j.mssp.2020.105481.

[67] T. Quang, Q. Viet, V. Hoang, N. Thi, H. Giang, Statistical screening and optimization of photocatalytic degradation of methylene blue by ZnO–TiO_2/rGO nanocomposite, Colloids Surfaces A Physicochem. Eng. Asp. 629 (2021) 127464.

[68] M.B. Shekardasht, M.H. Givianrad, P. Gharbani, Z. Mirjafary, A. Mehrizad, Preparation of a novel Z-scheme g-C_3N_4/RGO/$Bi_2Fe_4O_9$ nanophotocatalyst for degradation of Congo Red dye under visible light, Diam. Relat. Mater. 109 (2020) 108008. https://doi.org/10.1016/j.diamond.2020.108008.

[69] M. Maruthupandy, T. Muneeswaran, T. Vennila, M. Anand, W.-S. Cho, F. Quero, Development of chitosan decorated Fe_3O_4 nanospheres for potential enhancement of photocatalytic degradation of Congo red dye molecules, Spectrochim. Acta Part A Mol. Biomol. Spectrosc. 267 (2022) 120511. https://doi.org/10.1016/j.saa.2021.120511.

[70] H. Bian, Z. Zhang, X. Xu, Y. Gao, T. Wang, Photocatalytic activity of Ag/ZnO /AgO/TiO_2 composite, Phys. E Low-Dimensional Syst. Nanostructures. 124 (2020). https://doi.org/10.1016/j.physe.2020.114236.

[71] C. Ma, F. Wang, C. Zhang, Z. Yu, J. Wei, Z. Yang, Y. Li, Z. Li, M. Zhu, L. Shen, G. Zeng, Photocatalytic decomposition of Congo red under visible light irradiation using MgZnCr-TiO_2 layered double hydroxide, Chemosphere. 168 (2017) 80–90. https://doi.org/10.1016/j.chemosphere.2016.10.063.

Chapter 4.

Catalytic reduction of 4-Nitrophenol over Bimetallic Nanocomposites

4.1 Introduction

In recent years, the increasing rate of environmental pollution due to the rapid growth of industrialization is posing a major threat to the humanity and ecosystem, as huge amounts of lethal pollutants in industrial wastewater are discharged into water streams without any effective treatment [1]. Nitrophenols are among the most common organic pollutants and are referred to as "priority pollutants" owing to their superior solubility and stability in water [2,3]. Nitrophenols such as 4-nitrophenol (4-NP) are involved in the processes of various herbicides, pesticides, and synthetic dyes and thus exist as a by-product of agriculture and chemical industries [4]. Nitrophenols and other nitro-derivatives can also be formed as by-products of wastewater treatment processes [5,6]. They are highly toxic to living beings, even in trace amounts, as they can harm the kidney, blood, central nervous system, and liver of humans and animals owing to their extremely mutagenic and carcinogenic nature. However, because of the significant stability and low water solubility, the degradation of 4-NP to a harmless substance is quite challenging [7]. Thus, has become an important environmental subject and received significant attention in the 21st century.

Toxic nitrophenols can be easily converted into aminophenols by reduction processes [8,9]. From the application perspective, being a fundamental chemical reaction in organic synthesis developing technologies possessing innovative features for reduction process is really an effective strategy to eliminate toxic pollutants especially nitrophenols and for synthetizing anilines [2,10]. Conversely, aminophenols, are not only less toxic and can be easily removed and mineralized than nitrophenols but also essential ingredients for the fabrication of pigments, pesticides, dyes, plastics, analgesic and antipyretic drugs and in many other applications such as anti-corrosion agents and lubricants [3,10,11]. Thus, the organic transformation of 4-NP to 4-aminohenol (4-AP) through reduction is imperative, as 4-AP is far more beneficial than 4-NP.

For the reduction, 4-NP must interact with hydrogen (hydride ion) to obtain 4-AP. A strong reducing agent like sodium borohydride ($NaBH_4$) is commonly used to reduce dyes into non-toxic constituents as it is a good source of hydride ions. However, a highly stable 4-NP requires a larger number of hydrogen ions for efficient reduction. The insufficient number of hydrogen ions produced by the self-hydrolysis of $NaBH_4$ makes it unfit for reduction of 4-NP [12].

Moreover, mutual repulsion caused by negatively charged 4-NP and BH_4^- ions creates high kinetic barriers [13,14]. Although the reaction was a thermodynamically feasible process involving E_0 for 4-NP/4-AP = – 0.76 V and H_3BO_3/ BH_4^- = – 1.33 V versus normal hydrogen electrode (NHE), it was kinetically restricted in the absence of a catalyst [15]. Hence, a catalyst is necessary to overcome the kinetic barrier to achieve 4-NP reduction reaction [13]. The catalytic reduction of nitroarenes by heterogeneous nanocatalysts has attracted significant consideration due to clean processing, easy operation, economic nature and high efficiency. Accordingly, the suitable design of the heterogeneous nanocatalysts and their careful selection can considerably improve the reduction performance, thereby making further catalytic sustainability and efficiency [16].

In the recent decade, nanomaterials are more attractively explored for their catalytic activity and performances. To overcome the issues of lower hydrogen production rate and kinetic barrier of reaction, the new generation of nanomaterials needs to be explored with a more stable structure, efficient hydrogen generation in line with green chemistry. The rapid progress in the development of nanoparticles (NPs) opens another avenue to the design of catalysts with extraordinary superiority as compared with their bulk counterparts. Literature covers innumerous findings on the potential noble-metal catalysts, such as Pd [17], Pt [18], Ag [19], and Au [4] for the reduction of 4-NP. However, availability and cost are of key importance for the commercial application of such noble metal catalysts. A potential solution to overcome this difficulty is to employ the alloys of noble metals with abundant and low-cost non-noble metals. The noble metals can be alloyed with metals such as Cu, Ni, Co, Fe, etc. This reduces the amount of noble metals and offers an economic catalyst while preserving the overall performance [20].

In recent years, the proficiency of bimetallic nanostructures in accelerating the reduction of 4-NP has been explored through BNPs such as AgCu [21], Hg-Pd [22], CuNi [12], Au-Ag [23], Pd-Co [20], AuPt [24], PtPd [18], etc. The results obtained from these studies marked the remarkable enhancement in the catalytic performance of noble metal NPs upon alloying with other metals for the reduction of 4-NP. However, the aggregation of these BNPs during reaction restricts their application. Also, stabilizing agents may assist in circumventing aggregation only to some extent [18]. This indicates that the significant high surface energy of NPs induces unavoidable aggregation, reducing the active surface area, catalytic activity, and specifically reusability of NPs as a catalyst. To overcome this, the active sites of NPs can be fixed on suitable stabilizing supports. In addition, the support can also be beneficial to enhance particle

distribution along with reusability. An appropriate particle distribution provides the maximum exposure to the active sites of NPs during the reaction, which reduces the amount of noble metal catalysts required for the conversion [25].

Different types of materials such as CeO_2 [12], Al_2O_3 [26], SiO_2 [27], graphene [11], metal-organic framework [28], bentonite clay [29] and synthetic polymers [30] have been used as the substrates to stabilize the metals. The synthesis of Ag@Pt/sepiolite [31], organoplatinum(II) complex supported on graphene oxide [28], Au@silica [27], Fe_3O_4@SiO_2-Ag [15], Pt-Au/CeO_2 [24], etc. have been reported and explored for the catalytic reduction of 4-NP in the presence of $NaBH_4$. Although they exhibited good catalytic activity and stability, the cost for the catalyst is quite high as they consist of noble metals, and the supports are also inorganic. In the past decade, the design of metal-polymer hybrid nanocomposite (HNC) materials has attracted much attention for their wide applications in several fields from controlled devices to catalysis [32].

Increasing global inclination to follow 'green chemistry' principles leads to utilizing biopolymers as green alternatives due to their characteristic features such as plentifulness, biodegradability, and renewability [14,33]. Conventional methods to synthesise polymeric nanomaterial employ chemical compounds that may cause environmental toxicity later due to their long-term stability. By contrast, biopolymers are usually composed of safe monomers and are carbon neutral for the climate. Biopolymers facilitate the synthesis of nanomaterials because biomass morphology is often structured at the nano level [34]. Biopolymers are found in various organisms such as plants, algae, fungi, bacteria and animals. Biopolymers are unique in composition and have various physiological properties [35]. Biopolymeric nanomaterials can be formed by attachment of metals to biopolymers. In particular, biopolymers form molecular capsules by intra- molecular hydrogen bonding. For example, starch may incorporate metals or metal oxide, thus forming polymeric NCs [34]. Nanomaterials can be incorporated in biopolymers by both sorption and impregnation [36]. The most omnipresent polysaccharide family includes cellulose, chitosan, guargum, and starch [7,37,38]. Recently, utilization of cellulose has become significant in the green synthesis of nanomaterials and nanocomposites (NCs) and is one of the most favorable nanomaterials in wastewater treatment [19,39].

The significant properties of nanocellulose such as nanoscale size, biodegradability, powerful reinforcement, high aspect ratio, lightness and sustainability have driven widespread interests. Also, nanocellulose is categorized as a non-toxic, fully biodegradable material, which has no adverse effects on the environment [40]. Cellulose nanofibers (CNFs) exhibit a significant

association with the variety of functional groups due to the existence of hydroxyl group on their surface, as the hydroxyl group promotes functionalization. The functional groups can facilitate the precursors to adhere to the metal or metal oxide NPs. The HNCs of cellulose have proven to be efficient catalysts for various conversion, including oxidation, reduction, coupling and photocatalysis [33,41–43].

In this context, this study aims to synthesize the bimetallic Pt-Co and Ag-Co NPs supported on CNFs via the impregnation of the precursor salts on the support with simultaneous reduction, and explore their application in catalysis. The employment of CNFs as support could overcome the major issue of agglomeration of Pt-Co and Ag-Co NPs and might provide enhanced stability along with easy recovery of the catalyst. Also, the synthesis of bimetallic Pt-Co and Ag-Co NPs reduces the amount of Pt and Ag to be used and hence offers an economic catalyst. The electrospinning technique is beneficial to synthesize CNFs from cellulose acetate (CA). Electrospun nanofibers (NFs) have shown outstanding characteristics, such as high surface area, enhanced porosity and adsorption capacity, along with wide surface functionalization possibilities [44]. These CNFs act as the host for the fabrication of Pt-Co and Ag-Co NPs via wet impregnation method and limit the growth of the NPs up to the desired range. Furthermore, the catalytic performance of the as-produced NCs was studied for the reduction of 4-NP to 4-AP to explore their potential application in the field of catalysis and water remediation. CNFs provide a large surface area for the effective dispersion of the bimetallic Pt-Co and Ag-Co NPs and offer stable active sites during the catalytic process. This causes 4-NP molecules to absorb the electrons quickly. Besides, the excellent stability of Pt-Co and Ag-Co/CNF HNCs against agglomeration and sintering makes them reusable nanocatalysts for the reduction of nitrophenols.

4.2 Materials and methods

4.2.1 Chemicals

The reagents of analytical grade were used as obtained from the commercial suppliers. The silver nitrate ($AgNO_3$) (≥99 %), and cobalt nitrate ($Co(NO_3)_2$), were purchased from S.D. Fine Chemicals Ltd, India. The Indian Platinum Pvt. Ltd, India has provided hydrogen hexachloroplatinate (IV) (H_2PtCl_6). Polyvinylpyrrolidone (PVP, 11.5-12.8 %) $(C_6H_9NO)_n$ was obtained from Hi-Media laboratory Pvt. Ltd. and sodium borohydride ($NaBH_4$, 97 %) was received from Molychem. Acetone, dimethylacetamide (DMA), cellulose acetate (CA), sodium

hydroxide (NaOH), and 4-nitrophenol (4-NP, $C_6H_5NO_3$) (≥ 99 %) were received from Thermo Fisher Scientific Ltd., India.

4.2.2 Synthesis of cellulose nanofibers via electrospinning

The electrospun cellulose fibers were obtained based on the procedure reported earlier with slight modifications [44]. The mixed solvent comprised of DMA and acetone (2:1, v/v) was prepared, to which an appropriate amount of CA powder was dissolved under vigorous stirring to obtain a uniform colorless CA solution (16 % w/v). Electrospinning was performed at room temperature with a potential of 10 kV. A glass syringe (5 mL) was used to supply CA solution and was connected to a syringe pump to maintain a constant flow rate (0.6 mL/h) of CA solution for the spinning of polymer. The distance between the nozzle tip and the fiber collection barrel coated with an aluminum sheet was 13 cm. The rotation speed of the drum was 450 rpm. The electrospinning was performed for 4 h. The cellulose acetate nanofibers (CANFs) were then collected and treated with 0.05 M NaOH solution in ethanol for 2 h using mechanical stirring to regenerate CANFs into pure CNFs. The obtained CNFs were then washed with deionized water several times until the solution's pH was neutral. Then, CNFs were dried and stored for further use and analysis in a Petri dish sealed with Parafilm®.

4.2.3 Preparation of Pt-Co/CNF and Ag-Co/CNF NCs

The CNFs supported bimetallic Pt-Co and Ag-Co NCs were obtained by the ultrasound-assisted wet impregnation technique. At first, dispersion of CNF (0.02 g) in deionized water (25 mL) was made using ultrasonic irradiation (probe sonicator, 20 kHz, 20 mm tip diameter, 220 W, a pulse of 2 sec on and 2 sec off, Dakshin ultrasonicator, Mumbai, India) for 10 min. Then, for synthesis of Pt-Co/CNF NCs, H_2PtCl_6 (0.1 g), $Co(NO_3)_2.6H_2O$ (0.1 g) and PVP (0.005 g) were dissolved with vigorous stirring into the CNF dispersion (25 mL). Once the salts were dissolved completely, the ultrasound-assisted chemical co-reduction was carried out by the dropwise addition of 10 mL of $NaBH_4$ solution to the metal precursor solution in the presence of ultrasonic irradiation. The obtained black precipitate was then separated and washed with deionized water using centrifugation followed by drying to obtain the Pt-Co/CNF NCs. In a similar approach, Ag-Co NPs supported on CNFs were prepared using 0.1 g $AgNO_3$ in place of H_2PtCl_6. The schematic for the synthesis of Pt-Co/CNF and Ag-Co/CNF NCs is shown in Figure 4.1.

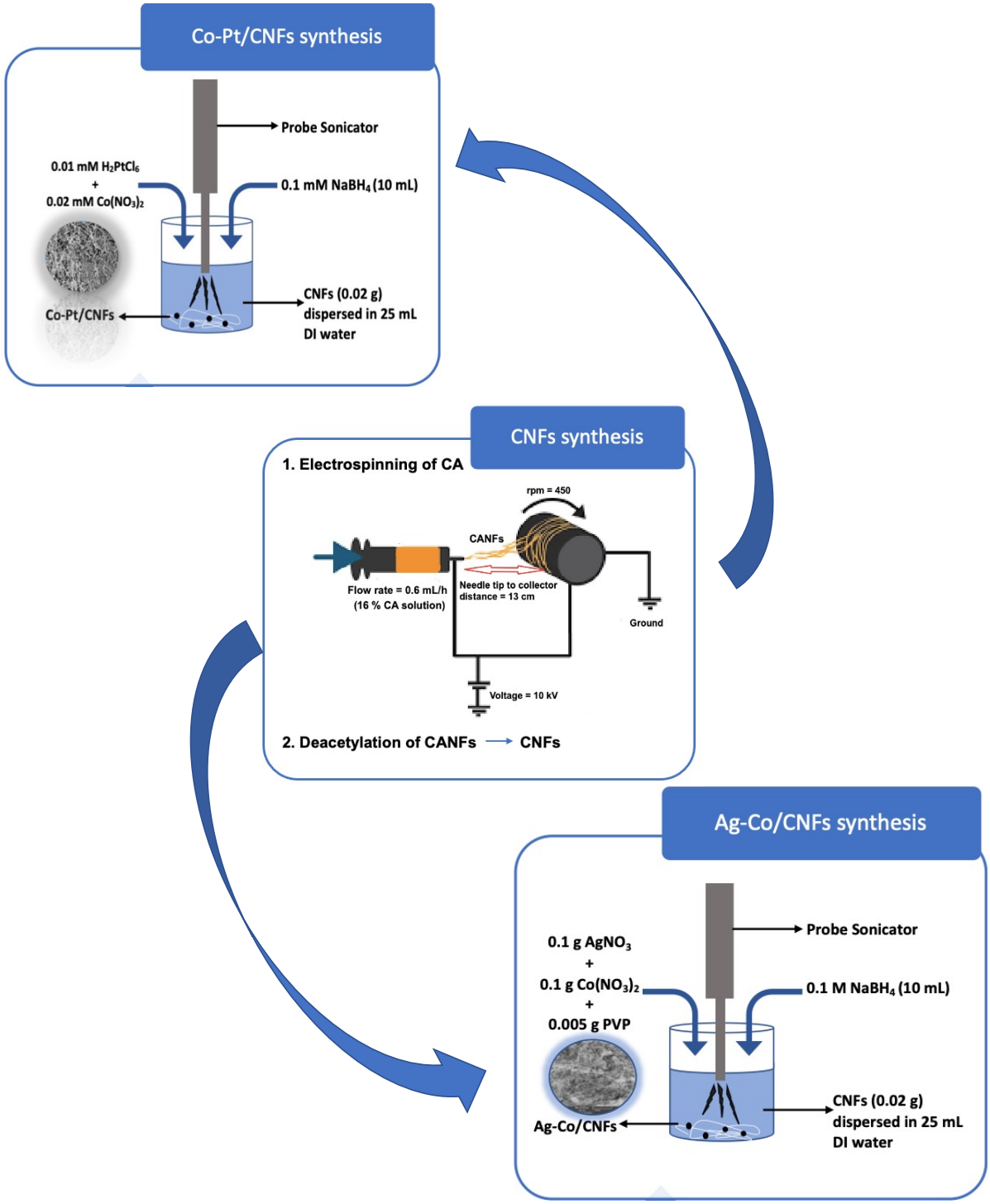

Figure 4.1 Schematic representation for synthesis of CNF and ultrasound assisted synthesis of Pt-Co/CNFs and Ag-Co/CNF NCs.

4.2.4 Characterization of the nanocomposite catalysts

The crystalline structure and phase-detection of the prepared NCs were carried out by X-ray diffraction (XRD) analysis executed on powder X-ray diffractometer (XRD, Bruker D8

Advance, Germany), using Cu K_α radiation (1.5406 Å) and was scanned between 10° and 90°. Fourier Transform Infra-Red (FTIR) spectroscopy was utilized to characterize the chemical changes of the samples and examine the functional groups. A Bruker-ALPHA II FTIR instrument was used to acquire the spectra with a 4 cm^{-1} resolution between 4000 cm^{-1} and 400 cm^{-1}. The microstructure and surface morphology of Pt-Co/CNF and Ag-Co/CNF NCs were observed using a scanning electron microscope (SEM; SEM-TESCAN-Vega 3 LMU, Fuveau, France). The fiber mat sample was obtained by cutting a small portion of it and was coated with gold using sputter coating. Energy-dispersive X-ray spectroscopy (EDX) and element dot mapping were obtained on an energy dispersive spectrometer with SEM-TESCAN-Vega 3 LMU electron microscope. The Carl Zeiss, EVO MA 15 (Oxford Instruments) field emission scanning electron microscope (FE-SEM) equipped with energy dispersive X-ray spectroscope was employed to determine the elemental composition and distribution of Pt and Co metals over CNF through EDX and elemental dot mapping analysis for Pt-Co/CNF NC catalyst. The Brunauer−Emmett−Teller (BET) surface area and pore size distribution of the Pt-Co/CNF and Ag-Co/CNF NCs were evaluated using the nitrogen adsorption-desorption isotherm with a Micromeritics ASAP 2020 automatic BET analyzer. The degassing/drying was done with cryofixing of nanocomposites in LN_2 (cryo-LN_2). The liquid propane (LPGS) was prepared by liquefying propane gas using LN_2 and cooled until its freezing temperature (-189 ºC) was nearly reached. The sample was placed on a TEM grid (300 mesh) and immediately plunged in LN_2 (approximately -196 ºC) or in LPGS. The cryofixed samples were placed on a LN_2 cooled metal plate and dried in a freeze drier at -50 ºC under vacuum overnight. The dried samples were kept in a desiccator until the BET-analysis was carried out. The extent of 4-NP reduction was examined spectrophotometrically at 400 nm using UV-vis spectrophotometer (UV-3600 plus Shimadzu UV-Vis Spectrophotometer).

4.2.5 Evaluation of the catalytic performance and stability of Pt-Co/CNF and Ag-Co/CNF NCs for the reduction of 4-NP

The catalytic performance of as-prepared Pt-Co/CNF and Ag-Co/CNF NCs was analyzed for the catalytic reduction of 4-NP. Initially, 0.1 mM aqueous 4-NP solution (3 mL) with perceptible light-yellow color was introduced to the quartz cuvette. Then, freshly prepared 0.2 M $NaBH_4$ (0.3 mL) was mixed with the 4-NP solution under stirring. This resulted in a color change of the reaction mixture from pale yellow to bright yellow, attributed to the formation of a 4-nitrophenolate anion. The reduction reaction was then triggered by the addition of 1 mg

catalyst (Pt-Co/CNF or Ag-Co/CNF). The UV-visible absorption spectra were used to analyze the reaction progress. At regular intervals of time, the absorption spectra of the reaction mixture were recorded using a UV-Vis spectrometer in the range of 250-600 nm. During the progress of the reaction, a large amount of H_2 gas was evolved, and the bright-yellow color of the solution was kept fading. Finally, it became colorless, indicating the generation of 4-AP. This reduction reaction was examined by tracking the characteristic peak of 4-NP at 400 nm, which disappears as the reaction continues and the distinct peak of 4-AP emerges at 300 nm.

The percentage conversion of 4-NP using the as-synthesized NCs was estimated using the following Eq. (4.1).

$$\%\ conversion = ((C_0 - C_t)/C_0) * 100 = ((A_0 - A_t)/A_0) * 100 \quad \text{(Eq. 4.1)}$$

Where C_0 is the initial concentration of 4-NP (mg/L), and C_t is the concentration of 4-NP in the reaction mixture (mg/L) at different times (t), and A_t is the absorbance at time t, and absorbance at time t=0 is A_0. Further, to evaluate the reusability and stability of the catalyst, it was recovered from the reaction mixture using centrifugation and recycled for five successive tests. Before recycling, deionized water wash was given to the recovered catalyst, followed by drying.

4.3 Results and discussion

At present, researchers are focusing on the evaluation of different models of the NPs such as alloys, core-shell, contact aggregates, and thin films [45,46]. Recent reports have shown that the BNPs show enhanced catalytic, electronic, magnetic, and optical properties leading to a wide range of applications in catalysis owing to the bi-metallization which may not be attainable with monometallic catalysts [20,22,31,47]. Generally, two major procedures are described in the synthesis of BNPs. In one method the BNP synthesis can be achieved by seed-mediated reduction and generation. In the second type, the BNPs can be synthesized by simultaneous reduction and stabilization. In this regard, herein the Pt-Co and Ag-Co BNPs were prepared via simultaneous reduction and stabilization over CNF in the presence of acoustic cavitation. The successful synthesis of proposed NCs was further characterized by nanomaterial characterization techniques as discussed below.

4.3.1 Catalyst characterization

4.3.1.1 Fourier transform infrared spectroscopy study

Infrared spectroscopy provides a relatively simple method to obtain direct information about the chemical changes occurring during chemical processing. Besides, FTIR analysis was performed to examine the existence of various functional groups attached to the samples. FTIR spectra of CANFs, CNFs, Pt-Co/CNFs and Ag-Co/CNFs are presented in Figure 4.2. CANF shows two distinct FTIR peaks at 1747 and 1230 cm^{-1}, corresponding to C=O stretching and –COO vibrations of the acetyl group, respectively [48]. These two peaks disappear in the spectra of CNFs. In contrast, the emergence of peaks at 3331.4 and 2902.2 cm^{-1} were observed for the -OH group stretching and aliphatic CH stretching, respectively, suggesting the successful elimination of the acetate group. It was observed that the band near 3331.4 cm^{-1} is tapered and showed high intensity for CNF, demonstrating that it contains more -OH groups than CANF. The presence of these peaks indicates that the fraction of cellulosic constituents increases after the removal of non-cellulosic materials through chemical treatment. The differences observed in the spectra of CANF and CNF confirm the completion of deacetylation. The vibration peaks noticed at 1628.8 cm^{-1}, and 1364.5 cm^{-1} for CNFs, Pt-Co/CNFs and Ag-Co/CNFs can be assigned to O-H bending vibration of the adsorbed water [48]. Also, the peak at 1025 cm^{-1} corresponds to asymmetric C-O-C stretching vibration in the cellulose chain at the –glycosidic linkage, which is present in CANF, CNFs, Pt-Co/CNFs and Ag-Co/CNFs as well [49]. The Pt-Co/CNFs and Ag-Co/CNFs catalyst exhibited similar FTIR spectra as that of CNF regarding the characteristic peaks attributed to cellulose, signifying that CNF retains its original nature despite the binding of Ag-Co and Pt-Co NPs on its surface. These results conclude the successful synthesis of CNF using electrospinning and anchoring of bimetallic Pt-Co and Ag-Co NPs over CNF through wet impregnation.

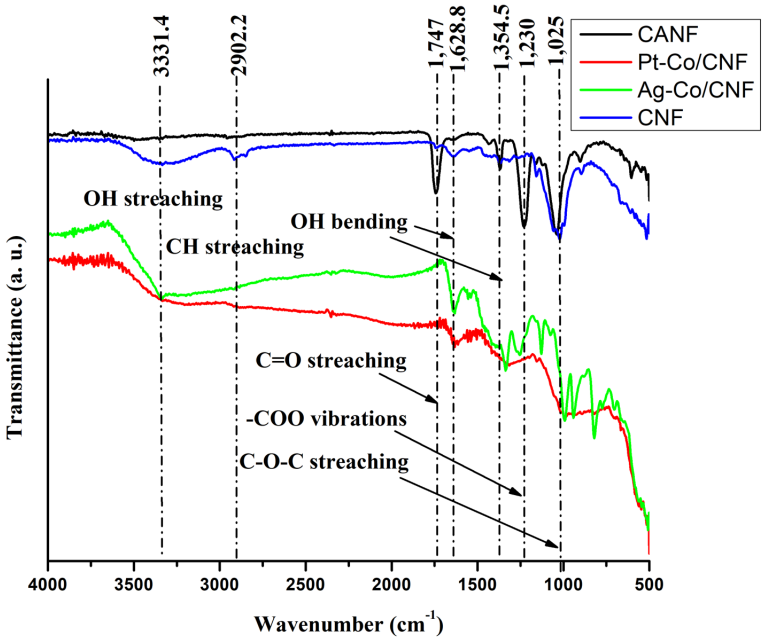

Figure 4.2 FTIR spectrum for CANFs, CNFs, Pt-Co/CNFs and Ag-Co/CNFs NCs.

4.3.1.2 X-ray diffraction study

The XRD analysis was executed to confirm the crystallinity index (CI) of as-prepared CNF and crystalline nature of synthesized Pt-Co/CNF and Ag-Co/CNF NCs. Figure 4.3 reveals the XRD diffractogram for CANF, CNF, Pt-Co/CNF and Ag-Co/CNF NCs respectively. The CANF shows amorphous nature as the characteristic peak for (002) plane present at 21.3° was found to be frail in the X-ray diffractogram of CANF (Figure 4.3A). Whereas, the distinctive peak related to (002) plane for crystalline phase of cellulose was revealed in the XRD pattern of CNF (Figure 4.3B) at 2θ around 21.54° [41]. In addition, the Segal equation was used to calculate the CI for CANF and CNF and is estimated to be 18.25 % for CANF, and 56.23 % in case of CNF respectively. This increase in CI can be justified by the presence of intense peaks in XRD diffractogram of CNF than CANF. This enhancement in CI is due to the breakage of acetate group during the deacetylation of CANF takes place first in the amorphous region. This is because the amorphous zone of cellulose chains is prone to the degradation due to chemical or enzymatic reactions than the crystalline zone [19]. On account of this, enhanced crystallinity was noticed in the CNF structure.

After interaction with $AgNO_3$ and $Co(NO_3)_2$ and reduction with $NaBH_4$, the diffraction peaks appeared at 2θ values of 32.03°, 38.27°, 44.41°, 64.57°, 77.39° and 81.62°, were attributed to (122), (111), (200), (220), (311), and (222) planes of the FCC structure of crystalline Ag (JCPDS card no. 04-0783), as exhibited in Figure 4.3C [50]. Whereas in the Ag-Co/CNF

composite, very weak diffraction peaks for Co are present at 44.41° and 48.04°, which represent (002) and (101) facets of the FCC structure of Co as per the JCPDS No. 05-0727 (Figure 4.3C) [51]. In the XRD diffraction patterns of Ag-Co/CNF NC, the presence of sharp and dominant peaks related to the FCC structure of crystalline Ag suggests that in the synthesized Ag-Co/CNF NC, Ag dominates the crystalline structure of the NC over Co. Moreover, a small hump at 2θ =22.49° related to the (200) reflection of CNFs was not seen for the NC, which may be due to the presence of highly intense metal peaks over CNFs [19].

Further, as displayed in Figure 4.3D, the newly emerged diffraction peaks present at 40.72°, 46.54°, 72.36°, and 82.03° suggests the formation of Pt-Co NPs on cellulose surface due to the reduction of $Co(NO_3)_2.6H_2O$ and H_2PtCl_6 with ultrasound assistance using $NaBH_4$ in presence of CNF. These peaks represent the characteristic Bragg's peaks for the crystalline Pt with the (111), (200), (220), and (311) planes for its FCC structure (JCPDS card no. 04-0802) [52], while the weak peaks at 40.09° and 45.66° can be indexed to (100) and (002) facets of Co (JCPDS No. 05-0727) [51]. In case of Pt-Co/CNF NC, the slight shift in the diffraction peaks for Pt towards higher angles was observed as compared to the standard diffraction peaks for Pt as per JCPDS card no. 04-0802 [53]. This signifies the alloy formation among Co and Pt with the lattice contraction in the FCC structure of Pt and is in line with the Vegard's law [54]. Furthermore, in XRD of Pt- Co/CNF at 2Θ = 22.49° a small hump was noticed related to the (200) plane of CNF. This is due to the presence of high intensity peaks for Pt-Co over CNF [19].

As can be deduced from Figure 4.3C and D, governing peaks for Co were not seen in XRD pattern for both Pt-Co/CNF and Ag-Co/CNF NCs. According to Baye et al. [13], the dominant peaks of Co are not seen owing to the amorphous nature of Co NPs obtained from Co^{2+} in $NaBH_4$. In comparison, Poglani et al. [55] indicated that the Co diffraction peaks might not be dominant due to alloy formation with noble metal which is in accordance with Vegard's law. This justifies the presence of weak diffraction peaks of Co in both the synthesized NCs.

In addition, the average grain size of Ag-Co/CNF and Pt-Co/CNF NCs was computed using the well-known Scherrer's equation $D = k.\lambda/\beta.\cos\theta$, where k is the shape factor (0.9), λ is the X-ray wavelength (1.5406 Å), θ is the peak position, and β refers to the full width at half maximum (FWHM) of the strongest peak. The calculated average crystallite size of 14.64 nm and 20.05 nm were obtained for Ag-Co/CNF and Pt-Co/CNF respectively. In case of both the NCs, the presence of sharp and dominant peaks related to the FCC structure of crystalline noble

metals (Pt and Ag) suggests that in the synthesized Pt-Co/CNF and Ag-Co/CNF NCs, noble metals dominate the crystalline structure of the NCs over Co. Thus, XRD analysis confirms the fabrication of crystalline Ag-Co/CNF and Pt-Co/CNF NCs.

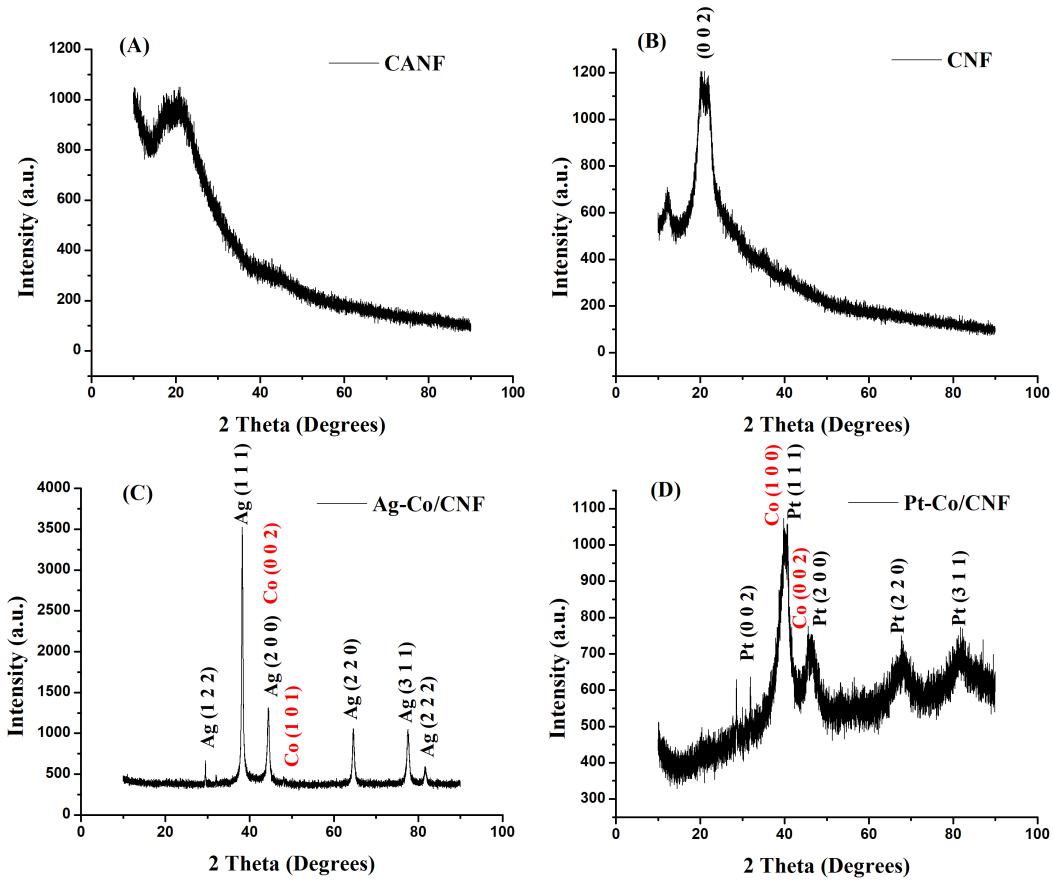

Figure 4.3 XRD pattern for (A) CANF, (B) CNF, (C) Ag-Co/CNF, and (D) Pt-Co/CNF.

4.3.1.3 Morphological Study

The morphological investigation of the Pt-Co/CNF NC was performed with SEM and FESEM and for Ag-Co/CNF it was done with SEM-EDX respectively. The SEM and FESEM images are presented in Figure 4.4 for Pt-Co/CNF and Ag-Co/CNF NCs. The uniform deposition of both the Pt-Co and Ag-Co NPs with spherical morphology on the fibrous structure of CNF is clearly seen in the SEM and FESEM micrographs. In addition to morphological studies, the elemental composition of Pt-Co/CNF and Ag-Co/CNF NCs was recorded with EDX spectra [Figure 4.5 and Table 4.1] and the nature of metals (Pt, Co and Ag) distribution over CNF surface was analyzed using EDX-elemental dot maps [Figure 4.6]. The EDX spectrum further confirms the existence of Pt, Ag, and Co along with C and O of cellulose in the as-produced

Pt-Co/CNF and Ag-Co/CNF NCs as shown in Figure 4.5. Through the elemental dot mapping demonstrated in Figure 4.6, the uniformly distributed Co, Ag, and Pt NPs over the CNF surface were clearly visible. This suggests the uniform immobilization of spherical Pt-Co NPs over CNF matrix with the particle size of about 20 nm which is in agreement with XRD results.

Table 4.1 Elemental composition of Pt-Co/CNF NC catalyst on weight basis.

Elemental composition	Pt (wt%)	Co (wt%)	O (wt%)	C (wt%)
Theoretical	20	20	30	30
FESEM-EDX	16.93	22.04	19.27	41.76

Table 4.2 Elemental composition of Ag-Co/CNF NC catalyst on weight basis.

Elemental composition	Ag (wt%)	Co (wt%)	O (wt%)	C (wt%)
Theoretical	20	20	30	30
SEM-EDX	21.48	18.03	22.27	38.22

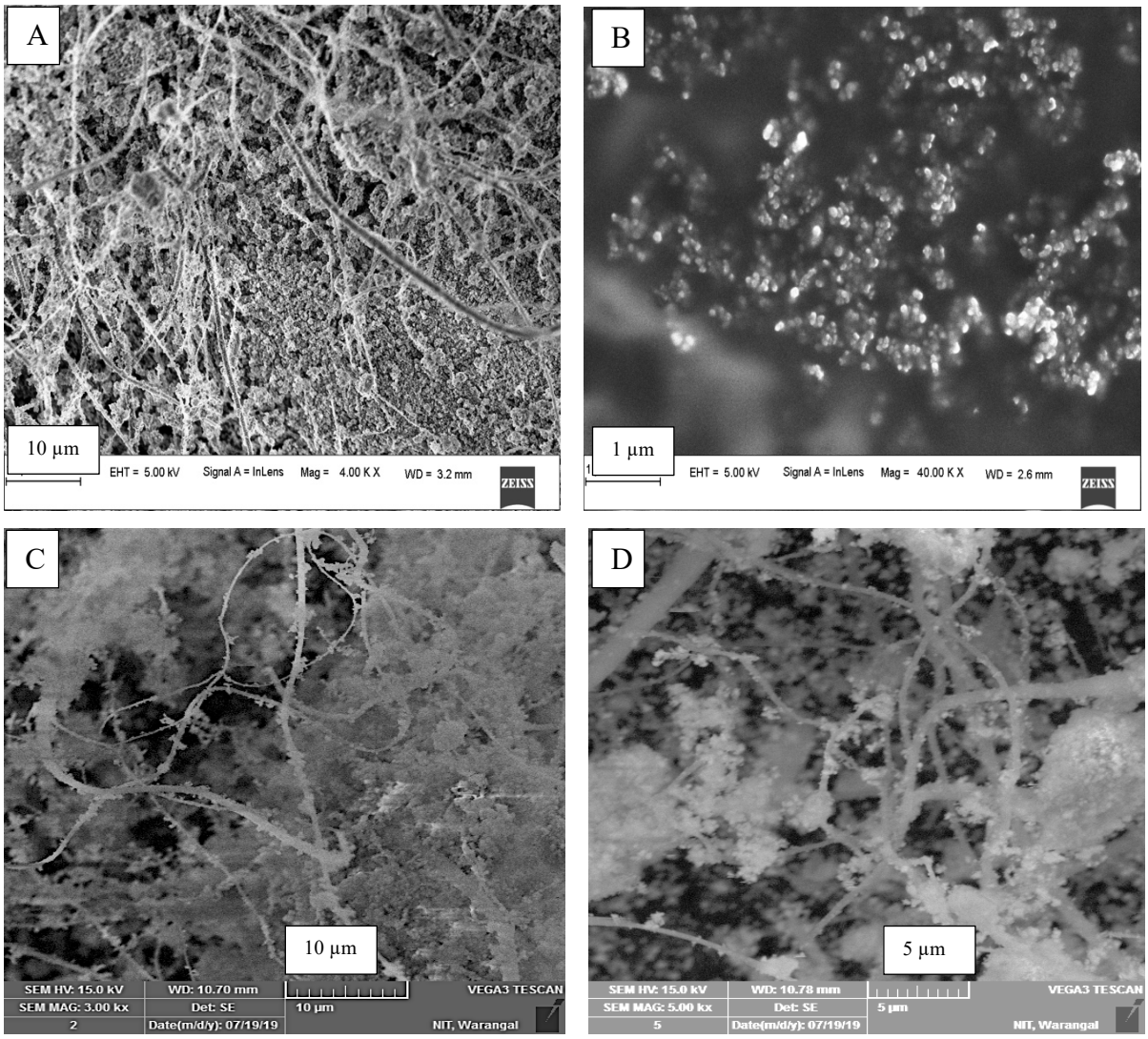

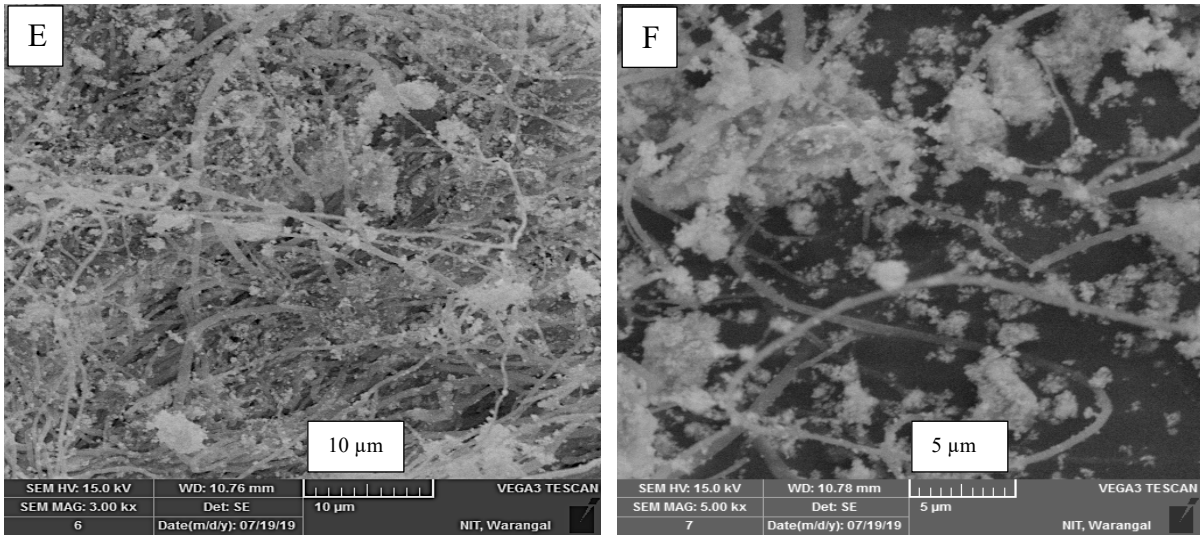

Figure 4.4 FESEM micrograph for Pt-Co/CNFs at (A) 10 µm, and (B) 1 µm scale bars; SEM micrographs for Pt-Co/CNFs at (C) 10 µm, and (D) 5 µm scale bars; SEM micrographs for Ag-Co/CNFs at (E) 10 µm, and (F) 5 µm scale bars.

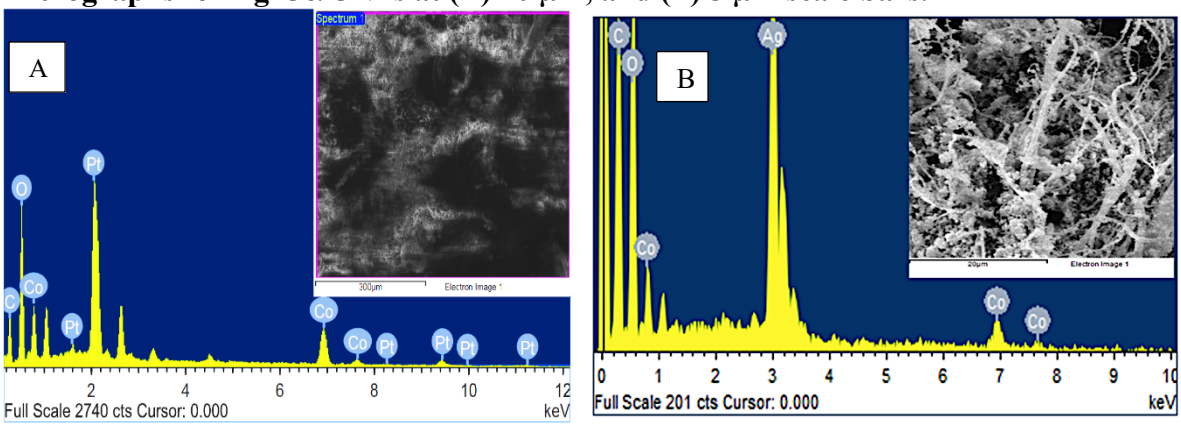

Figure 4.5 (A) FESEM-EDX of Pt-Co/CNF NC; (B) SEM-EDX of Ag-Co/CNF.

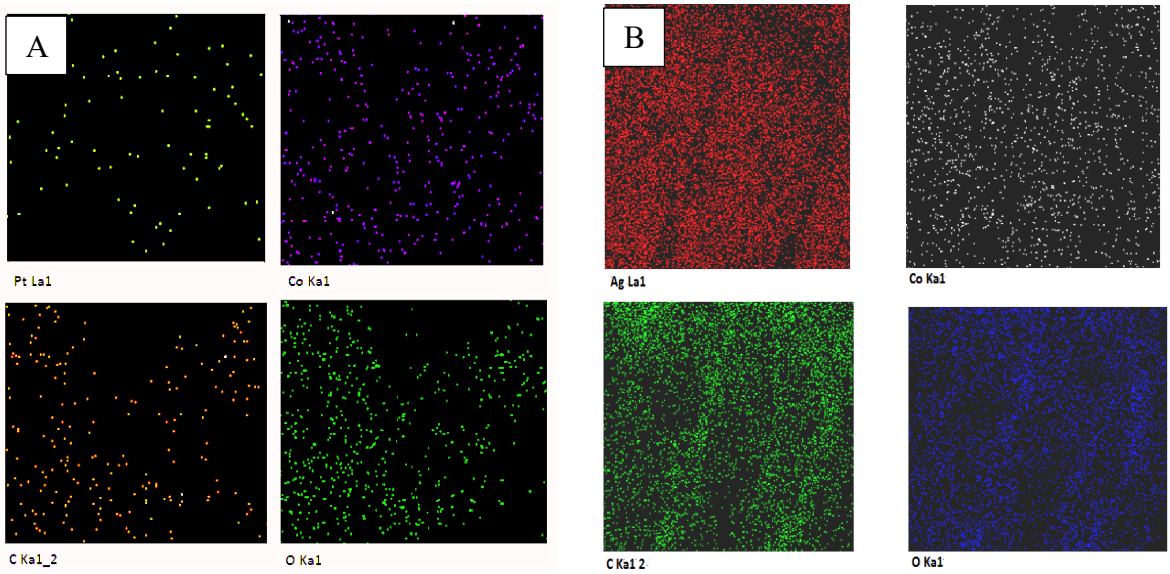

Figure 4.6 (A) FESEM-Elemental dot mapping for Pt-Co/CNF NC; (B) SEM- Elemental dot mapping for Ag-Co/CNF NC.

4.3.1.4 BET surface area measurements

Further, the BET surface area of the as-prepared Pt-Co/CNF and Ag-Co/CNF catalyst was evaluated from the BET isotherm linear plot determined at −196 °C (Figure 4.7). The BET surface area, pore volume, and average pore diameter of Ag-Co/CNF NC were 42.2 m^2/g, 0.023 cm^3/g, and 2.05 nm, respectively. While for Pt-Co/CNF NC, the BET surface area, pore volume, and average pore diameter of were found to be 53.16 m^2/g, 0.031 cm^3/g, and 2.15 nm, respectively.

Based on the above discussion it can be postulated that, the proposed ultrasound assisted simultaneous reduction of Pt, Co and Ag, Co precursors can successfully prepare uniform sized, spherical alloys of Pt-Co NPs and Ag-Co NPs and evenly anchor them onto CNF surface with wet impregnation in presence of acoustic cavitation at atmospheric conditions.

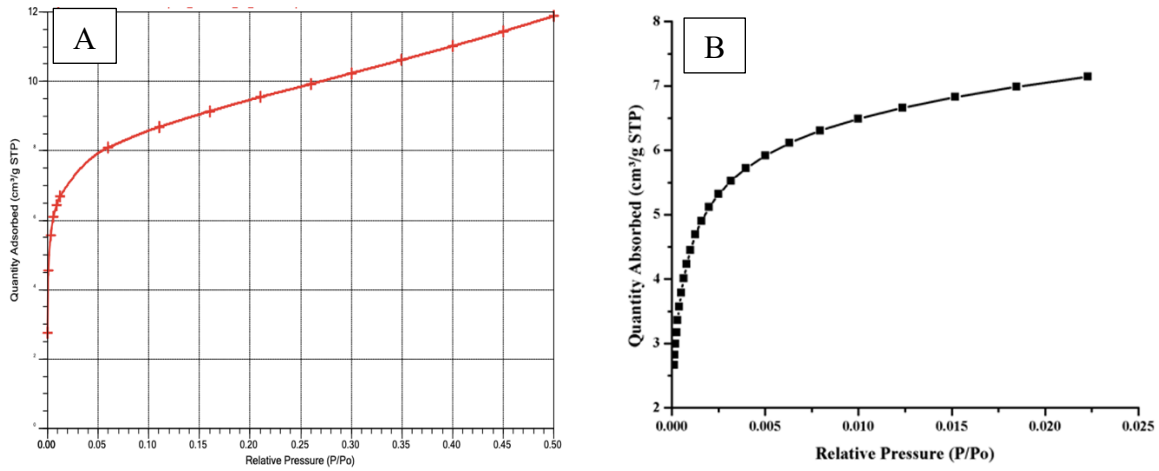

Figure 4.7 BET isotherm linear plot for (A) Pt-Co/CNF and (B) Ag-Co/CNF NCs.

4.3.2 Catalytic performance of Pt-Co/CNFs and Ag-Co/CNFs NCs for 4-NP reduction

The 4-NP reduction with $NaBH_4$ was conducted to assess the catalytic activity of the fabricated Pt-Co/CNF and Ag-Co/CNF NCs. The reduction of 4-NP was performed in a quartz cuvette. For this aqueous solution of 0.1 mM 4-NP (3 mL) along with 0.2 M $NaBH_4$ (0.3 mL) was added in the quartz cuvette with subsequent addition of 1 mg of NC catalyst (Pt- Co/CNF or Ag-Co/CNF) to set off the reaction. The reaction progress was analyzed with the help of UV-visible spectra of reaction samples measured at regular time intervals. The red shift in the characteristic peak for 4-NP was detected from 317 nm to 400 nm as a result of ionization induced by the addition of $NaBH_4$. As shown in Figure 4.8 the recorded absorbance of samples was plotted against reaction time. As the reaction time progresses, the characteristic peak present at 400

nm gradually declines and induces the appearance of a new peak at 300 nm which represents the characteristic peak for 4-AP. At the same time the change in color of reaction mixture from light yellow to colorless was perceived indicating the reduction of 4-NP to 4-AP. It can be inferred from Figure 4.8A that, with Pt-Co/CNF NC catalyst the peak representing 4-NP almost completely disappears after 98 s of reaction time and a dominant peak for 4-AP was emerged while. This implies that, the 4-NP was almost totally reduced to 4-AP within 98 s of reaction time in presence of Pt-Co/CNF catalyst (Figure 4.8A) whereas with Ag-Co/CNF the complete reduction of 4-NP took place in 110 s (Figure 4.8B).

The reaction was also conducted without a catalyst. It was witnessed that the lack of catalyst does not favor this reaction. As, even after hours, no change was noticed in the absorption spectra of the reaction mixture. This indicates that, without catalyst the reduction reaction of 4-NP with only $NaBH_4$ cannot occur. In the absence of the catalyst, the electrostatic repulsion between the negatively charged 4-NP and BH_4^- ions [13] and the significant potential energy gap between BH_4^- and the acceptor nitro (NO_2) groups make the reduction process less feasible, though, it is thermodynamically possible [38]. Further, the reaction was carried out in the presence of only CNFs under similar reaction conditions to assess the catalytic ability of the CNFs. No significant variation in the absorbance spectrum of 4-NP at 400 nm was noticed, signifying that the CNFs do not possess any catalytic activity to reduce 4-NP. Torkamani and Azizian have also investigated the catalytic performance of cellulose, and Ag NPs deposited on cellulose to reduce 4-NP. They have also reported that the cellulose does not favor this reaction [56]. In contrast, when the reaction was carried out with Ag NPs deposited on cellulose, 4-NP was reduced completely within 6 min with an apparent rate constant of 0.0008 s^{-1}. While, as mentioned earlier, 4-NP reduced completely within only about 110 s in the presence of proposed Ag-Co/CNF catalyst.

Lv et al. have assessed the catalytic activity of Pt NPs to reduce the 4-NP with $NaBH_4$. They have obtained the reduction of 4-NP with K_{app}= 0.0007 s^{-1} after 58 min of reaction time [57]. While, Mondal et al. examined the catalytic performance of Co NPs for 4-NP reduction with $NaBH_4$. They have reported that, around 90 % of 4-NP degradation was obtained within 8 min Co NPs were used as catalyst [58]. Whereas, in present study the 4-NP reduction using as-produced Pt-Co/CNFs catalyst was almost completed in around 98 s. The aforementioned results signifies that the alloying of Co with Pt and Ag has greatly enhanced the catalytic activity of the Pt-Co/CNF and Ag-Co/CNF NCs on account of the synergy developed in Pt-Co, and Ag-Co bimetallic alloys.

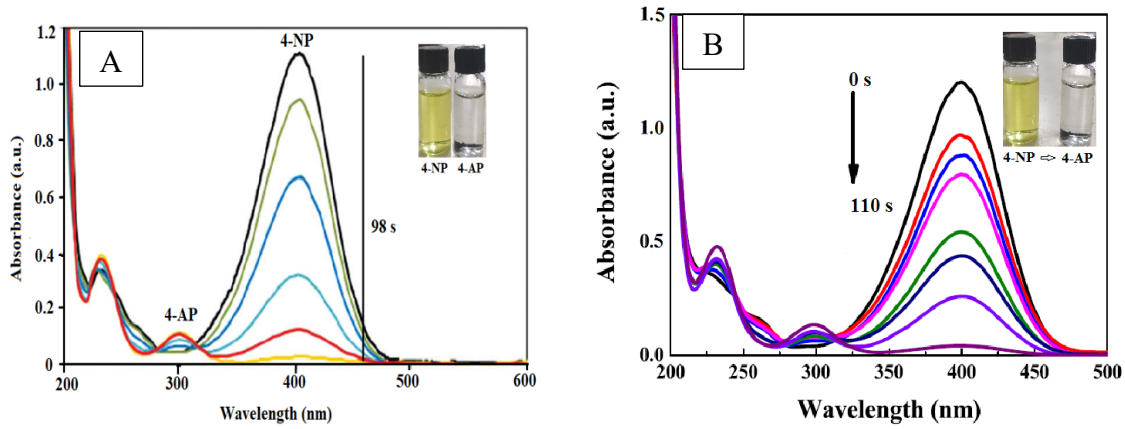

Figure 4.8 Time-dependent UV-vis spectra depicting the reduction of 4-NP using (A) Ag-Co/CNF, and (B) Ag-Co/CNF NC catalysts.

4.3.2.1 Study on the kinetics of 4-NP reduction reaction

Apart from monitoring the progress of the reaction, UV-vis spectroscopic investigation is also beneficial in the experimental calculation of rate constants. Considering that $NaBH_4$ is used in excess, several times the concentration of 4-NP, it is supposed that the rate of reduction is independent of the reductant concentration. For this transformation reaction, pseudo-first-order reaction kinetics was assumed based on the 4-NP concentration [20].

The kinetic equation for the reduction can be written, as shown in Eq. (4.2) or (4.3). Upon integrating Eq. (4.2), the apparent rate constant (K_{app}) is determined, where the absorbance at time t is A_t, and at time $t=0$ *is* A_0 which is directly proportional to its concentration in the solution.

$$-{}^{dC}/_{dt} = K_{app}C_t \qquad \text{(Eq. 4.2)}$$

$$\ln(C_t/C_0) = \ln(A_t/A_0) = -K_{app}\,t \qquad \text{(Eq. 4.3)}$$

Figure 4.9 depicts the kinetic studies of the catalytic reduction of 4-NP using Pt-Co/CNF and Ag-Co/CNF NCs as the catalyst. The obtained K_{app} for Pt-Co/CNF is 0.0286 s^{-1}, and for Ag-Co/CNF it is 0.0172 s^{-1} in reducing 4-NP revealing a high potential of the proposed NC catalysts to catalyze the desired reduction reaction. The K_{app} obtained is much superior in comparison with Pd@cellulose (0.0057 s^{-1}) [59], Ag@nanocellulose (0.00325 s^{-1}) [8], Ag-Ag_2S (0.0105 s^{-1}) [19], Pt–Au dendrites/rGO (0.0038 s^{-1}) [57], nitrogen and phosphorus co-doped carbon (0.00065 s^{-1}) [7], Fe_3O_4/Ag@Ca−AlLDH@starch (0.0076 s^{-1}) [38], $NiWO_4$-ZnO-NRGO

(0.024 s^{-1}) [60]. This signifies the superior catalytic performance of the synthesized NCs over the reported catalysts.

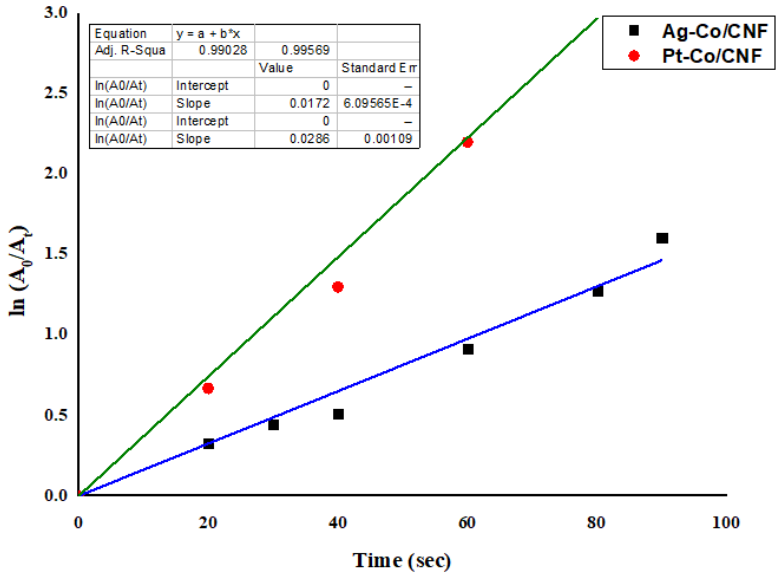

Figure 4.9 Graph of reaction kinetics for 4-NP reduction using Pt-Co/CNF, and Ag-Co/CNF NC catalyst.

Table 4.1 differentiates the catalytic performance of the presented NC catalysts with those reported earlier for the 4-NP reduction using $NaBH_4$. Based on the loading of catalyst used, K_{app} and reaction time required for 4-NP reduction, the catalysts studied in this work have presented high activity in comparison with those reported earlier. This can be due to the swift electron transfer over the catalyst surface and the high electronic conductivity of the metal alloys (Pt-Co, and Ag-Co) causes the rapid electron transfer.

As depicted in Table 4.1 the Pt-Co/CNF offers superior activity over reported catalysts (except $BaWO_4$/NRGO-g-C_3N_4) including Ag-Co/CNF presented in this work. This is because the enhancement occurred in the electronic properties of the proposed metal alloys (Pt-Co and Ag-Co) after alloying due to the mixing of electronegativities of the constituent active metals and promoter Co. As, the active metals used herein and the promoter have different electronegativities [Ag (1.93), Pt (2.28), and Co (1.88)], which may cause electrons to be transferred from promoter to active metal, leading to partial separation of charge onto the alloy surface. As a result of this, the enhancement in catalytic activity of presented Pt-Co/CNF and Ag-Co/CNF NCs was detected, since it may have not only increased the interaction of substrate with catalyst surface but also increases the interaction of catalyst with hydrogen molecules. The promising aspects such as high surface area, improved metal NP dispersion on cellulose

matrix and availability of ample amount of OH group over CNF offered by the Pt-Co/CNF and Ag-Co/CNF NCs makes them a potential option for the reduction of variety of nitro phenols.

Table 4.3 Differentiation in the activities of various catalysts used for the 4-NP reduction.

Catalyst	Catalyst loading (g/L)	$NaBH_4$		4-NP (mM)		k_{app} (s^{-1})	Reaction time (min)	Ref.
		Concentration (M)	Volume (mL)	Concentration (mM)	Volume (mL)			
Ag/zeolite	0.1	0.25	25	2.5	25	-	2.67	[61]
Co_3O_4	1	0.408	0.145	3.59	0.101	0.0115	5.5	[62]
Ag-Ag_2S	1.82	0.2	0.3	0.1	3	0.0105	10	[19]
$BaWO_4$/NRGO-g-C_3N_4	0.17	0.1	0.3	0.1	2.7	0.1883	1	[63]
NRGO-$FeWO_4$-Fe_3O_4	0.33	0.1	0.3	0.1	2.7	0.04338	0.75	[64]
Pd@Fe_3O_4/chitosan-agar	0.75×10^{-2} mol/L	0.05	1	0.125	1	0.0051	3	[65]
Cu/GO/MnO_2	0.1	0.25	25	2.5	25	-	5	[10]
PtCo NDs/N-rGO	1	0.5	1	0.7	1.5	0.0124	9	[66]
Fe_3O_4@SiO_2-Ag	1.699	0.012	20	0.12	30	0.0077	8	[15]
C@Co	0.222	0.1	0.5	20 ppm	4	0.033	2	[67]
Calcium alginate/Ag	1.200	0.1	2.5	0.1	0.025	-	8	[32]
rGO/CNT/Fe/Ag	0.0704	0.5	0.5	0.12	2	0.01466	6	[9]
Cu_2O-chitosan	0.285	3	0.004	0.1	7	0.0038	5	[37]
NP@C	1	1.5 mmol	-	0.015	-	0.00065	25	[7]
Pt–Au/rGO	0.043	0.5	-	0.7	-	0.0038	10	[57]
Pt black	0.43	0.5	-	0.7	-	0.0007	58	[57]
Co	0.15	2×10^{-5}	10	1×10^{-3}	10	-	8	[58]
Pt-Co/CNF	**0.300**	**0.2**	**0.3**	**0.1**	**3**	**0.0286**	**1.63**	**This work**
Ag-Co/CNF	**0.300**	**0.2**	**0.3**	**0.1**	**3**	**0.0172**	**1.83**	**This work**

Further, in order to investigate reaction mechanism, the kinetics of 4-NP reduction in presence of Pt-Co/CNF and Ag-Co/CNF NC catalysts was studied under diverse catalyst loading conditions, initial concentration of 4-NP, and $NaBH_4$.

4.3.2.2 Effect of catalyst loading on 4-NP reduction

The catalyst loading was changed from 0.5 to 3 mg, and the concentrations of 4-NP [0.1 mM] and $NaBH_4$ [0.2 M] were kept constant to assess the influence of Pt-Co/CNFs and Ag-Co/CNFs NC catalyst's loading on the reduction of 4-NP. Under these reaction conditions, it was observed that, with an increase in catalyst loading from 0.5 to 3 mg, the K_{app} also increases linearly for the reduction of 4-NP (Figure 4.10). This behavior is evident because, as the catalyst loading increases, the number of active sites available for the adsorption of reactants also increases. In addition, the availability of more surface area of the composite nanofibers enables an increase in the mobility of 4-NP. It hence decreases the resistance to phenol diffusion throughout the reduction process. As a result, the reaction kinetics is significantly enhanced, inducing an increase in the reaction rate constant [68]. This suggests that the catalyst loading plays a key role in the reduction of 4-NP.

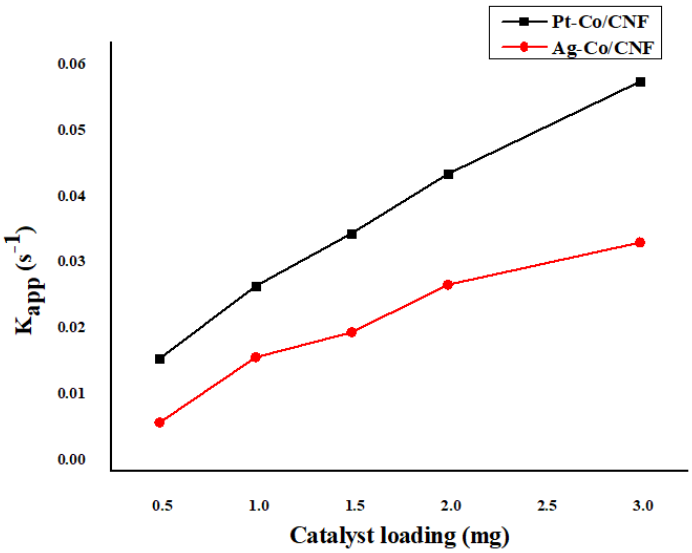

Figure 4.10 Effect of catalyst loading on 4-NP reduction.

4.3.2.3 Effect of initial concentration of 4-NP on reduction reaction

Since, the desired driving force necessary to overcome the resistance to mass transfer of all the molecules among the solid and water phases depends on the initial concentration of 4-NP, the impact of initial concentration of 4-NP on the reduction process was also examined. Figure 4.11 elucidates the effect of the concentration of 4-NP on the reduction process by using a constant concentration of $NaBH_4$ (0.2 M) and a fixed catalyst loading (1 mg). The results indicate that with an increase in the concentration of 4-NP from (0.05 mM to 0.15 mM) in presence of both Pt-Co/CNF and Ag-Co/CNF, the estimated value of K_{app} decreases. This

behavior may occur due to the accumulation of 4-NP molecules on the catalyst surface, resulting in the blocking of the catalyst's active sites [69].

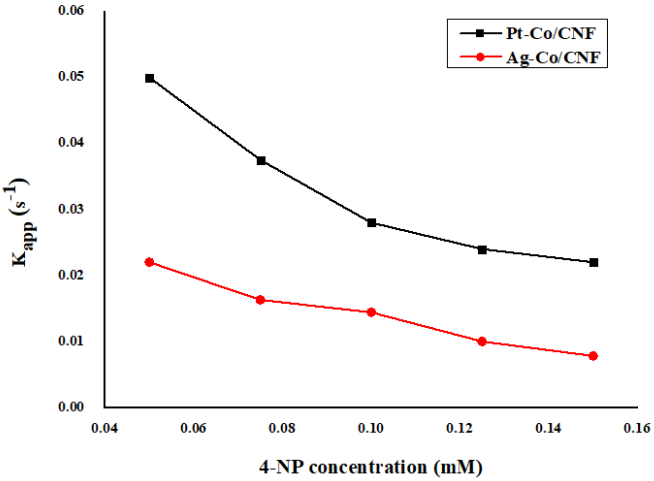

Figure 4.11 Effect of 4-NP concentration on its reduction.

4.3.2.4 Effect of $NaBH_4$ concentration on 4-NP reduction

Further, the 4-NP reduction was also explored by altering the concentration of $NaBH_4$ used (0.15 M - 0.35 M) for the reduction of 4-NP by keeping the 4-NP concentration [0.1 mM] and catalyst loading [1 mg] constant. As displayed in Figure 4.12**,** with increasing concentration of $NaBH_4$, nonlinear increase in K_{app} is observed in presence of both Pt-Co/CNF and Ag-Co/CNF NC catalysts. As the K_{app} values decreases with increase in 4-NP concentration and increases with increasing $NaBH_4$ concentration, the LH mechanism can be suggested for the 4-NP reduction with $NaBH_4$ over Pt-Co/CNF, and Ag-Co/CNF NC catalysts. Also, the nonlinear trend of K_{app} value with the initial 4-NP and $NaBH_4$ concentration implies the existence of competitive adsorption among both the reactants.

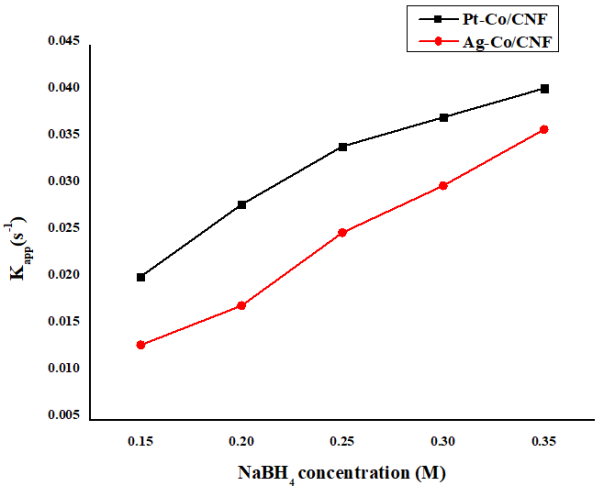

Figure 4.12 Effect of $NaBH_4$ concentration on 4-NP reduction.

4.3.2.5 Reaction mechanism for the reduction of 4-NP using Pt-Co/CNF and Ag-Co/CNF NC catalysts

The mechanism of 4-NP reduction using metal-based or supported metal catalysts in the presence of $NaBH_4$ have been explored by several researchers [22,26,51]. However, a limited number of comparative studies are available on applying a cellulose-based catalyst for the reduction of 4-NP, especially Pt-Co and Ag-Co impregnated CNF catalysts. Literature indicates that the reduction of 4-NP can proceed through two reaction mechanisms: the Langmuir–Hinshelwood (LH) mechanism or the Eley–Rideal (ER) mechanism [26]. In the LH model, the value of K_{app} decreases with an increase in the concentration of 4-NP, and increases with the increasing concentration of $NaBH_4$. While in the ER model, K_{app} increases with an increase in the concentration of 4-NP [25]. Thus, to determine which of the two kinetic models is valid for the reduction of 4-NP in the presence of the Pt-Co/CNF and Ag-Co/CNF NC catalysts, the dependence of K_{app} on the concentration of 4-NP and $NaBH_4$ was examined. From Figure 4.11 and Figure 4.12, it can be inferred that the value of K_{app} over both the NC catalysts decreases with an increase in the concentration of 4-NP, whereas it increases with the increase in $NaBH_4$ concentration. This implies that the reduction of 4-NP in the presence of as-prepared Pt-Co/CNF and Ag-Co/CNF catalyst follows the LH model.

Based on the above results, it is observed that the catalytic reduction of 4-NP over the NC catalysts used, leads to the same experimental facts. Thus, the 4-NP reduction follow an identical reaction path for both the NC catalysts. According to the LH mechanism, the adsorption of both the reactant molecules, i.e., 4-NP and borohydride (BH_4^-) ions, occurs on the catalyst surface before the interfacial electron transfer between them [31]. This indicate that, initially, before the adsorption of reactant molecules on the catalyst surfaces, the 4-NP is deprotonated to its corresponding nitrophenolate ion in alkaline medium, due to the presence of (Na^+, BH_4^-), as indicated by UV-vis analysis.

After that, the introduction of low amount of NC catalyst triggers the reduction of 4-NP on the catalyst surface. The initial step towards the reaction is the diffusion and penetration of 4-NP towards the active sites of the Ag-Co/CNF catalyst. At the same time, $NaBH_4$ is hydrolyzed in water to produce BH_4^- ions, which diffuses and adsorbs on the catalyst surface. Subsequently, the decomposition of borohydride ion is activated on the surface of the catalyst to generate hydrogen ions responsible for reducing 4-NP. Pt-Co/CNF and Ag-Co/CNF plays an important role in the transport of electrons from the oxidation site to the reduction site, i.e., the catalyst provides the pair of electrons dissociated from BH_4^- anion to the 4-NP ion. Thus, reduction of

the -NO_2 group in the 4-NP takes place on the catalyst surface and results in the production of 4-AP. As produced 4-AP has very low adsorbability compared with 4-NP; thus, it desorbs from the catalyst's surface immediately after generation [51].

These observations mean that the catalytic reaction between the substrates has occurred via the interaction of hydrogen and -NO_2^- group of nitrophenolate. The results show that the reduction of 4-NP depends on this step because the reduction rate constant of 4-NP is different for both the Pt-Co/CNF and Ag-Co/CNF catalyst. In addition, it is observed when preparing ($NaBH_4$ + 4-NP) solution in H_2O, H_2 gas is produced. But the reduction reaction of 4-NP does not occur in the absence of NC catalysts. Accordingly, the experimental observations indicate a progressive catalytic reduction of the NO_2^- group to 4-AP. Consequently, this indicates that metallic sites activate the adsorbed species of nitrophenolate and borohydride ions, which react superficially on the surface of catalysts. Afterward, 4-AP desorbs from the surface, releasing the active sites for a new cycle of catalytic reaction.

4.3.2.6 Catalyst stability

The reusability of the catalyst determines the adaptability of the catalyst for industrial applications. Therefore, it is critical to consider the reusability of the catalyst; thus, after every run, the NC catalyst was separated and after a water wash via centrifugation, dried at 60 °C, and used for a fresh successive run. The conversion obtained for the sequential five cycles of the catalyst reuse for both Pt-Co/CNF and Ag-Co/CNF is demonstrated in Figure 4.13. Based on the results, the catalyst maintains its high activity after the fifth cycle, with a slight increase in the reaction time. This shows the superior stability of the as-prepared Pt-Co/CNF and Ag-Co/CNF NCs with no considerable decrease in the activity up to five cycles.

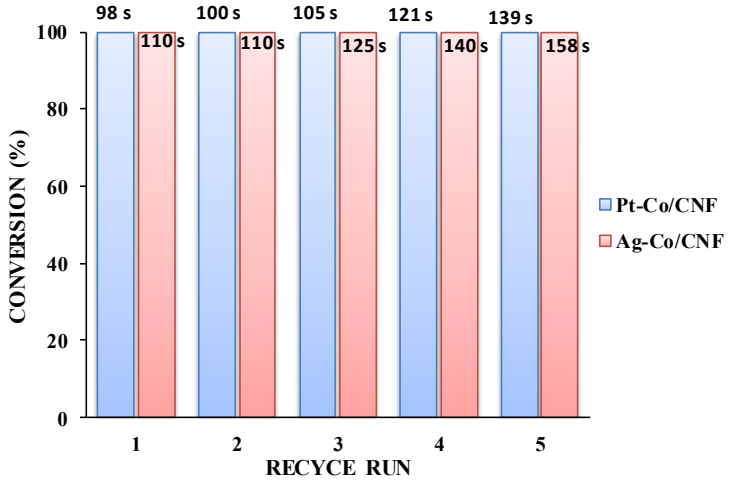

Figure 4.13 The recycle ability of Pt-Co/CNF and Ag-Co/CNF NCs for the 4-NP reduction.

This implies that the synthesized NCs demonstrates enhanced catalytic performance and better stability, making it an economically viable choice to reduce 4-NP over the reported catalysts (Table 4.1). It must be noted that the alloying of Pt with Co and Ag with Co on the surface of CNF support induces the synergistic effect by enhancing the structural and electronic properties of the NC. This, in principle, increases the number of unsaturated active sites for the adsorption of hydrogen onto the catalyst surface with improved electron transfer. Based on the above analysis, the superior performance of the Pt-Co/CNF and comparable performance of Ag-Co/CNF catalyst can be ascribed to the large surface area and surface roughness, offering extremely active sites. Conversely, bimetallic Ag-Co and Pt-Co alloys supported on plentiful interconnected CNFs could also present facile pathways for electron transfer by reducing the interfacial resistance. As a result, the synergistic effect of Pt-Co/CNF and Ag-Co/CNF finally causes an extremely comprehensive catalytic performance for the reduction of 4-NP. Overall, this study offers a facile approach to obtain efficient, economic due to superior stability, and environmentally benign nanocatalyst in treating pollutants such as 4-NP. Also, as the proposed NC catalysts can be separated and recycled effortlessly with better efficiency, it can be used for diverse catalytic applications in industries.

4.4 Conclusion

In summary, the successful synthesis of cellulose-based organic-inorganic NCs has been illustrated with the impregnation of Pt-Co, and Ag-Co NPs on the cellulose nanofibers (CNFs) with the assistance of ultrasound. As evident from electron microscopy, the resulting NCs revealed uniform distribution of metal NPs with spherical morphology on CNFs with a size of about 15-20 nm. Also, the presence of crystalline Pt, Ag and Co NPs on the CNFs was established by XRD, EDX, and elemental mapping analysis. The catalytic application of the as-prepared NCs was explored by the reduction of 4-NP using surplus $NaBH_4$, leading to pseudo-first-order reaction kinetics. The Pt-Co/CNF and Ag-Co/CNF NCs unveiled exceptional catalytic performance with 100 % reduction of 4-NP within 98 and 110 s respectively. The apparent rate constant of the bio-NCs [Pt-Co/CNF (0.0286 s^{-1}), Ag-Co/CNF (0.017 s^{-1})] evaluated using the pseudo-first-order kinetics revealed enhanced activity toward the reduction of 4-NP. The catalysts maintain their higher activity for several cycles without any considerable decrease in its performance. These favorable features of the nanohybrid composites could enable them to be developed into a promising catalytic material for reducing many nitro-aromatic contaminants and dyes.

References

[1] G. Boczkaj, P. Makos, A. Fernandes, A. Przyjazny, New procedure for the examination of the degradation of volatile organonitrogen compounds during the treatment of industrial effluents, J. Sep. Sci. 40 (2017) 1301–1309. https://doi.org/10.1002/jssc.201601237.

[2] M. Nasrollahzadeh, Z. Nezafat, M.G. Gorab, M. Sajjadi, Recent progresses in graphene-based (photo)catalysts for reduction of nitro compounds, Mol. Catal. 484 (2020) 110758. https://doi.org/10.1016/j.mcat.2019.110758.

[3] M.M. Ayad, W.A. Amer, M.G. Kotp, Magnetic polyaniline-chitosan nanocomposite decorated with palladium nanoparticles for enhanced catalytic reduction of 4-nitrophenol, Mol. Catal. 439 (2017) 72–80. https://doi.org/10.1016/j.mcat.2017.06.023.

[4] M. Ma, Y. Yang, W. Li, R. Feng, Z. Li, P. Lyu, Y. Ma, Gold nanoparticles supported by amino groups on the surface of magnetite microspheres for the catalytic reduction of 4-nitrophenol, J. Mater. Sci. 54 (2019) 323–334. https://doi.org/10.1007/s10853-018-2868-1.

[5] M. Gagol, E. Cako, K. Fedorov, R.D.C. Soltani, A. Przyjazny, G. Boczkaj, Hydrodynamic cavitation based advanced oxidation processes: Studies on specific effects of inorganic acids on the degradation effectiveness of organic pollutants, J. Mol. Liq. 307 (2020). https://doi.org/10.1016/j.molliq.2020.113002.

[6] G. Boczkaj, A. Fernandes, Wastewater treatment by means of advanced oxidation processes at basic pH conditions: A review, Chem. Eng. J. 320 (2017) 608–633. https://doi.org/10.1016/j.cej.2017.03.084.

[7] X. Xie, J. Shi, Y. Pu, Z. Wang, L. Zhang, D. Wang, Cellulose derived nitrogen and phosphorus co-dopedcarbon-based catalysts for catalytic reduction of p-nitrophenol, J. Colloid Interface Sci. (2020). https://doi.org/10.1016/j.jcis.2020.03.035.

[8] T.K. Das, S. Remanan, S. Ghosh, N.C. Das, An environment friendly free-standing cellulose membrane derived for catalytic reduction of 4-nitrophenol: A sustainable approach, J. Environ. Chem. Eng. 9 (2021) 104596. https://doi.org/10.1016/j.jece.2020.104596.

[9] X.T. Tran, M. Hussain, H.T. Kim, Facile and fast synthesis of a reduced graphene oxide/carbon nanotube/iron/silver hybrid and its enhanced performance in catalytic reduction of 4–nitrophenol, Solid State Sci. 100 (2020) 106107. https://doi.org/10.1016/j.solidstatesciences.2019.106107.

[10] S. Naghdi, M. Sajjadi, M. Nasrollahzadeh, K.Y. Rhee, S.M. Sajadi, B. Jaleh, Cuscuta reflexa leaf extract mediated green synthesis of the Cu nanoparticles on graphene oxide/manganese dioxide nanocomposite and its catalytic activity toward reduction of

nitroarenes and organic dyes, J. Taiwan Inst. Chem. Eng. 86 (2018) 158–173. https://doi.org/10.1016/j.jtice.2017.12.017.

[11] S. Kapoor, A. Sheoran, M. Riyaz, J. Agarwal, N. Goel, S. Singhal, Enhanced catalytic performance of Cu/Cu_2O nanoparticles via introduction of graphene as support for reduction of nitrophenols and ring opening of epoxides with amines established by experimental and theoretical investigations, J. Catal. 381 (2020) 329–346. https://doi.org/10.1016/j.jcat.2019.11.012.

[12] M. Kohantorabi, M.R. Gholami, Kinetic Analysis of the Reduction of 4-Nitrophenol catalyzed by CeO_2 nanorods-supported CuNi nanoparticles, Ind. Eng. Chem. Res. 56 (2017) 1159–1167. https://doi.org/10.1021/acs.iecr.6b04208.

[13] A.F. Baye, R. Appiah-ntiamoah, H. Kim, Synergism of transition metal (Co, Ni, Fe, Mn) nanoparticles and "active support" Fe_3O_4@C for catalytic reduction of 4-nitrophenol, Sci. Total Environ. (2019) 135492. https://doi.org/10.1016/j.scitotenv.2019.135492.

[14] V.K. Landge, S.H. Sonawane, S. Manickam, G.U. Bhaskar Babu, G. Boczkaj, Ultrasound-assisted wet-impregnation of Ag-Co nanoparticles on cellulose nanofibers: Enhanced catalytic hydrogenation of 4-nitrophenol, J. Environ. Chem. Eng. 9 (2021) 105719. https://doi.org/10.1016/j.jece.2021.105719.

[15] Y. Chi, Q. Yuan, Y. Li, J. Tu, L. Zhao, N. Li, X. Li, Synthesis of Fe_3O_4@SiO_2-Ag magnetic nanocomposite based on small-sized and highly dispersed silver nanoparticles for catalytic reduction of 4-nitrophenol, J. Colloid Interface Sci. 383 (2012) 96–102. https://doi.org/10.1016/j.jcis.2012.06.027.

[16] A. Hu, X. Lu, D. Cai, H. Pan, R. Jing, Q. Xia, D. Zhou, Y. Xia, Selective hydrogenation of nitroarenes over MOF-derived Co@CN catalysts at mild conditions, Mol. Catal. 472 (2019) 27–36. https://doi.org/https://doi.org/10.1016/j.mcat.2019.04.008.

[17] Z. Li, C. Han, Palladium nanoflowers supported on amino-fullerene as novel catalyst for reduction of 4-nitrophenol, Chinese Chem. Lett. 2 (2019) 10–12. https://doi.org/10.1016/j.cclet.2019.06.047.

[18] Y. Wang, Q. Li, P. Zhang, D.O. Connor, R.S. Varma, One-pot green synthesis of bimetallic hollow palladium-platinum nanotubes for enhanced catalytic reduction of p -Nitrophenol, J. Colloid Interface Sci. (2018). https://doi.org/10.1016/j.jcis.2018.12.053.

[19] D. Dutta, R. Hazarika, P.D. Dutta, T. Goswami, P. Sengupta, D.K. Dutta, Synthesis of Ag-Ag_2S Janus nanoparticles supported on environmentally benign cellulose template and their catalytic applications, RSC Adv. (2016). https://doi.org/10.1039/C6RA16941D.

[20] T.A. Revathy, T. Sivaranjani, A.A. Boopathi, S. Sampath, V. Narayanan, A. Stephen, Pd–Co alloy as an efficient recyclable catalyst for the reduction of hazardous 4-nitrophenol, Res. Chem. Intermed. 45 (2019) 815–832. https://doi.org/10.1007/s11164-018-3645-0.

[21] A.D. Verma, S. Pal, P. Verma, V. Srivastava, R.K. Mandal, I. Sinha, Ag-Cu bimetallic nanocatalysts for p -nitrophenol reduction using a green hydrogen source, J. Environ. Chem. Eng. 5 (2017) 6148–6155. https://doi.org/10.1016/j.jece.2017.11.057.

[22] V.K. Harika, H.K. Sadhanala, I. Perelshtein, A. Gedanken, Sonication-assisted synthesis of bimetallic Hg/Pd alloy nanoparticles for catalytic reduction of nitrophenol and its derivatives, Ultrason. Sonochem. (2019). https://doi.org/10.1016/j.ultsonch.2019.104804.

[23] H. Chen, X. Fan, J. Ma, G. Zhang, F. Zhang, Y. Li, Green route for microwave-assisted preparation of AuAg-alloy-decorated graphene hybrids with superior 4-NP reduction catalytic activity, Ind. Eng. Chem. Res. 53 (2014) 17976–17980. https://doi.org/10.1021/ie503251h.

[24] J. Zhang, G. Chen, D. Guay, M. Chaker, D. Ma, Highly active PtAu alloy nanoparticle catalysts for the reduction of 4-nitrophenol, Nanoscale. 6 (2014) 2125–2130. https://doi.org/10.1039/c3nr04715f.

[25] J. Liu, J. Li, R. Meng, P. Jian, L. Wang, Silver nanoparticles-decorated-Co_3O_4 porous sheets as efficient catalysts for the liquid-phase hydrogenation reduction of p-Nitrophenol, J. Colloid Interface Sci. 551 (2019) 261–269. https://doi.org/10.1016/j.jcis.2019.05.018.

[26] M. Aazza, H. Ahlafi, H. Moussout, C. Mounir, A. Fadel, A. Addad, H. Ahla, H. Moussout, C. Mounir, A. Fadel, A. Addad, Catalytic reduction of nitro-phenolic compounds over Ag , Ni and Co nanoparticles catalysts supported on γ -Al_2O_3, J. Environ. Chem. Eng. 8 (2020). https://doi.org/10.1016/j.jece.2020.103707.

[27] X. Xu, Y. Liu, Y. Gao, H. Li, Preparation of Au @ silica Janus nanosheets and their catalytic application, Colloids Surfaces A Physicochem. Eng. Asp. (2017). https://doi.org/10.1016/j.colsurfa.2017.06.048.

[28] R.H. Fath, S.J. Hoseini, H.G. Khozestan, A nanohybrid of organoplatinum(II) complex and graphene oxide as catalyst for reduction of p-nitrophenol, J. Organomet. Chem. (2017). https://doi.org/10.1016/j.jorganchem.2017.04.027.

[29] V.K. Landge, S.H. Sonawane, M. Sivakumar, S.S. Sonawane, G. Uday Bhaskar Babu, G. Boczkaj, S-scheme heterojunction Bi_2O_3-ZnO/Bentonite clay composite with enhanced photocatalytic performance, Sustain. Energy Technol. Assessments. 45 (2021) 101194. https://doi.org/10.1016/j.seta.2021.101194.

[30] N. Jadbabaei, R.J. Slobodjian, D. Shuai, H. Zhang, Catalytic reduction of 4-nitrophenol by palladium-resin composites, Appl. Catal. A Gen. 543 (2017) 209–217. https://doi.org/10.1016/j.apcata.2017.06.023.

[31] Y. Ma, X. Wu, G. Zhang, Core-shell Ag@Pt nanoparticles supported on sepiolite nanofibers for the catalytic reduction of nitrophenols in water: Enhanced catalytic performance and DFT study, Appl. Catal. B Environ. 205 (2017) 262–270. https://doi.org/10.1016/j.apcatb.2016.12.025.

[32] S. Saha, A. Pal, S. Kundu, S. Basu, T. Pal, Photochemical green synthesis of calcium-alginate-stabilized Ag and Au nanoparticles and their catalytic application to 4-nitrophenol reduction, Langmuir. 26 (2010) 2885–2893. https://doi.org/10.1021/la902950x.

[33] H. Helmiyati, R.T. Yunarti, F.W. Dini, Magnetic alginate–carboxymethyl cellulose to immobilize copper nanoparticles as a green and sustainable catalyst for 4-nitrophenol reduction, Heliyon. 9 (2023) e14111. https://doi.org/10.1016/j.heliyon.2023.e14111.

[34] S. Sarkar, N. Torres, P. Aparna, B. Rajib, B. Saravanan, Green polymeric nanomaterials for the photocatalytic degradation of dyes : a review, Environ. Chem. Lett. 18 (2020) 1569–1580. https://doi.org/10.1007/s10311-020-01021-w.

[35] M. Nasrollahzadeh, M. Sajjadi, S. Iravani, R.S. Varma, Starch, cellulose, pectin, gum, alginate, chitin and chitosan derived (nano)materials for sustainable water treatment: A review, Carbohydr. Polym. 251 (2021) 116986. https://doi.org/10.1016/j.carbpol.2020.116986.

[36] S. Shankar, J.W. Rhim, Bionanocomposite films for food packaging applications, in: Ref. Modul. Food Sci., Elsevier, 2018. https://doi.org/10.1016/B978-0-08-100596-5.21875-1.

[37] Y. Guo, M. Dai, Z. Zhu, Y. Chen, H. He, T. Qin, Chitosan modified Cu_2O nanoparticles with high catalytic activity for p- nitrophenol reduction, Appl. Surf. Sci. 480 (2019) 601–610. https://doi.org/10.1016/j.apsusc.2019.02.246.

[38] M. Dinari, F. Dadkhah, Swift reduction of 4-nitrophenol by easy recoverable magnetite-Ag/layered double hydroxide/starch bionanocomposite, Carbohydr. Polym. 228 (2020). https://doi.org/10.1016/j.carbpol.2019.115392.

[39] R.D.C. Soltani, M. Mashayekhi, M. Naderi, G. Boczkaj, S. Jorfi, M. Safari, Sonocatalytic degradation of tetracycline antibiotic using zinc oxide nanostructures loaded on nano-cellulose from waste straw as nanosonocatalyst, Ultrason. Sonochem. 55 (2019) 117–124. https://doi.org/10.1016/j.ultsonch.2019.03.009.

[40] N. Mahfoudhi, S. Boufi, Porous material from cellulose nanofibrils coated with aluminum hydroxyde as an effective adsorbent for fluoride, J. Environ. Chem. Eng. 8 (2020) 103779. https://doi.org/10.1016/j.jece.2020.103779.

[41] Z. Jebali, A. Granados, A. Nabili, S. Boufi, A.M.B. do Rego, H. Majdoub, A. Vallribera, Cationic cellulose nanofibrils as a green support of palladium nanoparticles: catalyst evaluation in Suzuki reactions, Cellulose. 25 (2018) 6963–6975. https://doi.org/10.1007/s10570-018-2085-8.

[42] P. Zhou, H. Wang, J. Yang, J. Tang, D. Sun, W. Tang, Bacteria cellulose nanofibers supported palladium(0) nanocomposite and its catalysis evaluation in heck reaction, Ind. Eng. Chem. Res. 51 (2012) 5743–5748. https://doi.org/10.1021/ie300395q.

[43] M. Bhardwaj, S. Paul, Palladium nanoparticles onto ethylenediamine functionalized silica–cellulose substrates [Pd(0)-EDA/SCs]: An efficient and sustainable approach for hydrogenation of nitroarenes and carbonyl compounds under mild conditions, Arab. J. Chem. 12 (2019) 4231–4239. https://doi.org/10.1016/j.arabjc.2016.05.008.

[44] T. Rojanarata, S. Plianwong, K. Su-uta, P. Opanasopit, T. Ngawhirunpat, Electrospun cellulose acetate nano fibers as thin layer chromatographic media for eco-friendly screening of steroids adulterated in traditional medicine and nutraceutical products, Talanta. 115 (2013) 208–213. https://doi.org/10.1016/j.talanta.2013.04.078.

[45] S. Velpula, S.R. Beedu, K. Rupula, Bimetallic nanocomposite (Ag-Au, Ag-Pd, Au-Pd) synthesis using gum kondagogu a natural biopolymer and their catalytic potentials in the degradation of 4-nitrophenol, Int. J. Biol. Macromol. 190 (2021) 159–169. https://doi.org/10.1016/j.ijbiomac.2021.08.211.

[46] D.S. Idris, A. Roy, Synthesis of bimetallic nanoparticles and applications-an updated review, Crystals. 13 (2023) 637. https://doi.org/10.3390/cryst13040637.

[47] J.R. Deka, D. Saikia, N.F. Lu, K.T. Chen, H.M. Kao, Y.C. Yang, Space confined synthesis of highly dispersed bimetallic CoCu nanoparticles as effective catalysts for ammonia borane dehydrogenation and 4-nitrophenol reduction, Appl. Surf. Sci. 538 (2021) 148091. https://doi.org/10.1016/j.apsusc.2020.148091.

[48] A. Khenblouche, D. Bechki, M. Gouamid, K. Charradi, L. Segni, Extraction and characterization of cellulose microfibers from Retama raetam stems, Polimeros. 29 (2019) 1–8. https://doi.org/10.1590/0104-1428.05218.

[49] C. Zhang, T. Uchikoshi, I. Ichinose, L. Liu, Surface modification on cellulose nanofibers by TiO_2 coating for achieving high capture efficiency of nanoparticles, Coatings. 9 (2019). https://doi.org/10.3390/coatings9020139.

[50] R. Dhanda, M. Kidwai, Reduced graphene oxide supported Ag_xNi_{100-x} alloy nanoparticles: A highly active and reusable catalyst for the reduction of nitroarenes, J. Mater. Chem. A. 3 (2015) 19563–19574. https://doi.org/10.1039/c5ta03779d.

[51] Y.Y.Y. Zhang, H. Fang, Y.Y.Y. Zhang, M. Wen, D. Wu, Q. Wu, Active cobalt induced high catalytic performances of cobalt ferrite nanobrushes for the reduction of p-Nitrophenol, J. Colloid Interface Sci. 535 (2018) 499–504. https://doi.org/10.1016/j.jcis.2018.10.022.

[52] D. Chen, Y. Zhao, X. Peng, X. Wang, W. Hu, C. Jing, S. Tian, J. Tian, Star-like PtCu nanoparticles supported on graphene with superior activity for methanol electro-oxidation, Electrochim. Acta. 177 (2015) 86–92. https://doi.org/10.1016/j.electacta.2015.03.066.

[53] M. Rosiene, A. Arcanjo, I.J. Silva, E. Rodriguez-castellon, A. Infantes-molina, R.S. Vieira, Conversion of glycerol into lactic acid using Pd or Pt supported on carbon as catalyst, Catal. Today. 279 (2017) 317–326. https://doi.org/10.1016/j.cattod.2016.02.015.

[54] P. Rajesh Kumar, Prashant L. Suryawanshi, Sarang P. Gumfekar, Bharat A. Bhanvase, Shirish H. Sonawane. Sonochemical synthesis of Pt-Co/C electrocatalyst for PEM fuel cell applications, Surfaces and Interfaces. (2018). https://doi.org/10.1016/j.surfin.2018.04.002.

[55] R.K. Polagani, P.L. Suryawanshi, S.P. Gumfekar, S. H, Sonawane, M. Ashokkumar, Ultrasound-assisted synthesis of Pt – Co/C bimetallic alloys for oxygen reduction in PEM fuel cells, Sustain. Energy Fuels. 00 (2018) 1–9. https://doi.org/10.1039/C8SE00100F.

[56] F. Torkamani, S. Azizian, Green and simple synthesis of Ag nanoparticles loaded onto cellulosic fiber as efficient and low-cost catalyst for reduction of 4-nitrophenol, J. Mol. Liq. 214 (2016) 270–275. https://doi.org/10.1016/j.molliq.2015.12.071.

[57] J. Lv, A. Wang, X. Ma, R. Xiang, J. Chen, J. Feng, One-pot synthesis of porous Pt – Au nanodendrites supported on reduced graphene oxide nanosheets toward catalytic reduction of 4-nitrophenol, J. Mater. Chem. A Mater. Energy Sustain. 3 (2014) 290–296. https://doi.org/10.1039/C4TA05034G.

[58] A. Mondal, B. Adhikary, D.K. Mukherjee, Cobalt nanoparticles as reusable catalysts for reduction of 4-nitrophenol under mild conditions, Bull. Mater. Sci. 40 (2017) 321–328. https://doi.org/10.1007/s12034-017-1367-3.

[59] X. Wu, C. Lu, W. Zhang, G. Yuan, R. Xiong, X. Zhang, A novel reagentless approach for synthesizing cellulose nanocrystal-supported palladium nanoparticles with enhanced

catalytic performance, J. Mater. Chem. A. 1 (2013) 8645–8652. https://doi.org/10.1039/c3ta11236e.

[60] M.M.J. Sadiq, U.S. Shenoy, D.K. Bhat, $NiWO_4$-ZnO-NRGO ternary nanocomposite as an efficient photocatalyst for degradation of methylene blue and reduction of 4-nitro phenol, J. Phys. Chem. Solids. 109 (2017) 124–133. https://doi.org/10.1016/j.jpcs.2017.05.023.

[61] A. Hatamifard, M. Nasrollahzadeh, S.M. Sajadi, Biosynthesis, characterization and catalytic activity of an Ag/zeolite nanocomposite for base- and ligand-free oxidative hydroxylation of phenylboronic acid and reduction of a variety of dyes at room temperature, New J. Chem. 40 (2016) 2501–2513. https://doi.org/10.1039/c5nj02909k.

[62] H.Y. Chiu, T. Wi-Afedzi, Y.T. Liu, F. Ghanbari, K.Y.A. Lin, Cobalt oxides with various 3D nanostructured morphologies for catalytic reduction of 4-Nitrophenol: A comparative study, J. Water Process Eng. 37 (2020) 101379. https://doi.org/10.1016/j.jwpe.2020.101379.

[63] M.M.J. Sadiq, U.S. Shenoy, D.K. Bhat, Synthesis of $BaWO_4$/NRGO–g-C_3N_4 nanocomposites with excellent multifunctional catalytic performance via microwave approach, Front. Mater. Sci. 12 (2018) 247–263. https://doi.org/10.1007/s11706-018-0433-0.

[64] M.M.J. Sadiq, U.S. Shenoy, D.K. Bhat, Enhanced photocatalytic performance of N-doped RGO-$FeWO_4$/Fe_3O_4 ternary nanocomposite in environmental applications, Mater. Today Chem. 4 (2017) 133–141. https://doi.org/10.1016/j.mtchem.2017.04.003.

[65] T. Baran, M. Nasrollahzadeh, Facile synthesis of palladium nanoparticles immobilized on magnetic biodegradable microcapsules used as effective and recyclable catalyst in Suzuki-Miyaura reaction and p-nitrophenol reduction, Carbohydr. Polym. 222 (2019) 115029. https://doi.org/10.1016/j.carbpol.2019.115029.

[66] X.F. Zhang, X.Y. Zhu, J.J. Feng, A.J. Wang, Solvothermal synthesis of N-doped graphene supported PtCo nanodendrites with highly catalytic activity for 4-nitrophenol reduction, Appl. Surf. Sci. 428 (2018) 798–808. https://doi.org/10.1016/j.apsusc.2017.09.200.

[67] M.A. Ahsan, O. Fernandez-Delgado, E. Deemer, H. Wang, A.A. El-Gendy, M.L. Curry, J.C. Noveron, Carbonization of Co-BDC MOF results in magnetic C@Co nanoparticles that catalyze the reduction of methyl orange and 4-nitrophenol in water, J. Mol. Liq. 290 (2019) 111059. https://doi.org/10.1016/j.molliq.2019.111059.

[68] H.S. Hassan, M.F. Elkady, A. Farghali, A.M. Salem, A.I.A. El-Hamid, Fabrication of novel magnetic zinc oxide cellulose acetate hybrid nano-fiber to be utilized for phenol decontamination, J. Taiwan Inst. Chem. Eng. 78 (2017) 307–316. https://doi.org/10.1016/j.jtice.2017.06.021.

[69] J. Huang, X. Wang, Q. Jin, Y. Liu, Y. Wang, Removal of phenol from aqueous solution by adsorption onto OTMAC-modified attapulgite, J. Environ. Manage. 84 (2007) 229–236. https://doi.org/10.1016/j.jenvman.2006.05.007.

Chapter 5.
Photocatalytic degradation of Congo red over binary S-scheme and ternary Z-scheme heterojunction

5.1. Introduction

Water pollution from numerous sectors is currently a major concern worldwide [1]. As a result, environmental preservation and water purification are the most critical criteria for conserving natural water resources necessary for advancing the world [2]. Contaminants can be found in wastewater from various industries and municipal and agricultural sources. The type of contaminants in the wastewater determines the best treatment technology criteria. Organic and inorganic recalcitrant pollutants such as azo dyes, phenolic compounds, and heavy metals are commonly found in industrial wastewaters. The recalcitrant pollutants have been detrimental to humans and aquatic life due to their non-biodegradability, high toxicity, and carcinogenic consequences. As a result, a major concern among researchers is their removal/degradation before discharge from the industry. Congo red (CR) (disodium 4-amino-3-[4-[4-(1-amino-4-sulfonato-naphthalen-2-yl)diazenylphenyl]phenyl]diazenyl-naphthalene-1-sulfonate), an azo dye, is a recalcitrant contaminant that is exceedingly difficult to decompose [3].

Advanced oxidation process (AOP) is one of the most successful strategies for removing colours from wastewater [4]. It is cost-effective, highly efficient, requires low energy consumption, operates under mild conditions, presents broad applicability, and reduces secondary pollution. AOPs are both destructive and low-/no-waste-producing solutions for the remediation of contaminated water. Contaminants and their intermediates can be mineralised by AOPs [5]. Recently, a great surge in interest in harnessing solar energy as a clean and sustainable energy source for the photodegradation of recalcitrant contaminants has been noticed [6]. Specifically, heterogeneous photocatalysts containing semiconductor materials demonstrate potential applications to numerous environmental pollution issues as they are quick, highly efficient, and economical and do not lead to any secondary pollution [7]. It can immediately transform recalcitrant contaminants into safer compounds in wastewater to gain the research community's interest.

Photocatalytic processes initiate upon the illumination of the light with photons having higher energy than the band gap energy of semiconductor material, causing the motion of electrons from the valence band (VB) to the conduction band (CB). Adsorbed substrates are oxidised, and active oxygen species are reduced by a hole–electron pair formed when the CB receives

an electron from the VB, leaving behind a hole. Adsorbed water or hydroxide ions in an aqueous solution are oxidised by holes in the VB, forming hydroxyl radicals, whilst molecular oxygen is reduced by the electrons in the CB and forms semiconductor superoxide radicals. Organic pollutants, such as dyes, are oxidised by hydroxyl and superoxide radicals and disintegrate into carbon dioxide and water [8].

The metal oxides are widely exploited in photocatalysis. Amongst them nanoparticles (NPs) play a critical role as they hold huge surface area, accounting for better catalytic performance and stability [9]. TiO_2 and ZnO NPs exhibiting wide-band-gap energies of 3.2 eV and 3.37 eV are capable materials for water treatment applications. They are inexpensive, non-toxic, and provide high surface area [10]. Nevertheless, the inherent disadvantages of these semiconductor oxides are the rapid interaction between electron-hole pairs and the broad band gap which can only be activated by ultraviolet irradiation and this part of light covers merely around 4 % of the solar spectrum, which forbid their practical usefulness [11].

The adsorption of pollutants, light-harvesting, and transport and separation of charges are the key aspects in photocatalysis. Due to this, several investigations have been conducted to either adjust the band gap energy of these semiconductor metal oxides or find alternatives to harness solar energy. To increase solar light sensitivity, many techniques are exploited, including (a) doping with other elements and (b) creation of heterojunction structures by mixing semiconductors with metals or other semiconductors [12,13].

Based on this, intense research is focused on improving the light-harvesting capacity and stability of TiO_2 and ZnO NPs by doping them with noble and non-noble metals. For example, Ag-ZnO [14], Cu-ZnO [15], ZnO-Sm [16], sulphated TiO_2-WO_3 [17], TiO_2-GO [18], Gd-ZnO [19], TiO_2-ZnO [20–23], Fe-TiO_2 and Ce-TiO_2 [24] have been reported for the photocatalytic applications. These heterojunction NC materials showed enhancement in photocatalytic activity compared to the individual nanomaterials. They have greater light-harvesting abilities and lower charge carrier recombination rates due to adequate surface imperfections and band alignment [16,20,25]. Among the most studied heterojunctions, TiO_2-ZnO type-II heterojunctions have received immense interest because of the synergic effects caused by the introduction of electrons to TiO_2 from the CB of ZnO, which reduces the electron–hole recombination [21–23,26–29]. However, it should be emphasised that the majority of the studies were carried out under UV radiation, suggesting that the TiO_2/ZnO lattice may still be employed effectively for visible light photocatalysis [30].

In addition, though photocatalysts of type-II heterojunction facilitates the separation of photo generated electron-hole pairs, they also have to endure some limitations from the kinetic and thermodynamic perspectives. To begin with, in view of kinetics, the transfer of electrons and holes amongst two semiconductors is restricted in case of type-II heterojunction as the force of electrostatic repulsion is generated in the CB electrons of the two semiconductors as well as amongst the VB holes of the associated semiconductors respectively. The limitation from the thermodynamic prospective is that, the redox potential of the system reduces greatly during the formation of type-II heterojunction, which adversely affects the driving force required for a particular photocatalytic reaction. Recently an innovative S-scheme (step-scheme) and ternary Z-scheme heterojunction of semiconductors is proposed by several researchers to surmount the limitations of conventional type-II heterojunction photocatalyst [31,32].

The charge-transfer through a S-scheme heterojunction is anticipated as follows: when the reduction photocatalyst (RP) with higher positions of CB and VB and smaller work function comes in contact with the oxidation photocatalyst (OP) with lower positions of CB and VB along with high work function, spontaneous diffusion of electrons from RP to OP takes place which results in the formation of electron depletion and accumulation layers next to the interface of the heterojunction. This produces the negatively charged OP along with positively charged RP and which in turn generates an interior electric field directed towards OP from RP. As a result of this interior electric field, rapid transfer of electron takes place from OP to RP, rather than the other way round. As soon as OP and RP make contact with each other in order to form a heterojunction their Fermi energy reaches equilibrium. As a result of this the Fermi level of OP shifts upwards whereas the Fermi level of RP shifts downwards. These band bendings are responsible for inducing the recombination of the photo generated electrons present in the CB of OP with the holes present in the VB of RP at the interface owing to the Coulombic attraction among the holes and electrons. In this way, in the S-scheme heterojunction photocatalyst, the dominant electron-hole pairs are preserved, whilst the futile electron-hole pairs are recombined, revealing a superior redox capability.

Bi_2O_3 possess a smaller band gap of 2.58-2.85 eV, and is susceptible to visible light illumination and thus exhibits enhanced photocatalytic performance towards degradation of various dyes [33]. This is due to its capability for the oxidation of water and generation of susceptible species, for instance, $O_2^{-\bullet}$ and OH• radicals. Based on this, Bi_2O_3 could be an excellent choice to form a novel S-scheme heterojunction with ZnO, to enhance the redox potential.

Although NPs perform a crucial role in wastewater treatment, their agglomeration, as well as separation and recovery from the reaction mixtures, are considered to be challenging issues [34]. To overcome these problems, metal and metal oxide NPs are dispersed or full-grown onto strong supports such as silicon dioxide [35], polymers [34], and carbon nanomaterials [36]. However, they are expensive, and their recovery or removal has few issues. Along these lines, the utilization of adsorbents that are economical is appealing. The natural bentonite is the plentiful and economical clay. Khaorapapong et al. [37] suggested that the surface area of bentonite clay can be employed to prevent the agglomeration of NPs. As, bentonite clay is easily accessible, economical and, can avert the NPs agglomeration, it is potentially utilized for the elimination of organic contaminants by adsorption from wastewater. The usefulness of semiconductor as a photocatalyst can be enhanced through generating nanocomposite (NC) materials via integrating it into natural clay [38]. These NCs demonstrated improved photocatalytic efficiency owing to their excellent cation exchangeability, huge surface area, and adsorption-desorption properties [39].

Few investigators have reported about designing of supported metal and metal oxide catalysts. Patil et al. [40] studied the degradation of CR dye using Bi_2O_3-montmorillonite NC. Further, they have described the removal of direct green using BiOBr-graphene oxide (GO) and Rh-B using Bi_2O_3-bentonite NCs [5,7]. Qu and Huanyan [41] investigated the degradation of methyl orange under UV light over $BiOCl_{0.5}Br_{0.5}$. In addition to S-scheme heterojunctions, some recent studies have explored doping of various noble, non-noble transition metals as an electron mediator (EM) onto the TiO_2-ZnO heterojunction to improve the catalytic performance under visible light through the formation of Z-scheme heterojunction [10,25,42]. Liang et al. demonstrated the effectiveness of ternary TiO_2-ZnO/Au NC over TiO_2, TiO_2-Au and TiO_2-ZnO for photocatalytic hydrogen production under visible-light illumination coupling of ZnO and TiO_2 and the localised surface plasmonic resonance of Au NPs [10]. However, the incorporation of noble metals is not cost-effective. Cu, on the other hand, is now employed as a competent dopant for several visible-light-responsive photocatalysts, exhibiting redox potentials as low as 0.52 V (Cu^{2+}/Cu) and 0.16 V (Cu^{2+}/Cu^{+}) [43,44]. Cu presents a low-band-gap energy (1.98–2.02 eV), is non-toxic, is chemically stable, possesses good thermal and electrical conductivities, is abundant, and is environmentally friendly, leading to its widespread employment in various applications. Even though adding a dopant to the ZnO/TiO_2 heterojunction may enhance its physical and chemical characteristics, only a few studies have looked into this aspect, which necessitates this investigation.

Based on this, a facile one-pot sonochemical co-reduction method to synthesise Bi_2O_3-ZnO binary metal oxide NPs supported on bentonite clay platelets and Cu-ZnO supported on TiO_2 NPs has been proposed in this study. As these S-scheme binary metal oxide heterostructured NC and ternary Z-scheme heterojunction catalyst is expected to show improved catalytic performance for the elimination of dyes and organic contaminants, its photocatalytic performance has been studied for the degradation of CR dye. This is the first work focusing on impregnating Bi_2O_3 and ZnO NPs onto bentonite clay to form S-scheme binary metal oxide heterojunction and the impregnation of Cu and ZnO NPs onto TiO_2 to form Cu-ZnO/TiO_2 ternary Z-scheme heterojunction NC photocatalysts to enhance the photocatalytic decomposition of CR azo dye under natural sunlight. The outcome of this study provides a roadmap to develop highly efficient NC photocatalysts for wastewater treatment and remediation with numerous synergies.

5.2 Photocatalytic degradation of CR dye over Bi_2O_3-ZnO/bentonite clay binary S-scheme heterojunction NC photocatalyst

5.2.1 Materials and methods

5.2.1.1 Reagents

Zinc acetate ($C_4H_6O_4Zn{\cdot}2H_2O$, 98.5 %) (S.D. Fine Chemicals Pvt. Ltd., India), and bismuth nitrate ($Bi(NO)_3.5H_2O$,98.0 %) (S.D. Fine Chemicals Pvt. Ltd., India) were used as metal precursors; Sodium borohydride ($NaBH_4$, 97 %) (Molychem, India) was used as a reducing agent. Bentonite clay ($Al_2H_2O_6Si$) and Hydrochloric Acid (HCl, 38 %) were procured from Thermo Fisher Scientific. Polyvinylpyrrolidone $(C_6H_9NO)_n$ (PVP,11.5-12.8 %, MW 40,000, Hi-Media Laboratories Pvt. Ltd., India) was employed as a stabiliser. CR dye was acquired from Sigma-Aldrich. The reagents of analytical grade were used as obtained from the commercial suppliers. Deionised (DI) water was used to prepare solutions of precursor and reducing agent.

5.2.1.2 Sonication assisted synthesis of Bi_2O_3-ZnO/bentonite clay binary S-scheme heterojunction NC photocatalyst

In a 250 mL beaker, about 1g bentonite clay was dispersed in 100 mL of 0.01 N HNO_3. It was sonicated with the help of a probe-type sonicator (20 kHz, 20 mm diameter, 220 W, a pulse of 5 sec on and 5 sec off, Dakshin ultrasonicator, Mumbai, India) for 15 min to exfoliate the clay platelets. To this solution, about 1.16 g Bismuth nitrate, 1.68 g Zinc acetate and 0.01g PVP

were added and sonicated for 45 min using the same probe-type sonicator, along with dropwise addition of 1 M $NaBH_4$ solution with mechanical agitation (Figure 5.1). The high-speed centrifuge (9000 rpm) was used for the separation of precipitate from the solution. Subsequently, the precipitate was washed with deionized water and acetone, and then dried at 80 °C (6 h) continued with calcination at 300 °C for 1 h to obtain Bi_2O_3-ZnO/bentonite clay NCs.

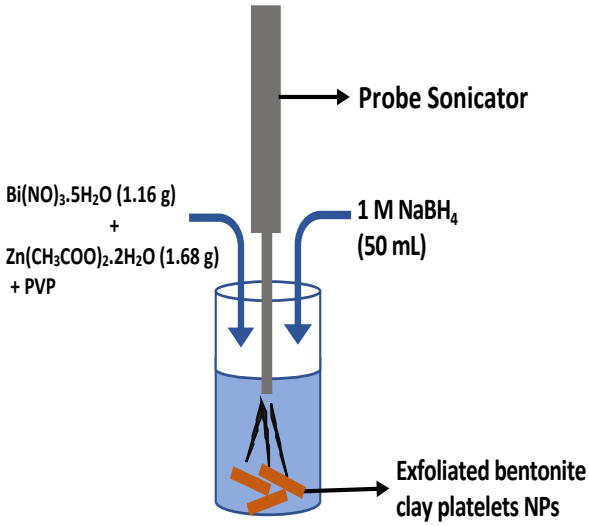

Figure 5.1 Schematic representation for the synthesis of Bi_2O_3-ZnO/Bentonite clay NCs photocatalyst.

5.2.1.3 Characterization of Bi_2O_3-ZnO/bentonite clay NC photocatalyst

The morphology and structure of the catalytic Bi_2O_3-ZnO/bentonite clay NCs were examined by means of several characterization techniques. The crystal structure, phase detection and average crystallite size estimation of the proposed NC was conducted by the XRD analysis. The X-ray diffraction (XRD) spectrum of Bi_2O_3-ZnO/bentonite clay NCs was recorded on Rigaku 600 W MiniFlex benchtop powder X-ray diffractometer with Cu K_α radiation and scanning at 2θ from 10° to 120°. The morphological characteristics, elemental composition and energy-dispersive X-ray spectroscopy (EDX) of the NC catalyst particles were determined using field emission scanning electron microscopy (FE-SEM) on FESEM - Carl Zeiss, EVO MA 15, Oxford Instruments, Abingdon, UK equipped with EDX analyzer. The Fourier transform infrared spectroscopy (FTIR) spectrum of the NC photocatalyst was recorded with Bruker-ALPHA II with a resolution of 4 cm^{-1} between 4000 cm^{-1} and 400 cm^{-1} FTIR spectrometer. The extent of CR dye degradation was analysed spectrophotometrically by the UV-Vis spectrophotometer (UV-3600 Plus Shimadzu UV-Vis Spectrophotometer).

5.2.1.4 Photocatalytic performance of the Bi_2O_3-ZnO/bentonite clay NC catalyst

The catalytic performance of the synthesised Bi_2O_3-ZnO/bentonite clay NCs was obtained by studying the oxidation of CR under irradiation of UV light. For all the experiments, 25 mL CR dye (200 mg/L) was added to a glass beaker (50 mL) and was kept under continuous stirring using a magnetic stirrer. An appropriate quantity of synthesized Bi_2O_3-ZnO/bentonite clay NCs was then added. The impact of various operating conditions such as catalyst loading, time of UV exposure, and concentration of H_2O_2 on the oxidation of CR dye was observed. The impact of catalyst loading on the oxidation of CR was studied with an initial CR concentration of 0.2 g/L and with 4 mL H_2O_2. The catalyst dosages used for this study were 0.05, 0.1, 0.15, 0.20, 0.25, and 0.30 g for 25 mL CR dye solution. The CR dye solution, along with catalyst, was stirred and placed inside the UV chamber. Samples of the suspension were withdrawn at regular time intervals of 0, 10, 20, 30, 40, 50, and 60 min. The effect of concentration of H_2O_2 was also studied at fixed CR dye concentration (0.2g/L) and catalyst loading (0.2 g). The amounts of H_2O_2 (30 % by volume) used were 1, 2, 3, 4, and 5 mL for 25 mL CR dye solution. At regular intervals, 1 mL of the reaction mixture was collected and centrifuged before determining the concentration of CR dye at its characteristic absorption of 498 nm by means of a UV-vis absorption spectroscopy. The percentage degradation of CR was evaluated by applying Eq. 5.1 as given below,

$$Congo\ red\ (CR)\ dye\ degradation\ (\%) = \frac{C_0 - C_t}{C_0} \times 100 \qquad \text{(Eq.5.1)}$$

Where, C_0 = initial concentration of CR solution (gL^{-1}) at t = 0 min, and C_t = CR dye concentration (gL^{-1}) at different intervals. Finally, the reusability of the catalyst was examined for 5 consecutive cycles.

5.2.2 Result and discussion

The S-scheme Bi_2O_3-ZnO/bentonite clay heterojunction was fabricated using one-pot sonication assisted co-reduction of the bismuth nitrate and zinc acetate in the presence of exfoliated bentonite clay platelets. The preliminary investigations on the photocatalytic degradation of CR dye over the proposed Bi_2O_3-ZnO/bentonite clay catalyst was conducted under direct sunlight. However, it was observed that the rate of CR degradation was much slower, thus the CR degradation was then attempted in the presence of UV-light irradiation and H_2O_2 in addition to photocatalyst. The detailed characterization and catalyst performance studies are discussed in the following sections.

5.2.2.1 Characterization of Bi_2O_3-ZnO/bentonite clay catalyst

A. X-ray diffraction studies

The XRD pattern for the as-synthesized Bi_2O_3-ZnO/bentonite clay NC was obtained in the range of 6° to 120° at room temperature, and is presented in Figure 5.2. The peaks at 2θ= 26.81°, 27.39°, 49.76°, and 54.09° correspond to (101), (202), (112), and (220) crystalline planes of bentonite clay [45]. The Bragg's diffraction peaks at 27.39°, 28°, 32.57°, 33.45°, 46.67°, 56.41°, and 58.72° correspond to (121), (201), (002), (220), (223), (203), and (402) planes of Bi_2O_3which represent its monoclinic phase [45,46]. The diffraction peaks at 31.72°, 33.45°, 46.67°, 56.41°, 66.25°, and 75.28° are assigned to (100), (002), (102), (110), (200), and (202) planes of ZnO and confirms the produced NPs exhibit good wurtzite hexagonal crystalline structure. These results are in line with the JCPDS Card no. 01-079-2205 [47].

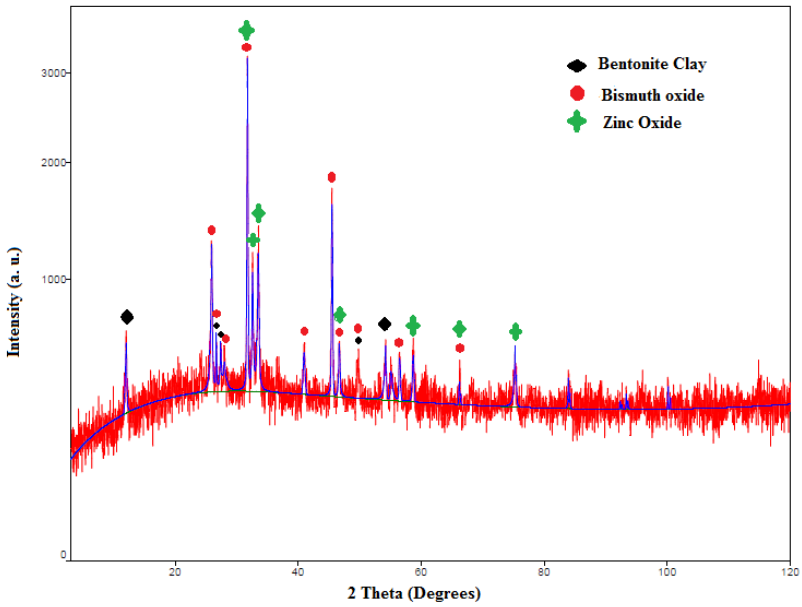

Figure 5.2 XRD spectrum of Bi_2O_3-ZnO/bentonite clay NCs.

As all the peaks are completely indexed for ZnO, Bi_2O_3, and bentonite clay, it confirms the successful formation of Bi_2O_3-ZnO/bentonite clay NCs. Further, the prepared Bi_2O_3-ZnO/bentonite clay NCs exhibit the combination of an α-monoclinic phase of Bi_2O_3 in the hexagonal wurtzite ZnO supported on bentonite clay platelets. The presence of sharp peaks in spectrum signifies that the as-synthesized catalytic NCs have been crystallized properly. The Debye-Scherrer method was used to calculate crystallite size at the high-intensity peak at 32.57°. The average crystallite size of Bi_2O_3-ZnO/bentonite clay was assessed by using the Eq. 5.2.

$$d = \frac{k\lambda}{\beta cos\theta} \qquad \text{(Eq.5.2)}$$

Where d is the crystallite size, k is the shape factor of particle, β is the width of the spectrum peak with high intensity, λ is the wavelength, and θ refers to the Bragg's angle. The average crystallite size of the obtained Bi_2O_3-ZnO/bentonite clay NCs using Debye-Scherrer formula was 45 nm.

B. Fourier transform infrared analysis

The FTIR spectrum from 4000 to 400 cm^{-1} for the obtained Bi_2O_3-ZnO/bentonite clay NCs is shown in Figure 5.3. The band appearing at 3614 cm^{-1} with a subsequent band at 3468 cm^{-1} indicate the occurrence of structured hydroxyl (OH- stretching) groups and water in the sample. The stretching vibration of Si-O-Si, which is a distinctive band for layered bentonite, could be noted by the sharp absorption band appearing at 1005 cm^{-1}. The band at 529 cm^{-1} is for the Al-O-Si bending vibration arising from the octahedral sheets of alumina in the bentonite clay. The bands at 529, 692, and 785 cm^{-1} attributes to the Si-O-Si stretching vibrations. A sharp band at 1380 cm^{-1} approves the existence of SiO_4 [48]. The O-Bi-O stretching vibration is reflected by the sharp band at 743 cm^{-1}. Further, the band at 1650 cm^{-1} confirms the Bi-O stretching vibration [46]. The band at 461 cm^{-1} is correlated to the metal oxide bond (ZnO) and attributed to the Zn-O stretching mode. The obtained FTIR results agree with the earlier results for bentonite [48], Bi_2O_3 [49], and ZnO [46].The absorption bands appearing at 3774, 3468, 1005, 912, 743, 529, and 461 cm^{-1} are due to the coexistence of Bi_2O_3 and ZnO in bentonite clay.

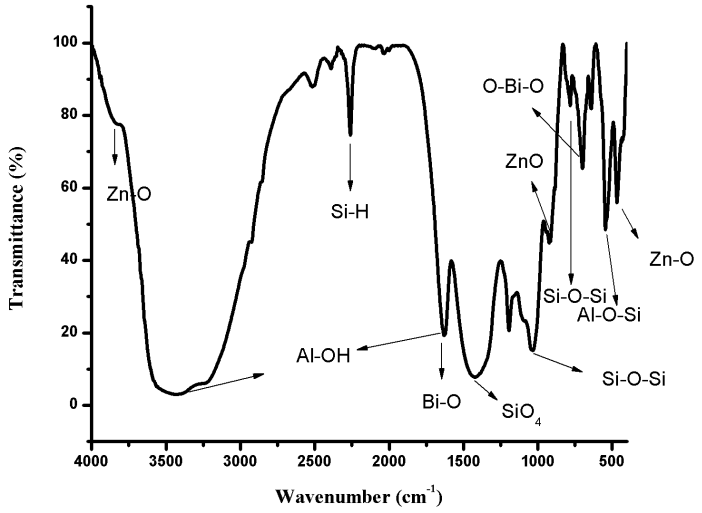

Figure 5.3 FTIR spectrum of Bi_2O_3-ZnO/bentonite clay NCs.

C. Field emission scanning electron microscopy analysis

The size and shape of the obtained NCs were characterized using FESEM, as displayed in Figure 5.4. The uniform dispersion of Bi_2O_3 and ZnO on bentonite clay platelets can be seen. Also, it could be noted that bentonite contains several agglomerated Bi_2O_3 and ZnO NPs with nearly uniform size and spherical morphology. As evident from the FESEM image, the particle size is approximately 40 nm, which supports the size calculations obtained through XRD analysis which is 45 nm.

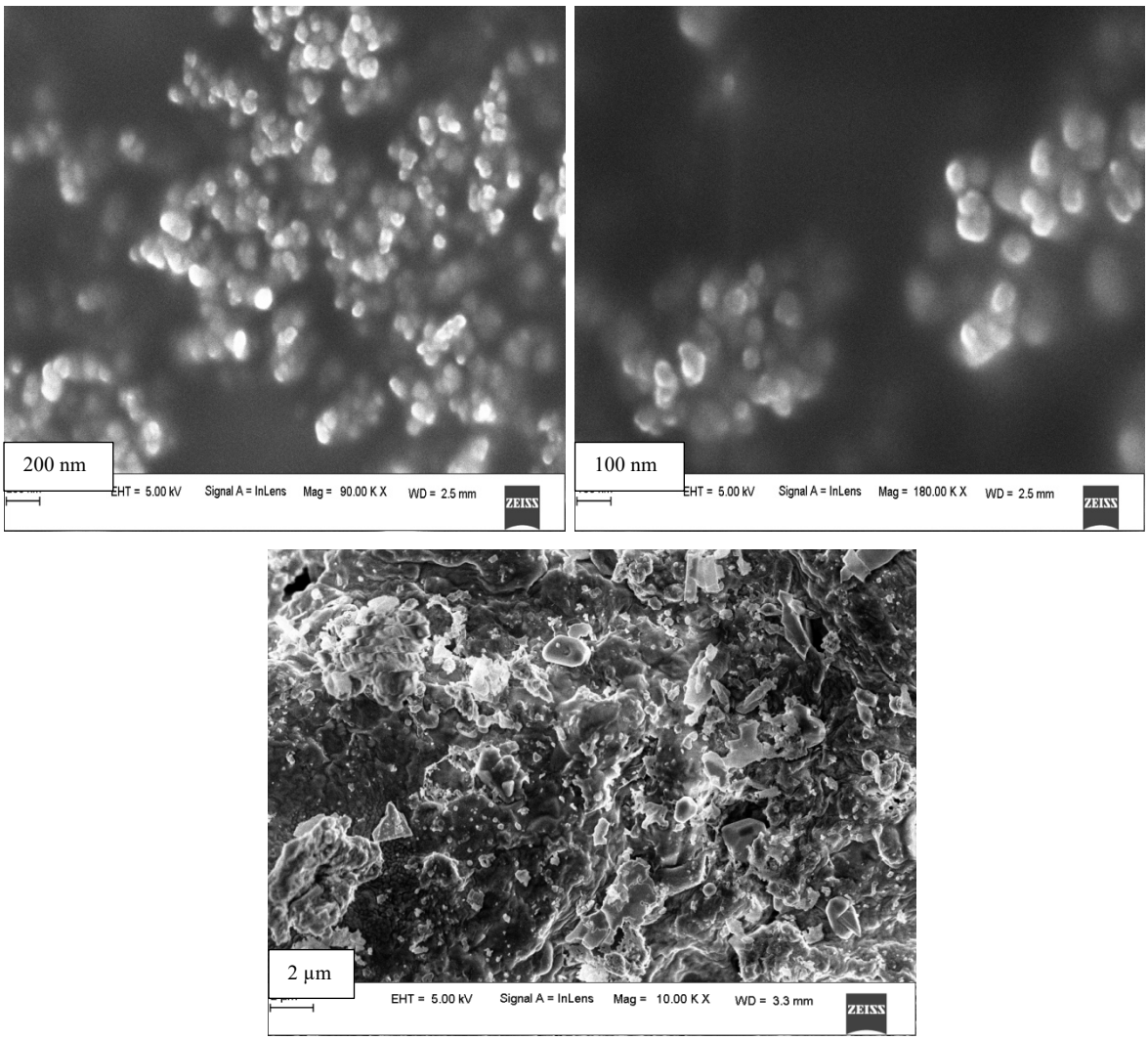

Figure 5.4 FESEM images of Bi_2O_3-ZnO/bentonite clay NCs with high and low magnification.

Further, the existence of Bi_2O_3 and ZnO on the surface of bentonite clay was confirmed by elemental mapping using EDX analysis, and the obtained results are depicted in Figure 5.5 and Figure 5.6. The elemental mapping shows the distribution of Bi and Zn on the support (Figure 5.5), and the FESEM-EDX spectra confirm the presence of Bi, Zn, O, along with Si, Na and

Al (Figure 5.6 and Table 5.1). This proves the successful synthesis of Bi_2O_3-ZnO/bentonite clay NCs through the sonochemical approach. Notably, the morphology and distribution of dopants on the support can be precisely controlled by using this sonochemical approach with moderate operating conditions.

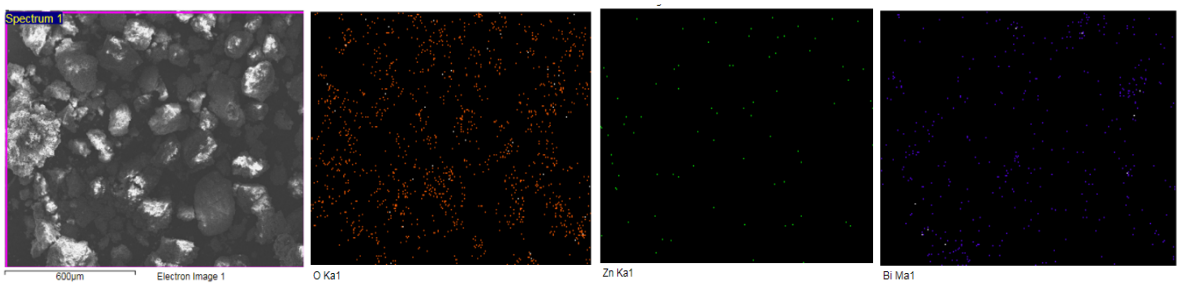

Figure 5.5 Elemental mapping for Bi_2O_3-ZnO/bentonite clay NCs.

Table 5.1 Elemental composition of Bi_2O_3-ZnO/bentonite clay NC photocatalyst on weight basis.

Composition	Bi (wt%)	Zn (wt%)	O (wt%)	Bentonite clay (wt%)	C (wt%)
Theoretical	10	10	20	60	-
FESEM-EDX	9.67	9.50	19.84	57.82	3.17

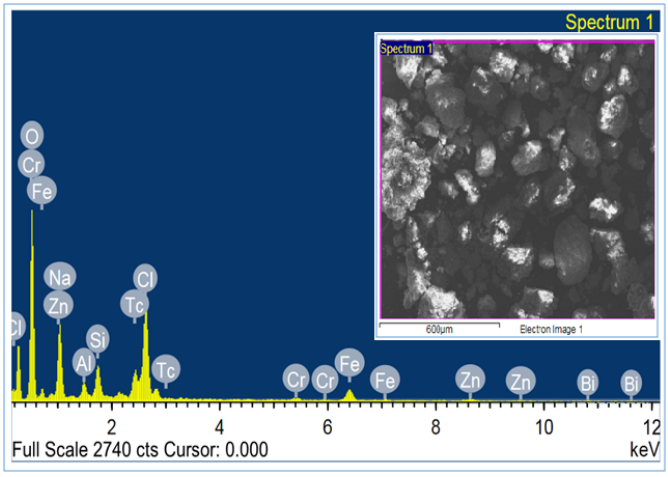

Figure 5.6 EDX spectrum of Bi_2O_3-ZnO/bentonite clay NCs.

5.2.2.2 Performance of catalytic Bi_2O_3-ZnO/bentonite clay NCs on the photocatalytic degradation of CR dye

The photocatalytic performance of the as-synthesised Bi_2O_3-ZnO/bentonite clay NC photocatalyst was assessed through photocatalytic degradation of CR. Upon the direct illumination of ultraviolet rays containing a higher amount of energy than the band gap energies of the photocatalyst, the transfer of electron occurs from the VB to the CB of the photocatalyst, which leaves a hole in the VB. This results in the generation of electron-hole pairs. Subsequently, these charges move towards the photocatalyst surface; where the electron

reacts with O_2 to give superoxide ($\bullet O_2^-$) radicals while holes react with H_2O to give hydroxyl (•OH) radicals. The produced $\bullet O_2^-$ and •OH radicals are highly oxidising radicals that play a major role in the degradation of adsorbed CR dye and produce H_2O, CO_2, and other mineralisation products [23,50]. The initial experimentation was conducted in the presence of UV light (direct photolysis) without using the catalytic NCs to assess the degradation of CR. No noticeable change in the absorbance of the CR dye solution or colour was observed even upto 200 min in the absence of catalytic NCs. Similarly, the impact of UV radiation on the CR dye degradation was also observed by conducting the reaction with addition of catalytic NCs in the dark up to 200 min, and no significant change in the absorbance of the solution was noted. From these initial experiments, it has been found that for the efficient removal of CR dye, UV light and catalyst are essential.

The photodegradation of CR dye was then conducted under UV radiation, and Bi_2O_3-ZnO/bentonite clay NCs followed by the addition of H_2O_2. The progress of this photocatalytic reaction was observed by computing the absorbance at regular interims by means of a UV-visible spectrometer. At time t = 0, i.e., before initiating the UV-light and adding photocatalyst along with H_2O_2 addition, the absorbance of CR solution was calculated (initial concentration of CR solution, C_0). After adding an appropriate amount of photocatalyst, H_2O_2 and in the presence of UV light irradiation, the concentration of the dye was determined at specific intervals. The absorption peak intensity at 498 nm was observed and found to be declining with an increase in the time (0 to 60 min) of UV light, indicating the removal of CR dye using Bi_2O_3-ZnO/bentonite clay as the photocatalyst in the presence of UV radiation. Figure 5.7 presents the results of time-dependent removal of CR dye with Bi_2O_3-ZnO/bentonite clay using UV-Vis absorption.

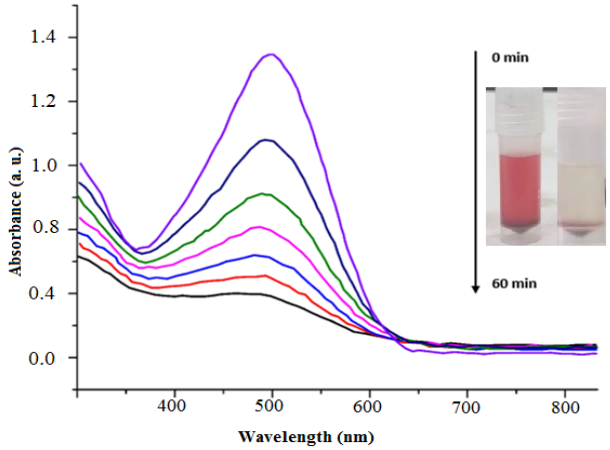

Figure 5.7 UV-Vis spectra of CR dye degradation at different intervals of time (reaction conditions for each experiment: 200 mg/L CR dye, 4 mL H_2O_2, catalyst loading 0.2 g, 1 h UV light irradiation).

A. Kinetic studies

The rate of photocatalytic oxidation of the CR dye was evaluated using the decreasing peak intensity at 498 nm, as revealed in Figure 5.7. The kinetic studies between Bi_2O_3-ZnO/bentonite clay and CR dye molecules were carried out using the Langmuir-Hinshelwood model. This model can be simplified to the pseudo-first-order equation as follows, if the initial concentration (C_0) of the CR dye is small (Eq. 5.3).

$$\ln \frac{C_0}{C_t} = K_{app}.t \qquad \text{(Eq.5.3)}$$

Hence, the rate constant, K_{app}, can be determined from the slope of $\ln(C_0/C_t)$ *Vs.* irradiation time obtained from the linear fit of the kinetic plot, as presented in Figure 5.8. The correlation between $\ln(C_o/C_t)$ and t agrees well to a linear regression line with R^2= 0.95. The value of K_{app} for the CR dye degradation using Bi_2O_3-ZnO/bentonite clay is found to be 0.031 min^{-1}. This demonstrates excellent photocatalytic performance of the synthesized binary metal oxide S-scheme heterojunction for the oxidation of CR under UV light irradiation in comparison with the different catalysts reported in literature as shown in Table 5.1. Further, the photocatalytic degradation studies were also performed to examine the influence of catalyst loading and H_2O_2 concentration.

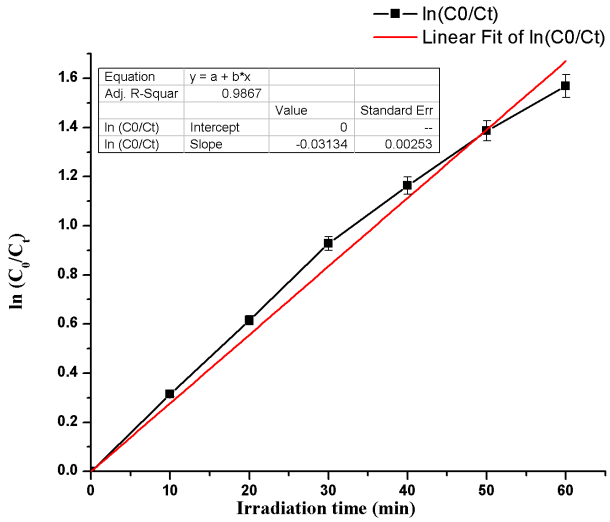

Figure 5.8 Pseudo-first-order kinetics plot with respect to time for the degradation of CR with Bi_2O_3-ZnO/bentonite clay irradiated with UV light.

Table 5.2 Comparative study for the degradation of CR using different photocatalysts.

Catalyst	Initial CR concentration	Catalyst Dosage (g/L)	Reaction time (min)	CR degradation (%)	Ref.
Zn-doped $CdTiO_3/TiO_2$	50 cc	0.6	15	90	[2]
ZnO	20 ppm	0.24	60	90	[51]
$PbTiO_3$	1 x 10^{-5} M	0.75	150	92	[52]
Fe	50 mg/L	1	120	90	[53]
TiO_2	25 µmol/L	0.5	30	87	[54]
chitosan-g-poly(acrylamide)/ZnS	2 x 10-5 M	0.2 (g)	120	75	[3]
Mn doped ZnO/rGO	20 mg/L	0.8	160	100	[55]
Sulfated TiO_2/WO_3	20 ppm	0.5	120	95	[17]
BiOCl/PANI/Fe^0	50 mg/L	1	120	80	[56]
Cellulose/ PVC/ZnO	3 ppm	0.6	120	90	[57]
FeNiSe-CHM	60 ppm	0.2 (g)	140	99	[58]
g-C_3N_4/RGO/$Bi_2Fe_4O_9$	10 mg/L	0.5	60	87	[59]
ZnO-CuO/ES	10 mg/L	1	240	83	[60]
Layered basic zinc acetate (LBZA)/Bentonite Clay	100 mg/L	0.50	210	67.4	[61]
Bi_2O_3-ZnO/bentonite clay	200 mg/L	8	60	100	Present work

B. Effect of operating conditions

The influence of catalyst loading on the mineralization of CR was estimated by changing the loading of photocatalyst from 0.05 to 0.3 g in the CR dye solution under UV light irradiation for an hour using an initial concentration of 4 mL H_2O_2. As illustrated in Figure 5.9a, it can be noticed that with an increase in the catalyst loading up to 0.2 g, the degradation of CR dye increases. However, a reduction in efficiency of CR degradation was observed with a further rise in the catalyst loading. The accessibility of free reactive sites and the surface area increase with an increase in the catalyst loading, and thus more reactive radicals can be produced. The contact between CR dye molecules and reactive species increases as a larger surface area of the catalyst is available for the contact; this enhances the efficiency of CR dye degradation. In contrast, a further rise in the catalyst dosage does not result in improving the degradation efficiency of CR dye; however, it slightly reduces the degradation efficiency. This is because

the dye solutions become increasingly impermeable to UV light irradiation as the catalyst loading increases [62]. Consequently, the availability of UV light that can be absorbed onto the reactive sites of the catalyst surface becomes inadequate, reducing the degradation efficiency of CR dye.

The availability of active radicals for the oxidation in AOP is directly dependent on the concentration of H_2O_2. This is due to that H_2O_2 produces hydroxyl radicals ($^{\bullet}OH$) for the reduction of contaminants. Thus, the significant effect of initial concentrations of H_2O_2 on the effective removal of CR dye was observed. Hence, in this study, the impact of initial H_2O_2 concentrations on the CR dye degradation was estimated by varying the initial concentration of H_2O_2 from 1 to 5 mL. Figure 5.9b indicates the impact of H_2O_2 concentration towards the CR dye reduction, and the observed results agree with the prevailing trend. The results display an increase in the efficiency of CR dye reduction with an increase in the concentration of H_2O_2 from 1 to 4 mL, resulted in the CR removal up to 99 % in 60 min. At the same time, a considerable decrease was observed with an initial excess concentration of H_2O_2.

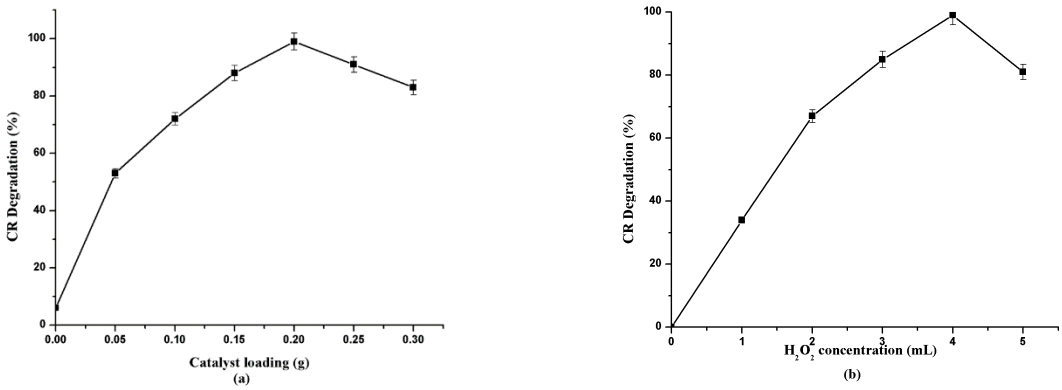

Figure 5.9 The influence of catalyst dosage (a) and H_2O_2 (b) on the photocatalytic activity of Bi_2O_3-ZnO/bentonite clay NCs.

At higher H_2O_2 concentration, generation and access to ·OH radicals increases, leading to the oxidation of CR dye. However, excess H_2O_2 might also behave like a scavenger, thereby reducing the degradation efficiency. Hence, in the photocatalytic degradation of CR dye, determining the optimum H_2O_2 concentration is an essential factor. At low H_2O_2 concentration, the reduction of CR dye was low owing to the insufficient generation of ·OH radicals [63]. However, it is found that with increasing H_2O_2 concentration, the efficiency of the removal of CR dye increases and achieves a maximum at the optimum H_2O_2 concentration of 4 mL. An

increase in the H_2O_2 concentration beyond the optimum decreases the effectiveness of removing CR dye.

C. Reusability and stability of the photocatalyst

The reusability and stability of the photocatalyst is a vital aspect to assess the superiority of the heterogeneous catalysts, as photo-dissolution may occur on the catalyst surface throughout the photocatalytic oxidation. In this study, the reusability of the catalyst was studied in the successive photocatalytic oxidation of CR dye. A simple centrifugal operation was used for the separation of catalyst at the end of each experiment. Subsequently, the recovered catalysts were then used again in another photocatalytic reaction. Figure 5.10 demonstrates the reusability of the catalyst and degradation efficiency of CR dye under UV light for five consecutive cycles. A slight fall in the photocatalytic activity was noticed after the third run.

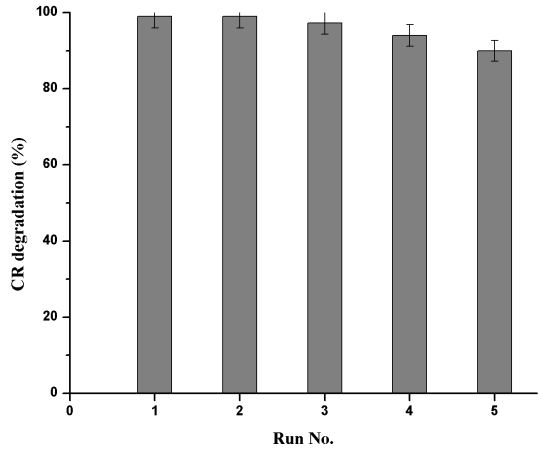

Figure 5.10 Recycling experiments for Bi_2O_3-ZnO/bentonite clay catalyst (reaction conditions for each experiment: 200 mg/L CR dye, 4 mL H_2O_2, catalyst loading 0.2 g, 1 h UV light irradiation).

D. Mechanism of CR dye degradation with Bi_2O_3-ZnO/bentonite clay NCs

The mechanism of CR dye degradation is based on the AOP in conjugation with heterogeneous photocatalysis. In AOP, the generation of the electron (e^-) and hole (h^+) takes place (Eq. 5.4) which induces the formation of potent oxidizing radicals, namely superoxide (O_2^-) and hydroxyl (OH-) (Eq. 5.5 to 5.8), which play a vital role in the mineralization of organic pollutants (Eq. 5.11 and 5.12). Moreover, upon UV-light irradiation, hydrogen ions generated from water molecules account for the degradation of contaminants by reducing them (Eq. 5.5). When the UV light illuminates the photocatalyst, the electrons present in the VB of the photocatalyst get excited and moves towards the CB. This results in the generation of the

equivalent amount of holes in the VB, leads to a series of reactions which, generate OH- and hydroperoxyl (-HO_2) radicals. In the case of ZnO photocatalyst, an unfavorable e^- and h^+ recombination may proceed rapidly, resulting in the reduction of photocatalytic activity. In the present case, this problem was resolved by the use of S-scheme heterojunction of Bi_2O_3-ZnO supported on bentonite clay through the efficient separation of photo induced charge transporters while boosting the redox potential. When Bi_2O_3 and ZnO comes in contact with each other, the electrons present in CB of the Bi_2O_3 instantly starts diffusing towards ZnO through the interface until the Fermi levels of Bi_2O_3 and ZnO reaches equilibrium. At the interface, due to the loss of electrons Bi_2O_3 gains positive charge, whereas the ZnO becomes negatively charged as it receives electrons. On account of this an internal electric field is induced at the interface. Upon UV-light illumination, the electrons are excited from VB to CB of ZnO and Bi_2O_3 respectively. The generated internal electric field along with the resulting band edge bending and Coulomb interaction results in the acceleration of the recombination of part of the electrons (present in CB of ZnO) and holes (present in VB of Bi_2O_3), and simultaneously prevents the recombination of dominant electrons (present in CB of Bi_2O_3) and holes (present in VB of ZnO). In this way, the proposed S-scheme heterojunction mechanism eliminates the comparatively futile electrons (present in CB of ZnO) and holes (present in VB of Bi_2O_3), while retains the helpful electrons (present in CB of Bi_2O_3) and holes (present in VB of ZnO). Therefore, this charge transfer mechanism provides the Bi_2O_3-ZnO/bentonite clay binary metal oxide heterojunction with superior redox capability, and offers strong driving force for the photocatalytic oxidation of CR.

The probable mechanism of CR dye degradation on the surface of Bi_2O_3-ZnO/bentonite clay NCs is illustrated in Figure 5.11. During degradation, initially, the CR dye molecules get adsorbed on the NC surface, and after subjecting to UV irradiation, e- and h^+ pairs are generated on the ZnO and Bi_2O_3 which intercalate on the bentonite clay platelets (Eq. 5.4). Followed by the generation of $^{\bullet}OH$ (Eq. 5.5, 5.6 and 5.10), O_2^- (Eq. 5.7), and -HO_2 (Eq. 5.8) the degradation of CR dye molecules occurs (Eq. 5.11 and 5.12). The various feasible reactions that arise from different reactive species throughout the photocatalytic CR dye degradation are as follows (Eq. 5.4 to 5.12).

$$Photocatalyst + h\nu \rightarrow h^+ + e^- \quad \text{(Eq. 5.4)}$$

$$H_2O + h^+ \rightarrow OH^{\cdot} + H^+ \quad \text{(Eq. 5.5)}$$

$$H_2O_2 + h\nu \rightarrow 2OH^{\cdot} \quad \text{(Eq. 5.6)}$$

$$O_2 + e^- \rightarrow O_2^{\cdot -} \quad \text{(Eq. 5.7)}$$

$$O_2^{\cdot -} + H^+ \rightarrow HO_2^{\cdot -} \quad \text{(Eq. 5.8)}$$

$$HO_2^{\cdot -} + H^+ \rightarrow H_2O_2 \quad \text{(Eq. 5.9)}$$

$$O_2^{\cdot -} + H_2O_2 \rightarrow OH^{\cdot} + OH^- + O_2 \quad \text{(Eq. 5.10)}$$

$$h^+ + CR\ molecules \rightarrow dye^{\cdot +} \rightarrow oxidation\ of\ dye \quad \text{(Eq. 5.11)}$$

$$OH^{\cdot} + CR\ molecules \rightarrow degradation\ of\ dye \quad \text{(Eq. 5.12)}$$

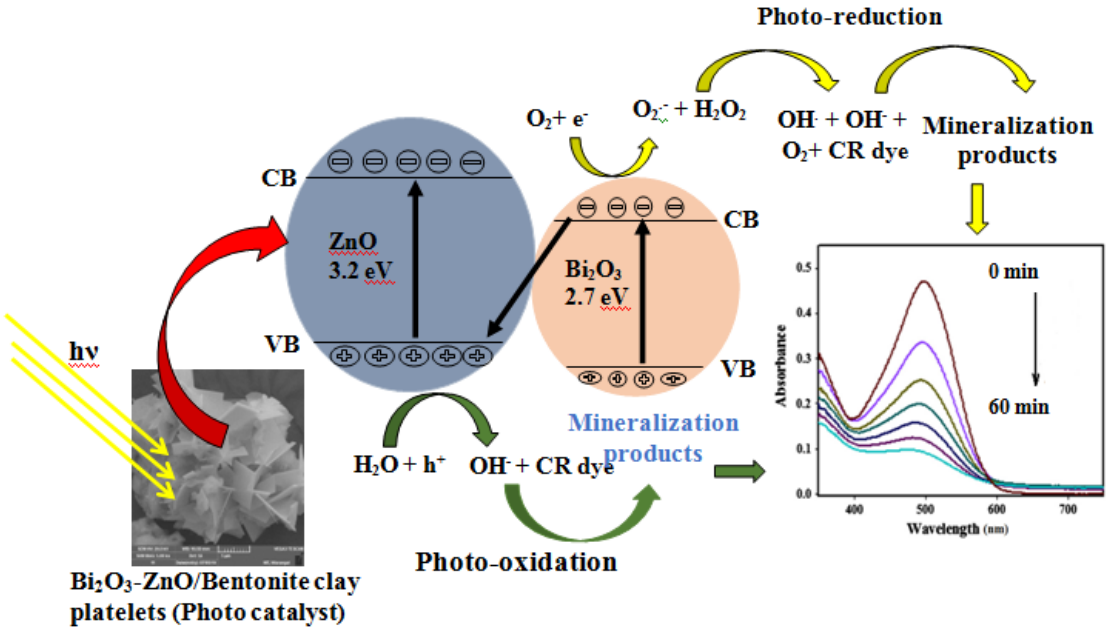

Figure 5.11 Reaction mechanism for the degradation of CR dye by photocatalysis on Bi_2O_3-ZnO/bentonite clay catalytic NCs.

When comparing to the already reported catalysts (Table 5.1), the as-produced catalytic Bi_2O_3-ZnO/bentonite clay NCs using the sonochemical approach turned out to be a far more effective photocatalyst for the oxidation of CR dye. The enhanced photocatalytic performance of Bi_2O_3-ZnO/bentonite clay is attributed to the synthesized binary metal oxide S-scheme heterojunction, which restrains the recombination of helpful electron-hole pairs, while facilitates the recombination of comparatively futile electron-hole pairs.

5.3. Photocatalytic degradation of CR dye over Cu-ZnO/TiO_2 Z-scheme NC photocatayst

5.3.1 Materials and methods

5.3.1.1. Reagents

As zinc precursor, zinc acetate ($C_4H_6O_4Zn{\cdot}2H_2O$, 98.5 %) (S.D. Fine Chemicals Pvt. Ltd., Chennai, India) was used. For copper, copper sulphate pentahydrate ($CuSO_4{\cdot}5H_2O$, 98.5 %) precursor from Hi-Media Laboratories Pvt. Ltd., Mumbai, India, was employed. The metals were reduced using sodium borohydride ($NaBH_4$, 97 %) obtained from Molychem, Mumbai, India. As a stabiliser, polyvinylpyrrolidone $(C_6H_9NO)_n$ (PVP, 11.5–12.8 %, MW 40,000, Hi-Media Laboratories Pvt. Ltd., India) was used. TiO_2 NPs support was obtained from Merck Pvt. Ltd., Bengaluru, India. Sigma-Aldrich (Hyderabad, India) provided the CR dye. De-ionized (DI) water was used to obtain precursor, reducing agent, and CR dye solutions.

5.3.1.2 Sonication assisted synthesis of Cu-ZnO/TiO_2 ternary heterojunction NC photocatalyst

The ternary Cu-ZnO/TiO_2 NC was synthesised via sonochemical co-reduction of $CuSO_4.5H_2O$ and $C_4H_6O_4Zn{\cdot}2H_2O$ in the presence of TiO_2 NPs as presented in Figure 5.12. At first, TiO_2 (0.25 g) NPs were dispersed in 100 mL DI water using ultrasonic irradiation for 10 min (20 kHz, 20 mm diameter, 220 W, pulse of 5 sec on and 5 sec off, Dakshin ultrasonicator, Mumbai, India). To this dispersion, 0.1 g $CuSO_4.5H_2O$, 0.1 g $C_4H_6O_4Zn{\cdot}2H_2O$ and PVP were added, and the solution was stirred until the metal precursors were completely dissolved. These metal precursors were then reduced with dropwise addition of 0.2 M $NaBH_4$ (50 mL) in the presence of ultrasonic irradiation. After the reaction, the resulting NC precipitate was separated and washed with DI water using centrifugation. The washed precipitate was then dried at 80 °C for 6 h to obtain the ternary Cu-ZnO/TiO_2 NC photocatalyst.

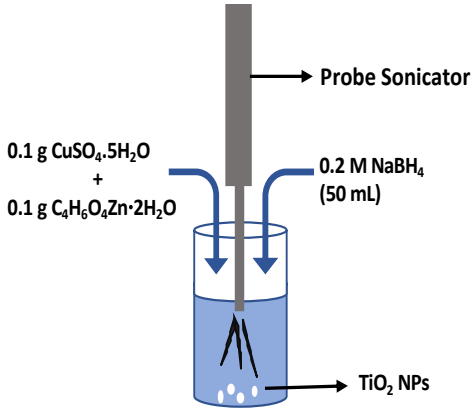

Figure 5.12 Schematic representation of synthesis of Cu-ZnO/TiO_2 NCs.

5.3.1.3 Characterization of as-prepared Cu-ZnO/TiO_2 NC photocatalyst

Fourier-transform infrared spectroscopy (FTIR) was carried out to check the functional groups bound to the surface of the as-prepared photocatalyst. The compact Fourier-transform infrared spectrometer of Bruker-ALPHA II with a resolution of 4 cm^{-1} between 4000 cm^{-1} and 400 cm^{-1} was utilised to record the FTIR. The crystal structure, phase detection and average crystallite size estimation of Cu-ZnO/TiO_2 were conducted using the XRD of the obtained Cu-ZnO/TiO_2. The XRD was performed using a Malvern Panalaytical X-ray diffractometer with CuKα radiation (1.5406 Å). The morphological aspects were studied with a high-resolution transmission electron microscope (HRTEM) (JEOL-JEM 2100, Tokyo, Japan) operated at 200 kV and the overall distribution of Cu, ZnO, and TiO_2 in the as-prepared NC was investigated with Carl Zeiss, EVO MA 15 (Oxford Instruments, Abingdon, UK) FESEM equipped with EDX. The optical properties of Cu-ZnO/TiO_2 were examined via UV-Vis-DRS conducted on Specord 210 Plus UV-vis spectrophotometer (Analytikjena, Jena, Germany). The surface area measurement was performed on Micromeritics ASAP 2020 BET analyser. Over time, the degradation of CR dye was observed via a double-beam UV-visible spectrophotometer (UV 2080 UV-visible spectrophotometer, Analytical Technologies Limited, Vadodara, India). The extent of CR dye mineralisation was investigated using a total organic carbon (TOC) analyser (TOC-L_{CPN} analyser, Shimadzu, Kyoto, Japan).

5.3.1.4 Photocatalytic performance of sunlight driven degradation of CR dye over Cu-ZnO/TiO_2

The photocatalytic efficiency of ternary Cu-ZnO/TiO_2 heterojunction NC catalyst was investigated to degrade CR dye under direct sunlight irradiation (average sunlight intensity = 800 W/m^2) in the month of March 2022 between 11:00 am to 12:00 pm. To a 50 mL CR dye solution (75 mg/L), 0.5 g/L Cu-ZnO/TiO_2 NC catalyst was added and maintained in the dark for up to 30 min with continuous stirring to establish the adsorption equilibrium. CR dye solution with catalyst was then subjected to direct sunlight illumination under constant stirring. The decrease in the concentration of CR with time was noted by recording the UV-visible absorbance of the reaction samples at regular intervals. The samples were collected at regular intervals, followed by catalyst separation using a centrifuge before UV-visible absorbance measurements. The CR degradation was computed using Eq. 5.1.

After the complete CR decomposition, the catalyst was extracted using a centrifuge, washed and dried. The stability of the catalyst was investigated by repeating the same photocatalytic

experiment using the recovered catalyst for five cycles consecutively, and the respective CR degradation was noted.

5.3.2 Results and discussion

A facile and rapid sonochemical approach facilitated the one-pot synthesis of the Cu-ZnO/TiO_2 NC photocatalyst. For comparison, pure Cu and pure ZnO catalysts were also synthesised using the sonochemical approach. Furthermore, a detailed characterization was conducted for the as-prepared NC photocatalyst using XRD, FTIR, BET, HRTEM, FESEM with EDX and elemental dot mapping to confirm the structural and morphological characteristics.

5.3.2.1 Structural and morphological characterization of Cu-ZnO/TiO_2 NC photocatalyst

A. Crystallographic study

The crystalline structure and average crystallite size were obtained through an XRD pattern. The XRD analysis was carried out at 10° to 100° at room temperature with Cu Kα radiation. The obtained XRD for the Cu-ZnO/TiO_2 NC photocatalyst, pure Cu, pure ZnO, and pure TiO_2 is presented in Figure 5.13. It could be observed that the characteristic diffraction peaks for individual Cu, ZnO, and TiO_2 shown in Figure 5.13 coincide with the peaks of the Cu-ZnO/TiO_2 NC photocatalyst and are indexed accordingly in Figure 5.13a. This confirms the presence of crystalline Cu and ZnO on the TiO_2 surface in the synthesized NC. The sharp diffraction peaks observed at 31.80°, 34.52°, 36.46°, 47.63°, 56.58°, and 62.97° in Figure 5.13a are attributed to (100), (002), (101), (102), (110), and (103) planes of the hexagonal crystalline structure of wurtzite ZnO. These results align with the JCPDS Card no. 36–1451 [64], while Cu displayed FCC structure in the Cu-ZnO/TiO_2 NC photocatalyst as (111), (200), (220), (311), and (222); planes were observed at 2θ = 43.34°, 50.52°, 74.2°, 89.90°, 95.22°, respectively, in Figure 5.13a and are indexed according to JCPDS card no. 04-0836 [65,66]. The XRD pattern (Figure 5.13a) also reveals the presence of mixed anatase and rutile phases of TiO_2 in the prepared NC as the characteristics peaks for rutile TiO_2 were observed at 36.46°(101), 43.34° (210), 56.58° (220), 62.97° (002) [JCPDS card no. 21-1276] along with anatase TiO_2 observed at 47.63°, 67.93°, and 74.20° corresponding to (200), (116), and (215) planes [JCPDS card no. 21-1272], respectively [21,67]. Figure 5.13d shows the XRD pattern for anatase TiO_2 according to JCPDS card no. 21-1272. While Figure 5.13a reveals the presence of both phases of TiO_2. The possible reason for the presence of both anatase and rutile phases of TiO_2 in the Cu-ZnO/TiO_2 NC photocatalyst could be the acoustic cavitation employed for the synthesis of Cu-ZnO/TiO_2 NC, as the local hot spots generated during cavitation can facilitate the

transformation of anatase to rutile phase owing to the high temperature and pressure conditions possessed by the local cavities. Munguti and Dejene [21] and Chen et al. [68] have also reported the transformation of anatase TiO_2 to rutile TiO_2 as a result of high temperature employed during the synthesis of NC.

The efficient production of Cu-ZnO/TiO_2 NC photocatalyst using the sonochemical technique is confirmed as the presented XRD pattern is entirely attributed to Cu, TiO_2, and ZnO (Figure 5.13a). The Cu-ZnO/TiO_2 NC synthesised via the sonochemical approach shows a highly crystalline structure and uniform particle size.

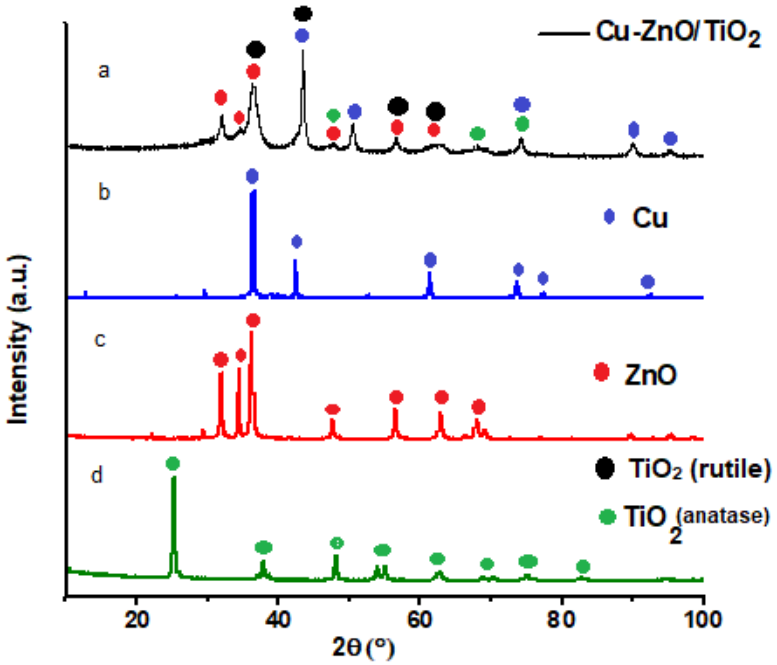

Figure 5.13 XRD pattern of the sonochemically synthesised Cu-ZnO/TiO_2 NC photocatalyst (a) Cu (b) ZnO (c) and TiO_2 (d) NPs.

B. Morphological analysis

The morphological characteristics of the Cu-ZnO/TiO_2 NC photocatalyst were studied using FESEM analysis (Figure 5.14a). The as-prepared NCs display spherical morphology with an approximately uniform size of 25 nm, as evident through the FESEEM micrograph, supporting the size calculations obtained through XRD analysis (24.27 nm). The distribution and composition of Cu-ZnO NPs over TiO_2 were investigated using FESEM-EDX and elemental dot mapping analysis, as shown in Figure 5.14b-c, respectively. The FESEM-EDX micrograph (Figure 5.14b) of the Cu-ZnO/TiO_2 NC reveals the sharp peaks of Cu, Zn, O, and Ti elements only, assuring the existence of Cu, ZnO, and TiO_2 in the NC photocatalyst.

In contrast, the peak corresponding to the C element arises due to the carbon tape used during EDX analysis. Table 5.2 lists the photocatalyst components and their wt%, with TiO_2 being the most abundant, followed by ZnO and Cu. The FESEM-EDX elemental dot mapping images (Figure 5.14c) illustrate the elemental dot distribution in the Cu-ZnO/TiO_2 NC photocatalyst. Overall, the uniform anchoring of Cu, Zn, Ti, and O was detected from the dot mapping of the constituent elements of the as-prepared NC photocatalyst, implying the achievement of even dispersion of Zn and Cu over the TiO_2 surface. This proves that the uniformity in shape, size, and distribution of dopant materials over the support surface is demonstrated through the co-reduction of Cu and Zn metal precursors over TiO_2 NPs assisted by ultrasound.

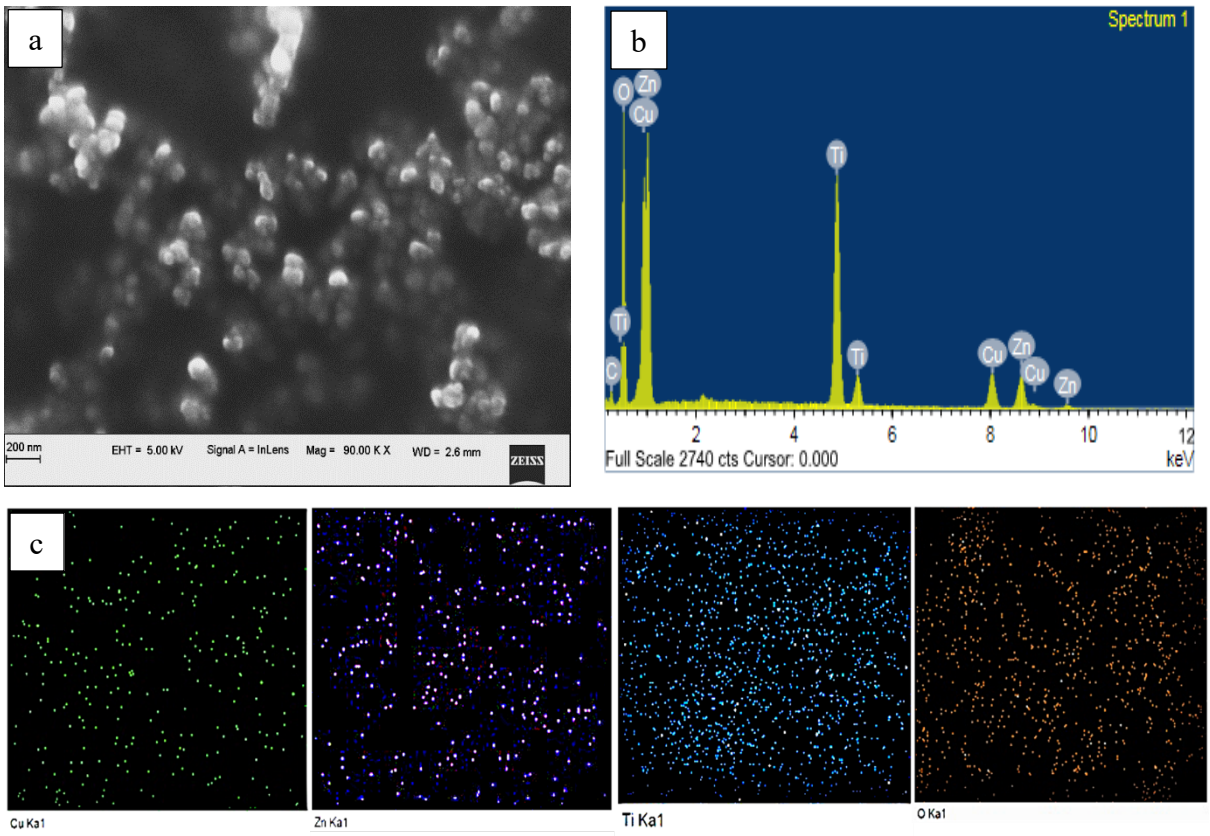

Figure 5.14 a) FESEM image (b) EDX (c) Elemental mapping images of Cu-ZnO/TiO_2 NC.

Table 5.3 Elemental composition of Cu-ZnO/TiO_2 NC photocatalyst on weight basis.

Cu-ZnO/TiO_2 NC	Cu (wt%)	Zn (wt%)	O (wt%)	Ti (wt%)	C (wt%)
Theoretical	10	15	60	20	-
FESEM-EDX	7.67	9.05	44.84	18.27	20.17

Furthermore, the detailed morphological characteristics of Cu-ZnO/TiO_2 NC were assessed by HRTEM images, as shown in Figure 5.15a-b. Figure 5.15a reveals that the as-synthesised NC photocatalyst displays a nearly spherical shape with the average NP size comparable to the crystallite size, which was deduced using the Debye–Scherrer equation. The uniform

deposition of Cu and ZnO over TiO_2 without aggregation can also be observed in Figure 5.15a. The HRTEM micrographs reveal the distinct lattice fringes indicating the formation of polycrystalline Cu-ZnO/TiO_2 NCs. As the TiO_2 and ZnO possess nearly the same characteristics, these semiconductors do not reflect any differences in the HRTEM images, as shown in Figure 5.15a. However, the dark-coloured particles represent Cu present on light-shaded TiO_2 and ZnO. Although TiO_2 and ZnO cannot be distinguished clearly through the HRTEM images, the lattice spacings of ca. 0.208 nm, 0.246 nm, and 0.19 nm belong to the diffraction planes of Cu (111), wurtzite ZnO (101), and anatase TiO_2 (200), respectively (Figure 5.15b). Thus, Figure 5.15b proves the co-existence of Cu and ZnO over TiO_2 and confirms the formation of a ternary Cu-ZnO/TiO_2 NC with Z-scheme heterojunction. In addition, the presence of Cu, ZnO, and TiO_2 was established through FESEM-EDX and elemental dot mapping analysis.

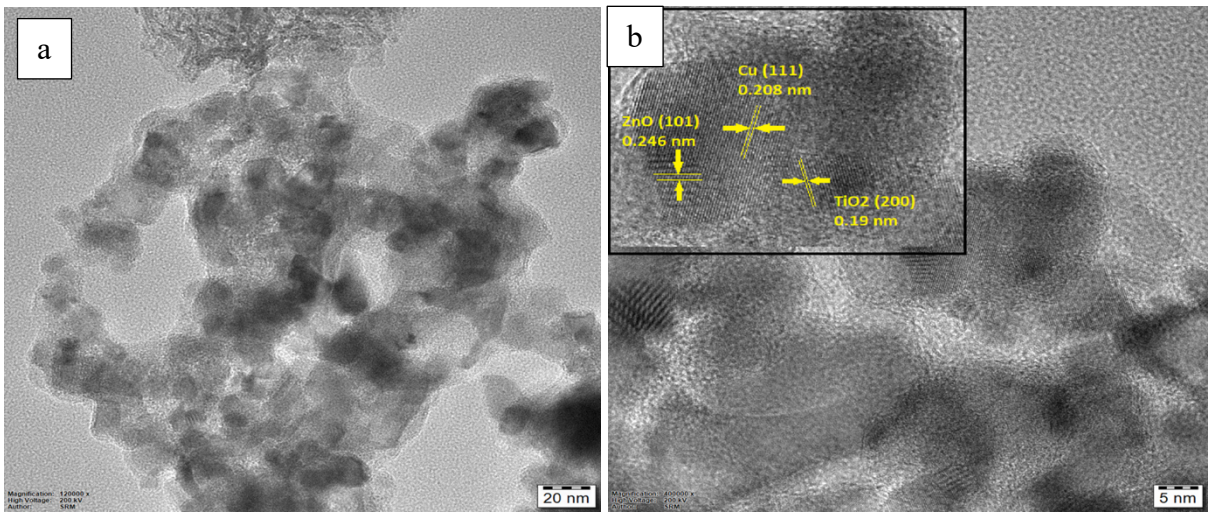

Figure 5. 15. (a-b) HRTEM images of Cu-ZnO/TiO_2 NC photocatalyst.

Notably, Cu-ZnO/TiO_2 NC fabrication exhibited uniform spherical Cu and Zn metal NPs with the particle size of the composite being about 25 nm and even distribution of Cu and ZnO over the TiO_2 surface is achieved successfully through the sonochemical approach.

C. FTIR analysis

The functional groups attached to the as-synthesised Cu-ZnO/TiO_2 NC photocatalyst were determined through the FTIR analysis conducted from 4000 to 400 cm^{-1}. The resultant FTIR spectrum for the Cu-ZnO/TiO_2 NC is depicted in Figure 5.16. The characteristic peaks belonging to the metal oxides lattice vibrations were below 1500 cm^{-1}. Accordingly, the band around 449 cm^{-1} is the distinctive peak for Zn-O stretching vibrations, while the band at 662 cm^{-1} arises due to Cu-O stretching. The bands related to Ti-O stretching vibration and Ti-O-Ti

skeleton bending vibrations could be observed at 713 and 1053 $cm^{-1,}$ respectively [25,27,69]. The symmetric and asymmetric stretching vibrations of Zn-O-Zn are observed through the intense peak at 1378 cm^{-1} [25]. The adsorbed moisture over the surface of Cu-ZnO/TiO_2 gives rise to the bending and stretching vibrations of -OH groups as seen through the bands at 1628 and 3446 cm^{-1}, respectively [69]. As reported, these -OH groups can be transformed into •OH radicals by releasing electrons to the available photogenerated holes [20,70]. Therefore, it is expected that the photocatalytic process can be boosted more exceptionally in the presence of such oxidative radicals. The band appearing at 2335 cm^{-1} is attributed to the adsorbed atmospheric CO_2, whereas the band at 2918 cm^{-1} indicates C-H stretching [21,66]. The IR peak of C-H at 2918 cm^{-1} may have appeared from the employed surfactant (PVP) molecules. Hence, FTIR confirms the facile synthesis of Cu-ZnO/TiO_2 via a sonochemical approach through the coexistence of Cu, ZnO and TiO_2 as their characteristic bands are revealed at 449, 622, 713, 1053 and 1378 cm^{-1}.

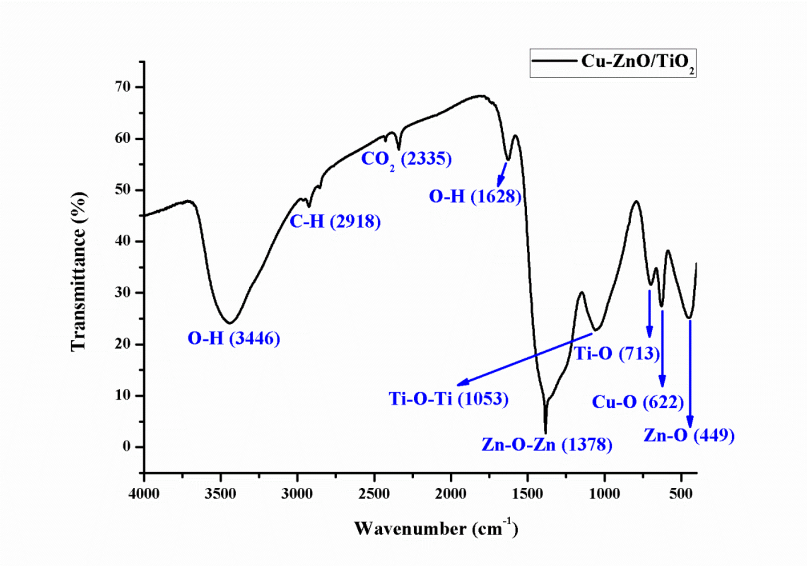

Figure 5.16 FTIR of the Cu-ZnO/TiO_2 NC photocatalyst.

D. BET measurements

The BET surface area of Cu-ZnO/TiO_2 evaluated from the BET surface area plot, as shown in Figure 5.17 a-b, was estimated to be 60.52 m^2/g. Before the test, sample was degassed at 523 K for 5 h in order to remove all the impurities like adsorbed gases and moisture from the sample. The external surface area and micropore volume were determined using the t-plot method and were 31.25 m^2/g and 13.98 m^2/g, respectively.

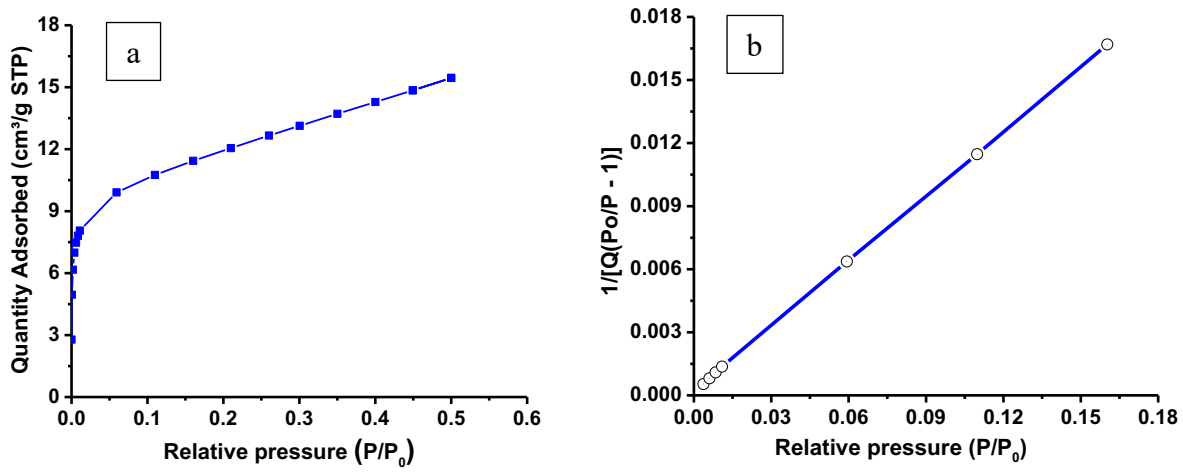

Figure 5.17 (a) BET isotherm linear plot (b) BET surface area plot for Cu-ZnO/TiO_2 (CZT-2) NC photocatalyst.

5.3.2.2 Photocatalytic performance of the Cu-ZnO/TiO_2 NC photocatalyst

The photocatalytic performance of the as-prepared catalytic Cu-ZnO/TiO_2 NC was estimated through the degradation of CR dye in the presence of natural sunlight. CR degradation studies were conducted under direct sunlight irradiation with and without the as-prepared NC photocatalysts. It was observed that CR degradation does not occur in the absence of photocatalyst even after 180 min of sunlight illumination. On the contrary, the CR degradation rates were higher in the presence of synthesised NC photocatalysts, which can be ascribed to the photocatalytic degradation of the catalysts. Then, CR degradation was attempted in the presence of as-prepared photocatalysts for up to 180 min in the dark. In the absence of sunlight illumination, significant colour change or change in the absorbance of CR dye was not detected. This suggests that the CR dye decomposition cannot proceed without the photocatalyst or sunlight.

The photocatalytic CR degradation was conducted under sunlight radiation over Cu-ZnO/TiO_2 photocatalysts. Before sunlight illumination, CR dye solution and photocatalyst were kept in the dark for about 30 min to ensure the adsorption and desorption equilibrium between the CR dye solution and photocatalyst. The UV-visible absorption spectra for the samples were recorded at fixed intervals. The absorbance for the distinctive peak of CR dye and the colour of CR dye gradually decreased with the sunlight illumination time, as shown in Figure 5.18. This implies the instantaneous onset of CR degradation with sunlight illumination over the Cu-ZnO/TiO_2 NC photocatalysts. The Cu-ZnO/TiO_2 NC photocatalysts offered higher photocatalytic performance than either individual ZnO, TiO_2, or Cu catalysts as reported by Munguti and Dejene [21], Pragathiswaran et al. [25], and Khaki et al. [30]. The Cu-ZnO/TiO_2

presented the improved photodegradation efficacy with almost complete photodegradation of CR dye after 20 min. This ultrafast CR dye decomposition was obtained due to the enhanced properties emerging from the synergy among Cu, ZnO, and TiO_2 in the NC photocatalyst. Figure 5.18 suggests that the characteristic absorbance peak of CR dye diminishes completely along with a simultaneous decrease in the intensity of dye solution colour until it becomes colourless within 20 min of sunlight exposure over Cu-ZnO/TiO_2 NC photocatalyst.

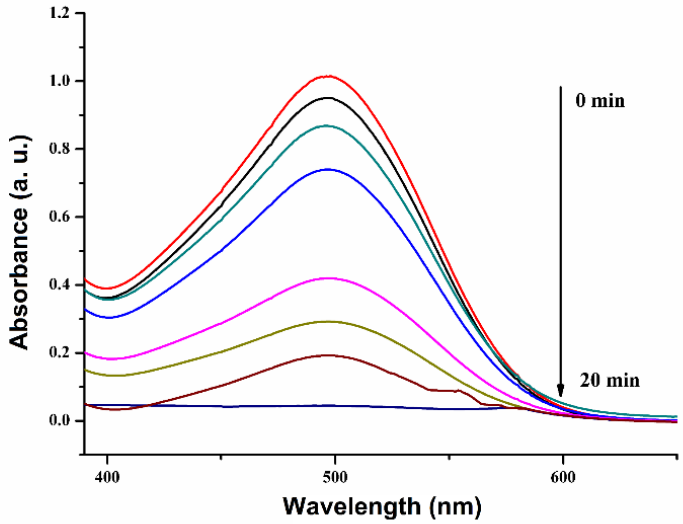

Figure 5.18 UV-Visible absorption spectra for CR degradation with time.

Khaki et al. reported similar catalytic activity for methyl orange and methylene blue dye degradation over Cu doped TiO_2/ZnO photocatalyst [30]. They have reported 85.45 % removal of methyl orange and 73.20 % removal of methylene blue over 0.6 g/L Cu-TiO_2/ZnO with an initial dye concentration of 20 ppm after 120 min of visible light irradiation. They synthesised the Cu-TiO_2/ZnO catalyst via the sol-gel method with three steps of sol preparation, drying of sol in electric oven followed by calcination and lastly ball milling to obtain the nano-sized Cu-TiO_2/ZnO composite. The synthesis process took approximately 18-20 h with an average crystallite size of 37.65 nm and rodlike morphology with the length of 300–400 nm and diameter of 50–60 nm. Whereas in this study with a sonochemical approach, the synthesis of Cu-ZnO/TiO_2 NC photocatalyst was accomplished within 45 min of sonochemical reduction followed by 6 h of drying. Moreover, an average crystallite size of 24.27 nm with spherical morphology was achieved. This suggests the superiority of the sonochemical approach for synthesising Cu-ZnO/TiO_2 NC photocatalyst over the sol-gel approach. Also, this insinuates the potential of as-prepared Cu-ZnO/TiO_2 NC photocatalyst for the removal of various recalcitrant dyes and phenolic compounds in wastewater streams using the sunlight energy.

A. Kinetic studies of CR decomposition over Cu-ZnO/TiO_2 NC photocatalyst

The UV-visible spectroscopy is useful to track CR degradation and is also useful for kinetic studies. Beer-Lambert law states that the absorbance intensity of dye is directly proportional to its concentration. Thus, the photocatalytic degradation rate of CR dye was investigated using the decreasing peak intensity at 498 nm, as illustrated in Figure 5.18. At the same time, the Langmuir-Hinshelwood model was employed to depict the kinetic studies between Cu-ZnO/TiO_2 photocatalyst and CR dye molecules. As the initial CR dye concentration (C_i) is small, this model can be considered to follow the pseudo-first-order rate equation (Eq. 5.3) [12,59].

This indicates that the apparent degradation rate constant (K_{app}) can be estimated from the slope of the linear fit of ln(C_i/C_t) *Vs.* irradiation time graph. Figure 5.19 elucidates the degradation kinetics plot for CR degradation over sunlight driven Cu-ZnO/TiO_2 NC photocatalyst. The correlation between ln (C_i/C_t) and t agrees well to a linear regression line with R^2= 0.99 and slope = 0.094, indicating that the K_{app} for photocatalytic CR degradation over Cu-ZnO/TiO_2 NC photocatalyst under sunlight irradiation is 0.094 min^{-1}.

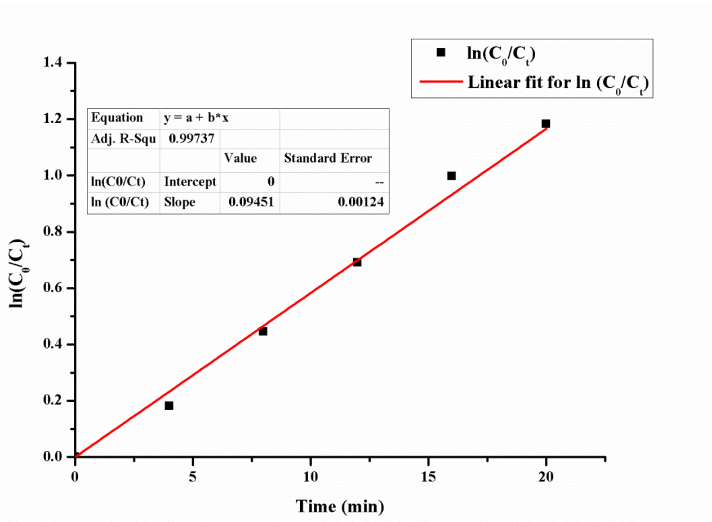

Figure 5.19 The CR degradation kinetic plot between ln (C_i/C_t) and time (t).

The degradation kinetics demonstrated by the Cu-ZnO/TiO_2 heterojunction NC photocatalyst for CR photocatalytic degradation is outstanding compared to the reported photocatalysts for CR degradation. Magdalane et al. reported 85 % CR degradation over TiO_2 doped $CoFe_2O_4$ photocatalyst after 120 min of visible light irradiation [71]. Yang et al. obtained 99.63 % CR degradation over ternary metal selenide-chitosan microspheres after 2 h of sunlight irradiation

[58]. Further, Aguilar et al. achieved 64.7 % CR degradation over ZnO-TiO_2 in 70 min of UV-light illumination. Whereas, with ZnO-TiO_2-Ag NC photocatalyst, 87.5 % CR degradation after 70 min of UV-light irradiation has been reported [42]. This signifies that the doping of ZnO-TiO_2 heterojunction with low-band-gap materials can greatly influence dye degradation [10,25]. The performance of various catalysts reported in the literature for CR dye degradation is exhibited in Table 5.3. As evident from Table 5.3, the composite materials reveal good photocatalytic efficiency compared to the individual materials. However, the Cu-ZnO/TiO_2 NC photocatalyst explored in this study manifested excellent efficiency towards CR removal in terms of initial CR concentration to catalyst-loading ratio, CR removal time, and K_{app} harnessing the natural sunlight. This swift removal of CR obtained in the present study can be attributed to the synergistic properties arising from incorporating Cu into ZnO-TiO_2 heterojunction. Also, a great improvement in photocatalyst's sunlight-driven excitation was observed due to the incorporation of Cu into the ZnO-TiO_2 heterojunction.

Table 5.4 Summary for the photocatalytic performance of different catalysts used for CR degradation

Catalyst	Catalytic Dosage (g)	CR Concentration (mg/L)	Degradation Time (min)	K_{app} (min^{-1})	Degradation (%)	Ref.
ZnO	0.05	16	60	0.0062	53.1	[12]
Pd-ZnO	0.05	16	60	0.0576	100	[12]
TiO_2 doped $CoFe_2O_4$	0.08	10	120	-	85	[71]
FeNiSe-CHM	0.2	60	140	-	99	[58]
ZBiSe-CM	0.225	40	120	0.045	99.63	[72]
ZnO/Geopolymer	0.2	5	60	0.048	96.97	[73]
g-C_3N_4/RGO/$Bi_2Fe_4O_9$	0.05	10	60	0.022	86.76	[59]
$PbTiO_3$	0.75	7	150	0.017	92	[52]
MgZnCr-TiO_2	0.05	100	40	-	98	[74]
TiO_2	0.1	17.4	30	-	87	[54]
CuO	0.05	20	210	-	67	[75]
CuO-ZnO/Egg shell	0.1	10	240	-	83	[60]
ZnO-TiO_2	0.1	70	70	0.0065	87.5	[42]
Cu-ZnO/TiO_2	**0.025**	**75**	**20**	**0.094**	**100**	**Present work**

B. Influence of catalyst loading, sunlight illumination time and initial CR concentration on the CR degradation

The catalyst loading has a considerable impact on the abasement of CR dye, as illustrated in Figure 5.20a. The impact of catalyst loading on the decomposition of CR was evaluated by varying the loading of Cu-ZnO/TiO_2 photocatalyst from 0.1 g/L to 0.8 g/L in the CR dye solution under sunlight irradiation for 20 min with an initial CR dye concentration of 75 mg/L. As illustrated in Figure 5.20a**,** it can be noticed that with an increase in the catalyst loading up to 0.5 g/L, the degradation of CR dye increases. This is because the accessibility of free reactive sites and the surface area increases with an increase in the catalyst loading and thus can generate more reactive radicals. The contact between CR dye molecules and reactive species increases as a larger surface area of the catalyst is available for the contact; this enhances the efficiency of CR dye decomposition up to 0.5 g/L catalyst loading. In contrast, a further increase in the catalyst loading does not improve the degradation efficiency of CR dye; however, it slightly reduces the degradation efficiency. This occurs as the dye solution becomes more and more impenetrable to sunlight irradiation as the catalyst loading increases. As a result, the availability of sunlight that can be absorbed on the reactive sites of the catalyst surface becomes inadequate, reducing the CR dye decomposition efficiency of the photocatalyst [50,72]. These results align with the studies reported by Khaki et al. [30] towards the photocatalytic degradation of methylene blue and methyl orange dye over sunlight activated Cu-TiO_2/ZnO.

The sunlight illumination time can greatly affect the CR degradation. As indicated earlier, without sunlight illumination, CR decomposition does not occur. Thus the decomposition of CR dye (75 mg/L) was observed from 0 min to 22 min over the Cu-ZnO/TiO_2 photocatalyst (0.5 g/L) and is as reflected in Figure 5.20b. The increase in CR degradation efficiency with increasing sunlight illumination time was observed until it reached 100 % after 20 min of sunlight illumination. Up to 15 min a rapid increase of 78 % CR decomposition after 15 min of contact time was recorded. On the contrary, beyond 15 min, the degradation rate increases gradually. This might occur due to the coverage of active sites on the surface of the photocatalyst as a high dye concentration (75 mg/L) was used for the photocatalytic decomposition studies. A similar trend in the decomposition of CR dye with time was also reported by Yang et al. [58].

Several researchers have reported that the decomposition of recalcitrant azo dyes can be significantly altered based on the initial CR dye concentration [30,52,58,76]. Hence, the CR removal efficiency of the as-prepared Cu-ZnO/TiO_2 photocatalyst was investigated by

changing the initial CR dye concentration from 55 mg/L to 95 mg/L with the catalyst loading of 0.5 g/L up to 15 min. As indicated in Figure 5.20c, it is evident that the CR removal efficiency declines with an increase in the initial CR concentration. The CR decomposition efficiency was reduced from 88 % to 60 % when the initial concentration increased from 55 mg/L to 95 mg/L after 15 min of sunlight. This phenomenon is apparent as the increasing CR concentration increases the rate of active site saturation of the photocatalyst surface and hinders the passage of photons to reach the photocatalyst surface by blocking the path of light due to excessive CR molecules in the suspension. Such interception of sunlight radiation reduces electron-hole pair generation, which significantly lowers the CR removal efficiency. This behaviour was also observed by Ma et al. [74], Bhagwat et al. [76], and Khan et al. [72].

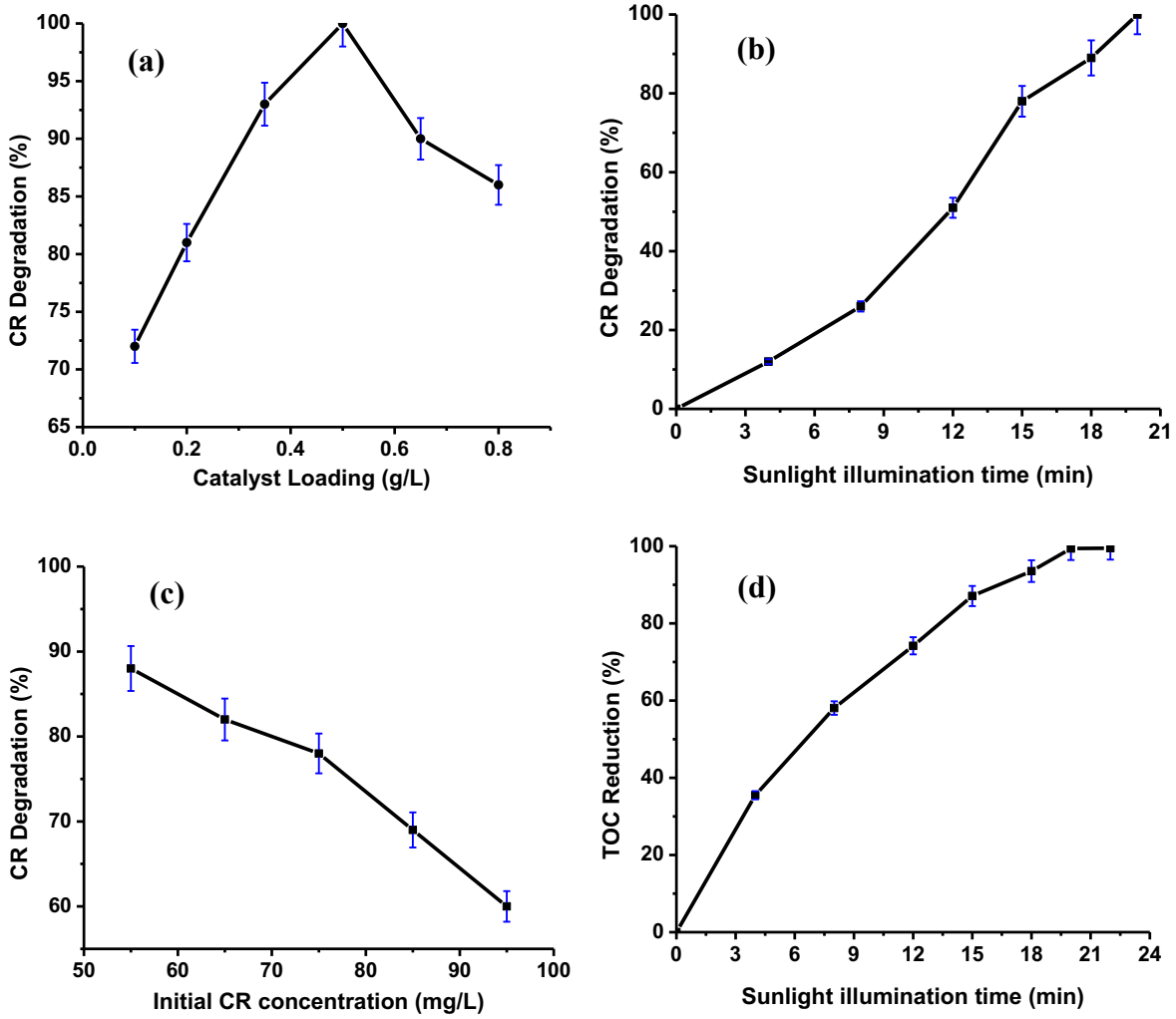

Figure 5.20 CR degradation efficiency with (a) Catalyst loading (b) Sunlight illumination time and (c) initial CR concentration and (d) TOC removal efficiency.

C. Assessment of TOC abatement during photocatalytic degradation of CR dye

The extent of mineralization of CR degradation (75 mg/L) was examined by analysing the TOC removal (%) with sunlight illumination time over Cu-ZnO/TiO_2 NC catalyst (0.5 g/L). The TOC removal efficiency is demonstrated in Figure 5.20d. A drastic reduction in TOC along with time could be observed, indicating increased mineralization with time. Almost complete mineralization of CR dye was achieved after 20 min of sunlight illumination, implying complete degradation of CR dye.

D. Photocatalyst stability

The stability and ease of recycling are the critical factors in determining the applicability of heterogeneous catalysts. The reusability of the photocatalyst in the sequential photocatalytic removal of CR dye was investigated in this work. In every recycle run, a fresh CR dye solution was used while the recycle photocatalyst was employed to conduct the recycle runs. The photocatalyst was separated and washed with DI water using a simple centrifugal operation at the end of each trial. The recovered photocatalysts were then utilized in another photocatalytic CR degradation process. Figure 5.21 depicts the reusability of the NC photocatalyst and the efficiency of CR dye degradation under sunlight illumination for five consecutive cycles. After the third run, a small drop in the catalytic activity was noticed. Overall, Cu-ZnO/TiO_2 photocatalyst demonstrates excellent stability for CR degradation up to 5 recycle runs with no significant loss in the catalytic activity.

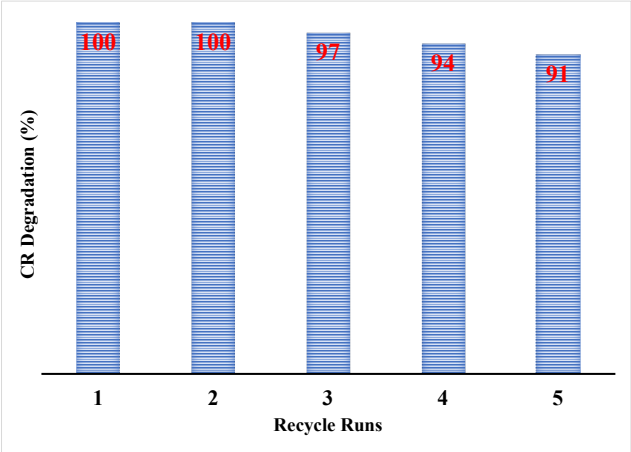

Figure 5.21 Reusability of Cu-ZnO/TiO_2 NC photocatalyst for CR degradation.

D. Plausible mechanism for the enhanced photocatalytic performance of Cu-ZnO/TiO_2 NC photocatalyst

Generally, for TiO_2-ZnO, type II heterojunction is reported between TiO_2 and ZnO, which is well known for obtaining an efficient degradation. In the TiO_2-ZnO type II heterojunction, mostly localization of electrons occurs on TiO_2 and holes are accumulated on ZnO, which prevents the recombination of the charge carriers, enhancing the photocatalytic activity [23]. However, the electron transfer is limited by the coulomb repulsions among photo-generated electrons. To overcome this, recently, a Z-scheme system has attracted widespread attention, which is an effective construction to boost the catalytic activities of photocatalysts [77]. An EM is added between the semiconductor heterojunction in the Z-scheme heterojunction. In the proposed NC photocatalyst, Cu plays the role of an EM between ZnO and TiO_2, which accelerates the transfer of electrons in the Cu-ZnO/TiO_2, thereby greatly improving the photocatalytic activity. As a result, the band alignment of Cu-ZnO/TiO_2 heterojunction is Z-scheme (Figure 5.22). Based on the above discussion and reported studies [68,77], a tentative mechanism for the photocatalytic degradation of CR dye over the Cu-ZnO/TiO_2 composite has been proposed.

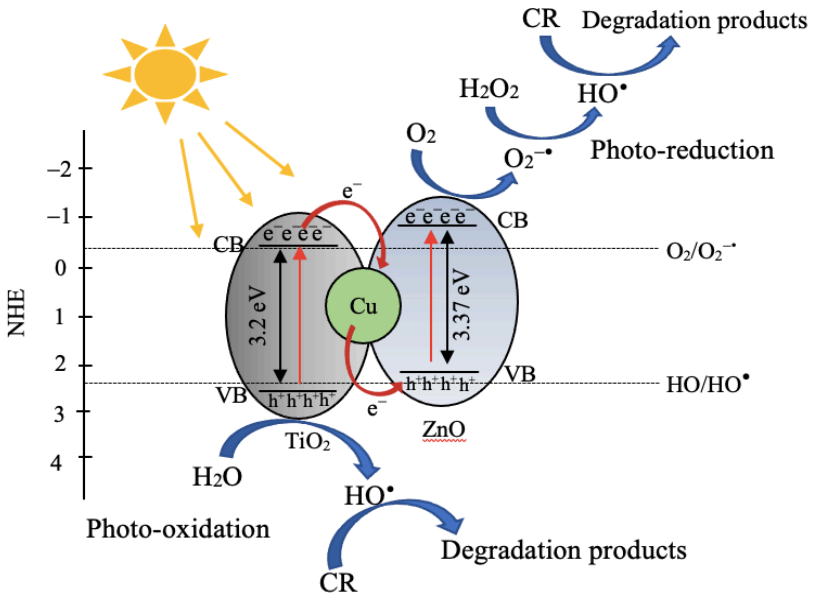

Figure 5.22 Charge transfer mechanism for Z-scheme Cu-ZnO/TiO_2 heterojunction photocatalyst for CR degradation.

The photo-induced electrons are preferably transferred from CB of TiO_2 to Cu, attributing to the more positive Fermi level of Cu than CB energy of TiO_2 by the strong interfacial built-in electronic field [77]. Since the Fermi level of Cu is lower than the VB energy of ZnO, the

trapped accumulated electrons in metal Cu will be partially transferred from the Fermi level of Cu to VB of ZnO, and the photo-generated holes of ZnO are quenched; hence, the photo-induced electrons of ZnO can be separated efficiently and enhance the reduction ability. Furthermore, the accumulated holes in the VB of TiO_2 will be able to oxidise the CR molecules. Owing to the reasons mentioned above, the Cu-ZnO/TiO_2 Z-scheme heterojunction exhibits an excellent photocatalytic activity. Thus, the Cu-ZnO/TiO_2 NC photocatalyst can efficiently promote photocatalytic degradation of CR dye. The possible charge transfer mechanism for the Cu-ZnO/TiO_2 NC photocatalyst towards CR dye degradation is illustrated in Figure 5.22.

5.4 Conclusion

In this study, S-scheme Bi_2O_3-ZnO/bentonite clay heterojunction and all solid-state Z-scheme Cu-ZnO/TiO_2 heterojunction NC photocatalysts were synthesized using the sonochemical approach. The average crystallite size of the Bi_2O_3-ZnO/bentonite clay and Cu-ZnO/TiO_2 NC photocatalysts was 45 nm and 24.27 nm respectively, as determined through XRD. The uniformity in shape and size with spherical morphology of the proposed NCs was illustrated through HRTEM and FESEM analyses. The photocatalytic activity of the Bi_2O_3-ZnO/bentonite clay and Cu-ZnO/TiO_2 NCs was evaluated for the photocatalytic CR dye decomposition. It was found that the Bi_2O_3-ZnO/bentonite clay heterojunction was more efficient UV-light irradiation whereas all solid-state Z-scheme Cu-ZnO/TiO_2 heterojunction showed excellent photocatalytic activity under natural sunlight irradiation. Nearly total degradation of CR was obtained in 1 h under UV light irradiation over the Bi_2O_3-ZnO/bentonite clay NC with pseudo-first-order rate constant of 0.029 min^{-1}. While, Cu-ZnO/TiO_2 photocatalyst revealed excellent photocatalytic efficacy as 100 % CR decomposition was attained after only 20 min of sunlight irradiation with the pseudo-first-order reaction rate constant of 0.094 min^{-1}. This enhancement in the photocatalytic activity was noted due to the excellent characteristics and catalytic properties offered by the synergy between Cu, ZnO, and TiO_2 present in the ternary Z-scheme heterojunction NC. Furthermore, both the Bi_2O_3-ZnO/bentonite clay and Cu-ZnO/TiO_2 NC photocatalyst's stability was studied for five successive recycle runs. Both the photocatalysts showed outstanding stability up to five recycle runs with no apparent loss in the catalytic performance. This implies that the NC photocatalysts synthesized via sonochemical approach can find its applications in wastewater treatment for photocatalytic degradation of various dyes, phenolic compounds, and other difficult-to-treat compounds. Furthermore, utilization of this

solar-light-responsive Cu-ZnO/TiO_2 NC photocatalyst can also offer the scale-up potential for treating textile wastewaters in bulk.

References

[1] M. Thomas, G.A. Naikoo, M. Ud, D. Sheikh, M. Bano, F. Khan, Effective photocatalytic degradation of Congo red dye using alginate/carboxymethyl cellulose/TiO_2 nanocomposite hydrogel under direct sunlight irradiation, J. Photochem. Photobiol. A Chem. (2016). https://doi.org/10.1016/j.jphotochem.2016.05.005.

[2] A. Moradzadeh, A. Mahjoub, M.S. Sadjadi, M.H. Sadr, N. Farhadyar, M. Seyed, M. Hossaini, N. Farhadyar, Investigation on synthesis, characterization and photo catalytic degradation of congo red by Zn-doped $CdTiO_3$/TiO_2, Polyhedron. 170 (2019) 404–411. https://doi.org/10.1016/j.poly.2019.05.060.

[3] D. Pathania, D. Gupta, A.H. Al-Muhtaseb, G. Sharma, A. Kumar, M. Naushad, T. Ahamad, S.M. Alshehri, Photocatalytic degradation of highly toxic dyes using chitosan-g-poly(acrylamide)/ZnS in presence of solar irradiation, J. Photochem. Photobiol. A Chem. 329 (2016) 61–68. https://doi.org/10.1016/j.jphotochem.2016.06.019.

[4] E. Cako, K.D. Gunasekaran, R.D. Cheshmeh Soltani, G. Boczkaj, Ultrafast degradation of brilliant cresyl blue under hydrodynamic cavitation based advanced oxidation processes (AOPs), Water Resour. Ind. 24 (2020). https://doi.org/10.1016/j.wri.2020.100134.

[5] S.P. Patil, B. Bethi, G.H.H. Sonawane, V.S.S. Shrivastava, S. Sonawane, Efficient adsorption and photocatalytic degradation of Rhodamine B dye over Bi_2O_3-bentonite nanocomposites: A kinetic study, J. Ind. Eng. Chem. 34 (2015) 1–8. https://doi.org/10.1016/j.jiec.2015.12.002.

[6] M.H. Habibi, M.H. Rahmati, The effect of operational parameters on the photocatalytic degradation of Congo red organic dye using ZnO–CdS core – shell nano-structure coated on glass by Doctor Blade method, Spectrochim. ACTA PART A Mol. Biomol. Spectrosc. 137 (2015) 160–164. https://doi.org/10.1016/j.saa.2014.08.110.

[7] S.P. Patil, R.P. Patil, V.K. Mahajan, G.H. Sonawane, V.S. Shrivastava, Semiconductor Processing Facile sonochemical synthesis of BiOBr-graphene oxide nanocomposite with enhanced photocatalytic activity for the degradation of Direct green, Mater. Sci. Semicond. Process. 52 (2016) 55–61. https://doi.org/10.1016/j.mssp.2016.05.008.

[8] N.F. Khairol, N. Sapawe, M. Danish, Excellent performance integrated both adsorption and photocatalytic reaction toward degradation of Congo Red by CuO / Eggshell, Mater. Today Proc. 19 (2019) 1340–1345.

[9] S. Wang, S.P. Jiang, Prospects of fuel cell technologies, Natl. Sci. Rev. 4 (2017) 163–166. https://doi.org/10.1093/nsr/nww099.

[10] Y. Liang, W. Li, X. Wang, R. Zhou, H. Ding, TiO_2–ZnO/Au ternary heterojunction nanocomposite: Excellent antibacterial property and visible-light photocatalytic hydrogen production efficiency, Ceram. Int. 48 (2021) 2826–2832. https://doi.org/10.1016/j.ceramint.2021.10.072.

[11] S.P. Pattnaik, A. Behera, S. Martha, R. Acharya, K. Parida, Synthesis, photoelectrochemical properties and solar light-induced photocatalytic activity of bismuth ferrite nanoparticles, J. Nanoparticle Res. 20 (2018). https://doi.org/10.1007/s11051-017-4110-5.

[12] N. Guy, S. Cakar, M. Ozacar, Comparison of palladium/zinc oxide photocatalysts prepared by different palladium doping methods for congo red degradation, J. Colloid Interface Sci. 466 (2016) 128–137. https://doi.org/10.1016/j.jcis.2015.12.009.

[13] E. Gong, S. Ali, C.B. Hiragond, H.S. Kim, N.S. Powar, D. Kim, H. Kim, S. Il In, Solar fuels: research and development strategies to accelerate photocatalytic CO_2 conversion into hydrocarbon fuels, Energy Environ. Sci. 15 (2021) 880–937. https://doi.org/10.1039/d1ee02714j.

[14] S.C. Motshekga, S.S. Ray, M.S. Onyango, M.N.B. Momba, Microwave-assisted synthesis, characterization and antibacterial activity of Ag/ZnO nanoparticles supported bentonite clay, J. Hazard. Mater. 262 (2013) 439–446. https://doi.org/10.1016/j.jhazmat.2013.08.074.

[15] K. Salehi, H. Daraei, P. Teymouri, B. Shahmoradi, A. Maleki, Cu-doped ZnO nanoparticle for removal of reactive black 5 : application of artificial neural networks and multiple linear regression for modeling and optimization, Desalin. Water Treat. 57 (2016) 22074–22080. https://doi.org/10.1080/19443994.2015.1130658.

[16] P. Pascariu, C. Cojocaru, N. Olaru, P. Samoila, A. Airinei, M. Ignat, L. Sacarescu, D.

Timpu, Novel rare earth (RE-La, Er, Sm) metal doped ZnO photocatalysts for degradation of Congo-Red dye: Synthesis, characterization and kinetic studies, J. Environ. Manage. 239 (2019) 225–234. https://doi.org/10.1016/j.jenvman.2019.03.060.

[17] S.M. Patil, S.P. Deshmukh, K. V More, V.B. Shevale, S.B. Mullani, A.G. Dhodamani, S.D. Delekar, Sulfated TiO_2/WO_3 nanocomposite: An efficient photocatalyst for degradation of Congo red and methyl red dyes under visible light irradiation, Mater. Chem. Phys. (2018). https://doi.org/10.1016/j.matchemphys.2018.12.041.

[18] H. Zhang, X. Wang, N. Li, J. Xia, Q. Meng, J. Ding, J. Lu, Synthesis and characterization of TiO_2/graphene oxide nanocomposites for photoreduction of heavy metal ions in reverse osmosis concentrate, RSC Adv. 8 (2018) 34241–34251. https://doi.org/10.1039/C8RA06681G.

[19] O. Yayapao, T. Thongtem, A. Phuruangrat, S. Thongtem, Synthesis and characterization of highly efficient Gd doped ZnO photocatalyst irradiated with ultraviolet and visible radiations, Mater. Sci. Semicond. Process. 39 (2015) 786–792. https://doi.org/10.1016/j.mssp.2015.06.039.

[20] A. Das, P.M. Kumar, M. Bhagavathiachari, R.G. Nair, Hierarchical ZnO-TiO_2 nanoheterojunction: A strategy driven approach to boost the photocatalytic performance through the synergy of improved surface area and interfacial charge transport, Appl. Surf. Sci. 534 (2020) 147321. https://doi.org/10.1016/j.apsusc.2020.147321.

[21] L. Munguti, F. Dejene, Effects of Zn : Ti molar ratios on the morphological , optical and photocatalytic properties of ZnO-TiO_2 nanocomposites for application in dye removal, Mater. Sci. Semicond. Process. 128 (2021) 105786. https://doi.org/10.1016/j.mssp.2021.105786.

[22] N. Suganthi, S. Thangavel, K. Kannan, Hibiscus subdariffa leaf extract mediated 2-D fern-like ZnO/TiO_2 hierarchical nanoleaf for photocatalytic degradation, FlatChem. 24 (2020) 100197. https://doi.org/10.1016/j.flatc.2020.100197.

[23] M.M. Ali, M.J. Haque, M.H. Kabir, M.A. Kaiyum, M.S. Rahman, Nano synthesis of ZnO–TiO_2 composites by sol-gel method and evaluation of their antibacterial, optical and photocatalytic activities, Results Mater. 11 (2021) 100199. https://doi.org/10.1016/j.rinma.2021.100199.

[24] S.R. Shirsath, D. V Pinjari, P.R. Gogate, S.H. Sonawane, A.B. Pandit, Ultrasound assisted synthesis of doped TiO_2 nano-particles : Characterization and comparison of effectiveness for photocatalytic oxidation of dyestuff effluent, Ultrason. -

Sonochemistry. 20 (2013) 277–286. https://doi.org/10.1016/j.ultsonch.2012.05.015.

[25] C. Pragathiswaran, C. Smitha, B.M. Abbubakkar, P. Govindhan, N.A. Krishnan, Synthesis and characterization of TiO_2/ZnO-Ag nanocomposite for photocatalytic degradation of dyes and anti-microbial activity, Mater. Today Proc. 45 (2021) 3357–3364. https://doi.org/10.1016/j.matpr.2020.12.664.

[26] S. Janitabar-Darzi, A.R. Mahjoub, Investigation of phase transformations and photocatalytic properties of sol-gel prepared nanostructured ZnO/TiO_2 composites, J. Alloys Compd. 486 (2009) 805–808. https://doi.org/10.1016/j.jallcom.2009.07.071.

[27] P. Van Viet, T. Hoang The Vinh, N. Thi Ngoc Dung, C. Minh Thi, Facile ball-milling synthesis of TiO_2 modified ZnO for efficient photocatalytic removal of atmospheric nitric oxide gas under solar light irradiation, Chem. Phys. Lett. 775 (2021) 138642. https://doi.org/10.1016/j.cplett.2021.138642.

[28] A. Hosseini, H. karimi, J. Foroughi, M.M. Sabzehmeidani, M. Ghaedi, Heterogeneous photoelectro-Fenton using ZnO and TiO_2 thin film as photocatalyst for photocatalytic degradation Malachite Green, Appl. Surf. Sci. Adv. 6 (2021) 100126. https://doi.org/10.1016/j.apsadv.2021.100126.

[29] T. Quang, Q. Viet, V. Hoang, N. Thi, H. Giang, Statistical screening and optimization of photocatalytic degradation of methylene blue by ZnO–TiO_2/rGO nanocomposite, Colloids Surfaces A Physicochem. Eng. Asp. 629 (2021) 127464.

[30] M.R. Delsouz Khaki, M.S. Shafeeyan, A.A.A. Raman, W.M.A.W. Daud, Evaluating the efficiency of nano-sized Cu doped TiO_2/ZnO photocatalyst under visible light irradiation, J. Mol. Liq. 258 (2018) 354–365. https://doi.org/10.1016/j.molliq.2017.11.030.

[31] Q. Xu, L. Zhang, B. Cheng, J. Fan, J. Yu, S-scheme heterojunction photocatalyst, Chem. 6 (2020) 1543–1559. https://doi.org/10.1016/j.chempr.2020.06.010.

[32] J. Fu, Q. Xu, J. Low, C. Jiang, J. Yu, Ultrathin 2D/2D WO_3/g-C_3N_4 step-scheme H_2-production photocatalyst, Appl. Catal. B Environ. 243 (2019) 556–565. https://doi.org/10.1016/j.apcatb.2018.11.011.

[33] C. Pan, Y. Yan, H. Li, S. Hu, Synthesis of Bismuth oxide nanoparticles by a templating method and its photocatalytic performance, Adv. Mater. Res. 557–559 (2012) 615–618. https://doi.org/10.4028/www.scientific.net/AMR.557-559.615.

[34] M. Chen, P. Liu, C. Wang, G. Diao, Fast catalytic reduction of an azo dye by recoverable and reusable Fe_3O_4@PANI@Au magnetic composites, New J. Chem. 38 (2014) 4566–

4573. https://doi.org/10.1039/C4NJ00806E.

[35] E. Binaeian, H.A. Tayebi, A.S. Rad, M. Payab, Surface modification of mesoporous silicate by tannin for immobilization of TiO_2 nanoparticles: Study of photocatalytic performance, Mater. Chem. Phys. 185 (2017) 14–23. https://doi.org/10.1016/j.match emphys. 2016.09.055.

[36] M. Tang, X. Li, C. Gao, X. Li, H. Qiu, Adsorption performance of $CuFe_2O_4$/rGO nanocomposites towards organic dye, Mater. Chem. Phys. 185 (2017) 114–121. https://doi.org/10.1016/j.matchemphys.2016.10.012.

[37] N. Khaorapapong, N. Khumchoo, M. Ogawa, Preparation of zinc oxide-montmorillonite hybrids, Mater. Lett. 65 (2011) 657–660. https://doi.org/10.1016/j.matlet.2010.11.052.

[38] S.P. Patil, V.S. Shrivastava, G.H. Sonawane, Photocatalytic degradation of Rhodamine 6G using ZnO-montmorillonite nanocomposite: a kinetic approach, Desalin. Water Treat. 54 (2015) 374–381. https://doi.org/10.1080/19443994.2014.883334.

[39] U. Riaz, S.M. Ashraf, A. Ruhela, Catalytic degradation of orange G under microwave irradiation with a novel nanohybrid catalyst, J. Environ. Chem. Eng. 3 (2015) 20–29. https://doi.org/10.1016/j.jece.2014.06.010.

[40] S.P. Patil, V.S. Shrivastava, G.H. Sonawane, S.H. Sonawane, Synthesis of novel Bi_2O_3-montmorillonite nanocomposite with enhanced photocatalytic performance in dye degradation, J. Environ. Chem. Eng. 3 (2015) 2597–2603. https://doi.org/10.1016/j. jece.2015.09.005.

[41] T. Qu, H. Xu, Photocatalytic degradation of Methyl Orange over $BiOCl_xBr_{1-x}$ ($0 \leq \times \leq 1$) solid solutions, 2014 Int. Conf. Mechatronics, Electron. Ind. Control Eng. MEIC 2014. (2014) 353–356. https://doi.org/10.2991/meic-14.2014.79.

[42] C.A. Huerta-Aguilar, V. Palos-Barba, P. Thangarasu, R.T. Koodali, Visible light driven photo-degradation of Congo red by TiO_2–ZnO/Ag: DFT approach on synergetic effect on band gap energy, Chemosphere. 213 (2018) 481–497. https://doi.org/10.1016/j.chem osphere.2018.09.053.

[43] T. Hou, L. Chen, Y. Xin, W. Zhu, C. Zhang, W. Zhang, S. Liang, L. Wang, Porous CuFe for plasmon-assisted N_2 photofixation, ACS Energy Lett. 5 (2020) 2444–2451. https://doi.org/10.1021/acsenergylett.0c00959.

[44] J. Nie, A.O.T. Patrocinio, S. Hamid, F. Sieland, J. Sann, S. Xia, D.W. Bahnemann, J. Schneider, New insights into the plasmonic enhancement for photocatalytic H_2 production by Cu-TiO_2 upon visible light illumination, Phys. Chem. Chem. Phys. 20

(2018) 5264–5273. https://doi.org/10.1039/c7cp07762a.

[45] C.M.B. Hincapie, M.J.P. Cardenas, J.E.A. Orjuela, E.R. Parra, J.J. Olaya Florez, Physical-chemical properties of bismuth and bismuth oxides: Synthesis, characterization and applications, DYNA. 79 (2012) 139–148.

[46] L.F. Dalvand, F. Hosseini, S.M. Dehaghi, E.S. Torbati, Inhibitory effect of bismuth oxide nanoparticles produced by Bacillus licheniformis on Methicillin-resistant staphylococcus aureus Strains (MRSA), Iran. J. Biotechnol. 16 (2018). https://doi. org/10. 21859/ijb.2102.

[47] P.K. Labhane, G.H. Sonawane, S.H. Sonawane, Influence of rare-earth metal on the zinc oxide nanostructures : application in the photocatalytic degradation of methylene blue and p-nitro phenol, Green Process. Synth. 4 (2018) 360–371.

[48] R. Reddy T, K. S, E. T, L. Reddy S, R.R. T, S. Kaneko, T. Endo, L.R. S, Spectroscopic characterization of bentonite, J. Lasers , Opt. Photonics. 4 (2017). https://doi.org/10. 4172/2469-410X.1000171.

[49] R. Parimaladevi, I. Suganya, Synthesis and photoluminescence property of bentonite doped zinc oxide nanoparticles, Int. J. Mater. Sci. Eng. Synth. 4 (2016) 133–138. https://doi.org/10.17706/ijmse.2016.4.2.133-138.

[50] V.K. Landge, S.H. Sonawane, M. Sivakumar, S.S. Sonawane, G. Uday Bhaskar Babu, G. Boczkaj, S-scheme heterojunction Bi_2O_3-ZnO/Bentonite clay composite with enhanced photocatalytic performance, Sustain. Energy Technol. Assessments. 45 (2021) 101194. https://doi.org/10.1016/j.seta.2021.101194.

[51] C. Vidya, C. Manjunatha, M.N. Chandraprabha, M. Rajshekar, A.R.M.A. L, Hazard free green synthesis of ZnO nano-photo-catalyst using Artocarpus Heterophyllus leaf extract for the degradation of Congo red dye in water treatment applications, Biochem. Pharmacol. (2017). https://doi.org/10.1016/j.jece.2017.05.058.

[52] U.O. Bhagwat, J.J. Wu, A.M. Asiri, S. Anandan, Photocatalytic degradation of congo red using $PbTiO_3$ nanorods synthesized via a sonochemical approach, ChemistrySelect. 3 (2018) 11851–11858. https://doi.org/10.1002/slct.201802303.

[53] G.B. Jegadeesan, S. Amirthavarshini, J. Divya, G.I. Gunarani, Catalytic peroxygen activation by biosynthesized iron nanoparticles for enhanced degradation of Congo red dye, Adv. Powder Technol. (2019). https://doi.org/10.1016/j.apt.2019.08.034.

[54] D. Ljubas, G. Smoljani, H. Jureti, Degradation of Methyl Orange and Congo Red dyes by using TiO_2 nanoparticles activated by the solar and the solar-like radiation, J.

Environ. Manage. 161 (2015) 83–91. https://doi.org/10.1016/j.jenvman.2015.06.042.

[55] P.K. Labhane, L.B. Patle, G.H. Sonawane, S.H. Sonawane, Fabrication of ternary Mn doped ZnO nanoparticles grafted on reduced graphene oxide (RGO) sheet as an efficient solar light driven photocatalyst, Chem. Phys. Lett. 710 (2018) 70–77. https://doi.org/10.1016/j.cplett.2018.08.066.

[56] R. Tanwar, S. Kumar, U. Kumar, Photocatalytic activity of PANI/Fe^0 doped BiOCl under visible light-degradation of Congo red dye, Journal Photochem. Photobiol. A Chem. 333 (2017) 105–116. https://doi.org/10.1016/j.jphotochem.2016.10.022.

[57] T. Linda, S. Muthupoongodi, X.S. Shajan, S. Balakumar, Photocatalytic degradation of congo red and crystal violet dyes on Cellulose/PVC/ZnO composites under UV light irradiation, Mater. Today Proc. 3 (2016) 2035–2041. https://doi.org/10.1016/j.matpr.2016.04.106.

[58] Y. Yang, N. Ali, A. Khan, S. Khan, S. Khan, H. Khan, S. Xiaoqi, W. Ahmad, S. Uddin, N. Ali, M. Bilal, Chitosan-capped ternary metal selenide nanocatalysts for efficient degradation of Congo red dye in sunlight irradiation, Int. J. Biol. Macromol. 167 (2021) 169–181. https://doi.org/10.1016/j.ijbiomac.2020.11.167.

[59] M.B. Shekardasht, M.H. Givianrad, P. Gharbani, Z. Mirjafary, A. Mehrizad, Preparation of a novel Z-scheme g-C_3N_4/RGO/$Bi_2Fe_4O_9$ nanophotocatalyst for degradation of Congo Red dye under visible light, Diam. Relat. Mater. 109 (2020) 108008. https://doi.org/10.1016/j.diamond.2020.108008.

[60] N.F. Khairol, N. Sapawe, M. Danish, Photocatalytic study of ZnO-CuO/ES on degradation of congo red, Mater. Today Proc. 19 (2019) 1333–1339. https://doi.org/10.1016/j.matpr.2019.11.146.

[61] S. Ahmad, X. Su, C. Yang, X. Wang, X. Liu, J. Wang, Space-confined growth of layered basic zinc acetate nanosheets and their orderly fragmented ZnO nanoparticles on clay platelets, J. Hazard. Mater. 371 (2019) 213–223. https://doi.org/10.1016/j.jhazmat.2019.02.111.

[62] Z. dong Fang, K. Zhang, J. Liu, J. yu Fan, Z. wei Zhao, Fenton-like oxidation of azo dye in aqueous solution using magnetic Fe_3O_4-MnO_2 nanocomposites as catalysts, Water Sci. Eng. 10 (2017) 326–333. https://doi.org/10.1016/j.wse.2017.10.005.

[63] C.S.D. Rodrigues, R.A.C. Borges, V.N. Lima, L.M. Madeira, p-Nitrophenol degradation by Fenton's oxidation in a bubble column reactor, J. Environ. Manage. 206 (2018) 774–785. https://doi.org/10.1016/j.jenvman.2017.11.032.

[64] S.B. Potdar, B.V.S. Praveen, S.H. Sonawane, Sonochemical approach for synthesis of zinc oxide-poly methyl methacrylate hybrid nanoparticles and its application in corrosion inhibition, Ultrason. Sonochem. 68 (2020) 105200. https://doi.org/10.1016/j.ultsonch.2020.105200.

[65] A. Khan, A. Rashid, R. Younas, R. Chong, A chemical reduction approach to the synthesis of copper nanoparticles, Int. Nano Lett. 6 (2016) 21–26. https://doi.org/10.1007/s40089-015-0163-6.

[66] V.K. Landge, S.H. Sonawane, R. V. Chaudhari, G.U.B. Babu, Selective oxidation of glycerol: a biomass-derived feedstock using the Pt-Cu Janus catalyst for value-added products, Ind. Eng. Chem. Res. 60 (2021) 185–195. https://doi.org/10.1021/acs.iecr.0c04626.

[67] M. An, L. Li, Q. Wu, H. Yu, X. Gao, W. Zu, J. Guan, Y. Yu, CdS QDs modified three-dimensional ordered hollow spherical $ZnTiO_3$-ZnO-TiO_2 composite with improved photocatalytic performance, J. Alloys Compd. 895 (2021) 162638. https://doi.org/10.1016/j.jallcom.2021.162638.

[68] B. Chen, J. Zhang, J. Yu, R. wang, B. He, J. Jin, H. Wang, Y. Gong, Rational design of all-solid-state TiO_{2-x}/Cu/ZnO Z-scheme heterojunction via ALD-assistance for enhanced photocatalytic activity, J. Colloid Interface Sci. 607 (2022) 760–768. https://doi.org/10.1016/j.jcis.2021.09.023.

[69] A.M. Mohammed, S.S. Mohtar, F. Aziz, M. Aziz, A. Ul-Hamid, W.N. Wan Salleh, N. Yusof, J. Jaafar, A.F. Ismail, Ultrafast degradation of Congo Red dye using a facile one-pot solvothermal synthesis of cuprous oxide/titanium dioxide and cuprous oxide/zinc oxide p-n heterojunction photocatalyst, Mater. Sci. Semicond. Process. 122 (2021) 105481. https://doi.org/10.1016/j.mssp.2020.105481.

[70] T. Khalafi, F. Buazar, K. Ghanemi, Phycosynthesis and enhanced photocatalytic activity of zinc oxide nanoparticles toward organosulfur pollutants, Sci. Rep. 9 (2019) 1–10. https://doi.org/10.1038/s41598-019-43368-3.

[71] C.M. Magdalane, G.M.A. Priyadharsini, K. Kaviyarasu, A.I. Jothi, G.G. Simiyon, Synthesis and characterization of TiO_2 doped cobalt ferrite nanoparticles via microwave method: Investigation of photocatalytic performance of congo red degradation dye, Surfaces and Interfaces. 25 (2021) 101296. https://doi.org/10.1016/j.surfin.2021.101296

[72] S. Khan, A. Khan, N. Ali, S. Ahmad, W. Ahmad, S. Malik, N. Ali, H. Khan, S. Shah, M. Bilal, Degradation of Congo red dye using ternary metal selenide-chitosan

microspheres as robust and reusable catalysts, Environ. Technol. Innov. 22 (2021) 101402. https://doi.org/10.1016/j.eti.2021.101402.

[73] C. Sarkar, J.K. Basu, A.N. Samanta, Synthesis of novel ZnO/Geopolymer nanocomposite photocatalyst for degradation of congo red dye under visible light, Environ. Nanotechnology, Monit. Manag. 16 (2021). https://doi.org/10.1016/j.enmm. 2021.100521.

[74] C. Ma, F. Wang, C. Zhang, Z. Yu, J. Wei, Z. Yang, Y. Li, Z. Li, M. Zhu, L. Shen, G. Zeng, Photocatalytic decomposition of Congo red under visible light irradiation using MgZnCr-TiO_2 layered double hydroxide, Chemosphere. 168 (2017) 80–90. https://doi. org/10.1016/j.chemosphere.2016.10.063.

[75] A. Sadollahkhani, Z. Hussain, S. Elhag, O. Nur, M. Willander, Photocatalytic properties of different morphologies of CuO for the degradation of Congo red organic dye, Ceram. Int. 40 (2014) 11311–11317. https://doi.org/10.1016/j.ceramint.2014.03.132.

[76] Ujwala O. Bhagwat, J.J. Wu, A.M. Asiri, S. Anandan, Sonochemical synthesis of Mg-TiO_2 nanoparticles for persistent Congo red dye degradation, Journal Photochem. Photobiol. A Chem. (2017). https://doi.org/10.1016/j.jphotochem.2017.06.043.

[77] J. Yang, C. Shi, Y. Dong, H. Su, H. Sun, Y. Guo, S. Yin, Efficient hydrogen generation of vector Z-scheme $CaTiO_3$/Cu/TiO_2 photocatalyst assisted by cocatalyst Cu nanoparticles, J. Colloid Interface Sci. 605 (2022) 373–384. https://doi.org/10.1016/j. jcis.2021.07.106.

Chapter 6.

Overall Conclusions

6.1. Summary on overall work

In consideration with the importance of catalysts in various industrial and environmental applications, the present work reported the development of supported metal, and metal oxides based nanocomposite (NC) catalysts for important catalytic conversions. The sonochemical approach was employed for the synthesis of bimetallic Pt-Cu/C (flower-shaped) and Cu-Ni/TiO_2 NCs; hybrid inorganic (metal)-organic Pt-Co/cellulose nanofibers (CNFs) and Ag-Co/CNFs NCs; and binary metal oxide Bi_2O_3-ZnO/bentonite clay and ternary Cu-ZnO/TiO_2 NCs as heterogeneous catalysts for the selective catalytic reactions (Glycerol oxidation, 4-nitrophenol reduction, & photodegradation of Congo red: an azo dye). The synthesis of NCs was confirmed with various nanomaterial characterization techniques for instance XRD, HR-TEM, FESEM, FESEM-EDX with elemental dot mapping, FTIR, BET surface area measurements. The prepared NCs showed uniform distribution over the support and exhibited the particle size in the range of 5-50 nm. In this research, the sonochemical method is successfully demonstrated as a prominent method to synthesize the heterostructured materials for catalytic application. Based on the research outcomes, the following conclusions have been established.

The seed mediated sonochemical approach was employed for the synthesis of bimetallic Pt-Cu/C and ultrasound assisted co-reduction was conducted for the synthesis of Cu-Ni/TiO_2 NCs as heterogeneous catalysts for the selective oxidation of GLY. The Pt−Cu/C show flowerlike morphology as a result of seed mediated growth of NC while the simultaneous reduction of metal precursors resulted in spherical morphology of Cu-Ni/TiO_2. The catalytic activity of the bimetallic Pt−Cu/C and Cu-Ni/TiO_2 NCs was studied for the aqueous phase partial oxidation of glycerol (GLY), a model oxidation reaction. The production of GA is favoured over Pt-Cu/C NC catalyst whereas Ni-Cu/TiO_2 NC catalyst offered production of LA. Under mild operating conditions, the GLY oxidation over Pt-Cu/C showed 96 % GLY conversion within 1hour of reaction time with a selectivity of 65 % towards GA. Further, after 4 hours of reaction time GLY conversion of 98.8 % was achieved with an excellent combined selectivity of 74 % towards value added dicarboxylic acids (58 % towards TA and 16 % towards GLYA). On contrary to this, ultrasound induced GLY oxidation over Ni-Cu/TiO_2 showed maximum selectivity for LA as 84 % with 98.4 % GLY conversion.

Further, the successful synthesis of cellulose-based organic-inorganic NCs has been illustrated with the impregnation of Pt-Co, and Ag-Co NPs on the cellulose nanofibers (CNFs) with the assistance of ultrasound. The catalytic application of the as-prepared NCs was explored for the reduction of lethal 4-nitrophenol (4-NP) as model reduction reaction using surplus $NaBH_4$, leading to pseudo-first-order reaction kinetics. The complete conversion of 4-NP was obtained within 98 s of reaction time over Pt-Co/CNF NC catalyst with k_{app} = 0.0286 s^{-1} whereas the reduction of 4-NP was completed within 110 s (k_{app} = 0.0172 s^{-1}) with Ag-Co/CNF. The promising catalytic activity of the reported NCs can offer prominent catalytic performance for the reduction of numerous nitro-aromatic noxious wastes and dyes with nitro groups.

While, in the third system the S-scheme Bi_2O_3-ZnO/bentonite clay heterojunction and all solid-state Z-scheme Cu-ZnO/TiO_2 heterojunction NC photo-catalysts were developed for the photocatalytic degradation of Congo red (CR) dye. It was found that the Bi_2O_3-ZnO/bentonite clay heterojunction was more efficient UV-light irradiation whereas all solid-state Z-scheme Cu-ZnO/TiO_2 heterojunction showed excellent photocatalytic activity under natural sunlight irradiation. The Bi_2O_3-ZnO/bentonite clay NCs exhibited good catalytic activity (k_{app} = 0.029 min^{-1}) towards degradation of CR. The complete degradation of CR was obtained within 1 h of UV light irradiation in the presence of Bi_2O_3-ZnO/bentonite clay NC photocatalyst. The photodegradation of CR was also conducted in the presence of Cu-ZnO/TiO_2. The superior visible light absorption capacity was obtained for Cu-ZnO/TiO_2 NC catalyst resulting in complete degradation of CR within 20 min of sun-light irradiation (k_{app} = 0.094 min^{-1}). This implies that the NC photocatalyst synthesised via sonochemical approach can find its applications in the field of wastewater treatment for photocatalytic degradation of various dyes, phenolic compounds and other difficult-to-treat compounds.

Overall, it was observed that, the NC catalysts developed via sonochemical approach showed remarkable enhancement in the conversion of reactants, selectivity of products and the stability of these heterogeneous NC catalysts. The superior catalytic performance of the proposed NCs is the result of the synergistic effect of the constituent elements of respective heterostructures. The reusability studies (4-5 times) of as-prepared NC catalysts showed no significant loss in the activity of catalyst and conversion of reactants.

6.2 Future outlook

Supported bimetallic heterostructured nanocomposite catalysts are an important class of heterogeneous catalysts due to their remarkable catalytic properties that are different compared to the individual metal components. It is worthy of note that recent times have seen significant developments in the control of bi-metal particle morphology, dimensions and synthetic techniques. In line with this, some of future prospective studies of the present work could be possible based on the following considerations:

A. Glycerol oxidation with base free conditions using solid base catalysts

Early studies suggested the presence of a base is essential for the oxidation of glycerol to initiate the oxidation process resulting in the formation of organic salts. Thus, further separation and processing (neutralization and acidification) is required to obtain the free acids. Hence, the selective oxidation of glycerol in a base-free condition is important for both academic research and industrial application. Hence, subsequent works in the in the development of a stable solid base catalyst that can overcome the need for a basic environment, deactivation caused by the over-oxidation and/or strong adsorption of acids or ketones on the surface of metal NPs anticipated in the future.

B. Oxidation of 5-hydroxy methyl furfural using Pt-Cu/C & Cu-Ni/TiO_2 HNC catalysts

The catalytic performance of as-prepared catalysts Pt-Cu/C & Cu-Ni/TiO_2 can be examined for other biomass conversion reactions to obtain the value-added products, for instance oxidation of 5-hydroxy methyl furfural to 2,5-furan dicarboxylic acid.

C. Development of NC catalysts based on biopolymeric supports

Considering that the extraordinary physical and chemical properties of biopolymers continued research can be performed for design and fabrication of high-performance biopolymer - based composite catalysts.

D. Application of Cu-ZnO/TiO_2 NC photocatalyst for textile wastewater treatment

The pilot scale application of as-prepared Cu-ZnO/TiO_2 nanocomposite photocatalyst can be evaluated for treatment of wastewater from textile industries using sun-light driven degradation.

Overall, the future outlook for bimetallic nanoparticles is promising, with potential applications in various fields and the development of advanced synthesis techniques and integration with emerging technologies.

Research outcomes

International Journals

1. **Landge, V. K.,** Sonawane, S. H., Chaudhari, R. V., & Babu, G. U. B. (2020). Selective Oxidation of Glycerol: A Biomass-Derived Feedstock Using the Pt–Cu Janus Catalyst for Value-Added Products. Industrial & Engineering Chemistry Research, 60(1), 185-195. DOI: 10.1021/acs.iecr.0c04626 (IF-3.72, Q1)
2. **Landge, V. K.**, Sonawane, S. H., Sivakumar, M., Sonawane, S. S., Babu, G. U. B., & Boczkaj, G. (2021). S-scheme heterojunction Bi_2O_3-ZnO/Bentonite clay composite with enhanced photocatalytic performance. Sustainable Energy Technologies and Assessments, 45, 101194. DOI: 10.1016/j.seta.2021.101194 (IF-5.35, Q2).
3. **Landge, V. K.,** Sonawane, S. H., Manickam, S., Babu, G. U. B., & Boczkaj, G. (2021). Ultrasound-assisted wet-impregnation of Ag-Co nanoparticles on cellulose nanofibers: Enhanced catalytic hydrogenation of 4-nitrophenol. Journal of Environmental Chemical Engineering, 105719. DOI: 10.1016/j.jece.2021.105719 (IF-5.9, Q1).
4. **Landge, V. K.,** Hakke V. S., Sonawane, S. H., Kakunuri M., Babu, G. U. B., & Boczkaj, G. (2022). Synthesis of bimetallic Co-Pt/Cellulose nanocomposites for catalytic reduction of p-nitrophenol. Reaction Chemistry & Engineering. 7, 641-652. DOI: 10.1039/D1RE00422K (IF-4.23, Q2).
5. **V. K. Landge**, Huang, C. M., V. S. Hakke, S. H. Sonawane, S. Manickam & Hsieh, M. C. (2022). Solar-energy-driven Cu-ZnO/TiO2 nanocomposite photocatalyst for the rapid degradation of Congo red azo dye. Catalysts, 12(6), 605. (2022) (IF-4.1, Q1).
6. Shirish Sonawane, Manoj P Rayaroth, **Vividha K. Landge**, Kirill Fedorov, Grzegorz Boczkaj (2022).Thermally activated persulfate based Advanced Oxidation Processes–recent progress and challenges in mineralization of persistent organic chemicals: A Review. Current Opinion in Chemical Engineering. 37, 100839. DOI: 10.1016/j.coche.2022.100839. (IF-5.1, Q1).
7. Vikas S. Hakke, **Vividha Landge,** Shirish Sonawane, G. Uday Bhaskar Babu, Sivakumar Manickam, Grzegorz Boczkaj, Cu (II) ions removal from wastewater using starch nanoparticles (SNPs): An Eco-sustainable approach, Canadian Journal of Chemical Engineering, 2022. https://doi.org/10.1002/cjce.24588. (IF-1.9, Q2).
8. Vikas S. Hakke, **Vividha Landge**, Shirish H Sonawane, G Uday Bhaskar Babu, Muthupandian Ashokkumar, Erico MM Flores, The physical, mechanical, thermal and barrier properties of starch nanoparticle (SNP)/polyurethane (PU) nanocomposite films

synthesized by an ultrasound-assisted process Ultrasonics Sonochemistry, Vol. 88, 2022,106069, ISSN 1350-4177, https://doi.org/10.1016/j.ultsonch.2022.106069. (IF-7.49, Q1)

International Conferences

1. **V. K. Landge**, V S Hakke and S H Sonawane, "Facile Synthesis Of Bi_2O_3-Zno/Bentonite Clay Nanocomposites For Photo-Catalytic Degradation Of Congo-Red", 3rd International Conference on Waste Management-Recycle 2020, 13th and 14th February, 2020, IIT Guwahati.
2. **V. K. Landge**, V. S. Hakke, S. H. Sonawane, G. U. B. Babu, M. Kakunuri, "Synthesis of bimetallic Co-Pt/Cellulose nanocomposites for catalytic reduction of p-nitrophenol", 26th International symposium on Chemical Reaction Engineering & 9th Asia-Pacific Chemical Reaction Engineering, 5th – 8th Dec 2021, IIT Dellhi.
3. **V. K. Landge**, V. S. Hakke, S. H. Sonawane, Nilesh Jadhav, A. B. Pandit, "Ultrasound induced catalytic oxidation of Glycerol to value added products using Ni-Cu/TiO_2", Pacifichem Congress, Sonochemistry: Fundamentals & Applications, Symposium #105, 16th – 21st Dec 2021, Honolulu, Hawaii.

Book Chapters

1. Shital Balasaheb Potdar, **Vividha K. Landge**, Shrikant S. Barkade, Potoroko Irina, Shirish H. Sonawane, (2020) "Flavour encapsulation and release studies in food" in book "Encapsulation of Active Molecules and Their Delivery System" 1st Edition DOI: 10.1016/B978-0-12-819363-1.00016-8.
2. **Vividha K. Landge,** Vikas S. Hakke, Sneha A. Korpe, P. Venkateswara Rao, and, Shirish Sonawane, Hybrid systems using hydrodynamic cavitation / ultrasound / Fenton processes for effective treatment of wastewater, Novel Approaches Towards Wastewater Treatment and Resource Recovery Technologies, Edited by Arvind Kumar Mungray, Alka A. Mungray, Shriram Sonawane, Shirish Sonawane, Elsevier, August 1, 2022. ISBN: 9780323906272. http:// doi.org/10.1016/B978-0-323-90627-2.00003-4.
3. Sneha A. Korpe, **Vividha K. Landge**, Vikas S. Hakke, Shirish H. Sonawane, P. V. Rao and, Shriram S. Sonawane, AOPs for Petrochemical/Textile/Tannery industry wastewater treatment, Novel Approaches Towards Wastewater Treatment and Resource Recovery Technologies, Edited by Arvind Kumar Mungray, Alka A. Mungray, Shriram Sonawane, Shirish Sonawane, Elsevier, August 1, 2022. ISBN: 9780323906272. https://doi.org/10. 1016/B978-0-323-90627-2.00002-2.

4. Vikas S. Hakke, **Vividha K. Landge**, and Shirish Sonawane, R. W Gaikwad. Mathematical, numerical and experimental investigations of metal extraction processes, Applications of Nanofluids in Chemical and Bio-medical Process Industry, Edited by Shriram Sonawane, Hussein A. Mohammed, Arvind Kumar Mungray, Shirish Sonawane Elsevier, June 1, 2022. ISBN: 9780323905640. https://doi.org/10.1016/B978-0-323-90564-0.00012-X.